Hybrid Charge Transfer States at Inorganic/Organic Interfaces and their Role in Photovoltaic Charge Generation

Dissertation
zur Erlangung des akademischen Grades

doctor rerum naturalium
(Dr. rer. nat.)
im Fach Physik
Spezialisierung Experimentalphysik

eingereicht an der
Mathematisch-Naturwissenschaftlichen Fakultät
der Humboldt-Universität zu Berlin

von

Dipl.-Phys. Moritz Eyer

Präsidentin der Humboldt-Universität zu Berlin
Prof. Dr.-Ing. Dr. Sabine Kunst

Dekan der Mathematisch-Naturwissenschaftlichen Fakultät
Prof. Dr. Elmar Kulke

Gutachter*innen:

1. Prof. Dr. Oliver Benson
2. Prof. Dr. Emil J. W. List-Kratochvil
3. Prof. Dr. Wolfgang Brütting

Tag der mündlichen Prüfung: 20. Juli 2018

Abstract

In this work, a fundamental framework for the understanding of photovoltaic charge generation at metal-oxide/organic hybrid interfaces is established. It is shown that hybrid charge transfer states (HCTS) play a crucial role in the power conversion process. Prior to full charge separation, pairs of electrons and holes situated at opposite sides of the heterojunction remain bound to each other by Coulomb interaction. Only if an HCTS is dissociated before it recombines, a contribution to a photocurrent can be made.

Planar heterojunctions of the material combinations ZnO/P3HT, ZnMgO/P3HT, and SnO_2/P3HT serve as model systems for a broad investigation of interface energetics, photovoltaic power conversion and the loss processes therein. Hereby, variation of the Mg content in ZnMgO allows to tune the hybrid energy gap ΔE_{IO} between inorganic conduction band and organic highest occupied molecular orbital (HOMO). A combined analysis of the electronic structure of the interface and the corresponding photovoltaic performance, also as a function of temperature, reveals that an HCTS consists of an electron in the conduction band of the metal-oxide and a hole in the HOMO of the polymer. Consequently, its formation is an intrinsic property of all metal-oxide/organic heterojunctions, independent of their chemical composition, interface morphology and the existence of localized trap states for carriers at the interface.

Electroluminescence (EL) spectroscopy proves to be a powerful tool in the analysis of HCTS and their physical properties. Their radiative recombination produces a broad signal in the near-infrared spectral range. Voltage-dependent EL measurements reveal a high degree of delocalization of both carriers in an HCTS, whereas EL spectra recorded over a wide range of temperatures show that non-radiative processes are by far the dominant recombination channel for HCTS at room temperature. During their long lifetime in the range of $500\,\mathrm{ns}$, electron and hole in an HCTS are able to migrate geminately along the interface plane.

A multistep model for a detailed description of the charge generation process in a metal-oxide/organic photodiode is derived from temperature-dependent measurements of the photovoltaic efficiency. It becomes apparent that the binding energy of electron and hole in an HCTS does not impose a significant limitation on device performance. The strong presence of non-radiative decay processes, however, causes severe losses both in photocurrent and open circuit voltage for all material systems that are investigated in this work.

It can be concluded that a single metal-oxide/organic heterojunction does not suffice for efficient charge separation in photovoltaic devices. In future research, tailored inorganic acceptor materials can serve to funnel charge carriers away from the interface in order to prevent their recombination. This work provides guidance for optimization of inorganic/organic hybrid photovoltaic devices.

Zusammenfassung

In dieser Arbeit wird ein grundlegender Rahmen für das Verständnis von photovoltaischer Ladungserzeugung an Grenzflächen zwischen einem Metalloxid und einem organischen Halbleiter geschaffen. Dabei wird gezeigt, dass hybride Ladungstransferzustände (HCTS) eine entscheidende Rolle im Energieumwandlungsprozess spielen. Vor ihrer endgültigen Trennung bleiben Elektronen und Löcher an gegenüberliegenden Seiten der Grenzfläche durch Coulomb-Interaktion aneinander gebunden. Nur wenn die Trennung eines solchen HCTS vor seiner Rekombination erfolgt, kann es zu einem Photostrom beitragen.

Planare Schichtsysteme der Materialkombinationen ZnO/P3HT, ZnMgO/P3HT und SnO_2/P3HT dienen als Modellsystem für eine ausführliche Studie über Energiestruktur der Grenzfläche, photovoltaische Energieumwandlung und die damit verbundenen Verluste. Durch Variation des Magnesiumgehalts in ZnMgO kann hierbei die Grenzflächen-Bandlücke ΔE_{IO} zwischen anorganischem Leitungsband und organischem HOMO verändert werden. Eine kombinierte Analyse von elektronischer Struktur der Grenzfläche und photovoltaischer Effizienz, auch in Abhängigkeit der Temperatur, zeigt, dass ein HCTS aus einem Elektron im Leitungsband des Metalloxids und einem Loch im HOMO des Polymers besteht. Folglich ist seine Entstehung eine intrinsische Eigenschaft von allen Grenzflächen zwischen einem Metalloxid und einem organischen Halbleiter, unabhängig von deren chemischer Zusammensetzung, Grenzflächenmorphologie oder dem Vorhandensein von lokalisierten Fallenzuständen für Ladungsträger an der Grenzfläche.

Elektrolumineszenzspektroskopie (EL) stellt sich als wirksame Methode zur Untersuchung von HCTS und deren physikalischen Eigenschaften dar. Deren strahlende Rekombination produziert ein breites Signal im nahen Infrarotbereich. Spannungsabhängige EL-Messungen zeigen den hohen Grad an Delokalisierung von beiden Ladungsträgern in einem HCTS. Elektrolumineszenzspektren, die über einen weiten Temperaturbereich aufgenommen wurden, zeigen, dass nichtstrahlende Prozesse mit Abstand der dominierende Zerfallsmechanismus für HCTS bei Zimmertemperatur sind. Während ihrer langen Lebensdauer um $500\,\mathrm{ns}$ sind Elektron und Loch in einem HCTS gemeinsam mobil in der Ebene parallel zur Grenzfläche.

Ein Modell aus mehreren Schritten für eine detaillierte Beschreibung des Stromerzeugungsprozesses kann aus temperaturabhängigen Messungen der photovoltaischen Effizienz abgeleitet werden. Hierbei wird deutlich, dass die Bindungsenergie von Elektron und Loch in einem HCTS keine bedeutende Einschränkung für die Leistungsfähigkeit einer Solarzelle darstellt. Die einflussreiche Rolle von nichtstrahlenden Zerfallsprozessen verursacht jedoch schwere Verluste sowohl an Photostrom, als auch an Leerlaufspannung. Dies gilt für alle Materialsysteme, die in dieser Arbeit untersucht werden.

Folglich genügt eine einzelne Grenzfläche zwischen einem Metalloxid und einem organischen Halbleiter nicht, um effiziente Ladungstrennung in Solarzellen zu erreichen. Künftige Forschung wird sich darauf konzentrieren, mit speziell angepassten anorganischen Schichtsystemen zu erreichen, dass Ladungsträger von der Grenzfläche wegbewegt werden, um ihre Rekombination zu verhindern. Diese Arbeit bietet somit Leitlinien zur Optimierung von organisch/anorganischen Hybridsolarzellen.

Contents

Chapter 1

Introduction

"Little darling, it's been a long cold lonely winter,
Little darling, it feels like years since it's been here.
Here comes the sun,
Here comes the sun, and I say,
It's all right."

The Beatles

In recent time, consequences of a global climate change are becoming more and more apparent. Hurricanes and typhoons bring devastation upon a steadily growing number of countries and cities in tropical and subtropical regions. At the same time, in temperate zones periods of aridity can cause severe bushfires and lead to desertification of formerly fertile landscapes. Thunderstorms and inundations cause thousands of fatalities each year and leave an even higher number of persons without shelter.

Sea levels have risen by ca. $20\,\mathrm{cm}$ since the pre-industrial age as a consequence of global warming and melting of ice in polar regions. Depending on future development of ambient conditions, a total sea level rise of $1\,\mathrm{m}$ or even more appears to be realistic in scientific models. Such a surge would permanently drown an area of $150\,000\,\mathrm{km}^2$, corresponding to almost half the size of Germany. A total of 180 million persons would lose their homes, including more than 20 million persons alone in Egypt and Bangladesh. Several islands might be lost entirely.[1]

The crucial parameter to long-term living conditions on planet Earth is the future development of global average temperature. In the Paris Agreement, which was established in 2015 and signed by 195 countries since then, the target of limiting global warming was sharpened to a value near $1.5\,\mathrm{K}$, compared to the Kyoto agreement of 1997 which contained a value of $2.0\,\mathrm{K}$. This tightening became necessary for preventing severe climatical consequences especially to poorer countries in the global south.

Either of these goals can only be reached by tremendous efforts in all parts of the earth. Following calculations of the United Nations Environment Programme, CO_2 emissions will have to be cut by nothing less than 90 % until 2050.[2] Swedish sustainability scientist Johan Rockström proposes a law guiding the path to this ambitious goal: Global CO_2 emission has to be halved every 10 years, while at the same time the share of carbon-free energy production is doubled every 5 to 7 years. The latter of these conditions has already been fulfilled in the last 15 years: The percentage of emission-free energy production is currently doubling every 5.4 years and reached a global average value of 2.8 % in 2015.[3] Thanks to extensive subsidies for regenerative energies, Germany is one of the leading countries with a ratio of 31.7 % regenerative electrical energy in 2016.[4]

A steadily growing share of carbon-free energy is provided by photovoltaic power conversion. Solar radiation is a quasi-unlimited source of energy, which means that it can be exploited for energetic supply in the long run, far beyond the reach of any natural resources on earth. By directly converting sunlight into electrical energy, no further transformation process is necessary, which simplifies the supply chain and evades further losses. In 2015, already 6 % of all energy consumption in Germany was supplied by solar cells. Thanks to rapid progress in technology and fabrication, solar energy has become cheaper and cheaper in the last decades. Starting from 1977, when the first commercial silicon solar cell modules cost 76 $ per Watt, the price dropped to 6 $/W by the year 2000 and is merely 0.37 $/W in 2016.[5] Similar to Moore's Law for the development of microprocessor performance, *Swanson's Law* has been established from observations on solar cell fabrication: The price of photovoltaic modules tends to drop 20 percent for every doubling of cumulative shipped volume. If external costs of energy production like environmental damage and adverse health effects are added to the price of electrical power, photovoltaic energy is already cheaper than traditional forms of energy like coal combustion and nuclear power.[6]

Over the last 40 years, photovoltaic technology has grown from laboratory research to an energy source which is suitable for the masses. However, modern devices still have their drawbacks. While device efficiencies in operation steadily approach the boundaries of the theoretically possible like the Shockley-Queisser limit of maximally 33.2 % power conversion efficiency,[7] device fabrication still requires a large investment of energy. Typical modern solar modules made from crystalline silicon have to run for up to 6 years before they reach their energetic break-even point.[8] In order to compensate for poor light absorption in silicon, active layers of solar cells have to be as thick as several hundreds of micrometers. Efficient charge transport can only be provided in a material of high crystallinity. Consequently, a high energy investment is necessary for crystal growth in device fabrication.

A solution to this dilemma can be provided by new semiconductor materials. Organic semiconductors like small molecules and polymers show a significantly stronger light-matter coupling, thus allowing for thinner absorption layers by several orders of magnitude. Combining organic materials of different chemical composition and physical properties, a donor-acceptor system for efficient charge separation at the interface can be established. The combination of the polymer *Poly(3-hexylthiophene)* (P3HT) and the fullerene derivative PCBM as the most extensively studied organic heterojunction delivers power conversion efficiencies of up to 5 % with typical layer thicknesses of only 50 to $100\,\mathrm{nm}$.[9] Fabrication of organic solar cells is energetically inexpensive and easily scalable, but their efficiency is seriously limited by poor transport and extraction of electrons and holes to the electrodes after the charge separation process. Furthermore, low stability of organic materials leads to device degradation under ambient conditions and requires a chemically resistive encapsulation.

Considering advantages and drawbacks of organic and inorganic materials, the next logical step is to combine both of them to form a hybrid device. Phyisical limitations of both material classes can be overcome by exploiting both efficient light absorption in an organic donor and good transport ability in a crystalline inorganic acceptor material. Previous studies proved the general functionality of hybrid photovoltaic devices involving several acceptor materials like ZnO, CdSe and TiO_2.[10–12]

Zinc oxide presents itself as a particularly promising candidate for hybrid photovoltaics due to its high availability and ease of fabrication. Due to its high work function of ca. $4\,\mathrm{eV}$, it forms a type II interface with most organic semiconductor materials. Such an energetic situation is necessary for dissociation of excitons produced by light absorption on either side of the interface. Furthermore, ZnO allows tailoring of nanostructures like nano-rods and nano-fibers and can form part of a bulk heterojunction if dispersed as nano-particles. Using these device morphologies, power conversion efficiencies between $0.5\,\%$ and $2\,\%$ can be reached.[13–15] All of them, however, fail to catch up with device efficiencies of bulk heterojunctions of P3HT and PCBM.

In this work, the physical background for these limitations in hybrid photovoltaic devices will be elucidated. A detailed physical model for the charge separation process will be derived and the role of recombination losses will be analyzed. Instead of optimizing device performance, a simplistic planar device layout with an atomically flat interface is chosen, allowing for exact quantification of photocurrent and losses in order to understand the underlying processes. Bound states formed by an electron and a hole situated on opposing sides of the hybrid interface, denominated as hybrid charge transfer states (HCTS) here, play a key role: Only if the Coulomb interaction between them is overcome, both carriers can reach their respective electrodes and contribute to a photocurrent. Once electron and hole in an HCTS recombine instead of being dissociated, they are lost for photocurrent generation and contribute to the pile of photovoltaic loss instead.

The process of charge separation and physical properties of HCTS will be investigated using planar model diodes combining a crystalline oxide (ZnO, ZnMgO or SnO_2) and the widely investigated polymer P3HT. A combined analysis of diode characteristics in the dark, photovoltaic measurements and electroluminescence spectroscopy will provide detailed insight into the processes of charge separation and recombination. All measurements are performed over a wide range of temperatures and thus provide a deep insight into the underlying physical processes.

After this short introduction, the fundamentals of semiconductor physics will be explained in chapter 2, along with an overview on current knowledge about photodiode device physics.

Donor and acceptor materials used for sample fabrication in this work are presented in chapter 3. Device architecture of model photodiodes is shown and the fabrication procedures are explained, particularly molecular beam epitaxy (MBE) for inorganic materials and spin-coating for organic polymers.

All measurement procedures conducted in the research for this work are presented in chapter 4.

Instrumentation and methods of data analysis are explained in all necessary detail, particularly for UV photoelectron spectroscopy, photovoltaic measurements and electroluminescence (EL) spectroscopy.

Chapter 5 is the first chapter to present experimental results. Photovoltaic functionality of planar ZnO/P3HT diodes is studied here and diode characteristics are analyzed. Electroluminescence spectra of direct recombination of electron and hole in an HCTS are presented. All three methods allow a rough estimate of the interface energetics between organic and inorganic component.

In chapter 6, ZnMgO/P3HT is set up as a model system for a quantitative study of interface energetics. Variation of the Mg content x in the alloy $\mathrm{Zn}_{1-x}\mathrm{Mg}_x\mathrm{O}$ from 0.01 to 0.14 allows to tune the hybrid energy gap ΔE_{IO} between organic HOMO and inorganic conduction band. In order to derive a detailed model of interface energetics, UV photoelectron spectroscopy measurements of the hybrid gap are compared to the results of temperature-dependent photovoltaic measurements and spectral positions of HCTS EL peaks. An in-depth study of EL spectra and their transients provides insight into the HCTS recombination process. From a temperature-dependent analysis of the photovoltaic quantum efficiency a multistep model for the charge separation process in a hybrid photovoltaic device can be postulated and insight into thermal activation energies of the underlying processes can be gained.

The combination of tin oxide and P3HT is presented in chapter 7 as an alternative material following reports on rapid and efficient charge separation at a $\mathrm{SnO_2}$/organic interface.[16] The photovoltaic potential of this material combination is evaluated and the possible influence of interfacial trap states in $\mathrm{SnO_2}$/P3HT diodes is discussed.

In chapter 8 the experimental results gained in the three previous chapters are compared in the search of a common model for charge generation in inorganic/organic hybrid photovoltaic devices. Qualitative differences between the three material systems are discussed and their overall photovoltaic efficiency is evaluated.

Chapter 9, provides the final conclusions gained in the course of this work. This includes a summary on HCTS and their role in photovoltaic power conversion. The models for charge separation and recombination losses are described in brief, and an overview on interface energetics and photovoltage losses is given for all three material systems. At last, a path towards more efficient photovoltaic devices is shown by learning the lesson from the race between dissociation and recombination of carriers at the hybrid interface.

These results will hopefully contribute to the future development of photovoltaic devices, which unify high conversion efficiencies and low production cost both in money and primary energy. Furthermore the use of toxic materials and limited mineral deposits can possibly be reduced by intelligent combinations of such disparate substances like inorganic crystals and organic molecules or polymers. Facing a steadily increasing demand for electric energy around the globe, a ”Herculean effort” will be necessary in the transformation towards carbon-free energy supply.[3]

”There is no lack of renewable energies. There is a lack of time.”
(Hermann Scheer 1944 - 2010, German politician)

Chapter 2

Fundamentals

In this chapter, fundamental knowledge on semiconductor materials and device physics necessary for understanding the process of photovoltaic power conversion in hybrid inorganic/organic photodiodes will be provided.

The first section gives a brief description of inorganic and organic semiconductor materials and introduces the concept of excitons and charge transfer states. In the following, different categories of photovoltaic devices are presented. A schematic outline of the physical processes converting optical excitations into an electric current is drawn for each device type.

Finally a general overview on device physics of hybrid inorganic/organic heterojunctions is given along with the essential parameters for assessment of device performance. The influence of radiative and non-radiative recombination is discussed as well as the role of hybrid charge transfer states and transport phenomena.

2.1 Basic Semiconductor Physics

In a single atom or small molecule, an electron is only allowed to occupy certain discrete energy levels. Depending on the number of electrons in a system, these states can be either occupied by an electron or unoccupied. In the absence of thermal fluctuations, the Fermi energy E_F marks the energy of the highest occupied state with only unoccupied states following above. In an extended crystalline solid, these discrete energy levels expand to a continuum of states as a consequence of interactions with a regular lattice. Consequently, a band structure is formed, providing 'allowed' energy ranges which can be populated by electrons and 'forbidden' energy gaps without available states. Depending on the energetic positions of occupied and unoccupied bands in relation to the Fermi energy, all crystalline solids can be subdivided into three classes: Isolators, semiconductors and metals.[17]

In an isolator, the gap between fully occupied and unoccupied states is so large that hardly any electrons can reach excited states allowing for charge transport. Consequently, all electrons are bound to their sites in the lattice and no electric current is possible by applying an external bias to the solid.

In a metal, the Fermi energy is situated within a band of states, which is then partially occupied with electrons. This mixture of electrons and free sites allows them to move around freely in the solid, which thus is conductive.

A semiconductor is a material, in which the gap of 'forbidden' states between the highest occupied energy band (valence band) and the lowest unoccupied band is small enough that a certain amount of electrons can populate the region above the forbidden zone, which is then called 'conduction band'. Charge transport is possible by either moving electrons in the conduction band or unoccupied states in the valence band. These empty sites are commonly called 'holes' and can be treated as a quasi-particle with a positive charge. Applying an external bias to a semiconductor material, holes appear to be moving in the opposite direction of the electron flow. Consequently, the transported charge is the sum of electron and hole current. Apart from thermal excitation, the concentration of free carriers in a semiconductor can also be manipulated by optical excitation or electric fields.[18]

2.1.1 Excitons in Semiconductors

When a photon is absorbed by a semiconductor solid an electron from the valence band or highest occupied orbital is lifted into the conduction band or lowest unoccupied orbital whereby a hole remains in its previous site. Electron and hole interact with each other by Coulomb interaction and can form bound states. Depending on the dielectric constant of the environment excitons can take different shapes, which are characterized by two limiting cases: Wannier-Mott excitons and Frenkel excitons.

2.1.1.1 Wannier-Mott Excitons

In materials with a high dielectric constant the interaction between charged carriers is significantly reduced. This leads to a large binding radius between electron and hole of an exciton, extending over many unit cells. Electron and hole can be described as separate particles, forming a system of a positive and negative charge which can be described by the same quantum mechanical model as a hydrogen atom.[19] The binding energy of Wannier-Mott excitons in inorganic crystalline materials is as low as a couple of meV, which in some materials like silicon directly leads to direct dissociation due to thermal activation at room temperature. In other crystalline semiconductors like ZnO Wannier-Mott excitons are stable at room temperature with a binding energy of ca. $60\,\mathrm{meV}$. This leads to a stronger light-matter coupling, which even allows to reach the strong coupling regime in suitable cavity structures.[20]

2.1.1.2 Frenkel Excitons

In semiconductors with a low dielectric constant and little screening the strong interaction between electron and hole results in a small exciton binding radius. The electron-hole pair can then be treated like a single particle.[21] A typical binding radius of a Frenkel exciton is at the scale of a unit cell of a semiconductor. Particularly in organic semiconductors this behavior can be observed, where electron and hole can both be located even on the same molecule like in fullerene. The binding energy of a Frenkel exciton can be in the range of $100\,\mathrm{meV}$ up to $1\,\mathrm{eV}$.

As the sum of charges in an exciton is zero they barely interact with a neutral crystal lattice in their surroundings. Consequently excitons are mobile in semiconductors which can be described as a diffusion or hopping process. Exciton diffusion lengths can vary from a few nanometers in organic molecular systems or polymers[22] to over $1\,\mathrm{\mu m}$ in perovskites.[23] Transport phenomena in disordered organic semiconductors are described in more detail in section 2.3.7.

2.1.2 Charge Transfer States

A *charge transfer state* (CTS), a special type of bound state between an electron and a hole can form at the frontier between two different semiconductor materials when electron and hole are residing on different sides of the interface. A fundamental requirement is a so-called staggered gap or type II level alignment, when both electron affinity and ionization potential of one material are higher than their counterparts on the other side of the interface. The component with the lower electron affinity and ionization potential is then called the *donor*, the material with the deeper lying energy levels is the *acceptor*. Between valence band or HOMO of the donor and the conduction band or LUMO of the acceptor an interface energy gap ΔE_{DA} is formed which is smaller than either of the band gaps of both materials. In case of a hybrid heterojunction formed by an organic donor and an inorganic acceptor this energy gap will be denominated ΔE_{IO}.

The properties of a charge transfer state are determined by the materials on both sides of the heterojunction as the wavefunction of an electron-hole pair extends to both sides of the interface. Its spatial extension into each of the components depends on the dielectric function of the materials, as on both sides different screening effects are active. The interaction between electron and hole can be described by a spatially averaged form of Coulomb's law which accounts for the different contributions of both materials to the hybridized state:

$$E_{\mathrm{B}}(r) = \frac{q^2}{4\pi\hat{\epsilon}r} \tag{2.1}$$

where q is the elementary charge, r the binding radius of electron and hole and $\hat{\epsilon} = \hat{\epsilon}_0 \cdot \hat{\epsilon}_{\mathrm{r}}$ is the averaged dielectric constant in the interface region, calculated as a weighted average over donor and acceptor material. The transition energy of a charge transfer state is then given by the interface energy gap reduced by the binding energy of the charge transfer state:

$$E_{\mathrm{CTS}} = \Delta E_{\mathrm{DA}} - E_{\mathrm{B}}. \tag{2.2}$$

In case of a very loose binding between electron and hole, the binding energy can be neglected and the transition energy of a CTS approaches the interfacial energy gap.

$$E_{\mathrm{CTS}} \approx \Delta E_{\mathrm{DA}} \tag{2.3}$$

In many inorganic heterojunctions the binding energy E_{B} is small compared to the thermal energy $k_{\mathrm{B}}T$ at room temperature and CTS instantaneously dissociate into free charges.

2.1.3 Charge Transfer States at Organic Interfaces

In organic photovoltaic systems like heterojunctions of polymers (e.g. P3HT or PTB7) and fullerenes or fullerene derivatives (e.g. $\mathrm{PC_{70}BM}$) charge transfer states and their role in the charge generation process have been extensively studied in recent years.[24] The wavefunction overlap of electron and hole has been found to be large enough to observe radiative recombination of charge transfer states both in electroluminescence[25, 26] and photoluminescence.[27] In bulk heterojunctions with their enhanced interface area, direct absorption of charge transfer states in organic donor-acceptor systems has also been observed, relating the properties of CTS to a combination of both materials involved.[25, 28] Due to the low dielectric constants in organic materials the binding radius of charge transfer states is assumed to be small and the carriers tend to be localized in direct proximity of the interfaces with a comparatively high binding energy. However no thermally activated dissociation of electrons and holes from charge transfer states have been observed in photovoltaic measurements so far.

In photoluminescence quenching measurements under an external electric field the binding energy of a CTS in a polymer-fullerene system has been determined to be as small as $46\,\mathrm{meV}$, compared to values of ca. $400\,\mathrm{meV}$ for singlet excitons in a pristine polymer.[29] This indicates that even in organic systems, the excitonic binding across an interface is rather loose. Under these conditions, thermal fluctuations in the molecular order at the interface are likely to facilitate charge separation. Furthermore, the role of tunneling processes,[30, 31] dynamic disorder and entropy[32] have been discussed to explain the absence of a thermal activation of photocurrent generation.

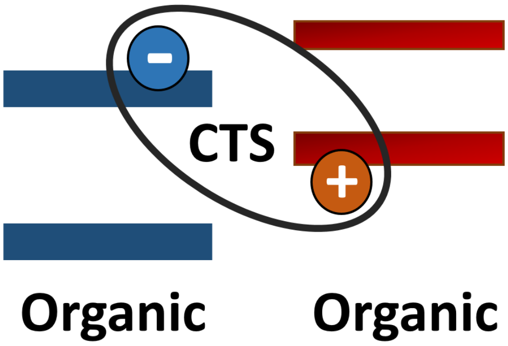

Figure 2.1: Schematic depiction of a charge transfer state at the heterojunction between an organic donor (red) and an organic acceptor (blue).

Charge transfer states have shown to be the decisive element in mediating the photovoltaic process in organic solar cells and determining all parameters of the resulting solar cell. Especially the open circuit voltage V_{OC} (see section 2.3.1) has been closely related to the interface energy gap at an organic heterojunction.[25, 33–36] On the other hand radiative and non-radiative interface recombination have shown to be the dominating loss mechanism in organic solar cells. Charge transfer states at photovoltaic heterojunctions are steadily subjected to a competition between dissociation and recombination. Only if they dissociate into free carriers fast enough they give rise to a photocurrent, otherwise they are annihilated and contribute to the losses, regardless of the exact mode of radiative or non-radiative recombination.

By means of Marcus theory (see 2.3.3) the transition energy of a charge transfer state has been connected to both emission and absorption processes at an interface.[25] Once its binding energy is known, UV photoelectron spectroscopy provides another access to the determination of E_{CTS}.[33]

2.1.4 Charge Transfer States in Hybrid Inorganic/Organic Heterojunctions

In recent time, existence and properties of *hybrid charge transfer states* (HCTS) at interfaces between inorganic and organic materials have become an important question. Due to the higher charge mobility and larger dielectric constant of crystalline inorganic semiconductors HCTS are expected to be even less localized on the inorganic side (see figure 2.2), which favors their dissociation and facilitates photovoltaic energy conversion. However, ab-initio calculations by *Wu et. al.* proposed the existence of bound charge transfer states between ZnO and polymers[37] and located them in close proximity to the interface, in contradiction to previous expectations. This would make them an obstacle in charge separation at photovoltaic heterojunctions which has to be overcome. In pump-push measurements by *Vaynzof et. al.* the contribution of HCTS at a ZnO/polymer interface to photovoltaic performance and the photocurrent losses due to HCTS recombination have been shown.[38]

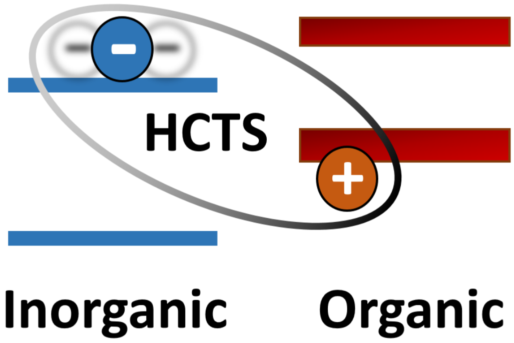

Figure 2.2: Schematic depiction of a hybrid charge transfer state at the heterojunction between an organic donor (red) and an inorganic acceptor (blue).

Direct absorption of HCTS at an interface of ZnO and small molecules have been shown by *Piersimoni et. al.* as well as their radiative recombination in electroluminescence measurements.[39] It has been shown that the transition energy of HCTS is directly linked to the interface energetics. It can be manipulated by application of self-assembled monolayers on the ZnO surface introducing an interface dipole between inorganic and organic component.[39, 40] Still subject of broad discussion is the exact shape of charge transfer states and their spacial extension into both inorganic and organic layer. Furthermore, it remains unclear, whether electron and hole are either trapped in a surface state or able to move freely in the conduction band while they form part of an HCTS.[41] Extensive theoretical work on the effect of HCTS in inorganic/organic structures has been done by *Renshaw and Forrest.*[42]

The transition energy of an HCTS E_{HCTS} is determined by the energetic difference ΔE_{IO} between the bands or orbitals, in which electrons and holes are situated. The strength of Coulomb interaction imposing a binding energy E_{B} has to be subtracted from this value.

$$E_{\text{HCTS}} = \Delta E_{\text{IO}} - E_{\text{B}} \tag{2.4}$$

If only band-to-band transitions are considered, ΔE_{IO} is defined by the difference between inorganic conduction band and organic HOMO. For systems involving carriers in localized trap states, E_{HCTS} is further reduced by the energetic depth of traps.

In this work the existence of hybrid charge transfer states on several inorganic/organic interfaces will be proven by electroluminescence measurements. A connection between interface energetics, HCTS transition energy and photovoltaic properties will be established, and the role of HCTS in the charge separation process will be elucidated. Finally the origin of losses in photovoltaic performance will be identified and a strategy to overcome this drawback will be proposed.

2.2 Photovoltaic Power Conversion

A solar cell is a contraption for direct conversion of incident light into electrical energy. The energy carried by photons serves to generate pairs of opposite charges which are extracted to two separate contacts of the device, cathode and anode. The potential difference between them allows to drive a load circuit using the energy converted from absorbed light.

2.2.1 Different Types of Photovoltaic Devices

For establishing a solar cell, at least one semiconducting material is necessary. Depending on their internal functionality, photovoltaic devices can be divided into several types. Two device concepts which form extreme points in functionality will be presented here in detail: p-i-n junction and donor-acceptor heterojunction. Two other commercially relevant device types, dye-sensitized solar cells and Perovskite cells can be seen as intermediate points between both previously mentioned concepts and are briefly presented here.[43]

p-i-n Junction Solar Cells

In a p-i-n junction (or p-n junction) a slab of an undoped crystalline semiconductor is sandwiched between two collector layers, of which one is n-type doped with foreign atoms forming donors and the other p-type doped in order to form acceptor states.[18, 44] Upon light absorption in the intrinsic i-type layer, the emerging excitons are dissociated rapidly from each other by thermal energy at room temperature and able to diffuse freely through the crystalline lattice. When reaching the doped layers of the devices, electrons and holes get extracted by the n-type and p-type doped layers, respectively. Commonly, the absorption layer also has a slight background doping, forming a space charge region which provides an electric field across the device and thus accelerates both types of carriers towards the doped regions on the top and bottom of the device. The most common material for p-i-n type solar cells is silicon. It provides rapid exciton dissociation and high carrier mobilities. Its low absorption coefficient, however, requires active layers in single-crystalline quality of more than $100\,\mu\mathrm{m}$ thickness to collect enough light for efficient power conversion. High consumption of material and power in the fabrication process curtail both ecologic benefit and economic prospects of silicon solar cells. Their efficiency is approaching the technical limit of $33.2\,\%$ set by the Shockley-Queisser limit,[7] the best efficiency of a silicon single junction cell is noted at $25.6\,\%$ as of 2014. In recent years, alternatives to single-crystalline silicon were investigated like the use of polycrystalline silicon as well as thin-film solar cells with reduced material consumption.

Donor-acceptor Solar Cells

In a donor-acceptor or excitonic solar cell, light absorption does not produce free electrons and holes instantly. Instead, both carriers are tied to each other by Coulomb interaction and form an exciton. The energy necessary for its dissociation exceeds the thermal potential at room temperature. Consequently an interface between donor and acceptor material is necessary for a sufficiently strong electric field as driving force to separate electron and hole from each other. After charge separation electrons and holes are collected by electrodes. Suitable interlayers adjacent to the electrodes can offer selectivity for electrons or holes in order to prevent leakage current of the 'wrong' carrier type as this would reduce the charge separation efficiency. The most common form of donor-acceptor heterojunctions are organic solar cells with an interface involving polymers or small molecules as donor and fullerene or its derivatives as acceptor. Recent organic solar cells offer power conversion efficiencies over $10\,\%$ and are currently reaching the threshold of widespread commercialization.[45–47] In this work an alternative form of donor-acceptor heterojunction will be discussed, the combination of a polymer and a crystalline wide band gap semiconductor. Therefore the function of this device type will be discussed in section 2.2.2 in more detail.

Dye-sensitized Solar Cells

In dye-sensitized or *Grätzel cells*[48] a molecular dye attached to an wide band-gap semiconductor surface acts as light absorber. Charge separation occurs by injection of an electron from the dye molecule to the conduction band of the solid. After passing the consumption circuit the electrons get injected into an electrolyte solution. From there they diffuse back to the oxidized dye molecule in order to reestablish its oxidized ground state. Dye-sensitized solar cells can be seen as a special form of donor-acceptor system in which not single charges are mediating the conversion process, but whole charged particles. As charge separation can only occur where solid absorber and electrolyte solution are in contact only the direct proximity of the interface can contribute to energy conversion. Therefore the dye molecules are commonly anchored in a porous 3D matrix of a wide gap semiconductor like TiO_2. Current prototypes of dye sensitized solar cells offer conversion efficiencies of more than 10 %. However, rapid degradation limits the practical use of this device type.

Perovskite Solar Cells

Lately, a new class of photovoltaic devices has rapidly emerged, reaching impressive conversion efficiencies after only few years of development.[49] In perovskite solar cells, the active medium is formed by a cubic crystalline metal halide framework embedding small organic ions. Perovskites allow a high carrier mobility and strong optical absorption at the same time, which are very favorable properties for photovoltaic devices. The functionality of perovskite cells is similar to a p-i-n junction. The interplay of organic and inorganic materials, however, also resembles charge separation mechanisms of donor-acceptor heterojunctions. In recent development, halide perovskite solar cells reached efficiencies of over 20 %.[50] On the way to commercialization two issues still have to be solved: Device stability and the use of toxic ingredients like Pb which are banned from electronic devices e.g. by directives of the EU.[51]

2.2.2 Donor-Acceptor Heterojunctions

In a donor-acceptor heterojunction charge separation occurs at the interface between two different materials. Commonly, the donor acts as light absorber, providing excitons for charge separation, but in certain material systems both components can give their contribution. Due to their very effective light-matter coupling, organic semiconductors offer the possibility to reduce the thickness of absorber layers in photovoltaic devices to the range of $100\,\mathrm{nm}$ and less.

The fundamental requirement for charge separation in a donor-acceptor heterojunction is a type II energy level alignment or *staggered gap* at the interface. Both ionization potential and electron affinity of the acceptor material have to be higher than their counterparts of the donor. The difference in electron affinity ΔE_C provides the driving force for an electron in the donor's LUMO to transfer to the acceptor material while the difference in ionization potentials ΔE_V forms a barrier which impedes the transfer of holes to the acceptor as depicted in figure 2.3. The energy difference between the HOMO or valence band maximum of the donor and the LUMO or conduction band minimum of the acceptor will be called *interface energy gap* in the following, and denominated ΔE_DA for organic donor-acceptor systems respectively ΔE_IO for inorganic-organic hybrid systems.

Light absorption in the acceptor provides the reverse case in which only holes can transfer to the

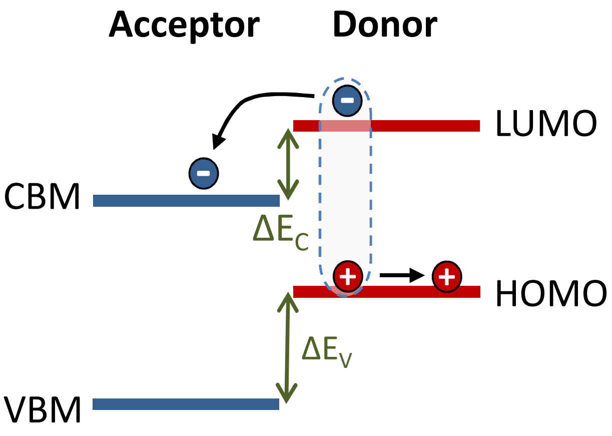

Figure 2.3: A type II interface formed by an organic donor and an inorganic acceptor. Power conversion occurs by light absorption in the donor and subsequent electron transfer to the acceptor.

donor material and electrons are blocked by the energy difference between the LUMO orbitals or conduction band. Consequently in donor-acceptor heterojunction solar cells light absorption in both components can contribute to a photocurrent as it has already been observed in the most common combination for organic photovoltaics of the polymer poly(3-hexylthiophene) (P3HT) and the fullerene derivative PCBM.[52]

Charge separation in donor-acceptor heterojunctions can only occur if the excitons produced upon light absorption reach the interface between donor and acceptor material before they recombine. Consequently, the limited exciton diffusion length in all organic semiconductor restricts the power conversion process to a thin slab of a few nanometers in direct vicinity of the interface.[22] Therefore, in order to increase the attainable photocurrent, the contact area between donor and acceptor has to be maximized by employing nanostructured surfaces, bulk heterojunctions or nanoparticles. In hybrid photovoltaics commonly the acceptor material is replaced by a crystalline inorganic semiconductor which provides efficient charge transport at the cost of a weaker light absorption ability. As a consequence in most hybrid systems only light absorption in the donor material significantly contributes to power conversion.

A crucial parameter for the performance of a donor-acceptor heterojunction is the charge separation efficiency at the interface. After transferring an electron from the LUMO of the donor to the LUMO or conduction band of the acceptor both charge carriers still are subjected to an attractive Coulomb interaction, so they can form bound states at the interface, so called *hybrid charge transfer states* (HCTS). If full charge separation is not possible during the mean lifetime of an HCTS, losses due to interfacial recombination will decrease the device efficiency. The properties of HCTS in different photovoltaic systems are discussed in section 2.1.4.

In summary the efficiency of a donor-acceptor heterojunction as a photovoltaic device is a product of six independent factors

$$\eta = \eta_{\text{absorption}} \cdot \eta_{\text{diffusion}} \cdot \eta_{\text{transfer}} \cdot \eta_{\text{dissociation}} \cdot \eta_{\text{transport}} \cdot \eta_{\text{extraction}} \tag{2.5}$$

of which $\eta_{\text{absorption}}$ is the absorption coefficient of the donor layer, $\eta_{\text{diffusion}}$ describes the probability of an exciton to diffuse to the interface. η_{transfer} is the probability of a charge tranferring to the acceptor and it depends on the coupling strength of donor and acceptor material, $\eta_{\text{dissociation}}$ is the ratio of electron-hole pairs dissociating at the interface, $\eta_{\text{transport}}$ gives the transport efficiency for single charges to the opposing electrodes and $\eta_{\text{extraction}}$ represents the extraction efficiency of single charges into the contacts and further into the consuming circuit. All six parameters depend on the choice of materials in the device, but only the efficiencies of charge dissociation,[53] transport and extraction depend on the electric field in the device.

2.3 Photovoltaic Device Physics

2.3.1 Photodiode Modeling and Performance Parameters

In the following section, the theoretical description of a photovoltaic device will be given. Although the model also applies to purely inorganic and organic devices, the nomenclature for hybrid inorganic/organic solar cells consisting of an organic donor and an inorganic acceptor will be used here. A photovoltaic device can be described as a diode combined with a current source providing the photocurrent density J_{ph} in opposite direction. The current-voltage characteristic of this model is described by the Shockley equation

$$J = J_0 \left[\exp\left(\frac{qV}{nk_{\text{B}}T} \right) - 1 \right] - J_{\text{ph}} \tag{2.6}$$

where J_0 denotes the saturation current density of the diode and q the elementary charge. The product of the Boltzmann constant k_{B} and temperature T gives the thermal energy (ca. $25\,\text{meV}$ at room temperature). V is the external bias applied to the device, while the ideality constant n is connected the mechanism of charge recombination in the device. It will be discussed in greater detail in section 2.3.4.

In real photovoltaic devices leakage current and series resistance have to be considered. Shunts contributing to a parasitic current in the device can be represented by a parallel resistance R_{p} while all contact resistances and voltage losses over the cross-section summarize to a series resistance R_{s}. Both phenomena can be included in an extended formulation of the Shockley equation:

$$J = J_0 \left[\exp\left(\frac{q(V - JR_{\text{s}})}{nk_{\text{B}}T} \right) - 1 \right] + \frac{V - JR_{\text{s}}}{R_{\text{p}}} - J_{\text{ph}} \tag{2.7}$$

Due to the implicit formulation of the current, analytical solutions to this model are only possible by the use of a Lambert omega function.[54] For practical purposes, commonly a numerical approach is chosen.

Although the described model was originally established for modeling inorganic solar cells, it has been successfully applied in the description of both organic[33] and inorganic-organic hybrid photovoltaics.[55] If the current is limited by a space charge region in one of the layers a drift-diffusion model under non-equilibrium conditions yields a more accurate description of real devices, see section 2.3.8.

The resulting relation between voltage and current from the Shockley model yields a small saturation current density in backward direction and an exponentially growing current in forward direction which is limited by the series resistance for higher forward bias. In the following work, all current quantities will be given as current densities to ensure comparability between different sample geometries.

There are three important parameters to assess the performance of photovoltaic devices: The short-circuit current J_{SC}, the open-circuit voltage V_{OC} and the fill factor η_{FF}. Under zero applied bias, the short circuit current J_{SC} of a photodiode can be measured in reverse direction. It depends on illumination density. As interface recombination also contributes to the balance under these conditions J_{SC} is not the exact number of photogenerated carriers. The photocurrent J_{ph} is a theoretical value which cannot be measured experimentally. Commonly, the photocurrent is assumed to be constant over voltage as a good approximation, and J_{ph} is replaced by J_{SC} at zero external bias.

At open circuit voltage V_{OC} the net current of a photodiode vanishes. Under these conditions the number of photogenerated carriers is exactly equalized by the the number of carriers recombining in the diode. In organic photodiodes the open circuit voltage is assumed to be defined by the splitting of the quasi Fermi levels for electrons and holes.[25, 34]

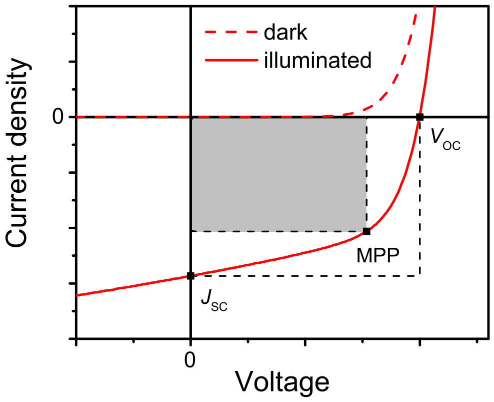

Figure 2.4: A typical J-V characteristic of a photodiode in the dark (dashed line) and under illumination (solid line). The short circuit current J_{SC}, the open circuit voltage V_{OC}, the maximum power point MPP and the areas defining the fill factor η_{FF} are marked.

In the range between short circuit and open circuit voltage the product $J \cdot V$ of applied voltage and current density is negative, which means that the photodiode is actually converting light into electric power. In order to obtain the highest possible power conversion efficiency, the solar cell is operated at the voltage V_{MPP} for which the output power is maximal. This point is called the maximum power point (MPP), yielding the current density J_{MPP}. The fill factor (FF) η is a very common figure for determining the charge extraction efficiency in a photovoltaic device. It is defined as the ratio between the maximal power output $J_{\mathrm{MPP}} \cdot V_{\mathrm{MPP}}$ and the product $J_{\mathrm{SC}} \cdot V_{\mathrm{OC}}$. It is a measure for charge separation efficiency[56] and is reflected in the shape of the J-V curve. A shunted device with a dominating Ohmic parallel resistance combined with a photocurrent source has a fill factor of 25 % while the best commercially available solar cells have fill factors of over 80 %. In figure 2.4 it is depicted how the fill factor can be obtained as the ratio between the rectangles formed by the MPP respectively J_{SC} and V_{OC}.

The fill factor is necessary to calculate the power conversion efficiency (PCE) of a solar cell:

$$\mathrm{PCE} = \frac{P_{\mathrm{max}}}{P_{\mathrm{light}}} = \frac{J_{\mathrm{MPP}} \cdot V_{\mathrm{MPP}}}{P_{\mathrm{light}}} = \frac{\eta_{\mathrm{FF}} \cdot J_{\mathrm{SC}} \cdot V_{\mathrm{OC}}}{P_{\mathrm{light}}} \tag{2.8}$$

It is given as the ratio of maximal electric output power per incident light intensity for an actual device in operation. If possible all three parameters J_{SC}, V_{OC} and η_{FF} should be maximized at the same time to obtain best solar cell performance.

In order to compare performances of different solar cells not only the illumination density has to be equal. Due to varying spectral sensitivities of the involved materials a standardized illumination spectrum is necessary. Such a measurement standard has been established by the American Society for Testing and Materials (ASTM) with the standard ASTM G173.[57] The testing conditions for photovoltaic devices are fixed by the following parameters: $25\,^{\circ}\mathrm{C}$ device temperature, $100\,\mathrm{mW/cm^2}$ illumination density and an air mass 1.5 global (AM 1.5G) spectrum simulating an extraterrestrial sunlight spectrum (air mass 0, AM 0) passing through 1.5 times the earth atmosphere corresponding to an angle of incidence of $48.19°$. Global irradiance means that also sky diffuse and diffuse reflected by soil are included in the spectrum. Both spectra AM 0 and AM 1.5G are shown in figure 2.5.

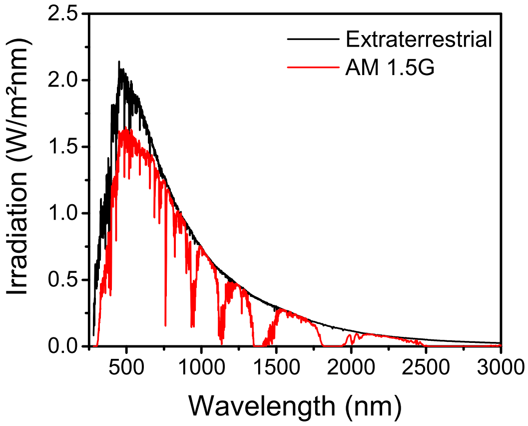

Figure 2.5: Reference spectra AM 0 (extraterrestrial) and AM 1.5G (air mass 1.5 global) according to standard ASTM G173.[57]

A closer look to the physical processes inside a solar cell can be gained by investigation of the spectral dependence of the power conversion process. Therefore a second measure for the cell efficiency has been defined, the *external quantum efficiency* (EQE) or *incident photon to current efficiency* (IPCE). It is defined as

$$\mathrm{EQE}(E) = \frac{E}{q} \frac{J_{\mathrm{SC}}(E)}{P_{\mathrm{light}}(E)}. \tag{2.9}$$

The ratio $\frac{J_{\mathrm{SC}}(E)}{P_{\mathrm{light}}(E)}$ is the *spectral response* of the device, indicating the produced current per light intensity at a certain photon energy E. The external quantum efficiency is the ratio of output electrons per incident photons for each photon energy E. It can often be used for assessing different physical processes in solar cells as it is commonly related to the absorption spectra of the active materials of a solar cell. For calculation of the EQE of a solar cell the incident light spectrum has to be measured in advance with a calibrated photodetector, for subsequent normalization of the measured photocurrent with the light spectrum.

2.3.2 The Detailed Balance Limit

In 1961 Shockley and Queisser published an analytical description for pn-homojunction solar cells in which they postulated a thermodynamical limit for the efficiency. A solar cell without a concentrator placed on earth can achieve a maximal power conversion efficiency of 33.2 %.[7] They described a solar cell as a radiating blackbody, which is in contact with an environment of the same temperature while being exposed to sunlight. Later their model has been extended towards excitonic and bulk heterojunctions which impose further efficiency reductions due to internal energy offsets and finite exciton diffusion length.[58, 59] These considerations allow an accurate description in order to predict the maximally attainable open circuit voltage depending on temperature and material combination.

2.3.2.1 Sun and Solar Cell as Radiating Black Bodies

Following Kirchhoff's law of heat radiation every body in thermal equilibrium emits electromagnetic radiation equivalent to its own absorption maintaining its temperature constant.[60] Both solar cell and sun can be described as black bodies with temperatures $T_{\mathrm{cell}} \approx 300\,\mathrm{K}$ and $T_{\mathrm{sun}} = 5778\,\mathrm{K}$. A solar cell in the dark is then itself subjected to a photon flux spectrum from its environment matching its own temperature.

$$\Phi_{\mathrm{bb}}^{T}(E) \approx \frac{2\pi}{h^3 c^2} E^2 \exp\left(-\frac{E}{k_{\mathrm{B}} T}\right) \tag{2.10}$$

where E is the photon energy, h the Planck constant, c the vacuum speed of light and $k_{\mathrm{B}}T$ gives the thermal energy. For simplicity of the calculations, only vertical incidence and emission are considered here. Since the black body is a solar cell, each incident photon will generate an electron-hole pair with a probability corresponding to the external quantum efficiency of the solar cell $\mathrm{EQE}_{\mathrm{PV}}$. Under illumination by the sun a solar cell produces an excess current, corresponding to the short circuit current density J_{SC} described in the previous section[61]:

$$J_{\text{SC}} = q \int_0^\infty \text{EQE}_{\text{PV}}(E) \cdot t_{\text{s}} \Phi_{\text{sun}}(E) \, \mathrm{d}E \tag{2.11}$$

with Φ_{sun} corresponding to the spectrum of a black body at $T_{\text{sun}} = 5778\,\text{K}$ according to equation 2.10. The factor $t_{\text{s}} = 2.8 \cdot 10^{-5}$ accounts for the fact that the sun emits its radiation isotropically into all directions, but only covers the fraction t_{s} of the spherical angle when seen from earth.

In absence of external illumination, the solar cell is only exposed to thermal radiation from its immediate environment. The photocurrent it produces then corresponds to the blackbody radiation at its own temperature, weighted by its own photon-to-current quantum efficiency:

$$J_{\text{SC},0} = q \int_0^\infty \text{EQE}_{\text{PV}}(E) \cdot \Phi_{\text{bb}}^T(E) \, \mathrm{d}E \tag{2.12}$$

$\Phi_{\text{bb}}^T(E)$ gives the spectrum of the ambient photon flux at temperature T. As in thermal equilibrium the total current of a solar cell is zero, this 'dark' photocurrent must be accompanied by a recombination current $J_{\text{em},0}$ at the heterojunction. This even holds true for every photon energy on its own and results in the detailed balance[61]:

$$\delta J_{\text{SC},0}(E) = \delta J_{\text{em},0}(E) = q\text{EQE}_{\text{PV}}(E) \cdot \Phi_{\text{bb}}^T(E). \tag{2.13}$$

This reciprocity relation can be used to predict the electroluminescence spectrum of a solar cell once the external quantum efficiency is known and vice versa. The integrated quantity $J_{\text{em},0}$ corresponds to the reverse saturation current J_0 which was introduced before, and the Shockley equation for an ideal diode can now be reformulated as

$$J(V) = J_{\text{em},0} \exp\left(\frac{qV}{k_{\text{B}}T}\right) - J_{\text{SC},0} = J_0 \exp\left(\frac{qV}{k_{\text{B}}T} - 1\right) \tag{2.14}$$

with the external bias V applied to the diode. Under open circuit conditions, recombination current and photocurrent cancel out each other, which gives the open circuit voltage as

$$qV_{\text{OC}} \approx k_{\text{B}}T \ln\left(\frac{J_{\text{SC}}}{J_0} + 1\right). \tag{2.15}$$

This holds true if $qV_{\text{OC}} \gg k_{\text{B}}T$ and J_{ph} is assumed to be independent from applied voltage, so that $J_{\text{SC}} = J_{\text{ph}}$ remains as a constant.

The dark recombination current J_0 is produced when electrons surpass the energetic barrier imposed by the interface energy gap ΔE_{IO}. Under presence of bound charge transfer states at the interface, the energetic barrier is reduced by their binding energy E_{B}. As the strength of HCTS binding and its influence on the device behavior is not yet clarified, the transition energy $E_{\text{HCTS}} = \Delta E_{\text{IO}} - E_{\text{B}}$ will be used in the following in order to give a more general expression. The thermally activated recombination current can be described as

$$J_0 = J_{00} \cdot \exp\left(\frac{-E_{\mathrm{HCTS}}}{k_{\mathrm{B}}T}\right) \tag{2.16}$$

where the temperature-independent prefactor J_{00} describes the coupling strength between the donor and acceptor material of the heterojunction. This definition placed in equation 2.15 yields the relation

$$qV_{\mathrm{OC}} \approx E_{\mathrm{HCTS}} - k_{\mathrm{B}}T \ln\left(\frac{J_{00}}{J_{\mathrm{SC}}}\right). \tag{2.17}$$

This gives a very general relation between the open circuit voltage of a diode and the energetic lineup at the interface. The transition energy E_{HCTS} is the theoretical maximum value for the open circuit voltage $V_{\mathrm{OC,max}}$, the second term gives the photovoltaic losses due to carrier recombination. These are only suppressed as the temperature approaches 0 K. In many real solar cells the short circuit current J_{SC} is approximately independent from temperature in a certain range of temperature (e.g. between 200 K and 300 K) which allows to extend the curve of V_{OC} over T from this range to 0 K) in order to obtain a good estimate for $V_{\mathrm{OC,max}}$.[25]

2.3.3 Absorption and Emission of Charge Transfer States

Marcus theory[62] provides a framework to describe both absorption and emission spectra of a system where excitation is connected to an electron transfer. In both cases it yields a Gaussian lineshape with a variance of σ. In a planar heterojunction, the resulting IPCE peak from direct charge transfer absorption is centered around the energy E_0 with the variance σ:

$$\mathrm{EQE}_{PV}(E) = \frac{f}{E\sqrt{2\pi}\sigma} \exp\left(-\frac{(E_0 - E)^2}{2\sigma^2}\right) \tag{2.18}$$

The prefactor f here is a product of absorption coefficient and coupling strength between donor and acceptor material. The corresponding emission intensity is

$$I_{EL}(E) = E \cdot \frac{f_{\mathrm{I}}}{\sqrt{2\pi}\sigma} \exp\left(-\frac{(E_0 - \frac{\sigma^2}{k_{\mathrm{B}}T} - E)^2}{2\sigma^2}\right) \tag{2.19}$$

with the coupling constant f_{I} here, which like f is independent from E.[25]

Absorption and luminescence spectra are two normal distributions with a variance of σ mirrored at the energy $E_0 - \frac{\sigma^2}{2k_{\mathrm{B}}T}$ which can be associated with the transition energy of the charge transfer state E_{HCTS} (see figure 2.6). If the transition is homogeneously broadened then $\lambda = \frac{\sigma^2}{2k_{\mathrm{B}}T}$ is the reorganization energy while in case of inhomogeneous broadening $\frac{\sigma^2}{2k_{\mathrm{B}}T}$ is the averaged transport energy from an arbitrary initial state in the potential landscape to a state of thermal equilibrium, independent of the exact broadening mechanism.[63]

The variance of a homogeneously broadened transition is directly related to the reorganization energy by $\sigma_{\mathrm{h}} = \sqrt{2\lambda \cdot k_{\mathrm{B}}T}$. In case of an inhomogeneous broadening the variance is given

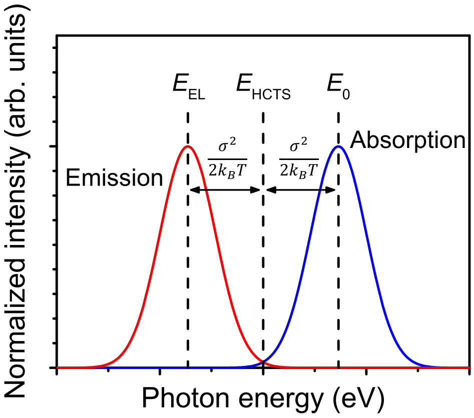

Figure 2.6: Absorption and emission spectra of a hybrid charge transfer state simulated as Gaussian peaks. Their maxima are separated by twice the reorganization energy energy $\lambda = \frac{\sigma^2}{2k_{\mathrm{B}}T}$, mirrored by the HCTS transition energy E_{HCTS}.[62]

by $\sigma = \sqrt{\sigma_{\mathrm{h}}^2 + \sigma_{\mathrm{i}}^2}$ comprising the contributions of homogeneous and inhomogeneous broadening. In organic photovoltaics both electroluminescence and direct absorption from charge transfer states have been measured and confirmed the predictions of Marcus theory.[25] The reorganization energy λ strongly depends on the materials present in the heterojunction. It can be disentangled into separate contributions of donor and acceptor, which for small molecules range from $60\,\mathrm{meV}$ to almost $500\,\mathrm{meV}$.[64]

2.3.4 The Role of Non-radiative Recombination

Up to this point all considerations were made about ideal photodiodes which only show recombination between two free charge carriers and excluding all kinds of non-radiative processes. However, non-radiative recombination has a serious impact on the functionality of real devices, so this has to be accounted for in related theory.

Traditionally it is assumed that the ideality factor n is connected to the predominant mechanism of charge recombination, $n \approx 1$ for band-to-band transitions of free carriers, $n \approx 2$ for recombination occuring at localized traps at the donor-acceptor interface described by the Shockley-Reed-Hall statistics. Recent work, however, has pointed out the more complex origin of this parameter, so that even ideality factors larger than 2 have their physical meaning.[56, 65, 66]

The prefactor J_0 to the single-exponential Shockley equation (equation 2.6) is commonly referred to as ”reverse saturation current” originating from the assumption that it can be readily measured by reverse biasing the diode. Recently it has been pointed out by *Cuevas* that ”thermal equilibrium recombination current” would be a much better term[67] as it bears much more physical meaning. Its value is closely connected to the materials involved in the heterojunction as well as the device temperature. In the ideal Shockley model presented before, J_0 is independent from applied bias V or incident photon flux ϕ. In actual devices, however, J_0 depends on the operating conditions and is thus a variable parameter $J_0 = J_0(V, T, \phi)$.

In order to obtain a constant value for the recombination current prefactor, its voltage dependence can be extracted by introducing an ideality factor n to the exponential term in the Shockley equation:[65]

$$J(V) = J_0(V) \cdot \left(\exp\left(\frac{qV}{k_\mathrm{B}T} \right) - 1 \right) = J_{0,n} \cdot \left(\exp\left(\frac{qV}{nk_\mathrm{B}T} \right) - 1 \right) \tag{2.20}$$

In this equation, the prefactor $J_{0,n}$ it then independent from the applied bias. The ideality factor n must also account for the presence of non-radiative recombination processes which contribute to the total recombination current. The radiative quantum efficiency EQE_EL gives the ratio between the radiative recombination current J_rad and the total recombination current J and can be voltage-dependent itself. The prefactor J_0 can be separated into the shares of radiative and non-radiative processes.

$$J_0(V) = J_0^\mathrm{rad} + J_0^\mathrm{nonrad}(V) = J_0^\mathrm{rad} \cdot \frac{1}{\mathrm{EQE}_\mathrm{EL}(V)} \tag{2.21}$$

The process of radiative recombination is only regulated by thermodynamics and ideally only depends on the population of energy levels involved in the recombination process.[43] Non-radiative processes, however, can be greatly dependent on the applied bias to the heterojunction. Consequently, the radiative quantum efficiency also inherits a voltage dependence.

In the analysis of data presented in this work, the denomination J_0 will be used to represent the voltage-independent prefactor $J_{0,n}$ whenever the whole recombination current of a diode is discussed and an ideality factor n is present in the model.

2.3.5 Thermal Activation of the Recombination Current

As clarified before in equation 2.16, the equilibrium recombination current J_0 of a diode is a thermally activated quantity. While in an ideal diode only the Boltzmann statistics regarding the transition energy E_HCTS determines thermal activation, the activation energies measured in actual devices are smaller. In order to account for non-radiative processes, an effective gap energy $\Delta E_\mathrm{eff} = \frac{E_\mathrm{HCTS}}{n'}$ scaled down by its own ideality factor n' has to be introduced.[68]

$$J_0 = J_{00} \cdot \exp\left(\frac{\Delta E_\mathrm{eff}}{k_\mathrm{B}T} \right) = J_{00} \cdot \exp\left(\frac{E_\mathrm{HCTS}}{n'k_\mathrm{B}T} \right). \tag{2.22}$$

According to *Potscavage et. al.*, the ideality factors n and n' are intrinsically different from each other, but are usually regarded as the same figure for practical purposes.[68]

Knowledge about the temperature dependence of J_0 allows the formulation of a factorized version of Shockley's law,[65] if $qV/k_\mathrm{B}T \gg 1$:

$$J = J_{00} \cdot \exp\left(\frac{-E_{\mathrm{HCTS}}}{nk_{\mathrm{B}}T}\right) \cdot \exp\left(\frac{qV}{nk_{\mathrm{B}}T}\right) = J_{00} \cdot \exp\left(\frac{qV - E_{\mathrm{HCTS}}}{nk_{\mathrm{B}}T}\right) \tag{2.23}$$

The relation between open circuit voltage and temperature as given in equation 2.17 can then be reformulated for devices bearing non-radiative losses in two ways. One possibility is introducing an ideality factor n, yielding

$$qV_{\mathrm{OC}} \approx E_{\mathrm{HCTS}} - nk_{\mathrm{B}}T \ln\left(\frac{J_{00}}{J_{\mathrm{SC}}}\right). \tag{2.24}$$

The other possibility is restricting the relation to radiative recombination only, scaled by its radiative quantum efficiency $\mathrm{EQE}_{\mathrm{EL}}$:

$$qV_{\mathrm{OC}} \approx E_{\mathrm{HCTS}} - k_{\mathrm{B}}T \ln\left(\frac{J_{00}^{\mathrm{rad}}}{\mathrm{EQE}_{\mathrm{EL}} J_{\mathrm{SC}}}\right) = E_{\mathrm{HCTS}} + k_{\mathrm{B}}T \ln(\mathrm{EQE}_{\mathrm{EL}}) - k_{\mathrm{B}}T \ln\left(\frac{J_{00}^{\mathrm{rad}}}{J_{\mathrm{SC}}}\right) \tag{2.25}$$

with the coupling constant for radiative recombination J_{00}^{rad}:

$$J_{0}^{\mathrm{rad}} = J_{00}^{\mathrm{rad}} \exp\left(\frac{-E_{\mathrm{HCTS}}}{k_{\mathrm{B}}T}\right) \tag{2.26}$$

From equation 2.25 it is visible that the estimation of the maximal V_{OC} by extending the initial slope of the qV_{OC} vs. T curve commonly overestimates the real HCTS transition energy due to non-radiative emission, and has to be corrected after measurement of the electroluminescence quantum efficiency.

2.3.6 Determination of the Ideality Factor n

Knowing the ideality factor n of a diode can provide valuable information on the carrier recombination mechanisms present in a device. Recent research on organic and hybrid diode devices has shown that n is greatly dependent on intrinsic device parameters like material selection and interface structure and likewise on external influences like temperature, external bias and incident photon flux.[42, 56, 65, 66] Due to the intricate interdependencies of n its determination is often complicated and goes far beyond a single exponential fit with a standard Shockley diode model. Particularly the influence of series and shunt resistances occurring in all actual devices can distort the behavior of a diode and significantly alter the shape of a J-V characteristic away from an idealistic model.

If the J-V curve of a diode has a pronounced exponential regime, a straightforward estimate for the ideality factor n can be made by applying a standard single-exponential model according to equation 2.6. In some cases even different regimes involving more than one ideality factor can be identified and assigned to physical processes in a diode, e.g. filling of trap states and subsequent recombination of free carriers.[42] If a suitable model for the current roll-off at larger forward bias is available, regions of higher current density can be included into the analysis. A framework for this approach is provided in section 2.3.8.

This method can, however, easily produce misleading data, as the influence of series resistance and injection barriers is not always visible at first sight. Following the analysis of *Wolf and Rauschenbach*,[69] it is possible to separate the influence of a series resistance from the behavior of a bare (inorganic) p-n junction.

2.3.6.1 The J_{SC}-V_{OC} Method

The J_{SC}-V_{OC} method delivers a more accurate possibility to analyze the behavior of a real diode device. It was first proposed as "Sinton's flash lamp method"[70] and is well described in reference [65] by *Tvingstedt et. al.*

Under open circuit conditions (i.e. at an external bias of V_{OC}) the recombination current in a diode equals the photocurrent produced by light irradiation. As no net current flows to or away from the heterojunction, all influence from series resistance is eliminated. The general Shockley equation 2.7 yields under open circuit conditions ($J = 0$):

$$J_{\mathrm{ph}} = J_0 \exp\left(\frac{qV_{\mathrm{OC}}}{nk_{\mathrm{B}}T}\right) + \frac{V_{\mathrm{OC}}}{R_{\mathrm{p}}} \tag{2.27}$$

Only under very weak illumination, the current dissipated by the shunt resistance R_{p} will define the behavior of equation 2.27. At higher light densities, the exponential term will dominate. Consequently the relation between open circuit voltage and photocurrent recorded at a series of illumination densities can deliver an accurate description for an isolated heterojunction as given in the simple form of the Shockley equation 2.6.

The only remaining question from equation 2.27 is then to determine the photocurrent J_{ph}. Although an exact treatment of field-dependent photogeneration has shown that the photocurrent under open circuit conditions is slightly smaller than the short circuit current J_{SC}[53, 71, 72], both quantities are frequently treated as equivalent. This assumption is valid as long as no big series resistances or extraction barriers are hampering the transport of dissociated carriers away from the interface. Such limitations are easily visible in a small fill factor of a device and should be excluded in advance before performing the J_{SC}-V_{OC} analysis.

Figure 2.7 shows the J-V characteristic of a simulated diode device involving both series and shunt resistances. The red circles are hypothetical results of a simulated J_{SC}-V_{OC} analysis that allows to eliminate the influence of transport phenomena (grey area).

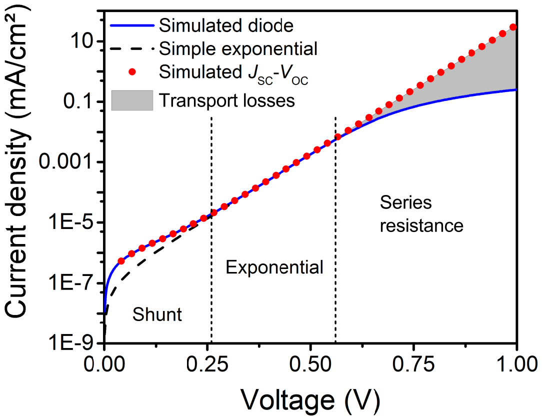

Figure 2.7: The comparison of a simulated diode characteristic to a simple exponential function shows that the regime for determination of the ideality factor n is often only very small or even not clearly distinguishable from the rest of the curve. The J_{SC}-V_{OC} method (represented by simulated measurements as red circles) allows to isolate the transport losses inflicted by a series resistance (grey area).

In real diodes, the ideality factor is not a constant, but depends not only on temperature, but also on the carrier density in the device. This is especially the case if several recombination mechanisms can appear and saturate at different current densities.[42, 73] Consequently, it is not sufficient to perform a single exponential fit to the data from paired J_{SC} and V_{OC} data to obtain a full scale diode model.

A more detailed analysis can be performed by regarding the differential formulation for the ideality factor n:[65, 66]

$$n = \frac{q}{k_{\mathrm{B}}T} \cdot \frac{\partial V_{\mathrm{OC}}}{\partial \left(\ln J_{\mathrm{SC}}\right)} \tag{2.28}$$

From a data series of J_{SC} and V_{OC} data recorded over a range of illumination densities, n can be calculated as a function of the short circuit current. Local values of n greater than 2 at low illumination densities originate in the influence of shunt resistances, while at high excitation the ideality factor can be smaller than 1 and even become negative because of surface recombination effects in organic heterojunctions.[66]

2.3.7 Transport in Organic Semiconductors

While dissociation of excitons at organic or hybrid type II heterojunctions is a process of good efficiency, power conversion efficiency of photovoltaic devices frequently is limited by transport phenomena. Two major transport processes are involved: At first, following light absorption the generated exciton diffuses from the bulk of the donor material to the interface. After successful charge separation, hole and electron are transported to the respective electrodes attached to donor and acceptor. Insufficient transport capacity can lead to losses in photovoltaic efficiency by carrier recombination in the device.

2.3.7.1 Transport of Excitons

Two mechanisms for exciton transfer between molecules or polymer chains can be distinguished: Förster resonant energy transfer and Dexter electron transfer. Both lead to a displacement of the quasi-particle representing a localized excitation in an organic material by different means.

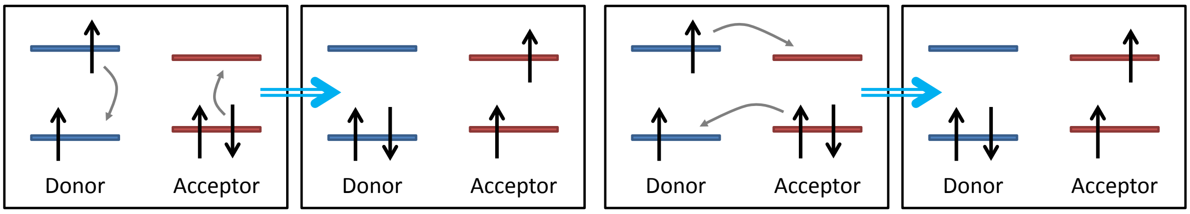

(a) Förster resonant energy transfer

(b) Dexter electron transfer

Figure 2.8: Schematic depictions of (a) Förster resonant energy transfer and (b) Dexter electron transfer from a singlet excitation at a donor to an acceptor in ground state.

Förster transfer occurs by resonant coupling of a donor and an acceptor brought into proximity of each other. Coupling efficiency is determined by distance, spectral overlap between the emission of the donor and the absorption of the acceptor, and by the orientation of their dipoles. It follows the relation

$$\eta(r) \propto \frac{1}{1+\left(\frac{r}{R_0}\right)^6} \tag{2.29}$$

with r being the separation between donor and acceptor and R_0 the Förster radius of the system, describing the donor-acceptor separation with a transfer efficiency of 50 %.[74] The efficiency of Förster transfer is independent from temperature. Due to energy conservation, Förster transfer can only occur towards acceptor states with transition energies lower than the donor state. In the transfer process, only the excitation energy is transported, while all involved electrons maintain their places (see figure 2.8(a)).

In contrast to this, Dexter electron transfer describes the migration of a localized excitation by an exchange of charge carriers as schematically depicted in figure 2.8(b).[75] Its transfer rate follows the relation

$$k_{\text{tr}}(r) \propto J \cdot \exp\left(\frac{-2r}{L}\right) \tag{2.30}$$

where L is the sum of the Van-der-Waals lengths of donor and acceptor describing the wavefunction overlap between them and J is the integral of spectral overlap between the respective emission and absorption spectra of donor and acceptor. While L is independent from temperature, J increases towards higher temperatures in case of a slight detuning between the transition energies of donor and acceptor due to thermal broadening of the spectra.

Due to their strong dependence on the separation r, both types of energy transfer can only be active in the direct vicinity of an excited molecule or polymer. Transfer processes in organic semiconductors are thus a series of cascading short range transfers. Measurements by *List et. al.* have shown that in a semiconducting polymer both transfer mechanisms can be observed. Their influences can be separated by regarding their different thermal activation behavior.[76] Due to rapid recombination of excitons, the exciton diffusion length in conjugated polymers is restricted to a couple of nanometers at room temperature and even decreases towards lower temperatures.[22, 77–79]

2.3.7.2 Transport of Single Carriers

While excitons are uncharged quasi-particles which interact only weakly with their environment, single electrons can have a significantly stronger interaction due to the charge they are carrying. Consequently, the movement of electrons and holes is determined by both diffusion and drift in an electric field. In a crystalline solid, the environment around a free carrier tends to screen the electric field of the carrier by imposing local lattice deformation, leading to a ’cloud’ of phonons accompanying each electron in the conduction band or LUMO. The quasi-particle formed like this is called ”polaron” and was first described by *Landau and Pekar*.[80] Polaron formation reduces the mobility of free electrons in a semiconductor and increases the effective carrier mass. In case of strong interaction and a weak electric field, a self-trapping effect can occur with electrons being captured in a potential pot formed by the polaron around them. In p-type semiconducting materials the same can happen to holes.

Transport of charges happens by polaron hopping, requiring to surpass activation barriers while transferring from one host to another.[81] This commonly occurs with assistance from phonons and gives charge transport a strong dependence on temperature, especially in disordered organic systems with a broad distribution of barrier heights.[82] As expected, the activation energy for the transport of single charges in an organic semiconductor is higher than for the transport of excitons.[83] At higher temperatures, the influence of phonon scattering is proposed to limit charge transport in organic semiconductors.[84] Distortions in the lattice induced by increased motion of molecules and polymer chains are likely to reduce the interaction between neighboring sites in the material and thus limit the carrier mobility at high temperatures and violate the universal Meyer-Neldel rule of conductivity.[85] Experimental data, however, shows a continuous thermally activated behavior of carrier mobilities in conjugated polymers up to room temperature.[82, 86, 87]

2.3.8 Space Charge Limited Transport in Diodes

Carrier transport plays a significant role in actual photovoltaic devices. The underlying phenomena have to be understood in order to overcome limitations to device performance. Detailed modeling of a photodiode is a very challenging task due to the interplay of several materials and the important role of interface processes.

Under forward bias the current density in an ideal diode increases exponentially. Real devices generally show a current roll-off, where the J-V curve departs from an exponential increase and grows more slowly. A common way to describe this is the introduction of a series resistance like in equation 2.7. However a current roll-off can have various reasons and an Ohmic resistance often does not suffice for description of the actual device behavior.

In the samples used in this work, series resistances due to contact resistance at the electrodes and other contributions in the measurement circuit are negligible. However, limited charge carrier mobility in the thick organic layer leads to significant deviation from a simple exponential characteristic. This is a consequence of thermally activated hopping transport in disordered systems, and leads to the formation of a space charge region. Charge transport is only possible under non-equilibrium conditions with a voltage drop across the layer. The treatment proposed by *Renshaw et. al.* [42] and *Panda et. al.* [55] in two connected publications will be employed to interpret the measured curves.

Non-equilibrium conditions emerge when the quasi-Fermi level for either holes or electrons is not flat anymore and a space charge region is formed. In a single organic layer with the thickness d the current approaches the Mott-Gurney law[88] $J = (9/8)(\epsilon_\mathrm{O}\mu_\mathrm{O}V^2/d^3)$ with the dielectric constant of the material ϵ_O and the carrier mobility μ_O. In an inorganic/organic diode the charge carrier densities and voltage distribution over organic and inorganic layer has to be determined by simultaneously solving the drift-diffusion equation

$$J = q\mu_\mathrm{O}PF - qD\nabla P \tag{2.31}$$

coupled with the Poisson equation

$$\nabla \cdot F = \frac{q\,(P - P_\mathrm{D})}{\epsilon_\mathrm{O}} \tag{2.32}$$

where F is the electric field and D the diffusivity. P gives the carrier concentration while P_D is the background carrier concentration in equilibrium and μ_O is the carrier mobility.

At current densities $|J| \gg 0$ the quasi-Fermi level for holes is no longer flat in the organic. The Fermi level bending $\Delta E_\mathrm{f,p}$ as depicted in figure 2.9 imposes an additional barrier for holes

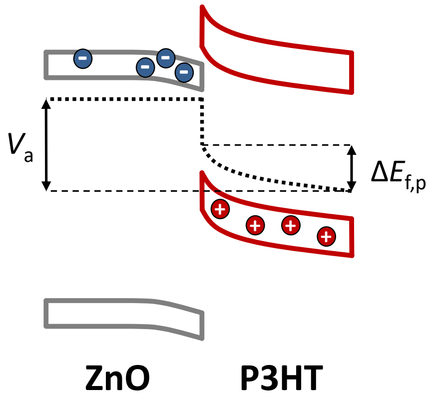

Figure 2.9: A space charge region in P3HT produces a voltage drop $\Delta E_{\mathrm{f,p}}$ and thus reduces the actual voltage at the heterojunction.

reducing the number of carriers available for recombination at the interface. The resulting J-V characteristic can then be calculated either from charge densities at the interface or by applying the transformation $V_{\mathrm{a}} \rightarrow V_{\mathrm{a}} - \Delta E_{\mathrm{f,p}}$ to the applied voltage V_{a}.[42]

In order to provide an analytical solution a couple of simplifications can be made to the system: The charge carrier mobility on the inorganic side $\mu_{\mathrm{I}} \approx 10 - 50\,\mathrm{cm}^2/(\mathrm{V\,s})$ is generally large compared to the organic mobility $\mu_{\mathrm{O}} \approx 10^{-5} - 10^{-2}\,\mathrm{cm}^2/(\mathrm{V\,s})$, so that the quasi-Fermi level for electrons is flat throughout the inorganic side. Furthermore the background carrier density in the inorganic is high due to unintentional background doping, which leads to an extended screening effect of the electric field, restricting the voltage drop almost entirely to the organic layer. Lastly it can be assumed that drift is the dominant transport mechanism in the organic, as the low background carrier density only provides a negligible influence of diffusion.

The resulting simplified form of the drift-diffusion and Poisson equations (equations 2.31 and 2.32) read $J = q\mu_{\mathrm{O}} P_{\mathrm{O}}^{\mathrm{sc}} F_{\mathrm{O}}$ and $\nabla \cdot F_{\mathrm{O}} = q P_{\mathrm{O}}^{\mathrm{sc}}/\epsilon_{\mathrm{O}}$ now with $P_{\mathrm{O}}^{\mathrm{sc}}$ being the hole density only imposed by the space charge region and F_{O} the electric field in the organic layer.[55]

Solving the two equations leads to the voltage distribution and carrier density at position x in the organic

$$V_{\mathrm{O}}^{\mathrm{sc}}(x) = \frac{\epsilon_{\mathrm{O}}\mu_{\mathrm{O}}}{3J}\left[\left(\frac{2Jx}{\epsilon_{\mathrm{O}}\mu_{\mathrm{O}}} + F_{\mathrm{c}}^2\right)^{\frac{3}{2}} - F_{\mathrm{c}}^3\right] \tag{2.33}$$

$$P_{\mathrm{O}}^{\mathrm{sc}}(x) = \frac{J}{q\mu_{\mathrm{O}}}\frac{1}{\sqrt{\frac{2Jx}{\epsilon_{\mathrm{O}}\mu_{\mathrm{O}}} + F_{\mathrm{c}}^2}} \tag{2.34}$$

with the electric field at the anode F_{c} as a boundary condition. This yields the change in quasi-Fermi level over the organic

$$\Delta E_{\mathrm{f,p}} = qV_{\mathrm{O}}^{0} + qV_{\mathrm{O}}^{\mathrm{sc}} - k_{\mathrm{B}}T \ln \left[\frac{P_{\mathrm{HJ}}^{\mathrm{sc}}}{P_{\mathrm{c}}'} + \frac{P_{\mathrm{c}}}{P_{\mathrm{c}}'} \exp \left(\frac{qV_{\mathrm{O}}}{k_{\mathrm{B}}T} \right) \right]. \tag{2.35}$$

Here P_{c} is the hole density at the anode without a flowing current and $P_{\mathrm{c}}' = P_{\mathrm{c}} + J/q\mu_{\mathrm{O}}F_{\mathrm{c}}$ gives the density for $J > 0$.

Due to the assumption that the voltage drop entirely occurs in the organic layer only a built-in voltage V_{bi} derived from the difference in electrode potentials is subtracted from the applied external bias V_{a}:

$$V_{\mathrm{O}} = V_{\mathrm{a}} - V_{\mathrm{bi}}. \tag{2.36}$$

The function

$$J(V_{\mathrm{a}}) = J_0 \cdot \left(\frac{V_a - \Delta E_{\mathrm{f,p}}}{nk_{\mathrm{B}}T} \right) \tag{2.37}$$

with the reverse saturation current J_0 and the ideality factor n then serves as a model for the measured J-V characteristics. The curve consists of two parts: Below the built-in voltage and at reverse bias the organic layer is depleted and therefore $\Delta E_{\mathrm{f,p}} = 0$. The reverse saturation current J_0, the ideality factor n and the organic carrier mobility μ_{O} serve as fit parameters in the approximation, which for $V_{\mathrm{a}} > V_{\mathrm{bi}}$ has to be performed implicitly due to the appearance of J in $\Delta E_{\mathrm{f,p}}$.

Chapter 3

Materials and Sample Preparation

3.1 Materials

In this section, the materials used for the fabrication of hybrid inorganic/organic photodiodes are presented: Zinc oxide (ZnO), ZnMgO and tin oxide (SnO_2) are inorganic acceptor materials, with poly(3-hexylthiophene) (P3HT) as organic donor. Molybdenum oxide (MoO_3) acts as an interlayer for improving hole extraction at the anode. Silver contacts on both cathode and anode allow for integration into a measurement circuit.

In section 3.2 the techniques used in device fabrication are shown: Inorganic acceptor layers are grown by molecular beam epitaxy (MBE), P3HT is deposited by spin coating. Onto these layer structures silver contacts and MoO_3 interlayers are attached by vacuum deposition. In the last part of the chapter the device layout for planar hybrid photodiodes is presented as it is used for all device characterization measurements in this work.

3.1.1 Zinc Oxide

Zinc oxide (ZnO) is a II-VI semiconductor material with a wide direct band gap. It is transparent to visible light and only absorbs in the UV. It is non-toxic and widely available and thus well suited for future applications in photovoltaics and light emitting devices. ZnO can be prepared in a wide variety of procedures like sol-gel processing, pulsed laser deposition, electron beam evaporation, spray pyrolysis, atomic layer deposition (ALD), molecular beam epitaxy (MBE) and metal organic chemical vapor deposition (MOCVD).[89] The degree of crystallinity, intrinsic doping and electronic properties of ZnO vary over a wide range for the different fabrication techniques. In this work all ZnO has been prepared by molecular beam epitaxy, which will be described in more detail in section 3.2.1. Previous research has been performed on zinc oxide as acceptor material in photovoltaics as nanoparticles[10], nanofibers[14] and nano-structured rod-like substrates.[90]

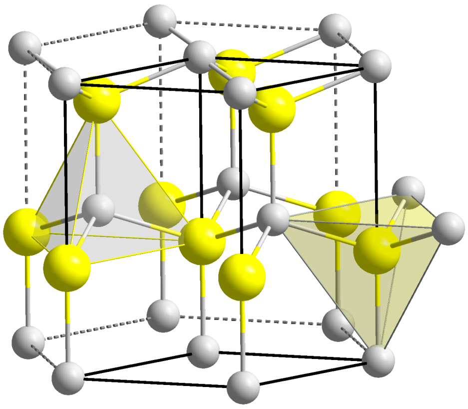

Figure 3.1: ZnO in Wurtzite crystal structure with zinc atoms in yellow and oxygen in grey.[91]

Zinc oxide possesses a wurtzite crystal structure with a hexagonal unit cell as depicted in figure 3.1. It belongs to the space group C_{6v}^4 in Schoenflies notation. At room temperature the lattice constants are $a \approx 3.25$ Å and $c \approx 5.21$ Å.[92] The orientation of a ZnO single crystal determines its surface structure and thus the physical properties even up to the macroscopic regime where the energetic alignment at an interface involving zinc oxide can shift by several hundreds of meV.[93] There are two polar surfaces of a ZnO single crystal, the Zn-polar $(0\,0\,0\,1)$ and O-polar $(0\,0\,0\,\bar{1})$ planes, which show an outwardly respectively inwardly pointing surface dipole moment.[94] Their surfaces are covered only with the element giving them their respective name. Other, non-polar surfaces like the $(1\,0\,\bar{1}\,0)$ plane have an alternating structure of zinc and oxygen atom rows and a flat lying dipole moment parallel to the surface.

At room temperature the optical gap energy of ZnO is about $3.37\,\mathrm{eV}$ with a large exciton binding energy of ca. $60\,\mathrm{meV}$.[89] Due to its high electron affinity of ca. $4\,\mathrm{eV}$ it forms a type II interface with most organic semiconductor materials and is therefore well suited for photovoltaic applications in hybrid inorganic-organic systems.[95] ZnO and ZnMgO layers grown by MBE have an intrinsic n-type doping density of ca. $1 \times 10^{18}\,\mathrm{cm}^{-3}$, which leads to the Fermi level being situated ca. $100\,\mathrm{meV}$ below the conduction band in thermal equilibrium.[96]

3.1.2 ZnMgO

The band gap energy of ZnO can be tuned by alloying it with other metal oxides without affecting its wurtzite crystal structure. Alloying it with cadmium oxide decreases the band gap down to the visible yellow region at ca. $2.4\,\mathrm{eV}$[97] while alloying with magnesium oxide allows to increase the band gap up to $4.4\,\mathrm{eV}$.[98] In spite of pure MgO having a rocksalt crystal structure it can be included into the wurtzite lattice of ZnO to an extent of up to $40\,\%$ before phase separation occurs. Determining the Mg content x by energy-dispersive x-ray (EDX) analysis allows to put forward a relation between magnesium doping and band gap widening. Figure 3.2(a) shows absorption spectra of ZnO and all ZnMgO alloys used in this work, in figure 3.2(b) the widening of the band gap with increasing Mg content is shown. The band gap of $\mathrm{Zn}_{1-x}\mathrm{Mg}_x\mathrm{O}$

is then according to the experimental data $E_\mathrm{g} = 3.34 + 2.64x$.[98]

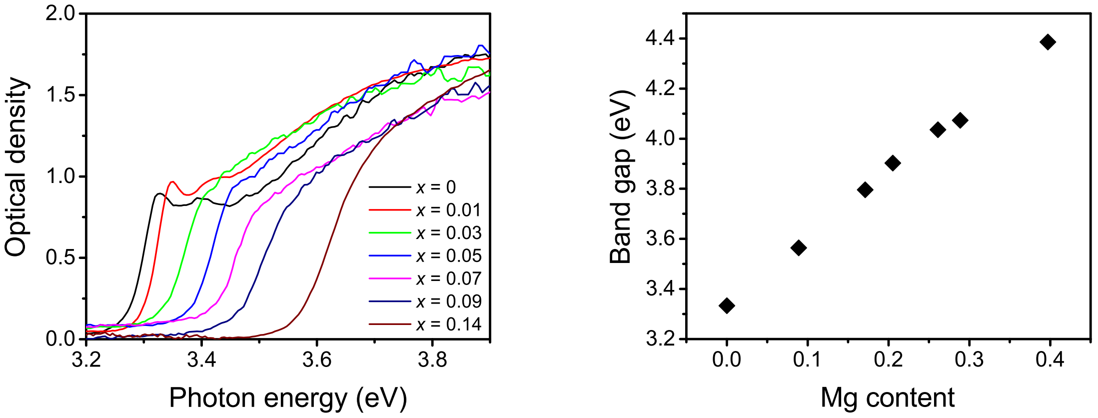

(a) Absorption spectra

(b) Optical band gaps

Figure 3.2: (a) Absorption spectra of a pristine ZnO film and several $\mathrm{Zn}_{1-x}\mathrm{Mg}_x\mathrm{O}$ alloys with Mg content x between 0.01 and 0.14. All layers are deposited on top of a Ga-doped layer with the same Mg content serving as a conductive electrode as described in section 3.1.4. The Ga-doped layer has slightly increased band gap energy, ensuring light transmission to the undoped component. (b) Optical band gap energies for $\mathrm{Zn}_{1-x}\mathrm{Mg}_x\mathrm{O}$ with magnesium contents x between 0 and 0.40. Data taken with permission from reference [98].

Calculations based on density-functional theory predict a slightly lower slope of 2.33.[99] Upon inclusion of Mg both valence band and conduction band observe an energetic shift away from each other. Calculations predict a ratio between conduction band offset and valence band offset of $E_\mathrm{CB}/E_\mathrm{VB} = 67/33$.[99] Experimental findings provide values between $60/40$ and $70/30$.[100, 101]

3.1.3 Tin Dioxide

Tin and oxygen can form two stable crystalline compounds, distinguished by different oxidation states of tin: tin(II) oxide SnO and tin(IV) oxide (or tin dioxide) $\mathrm{SnO_2}$. In this work tin dioxide is used as a donor in planar photodiodes. It is a n-type semiconductor with a wide band gap of ca. $3.9\,\mathrm{eV}$ and a high work function similar to ZnO.[102, 103]

Tin dioxide crystallizes in a rutile structure as depicted in figure 3.3. The point group of rutile is D_{4h} in Schoenflies notation. Sn atoms are six coordinate and O atoms three coordinate, the lattice constants are $a = 4.737\,\text{Å}$ and $c = 3.185\,\text{Å}$.

In contrast to ZnO, the band gap of $\mathrm{SnO_2}$ is indirect.[105] Due to slight oxygen-deficiency, tin dioxide commonly is an n-type semiconductor. The Fermi level is placed some hundreds of meV below the conduction band. Several types of vacancies and surface states can also form intermediate states within the optical band gap,[103] blurring out the absorption edge as visible in figure 3.4. The $(1\,0\,1)$ plane is the second most stable surface of $\mathrm{SnO_2}$. In contrast to

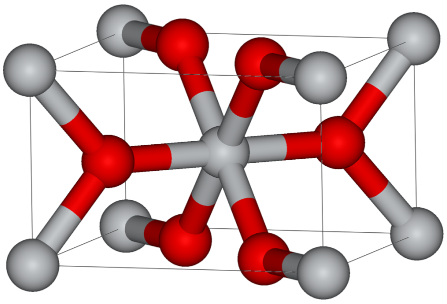

Figure 3.3: SnO_2 crystallizes in a rutile structure as depicted here with Sn atoms in grey and O in red.[104]

the energetically more favorable $(1\,1\,0)$ surface, it provides a protective layer of oxygen atoms which prevent any surface reconstruction.[106] SnO_2 $(1\,0\,1)$ is the preferred growth mode in oxygen-rich conditions.

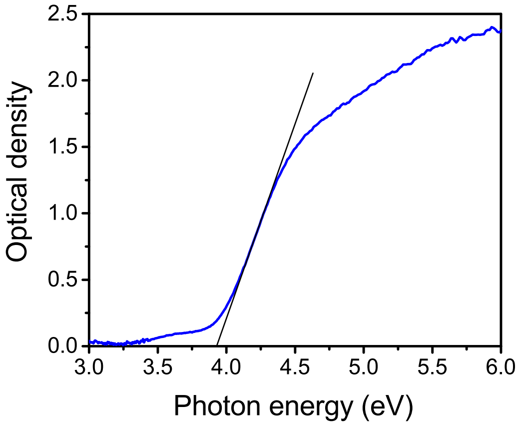

Figure 3.4: Absorption spectrum of a $100\,\mathrm{nm}$ thick SnO_2 layer deposited on top of a $150\,\mathrm{nm}$ thick SnO_2:Sb layer by molecular beam epitaxy on a sapphire substrate. The Sb-doped layer serves as a conductive electrode, as described in section 3.1.4. Its optical band gap is slightly shifted towards higher energies, enabling light transmission to the pristine layer in case of illumination through the sapphire substrate.

The high exciton binding energy in SnO_2 of $130\,\mathrm{meV}$ combined with its indirect band gap suppresses radiative carrier recombination, leading to a comparatively long exciton lifetime and low PL quantum yield.[107] Furthermore, pump-probe spectroscopy measurements have shown a rapid charge transfer from organic donor materials to the conduction band of tin dioxide.[16] Both facts are promising to help reducing losses in a SnO_2 based photovoltaic device.

3.1.4 Doping of Zinc Oxide and Tin Dioxide with Ga and Sb

The low conductivity of ZnMgO and SnO_2 is a limiting factor in the performance of actual photoelectronic devices. However this problem can be solved by introducing a layer of a heavily doped species of the same material. Adding gallium to ZnO leads to n-type doping which can easily reach degeneracy and produces carrier concentrations up to almost $1 \times 10^{21}\,\mathrm{cm}^{-3}$ without affecting the crystalline structure.[108] Band gap engineering by alloying ZnO and MgO can still be performed with the Ga-doped variant which makes ZnMgO:Ga an ideal transparent electrode for optoelectronic devices increasing the conductivity from $2.6\,\Omega^{-1}\mathrm{cm}^{-1}$ to $900\,\Omega^{-1}\mathrm{cm}^{-1}$. Due to the Burstein-Moss effect degeneratively doped semiconductors have a larger band gap than their undoped equivalent as depicted in figure 3.5(a). Consequently the band gap of Ga-doped ZnMgO is ca. $150\,\mathrm{meV}$ larger than in the undoped case which assures that the electrode is transparent in the whole spectral range below the acceptor band gap energy.

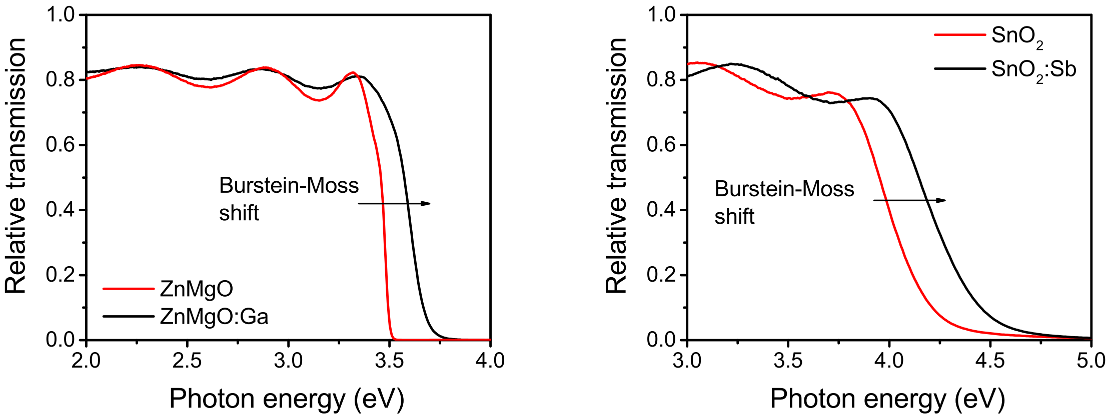

(a) ZnMgO & ZnMgO:Ga

(b) SnO_2 & SnO_2:Sb

Figure 3.5: (a) Transmission spectra of $420\,\mathrm{nm}$ thick ZnMgO and ZnMgO:Ga layers with Mg content of $x = 0.09$ each. Carrier density in the gallium doped layer is ca. $1.0 \times 10^{20}\,\mathrm{cm}^{-3}$. The band gap of ZnMgO:Ga is widened by ca. $150\,\mathrm{meV}$ due to the Burstein Moss shift. (b) Transmission spectra of $294\,\mathrm{nm}$ thick SnO_2 and SnO_2:Sb layers. The doping density in SnO_2:Sb is ca. $2.4 \times 10^{20}\,\mathrm{cm}^{-3}$, causing a band gap widening of ca. $200\,\mathrm{meV}$.

Similarly SnO_2 can be doped with antimony in order to reach a conductivity as high as $1500\,\Omega^{-1}\mathrm{cm}^{-1}$ and carrier concentrations of $7.9 \times 10^{20}\,\mathrm{cm}^{-3}$.[102, 109]

3.1.5 Poly(3-hexylthiophene)

Poly(3-hexylthiophene) (P3HT) is a very widespread conjugated semiconductor polymer. Its monomer consists of a thiophene ring with a hexyl sidechain attached to its position 3 (see figure 3.6(a)). The asymmetric position of the hexyl leads to the existence of three different configurations between neighboring monomers, head-head (HH), head-tail (HT) and tail-tail (TT). Regiorandom P3HT shows all three configurations in arbitrary sequence, while regioregular P3HT

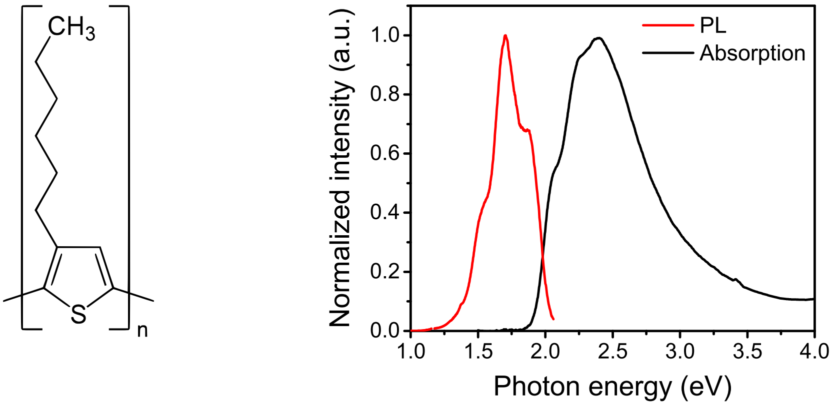

(a) Molecular structure

(b) Spectra of absorption and PL

Figure 3.6: (a) The molecular structure of Poly(3-hexylthiophene) (P3HT). (b) Absorption (black line) and photoluminescence (red line) spectra of a P3HT film on a sapphire substrate. PL was recorded under laser excitation with $\lambda = 532\,\mathrm{nm}$ at room temperature.

predominantly consists of the same type of conjunction. Most commonly HT-regioregular P3HT is used in optoelectronics due to its high carrier mobility of up to $3.1\frac{cm^2}{Vs}$.[110] A regular structure allows extended π stacking of polymer chains which results in a semi-crystalline structure of spin-coated P3HT films. Advanced techniques like high-temperature rubbing even allow to produce lamellar structures of high crystallinity.[111] The optical band gap of P3HT is frequently reported in literature with values around $2.0\,\mathrm{eV}$. Combined measurements of UV photoelectron spectroscopy and inverse photoelectron spectroscopy, however, yield a gap energy of $2.5\,\mathrm{eV}$ including a large exciton binding energy of ca. $0.4\,\mathrm{eV}$.[112, 113] The ionization potential can vary by up to $0.5\,\mathrm{eV}$ depending on the structural conformation on an acceptor surface.[114]

In the experiments performed for this work P3HT with a regio-regularity above 96 % and average molar mass of more than 40.000 was used (purchased from Rieke Metals).

3.1.6 Contact Materials

3.1.6.1 Silver

Silver is a metal with a work function between $4.26\,\mathrm{eV}$ and $4.72\,\mathrm{eV}$.[115] It is widely used for electronic contacts in devices mostly as an anode, often joined by a thin hole-selective interlayer.[116] It can be thermally evaporated at temperatures around $900\,^{\circ}\mathrm{C}$ from a boron nitride crucible or a molybdenum boat. Although it is still highly controversial in literature if silver forms an ohmic or a Schottky contact on ZnO[117, 118] it was chosen both as cathode and anode contact in this work after verifying that it forms an ohmic contact on the ZnO $(0\,0\,0\,\overline{1})$, ZnMgO $(0\,0\,0\,\overline{1})$ and SnO_2 $(1\,0\,1)$ substrates fabricated by molecular beam epitaxy.

3.1.6.2 Molybdenum Trioxide

Molybdenum trioxide (MoO_3) is one of two oxide compounds of molybdenum, involving molybdenum in the oxidation state $+6$. It boasts a huge electron affinity of ca. $6.7\,\mathrm{eV}$ and an ionization energy of ca. $9.7\,\mathrm{eV}$.[119] A thin molybdenum oxide interlayer is commonly used to improve the hole injection from metal contacts into organic molecules and polymers.[120] In the past there has been discussion about the true energetic situation of MoO_3, but UV photoelectron spectroscopy experiments have proven the high ionization energies mentioned above in favor of other claims with energy levels as much as $4\,\mathrm{eV}$ higher (e.g. [121]).

Interlayers of oxides with high work function significantly reduce the injection barrier from metal contacts to an organic semiconductor by contact doping. Electrons transfer from the organic HOMO to the oxide conduction band. The Fermi level situated close to the HOMO of the p-type organic material is pinned to the conduction band of the strongly n-type molybdenum oxide.[122, 123] In organic and hybrid inorganic/organic photovoltaics an interlayer thickness of $5\,\mathrm{nm}$ to $20\,\mathrm{nm}$ of MoO_3 has appeared to be optimal for device performance.[124, 125] In this work a layer thickness of $15\,\mathrm{nm}$ has been chosen. Another benefit of an oxide interlayer is that it protects the organic layer below from damages inflicted during evaporation of silver or gold contacts on top.

3.2 Sample Preparation Methods

3.2.1 Radical Source Molecular Beam Epitaxy

The inorganic layers of all samples presented in this work were fabricated by radical source molecular beam epitaxy (RS-MBE or short MBE) in a vacuum chamber (DCA-450) with a base pressure of $10^{-9}\mathrm{mbar}$. The metals zinc, tin, magnesium, gallium and antimony are provided by thermal evaporation from Knudsen cells, each cell can be opened and closed separately with a magnetically driven shutter made from tantalum. The metal beam flux is controlled by a Bayard-Alpert (nude ionization) gauge which can be placed in front of the substrate. A plasma of reactive oxygen is provided by a radio-frequency source. The oxygen partial pressure is regulated by a leak valve, ensuring oxygen-rich conditions for oxide deposition.

During growth the crystalline quality can be monitored in-situ by using a reflection high energy electron diffraction (RHEED) system. An electron gun produces a beam of electrons with a high kinetic energy of more than $10\,\mathrm{keV}$ striking the samples surface at a very small angle of $\theta \approx 2°$. Electrons diffracted at the crystal lattice of the samples can interfere constructively with each other if the in-plane component of the electron k-vector coincides with the in-plane k-vector of the electron wavefunction in the lattice. This corresponds to a Bragg reflection in the reciprocal space.[126] Consequently, a regular atomic lattice at the sample surface will lead to sharp peaks of diffracted electrons that can be monitored on a phosphorous screen and captured by a CCD camera outside the vacuum chamber.

The maxima of the RHEED pattern oscillate during crystal growth as only after completion of

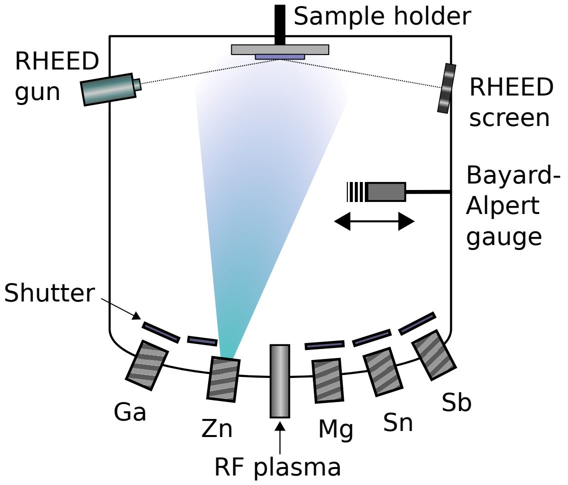

Figure 3.7: The molecular beam epitaxy (MBE) chamber features thermal evaporation sources for Zn, Mg, Sn, Ga and Sb. The beam flux is controlled by a nude Bayard-Alpert gauge which can be placed in front of the sample holder. Oxygen is provided by a RF plasma source. The sample surface can be analyzed with a RHEED system.

a full atomic layer on the crystalline surface the diffraction signal is maximal, while incomplete layers on the surface diminish the signal. It also provides information on the crystalline quality. The oscillations in RHEED signal are used to count the number of deposited monolayers in order to calculate the thickness of the layer.

ZnO:Ga/ZnO and ZnMgO:Ga/ZnMgO samples were grown on $(1\,\bar{1}\,0\,2)$ (a-plane) sapphire, enabling epitaxial growth of O-terminated $(0\,0\,0\,\bar{1})$ Zn(Mg)O. For SnO_2:Sb/SnO_2 samples r-terminated $(1\,\bar{1}\,0\,2)$ sapphire was used, resulting in a $(1\,0\,1)$ SnO_2 surface.

3.2.2 Vacuum Thermal Evaporation

Vacuum thermal evaporation is a widespread fabrication technique for thin layers of small molecules and a wide variety of other materials including metal contacts and oxide interlayers. In all cases the evaporation source is formed by a crucible, boat or cage of a heat resistant material containing the substance that is to be deposited. It is heated up in an effusion cell either with a heating wire or by applying a voltage directly to different ends of the evaporation source. Under high vacuum the molecules or atoms leave the evaporator in one straight direction and shape an evaporation cone. A substrate placed inside that cone will be covered with a very homogeneous layer.

The thickness of the deposited material is measured using a quartz microbalance which consists of an oscillating quartz crystal placed in proximity of the substrate. A controller device constantly sweeps excitation frequencies and measures the resonance frequency of the crystal which shifts in case of material deposition on top of the crystal. A careful calibration performed for each evaporation source and material allows to calculate the layer thickness produced on the

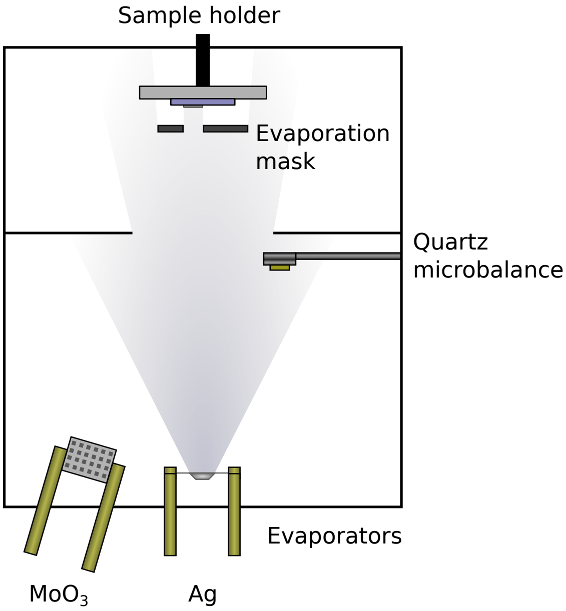

Figure 3.8: The thermal evaporation chamber used for fabrication of Ag and MoO$_3$ layers

sample substrate in relation to the resonance shift recorded by the microbalance.

The evaporation chamber used in this work (see figure 3.8) allows deposition of Ag and MoO$_3$ layers from a molybdenum boat respectively tungsten cage source heated by a current throughput of up to $200\,\mathrm{A}$. The base pressure is between 1×10^{-9} and $1 \times 10^{-8}\,\mathrm{mbar}$. An automatic mask system controlled by a step motor allows precise placement of single contacts with a predefined shape on the sample.

The sample is placed ca. $40\,\mathrm{cm}$ away from the evaporation source, typical evaporation rates are $1.5\,\mathrm{\AA/s}$ for Ag respectively $0.25\,\mathrm{\AA/s}$ for MoO$_3$.

3.2.3 Spin Coating

Thin films of polymers and other solution processable materials are commonly produced by the technique of spin coating (or spin casting). A small amount of solution is dispensed on the substrate by means of a syringe, subsequently the sample is rotated at a speed of 1000 to 6000 rotations per minute removing excess solution from the surface and forming a very homogeneous film on the substrate. In commercially available spin coaters the substrate is fixed onto the rotating chuck by vacuum established either actively with a connected pump or - like in this work - passively by jet holes in the chuck utilizing the centrifugal force on air in the rotating chuck. Figure 3.9 shows the phases of spin coating from dispensing the solution via film thinning to film drying. The resulting layer thickness of a certain material is defined by the choice of solvent, the concentration in solution and the rotation speed. During spin coating of P3HT in most solvents a clear change of color marks the transition between solution phase (light orange) and solid film (dark red).

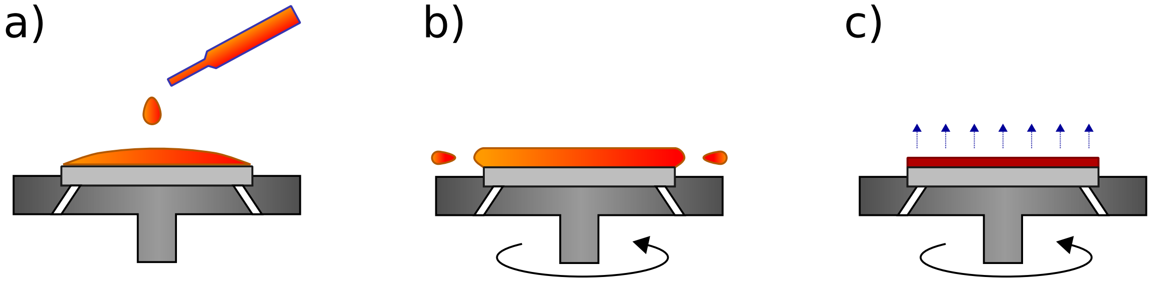

Figure 3.9: Three phases of spin coating: a) dispensing the solution onto the substrate b) film thinning by substrate rotation c) solvent evaporation and film drying

3.3 Sample Design

For a qualitative and quantitative investigation of charge separation processes between a metal oxide and an organic polymer, a diode structure has to be designed with a well defined planar interface between both components. An additional requirement is the possibility to contact both sides in a measurement circuit without high series resistance on either point disturbing the measurements. A sandwich-like structure involving pure ZnO, ZnMgO and SnO_2 cannot meet these conditions as the conductivity of either of these materials is too low to serve as backside electrode. However, utilizing a template patterned with a highly conductive layer of indium tin oxide (ITO) would not permit to grow single crystalline layers on top. This issue can only be solved by using a conductive electrode of doped semiconductor material. As described in section 3.1.4, gallium doping of ZnO or ZnMgO does not affect its crystal structure and neither does antimony doping to SnO_2. Consequently, fabrication of devices with a perfectly planar interface is possible by overgrowing the electrode of doped material with an undoped layer.

The thickness of the conductive electrode has to be chosen big enough to provide good electronic contact for the device, the thickness of the intrinsic layer is defined by the necessity of screening the electric field induced by excess electrons in the doped layer. The reach of electrostatic interaction in a semiconductor is defined by the Debye length

$$\lambda_D = \sqrt{\frac{\epsilon U_T}{e n_0}} \tag{3.1}$$

where e is the elementary charge, $U_T = \frac{k_B T}{e}$ the thermal voltage, $\epsilon = \epsilon_0 \epsilon_r$ the dielectric constant of the material and n_0 the intrinsic carrier density in the undoped material. λ_D gives the length over which the electric field drops to $\frac{1}{e}$ of its maximal value.[17] For nominally undoped ZnO with a background carrier density of $1 \times 10^{17}\,\mathrm{cm}^{-3}$ and a relative dielectric constant of 8 the Debye radius at $300\,\mathrm{K}$ is about $11\,\mathrm{nm}$ and even smaller at lower temperatures. Consequently an undoped layer of $100\,\mathrm{nm}$ thickness is enough to provide an interface without electrostatic influence from the doped layer.

3.4 Sample Layout and Device Fabrication

The bottom contact of the investigated diode structures is realized by a $150\,\mathrm{nm}$ thick layer of gallium-doped ZnMgO grown on an a-plane sapphire substrate. Its carrier concentration is about $1 \times 10^{20}\,\mathrm{cm}^{-3}$ and its conductivity $900\,\Omega^{-1}\mathrm{cm}^{-1}$. This is followed by $100\,\mathrm{nm}$ thick nominally undoped ZnMgO with the same magnesium contact which forms the inorganic part of the p-n-heterojunction. Both layers are prepared by plasma-assisted molecular beam epitaxy as described in section 3.2.1 resulting in single crystalline oxygen-polar ZnMgO $(0\,0\,0\,\bar{1})$ layers. A molybdenum mask attached to the sample during epitaxy leaves a stripe of sapphire uncovered. The samples are transfered to a metallization chamber in a vacuum vehicle maintaining a pressure as low as $1 \times 10^{-5}\,\mathrm{mbar}$. There a Ag contact is deposited on top of the ZnMgO layer, realizing an ohmic contact. Lateral charge transport in the devices almost entirely occurs in the doped ZnMgO:Ga layer. The thin undoped layer, which is passed twice in the measurement circuit, only induces a negligible series resistance.

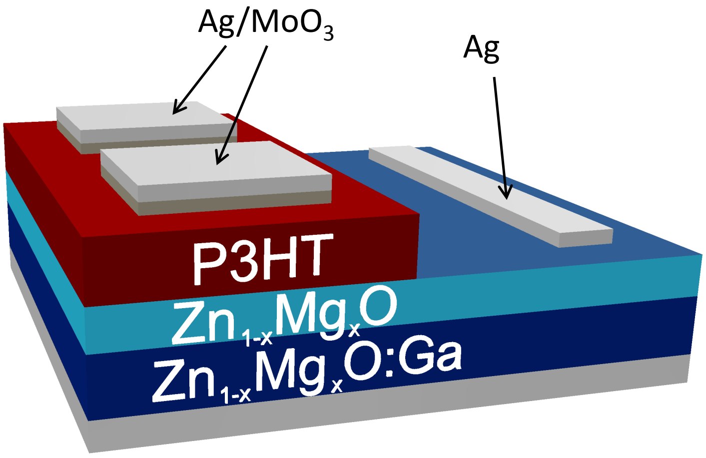

Figure 3.10: Schematic depiction of the device layout. The active area of a planar ZnMgO/P3HT photodiode is defined by the overlap of the Ag/MoO_3 anode and the ZnMgO acceptor layer.

The P3HT layer is spin-coated on top from a chlorobenzene solution. Different concentrations of P3HT in solution were used to produce layer thicknesses between $75\,\mathrm{nm}$ and $500\,\mathrm{nm}$. AFM scans show an average RMS roughness of 5 nm. The top contact is realized by depositing a $15\,\mathrm{nm}$ interlayer of MoO_3 ensuring an ohmic contact to P3HT, followed by $50\,\mathrm{nm}$ of silver. The base pressure in the metallization chamber was $1 \times 10^{-8}\,\mathrm{mbar}$, spin coating was performed in a glovebox providing an inert N_2 atmosphere. The samples were never exposed to air during the whole fabrication process.

In figure 3.10 the structure of the whole device is shown. The Ag/MoO_3 anode contact overlaps the bottom ZnMgO:Ga/ZnMgO layer by ca. $1\,\mathrm{mm}$ forming an active area of about $1\,\mathrm{mm}^2$. The actual size of the active area is determined for each sample by taking a photography and comparing the active area to the known substrate size of $10\,\mathrm{mm}$ by $10\,\mathrm{mm}$. Prior to integration into a measurement circuit, the P3HT on top of the Ag cathode contact is removed by scratching.

The samples involving ZnO are prepared in the same way and with the same dimensions, only replacing ZnMgO by ZnO in $(000\bar{1})$ orientation and using a doped electrode made from ZnO:Ga. For SnO_2/P3HT diodes the same layout was used with SnO_2 as acceptor and SnO_2:Sb as conductive electrode. In order to reduce series resistance of the sample, the antimony-doped layer was $200\,\mathrm{nm}$ thick. The undoped SnO_2 (101) acceptor layer remains with a thickness of $100\,\mathrm{nm}$.

3.5 Fabrication Protocol

The function and performance of the devices are very sensitive to fabrication conditions. Not only external impurities but also intrinsic degradation can seriously affect the sample quality. Surface reconstruction processes in ZnMgO and ZnO can rapidly change its electronic properties as long as it is not covered (e.g. by an organic layer). This even happens if stored in vacuum, leading to pronounced band bending effects.[93] In figure 3.11 is visible that the open circuit voltage of a ZnMgO/P3HT photodiode decreases by almost $300\,\mathrm{meV}$ if the sample is stored in vacuum for ca. 24 hours during fabrication before spin-coating the P3HT.

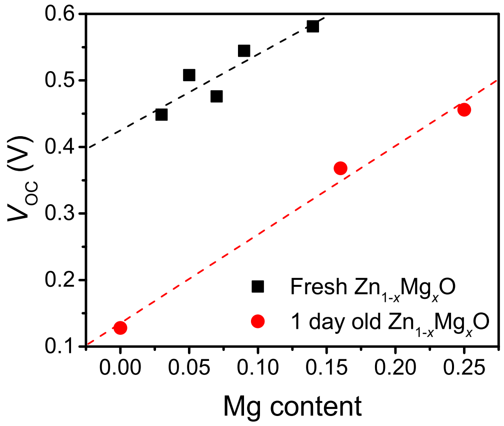

Figure 3.11: Storing the ZnMgO substrate in vacuum for 1 day before adding the organic layer decreases the open circuit voltage of a ZnMgO/P3HT photodiode under $100\,\mathrm{mW/cm^2}$ AM 1.5 G illumination by almost $300\,\mathrm{meV}$.

Consequently a strict fabrication protocol has to be employed during the fabrication of all samples, in which the P3HT is spin-coated on top of the ZnMgO or ZnO substrate between 3 and 5 hours after finishing the molecular beam epitaxy process. Once the inorganic was covered no further loss of sample quality was observed in case of delay in fabrication of the top contacts, and the samples could be used in measurements for up to 4 months without significant aging. As degradation effects on the sample surface also affect the chemical potential at the interface, samples dedicated for UV photoelectron spectroscopy have to be prepared within the same time schedule. The blank substrate is measured less than 4 hours after fabrication and spin-coating the P3HT layer was performed directly afterwards in order to complete the UPS measurements on the same day.

Chapter 4

Characterization Methods

This chapter gives an overview over the experimental techniques used in device characterization for this work. Interfacial level alignment between donor and acceptor layers are determined by UV photoelectron spectroscopy (UPS). Photoluminescence (PL) spectroscopy proves the general possibility of charge separation at an inorganic/organic hybrid interface. By employing various types of photovoltaic characterization under different illumination conditions and temperatures, photovoltaic functionality of planar photodiodes is investigated quantitatively and loss quantities are estimated. Electroluminescence measurements provide evidence for the existence of hybrid charge transfer states and shed light onto their physical properties. At last, atomic force microscopy (AFM) serves to investigate layer morphology and interface geometry.

4.1 UV Photoelectron Spectroscopy

Photoelectron spectroscopy (PES) is a common way to gain knowledge about the energetic structure of occupied electron states in a metal or semiconductor material. It is based on the photoelectric effect, i.e. the emission of an electron caused by absorption of a photon with sufficiently high energy.[127] Two types of PES can be distinguished along the different types of light sources used: Ultraviolet photoelectron spectroscopy (UPS) and X-ray photoelectron spectroscopy (XPS). While UPS is able to provide knowledge about the frontier occupied orbitals of organic materials and valence bands of inorganic semiconductors, XPS yields information about the core levels of atoms in the sample.

A monochromatic UV light source, commonly a helium discharge lamp or an undulator of a synchrotron, produces a sharp excitation spectrum on the sample surface and ejects electrons in its immediate proximity.[128] Electrons tossed into vacuum by incident photons are collected for measurement using a system of electrostatic lenses. The beam of electrons is focused onto the entrance slit of the hemispherical analyzer as depicted in figure 4.1. A bias between the inner and outer hemisphere of the analyzer deflects electrons according to their kinetic energy and only allows electrons with a certain pass energy to reach the detector. By performing a voltage sweep a whole spectrum over a range of kinetic energies can be recorded.

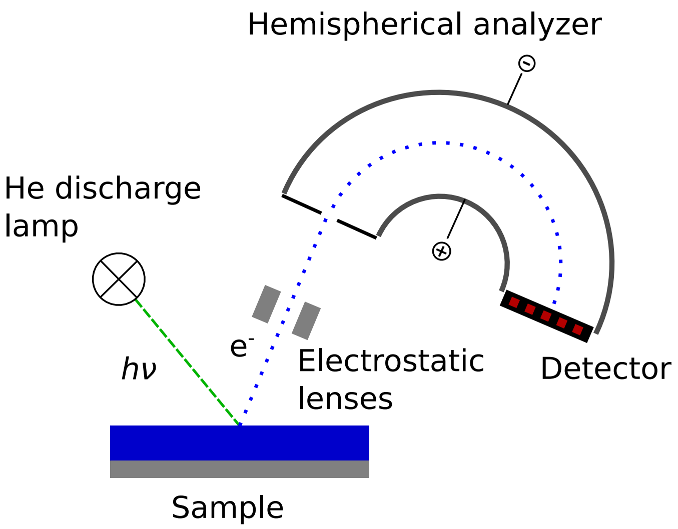

Figure 4.1: Monochromatic UV illumination from a He discharge lamp ejects electrons from the sample. A system of electrostatic lenses collects ejected electrons and focuses them onto the entrance slit of the hemispherical analyzer. A sweep of the bias between inner and outer hemisphere of the analyzer is performed, recording the number of incident electrons for each pass energy with the detector.

An electron ejected into vacuum has to overcome the ionization energy (IE) which is the sum of binding energy E_B and work function ϕ. If the energy of an incident photon $h\nu$ is sufficiently high, the ejected electron holds the kinetic energy $E_\text{kin} = h\nu - E_\text{B} - \phi$. As sample and detector are connected electrically, the contact potential difference between the Fermi levels of sample material and detector additionally accelerates or retards the electrons on their way to the detector, yielding the measured kinetic energy $E'_\text{kin} = E'_\text{kin} + \phi - \phi_\text{Det}$, additionally depending on the work function of the detector material ϕ_Det. If the work function of the detector is known, the binding energy of an occupied state in the sample material can then be calculated (see figure 4.2 and [129]) as

$$E_\text{B} = h\nu - E'_\text{kin} - \phi + (\phi - \phi_\text{Det}) = h\nu - E'_\text{kin} - \phi_\text{Det}. \tag{4.1}$$

If ϕ_Det is not known a priori, it can be determined by measuring the valence band spectrum of a clean metal surface (e.g. Au) and considering that electrons at the Fermi level of a metal have zero binding energy per definition.

Not all electrons absorbing a UV photon are thrown into vacuum directly. Inelastic scattering in the sample material causes electrons to lose energy and produces secondary electrons which can also leave the sample material if their kinetic energy still is high enough to overcome the ejection barrier imposed by the work function. Consequently a broad emission spectrum can be observed. A sharp cut-off on the low energy side (secondary electron cut-off, SECO) gives the value of the work function at the sample surface, because below this energy the electrons are not able to leave the material. As electrons arriving at the detector can create secondary electrons in

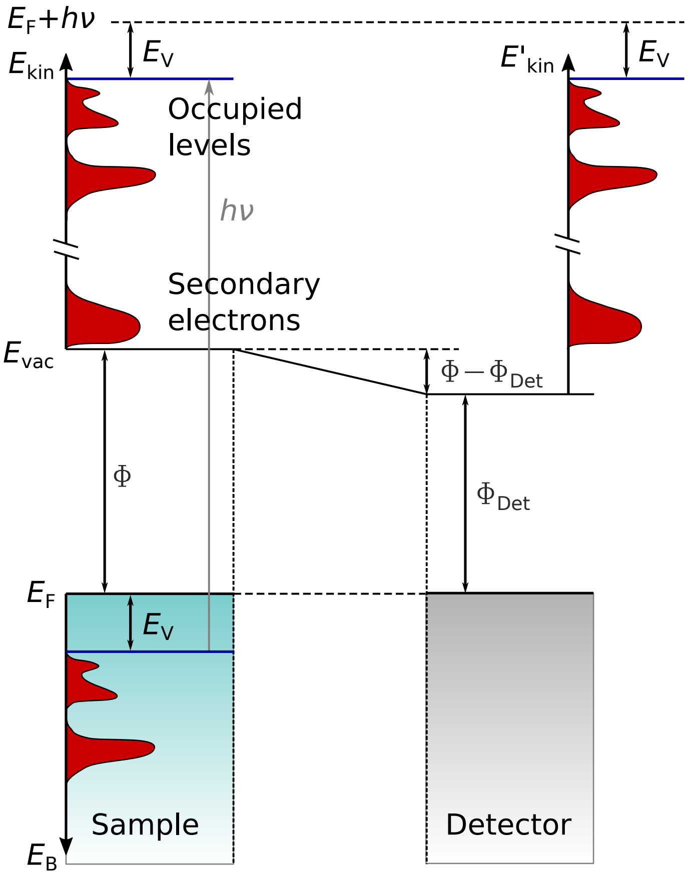

Figure 4.2: Schematic depiction of occupied energy levels in the sample, kinetic energies of ejected electrons E_{kin} and the photoemission spectrum E'_{kin} measured by the detector. The energy level $E_{\text{F}} + h\nu$ has to be determined by measuring the photoemission spectrum of a clean metal surface. Image adapted from reference [129].

the detector material as well, commonly a bias is applied between detector and sample in order to energetically separate SECO and detector secondary electrons from each other. This voltage has to be taken into account for calculation of the work function ϕ.

The UPS measurements in this work were carried out under illumination from a helium discharge lamp providing the He I spectral line at $h\nu = 21.22\,\text{eV}$. An aluminum filter was used to reduce the UV intensity by a factor of 0.07 and to avoid exposure to visible light from the UV source. By reducing the radiation intensity, sample degradation effects during measurement could be minimized. The photoemission spectra were checked for stability and reproducibility under several illumination densities. A Phoibos 100 hemispherical analyzer by SPECS was used for analyzing the photoelectrons together with a 5 channel electron multiplier. The work function of the detector was calibrated with a cleaned Au(III) single crystal. HOMO and valence band onsets and SECO positions were determined by intersecting a linear extrapolation of the baseline and the tangent to the slope of the measured spectrum.[130]

The samples for UPS analysis were fabricated in the same way as the samples used for photodiodes with a $150\,\mathrm{nm}$ thick ZnMgO:Ga layer followed by $100\,\mathrm{nm}$ thick ZnMgO on top of a sapphire substrate. The UPS measurements were intended to reproduce the sample fabrication protocol described in section 3.5 as exactly as possible. The inorganic samples were transported to the UPS spectrometer in N_2 atmosphere directly after fabrication, where the binding energy and work function of the bare ZnMgO surface was measured. Then, a $15\,\mathrm{nm}$ thick P3HT layer was spin-coated on top in a glove box under N_2 atmosphere, and UPS measurements were repeated with the hybrid sample. The whole time between ZnMgO epitaxy and the second UPS measurement did not exceed 5 hours.

4.2 Photoluminescence Spectroscopy

In photoluminescence (PL) measurements the sample is illuminated with a monochromatic light source and subsequently its photoluminescence response is measured with a suitable detector. This can happen both time-integrated or time-resolved. For this work the samples fabricated for photoluminescence measurements were mounted into a CryoVac bath cryostat directly after fabrication providing the possibility to cool them down to ca. $7\,\mathrm{K}$ with liquid helium. Optical excitation was performed with a frequency-doubled Nd:YVO4 laser (Vanguard by Spectra Physics) with a pulse width shorter than $13\,\mathrm{ps}$ and an excitation wavelength of $532\,\mathrm{nm}$, corresponding to a photon energy of $2.33\,\mathrm{eV}$.

The photoluminescence signal was spectrally analyzed by a Jobin-Yvon HR 250 double monochromator with a focal length of $250\,\mathrm{mm}$ and a 600 grooves/mm grating. Time-integrated PL spectra were recorded with a photomultiplier and the monochromator performing a wavelength sweep over the visible range. Time-resolved luminescence transients were recorded with a Hamamatsu microchannel photomultiplier tube with a transit time speed FWHM of $25\,\mathrm{ps}$ defining the temporal resolution. In data analysis the instrumental response function has to be taken into account. The fit functions have to be convoluted with the instrumental response function before being matched to the actual measurement results.

4.3 Electrical and Photovoltaic Characterization

After fabrication all photodiode samples were mounted onto a small circuit board which provides the possibility to contact the structures with thin gold wires and a conductive epoxy glue containing silver particles as depicted in figure 4.3. During the mounting process, the samples were exposed to air for ca. 15 minutes. After curing the glue for 24 hours, the circuit board was placed in a CryoVac bath cryostat which can be either flushed with N_2 gas at room temperature in order to prevent sample degradation or filled with liquid N_2 or He for measurements at low temperatures. Several quartz windows in the chamber allow both illumination of the samples and luminescence spectroscopy in the whole spectral range from UV to near IR. A Keithley 2601 SourceMeter is used for all current-voltage measurements, a Xe arc lamp (LOT Oriel) combined with a Gemini 180 double monochromator serves as light source.

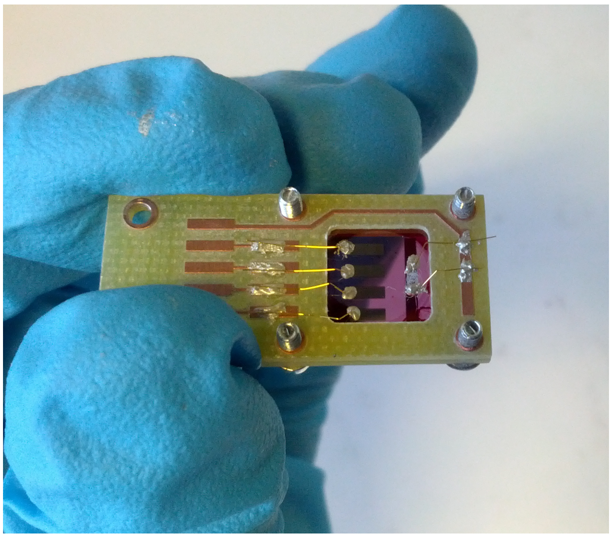

Figure 4.3: A diode sample mounted into a circuit board and contacted by gold wires

Two types of measurements were performed: For current-voltage characteristics in the dark or under illumination the current flowing through a photodiode structure was recorded over a range of voltages applied to the device. Spectrally resolved measurements of power conversion efficiencies were performed under zero external bias by measuring the short circuit current of the sample while performing a sweep of photon energies in excitation.

Stable results over several measurement runs were obtained if the applied bias to a device did not exceed $1\,\mathrm{V}$. At higher voltage electrochemical doping processes[131] and permanent formation of conductive metal filaments in the organic layer[132] significantly decrease the rectification ability of the device. This behavior provides promising opportunities for the development of new non-volatile memory devices,[133, 134], but is clearly detrimental to the function of photovoltaic cells. For this reason, all J-V characteristics were recorded only in a range between $-1\,\mathrm{V}$ and $1\,\mathrm{V}$. This range was only slightly extended when the open circuit voltage of a device was larger than $1\,\mathrm{V}$. In electroluminescence measurements, the exposure of the devices to higher bias was minimized and the current density was carefully monitored in order to prevent significant degradation effects in the device characteristics.

4.3.1 Current-Voltage Characteristics under Illumination

For characterizing the photovoltaic devices the standardized air mass 1.5 global (AM 1.5G) spectrum is employed (see section 2.3.1). It simulates incident sunlight after passing 1.5 times the thickness of the atmosphere (corresponding to an incident angle of $48.2°$). It can be obtained for laboratory by using a Xe arc lamp combined with a certified filter. For samples including ZnMgO and ZnO a different spectrum is used in order to circumvent persistent photocurrent effects originating from defect excitations under UV light (see appendix A). To the AM 1.5G filter a longpass filter is added which cuts out all UV radiation at wavelengths below $395\,\mathrm{nm}$. For samples containing SnO_2 the simulated AM 1.5G spectrum can be used without an additional filter. The resulting spectrum measured by a Si CCD camera (Princeton Instruments) is depicted in figure 4.4.

In the measurement setup, the light of a Xe arc lamp first passes through the Gemini monochromator at zero diffraction order. A rectangular aperture mask is projected onto the active area of the sample by two quartz lenses, matching up the size of the contact area. The irradiation density is controlled by a thermal power meter (SpectraPhysics) connected to the beam path by a flippable mirror. A series of neutral density filters allows power-dependent measurements at light densities between $0.35\,\mathrm{mWcm^{-2}}$ and $310\,\mathrm{mWcm^{-2}}$. Current-voltage characteristics can also be recorded under single-wavelength illumination by using the first diffraction order output of the monochromator.

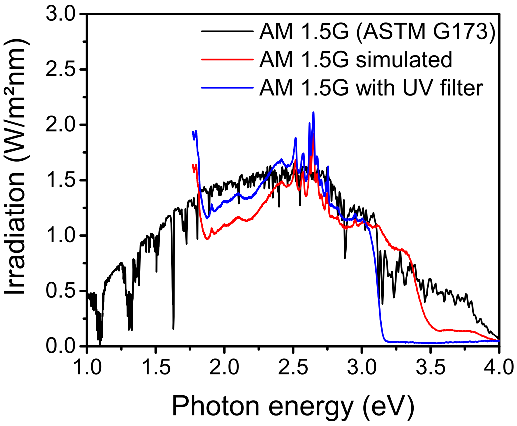

Figure 4.4: Simulated solar spectra in comparison to the standardized AM 1.5G spectrum. The blue line represents the AM 1.5G spectrum modified by an additional band edge filter, cutting off UV irradiation. This illumination spectrum is used for characterization of samples involving ZnO and ZnMgO. For measurements on SnO_2/P3HT diodes the unmodified AM 1.5G spectrum (red line) is used.

4.3.2 EQE Measurements

Wavelength-dependent measurements of the *external quantum efficiency* (EQE) are performed using a Xe arc lamp and a Gemini 180 double monochromator and the same imaging lineup as described in section 4.3.1 without additional filters. The spectral output is recorded by a Si diode with known quantum efficiency spectrum. Before each wavelength sweep the spectral density is measured at a single wavelength of $350\,\mathrm{nm}$ with a power meter (Thorlabs). This value is used to scale the global intensity of the irradiation spectrum when calculating the photon conversion ratio. The wavelength sweeps are performed with a slit width of $2\,\mathrm{mm}$ which gives a spectral resolution of $4.6\,\mathrm{nm}$ at a step width of $1\,\mathrm{nm}$.

4.4 Electroluminescence Spectroscopy

For electroluminescence spectroscopy the sample is fixed in the same CryoVac cryostat as in the photovoltaic measurements. Light emission from the diode contacts is projected onto the entrance slit of an Acton SpectraPro300i monochromator with $300\,\mathrm{nm}$ focal length by two achromate lenses with anti reflection coating for the NIR spectral range. The spectra are recorded by a nitrogen-cooled InGaAs detector (Princeton Instruments OMA V:InGaAs) providing high detection efficiency in a range between 900 and $1550\,\mathrm{nm}$ and a region with less sensitivity at wavelengths under $900\,\mathrm{nm}$. The efficiency of detection is calibrated with a black body source of known temperature. For alignment a monochromatic laser beam ($405\,\mathrm{nm}$ or $532\,\mathrm{nm}$) is focused onto the active photodiode area and the photoluminescence signal of P3HT is maximized in detection. Subsequently the laser is switched off and the EL spectrum originating from the same spot on the sample is recorded.

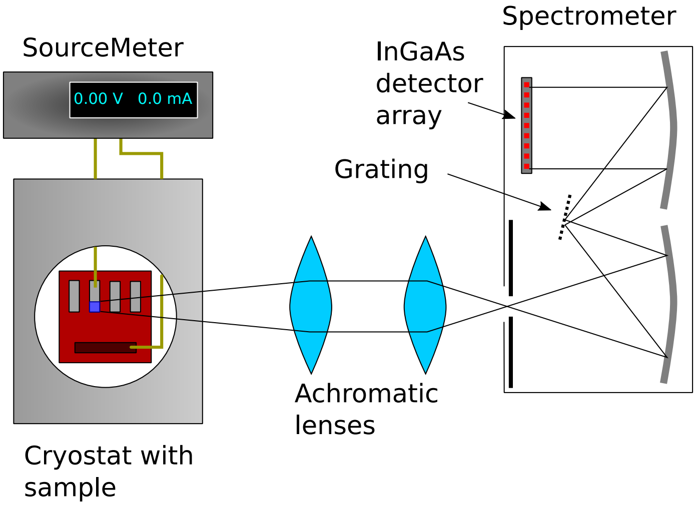

Figure 4.5: The measurement setup for electroluminescence spectroscopy: A planar photodiode is mounted into a cryostat under N_2 atmosphere. A Keithley SourceMeter connected to the contact pads on the device acts as voltage source. Detection of the EL signal occurs through a quartz window in the cryostat using the combination of a monochromator and an InGaN detector.

Electroluminescence emission spectra of the samples analyzed in this work span over a range of up to $1000\,\mathrm{nm}$ which requires to glue together several recordings taken at different spectral positions of the monochromator. For each full spectrum, three partial spectra are recorded with an overlap of ca. $200\,\mathrm{nm}$ each in order to join the spectrally corrected parts for a total spectrum of P3HT and HCTS luminescence. In continuous EL measurements a Keithley 2601 SourceMeter is used as voltage source and current meter at the same time. Over the timespan of each recording the current is constantly monitored in order to exclude permanent sample degradation due to filament formation and electrochemical reactions as described in section 4.3.

4.4.1 Time-resolved Electroluminescence Measurements

Voltage pulses for measurement of electroluminescence transients were provided by an Agilent function generator. In order to minimize reflection effects in the measurement circuit and to provide a clear pulse profile with sharp pulse edges of only ca. $3\,\mathrm{ns}$ width, the sample was contacted in a parallel circuit together with a $50\,\Omega$ termination resistor using coaxial cable. The resulting voltage pulses are depicted in figure 4.6, as measured by a Hewlett Packard 54522A digitizing oscilloscope.

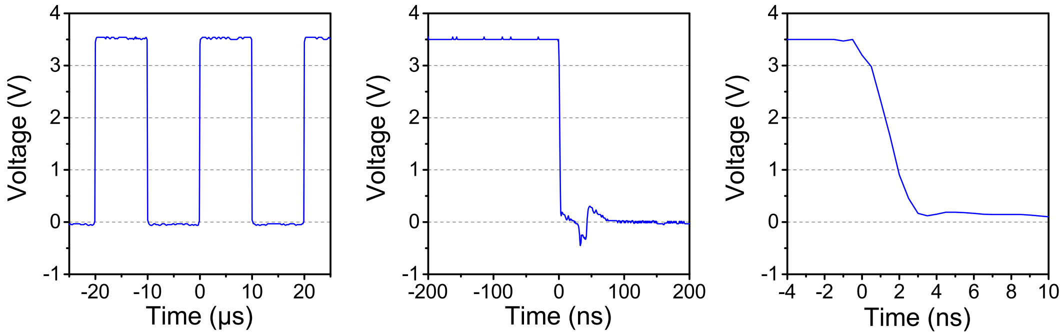

Figure 4.6: $10\,\mu\mathrm{s}$ long voltage pulses as used for time-resolved electroluminescence measurements, analyzed in three different timescales. The width of falling edges is ca. $3\,\mathrm{ns}$.

Time-resolved electroluminescence transients are recorded with a Hamamatsu InP/InGaAsP (H10330B-25) photomultiplier with spectral response between 950 and $1200\,\mathrm{nm}$, providing a temporal resolution of $2\,\mathrm{ns}$. The photomultiplier is connected to the same SpectraPro300i monochromator as the InGaAs detector for steady state measurements. With the entrance and exit slit fully opened to $2\,\mathrm{mm}$ in order to maximize the signal for detection and a grating with 300 grooves/mm blazed at $1000\,\mathrm{nm}$ a spectral resolution of $22\,\mathrm{nm}$ is achieved. Such a resolution is absolutely sufficient for analysis of charge transfer electroluminescence, as its spectral features stretch over several hundreds of nanometers.

Besides the temporal resolution of the detection unit, the instrumental response function in electroluminescence transient measurements is defined by the response time of the measurement circuit to changes in applied voltage. The diode structures used in this work can be regarded as a capacitor consisting of two plates formed by the bottom ZnMgO:Ga layer and the Ag/MoO_3 top contact as outer plates enclosing two dielectric layers of P3HT and undoped ZnMgO. Together with the series resistance imposed by lateral transport in the ZnMgO:Ga layer and traversing of the ZnMgO layer again below the Ag cathode, a RC circuit is formed. Then, the time necessary to build up the fraction $1/e$ of the applied voltage V_0 on the diode device is the time constant $\tau = R \cdot C$.

The capacitance of a ZnMgO/P3HT diode with a P3HT thickness of $240\,\mathrm{nm}$ is ca. $150\,\mathrm{pF}$ under the assumption that the organic layer is entirely depleted. The resistance imposed by transport through ZnMgO:Ga over a distance of $1\,\mathrm{mm}$ at a channel width of $1\,\mathrm{mm}$ and a material thickness of $150\,\mathrm{nm}$ is ca. $75\,\Omega$ with a negligible contribution from crossing the undoped ZnMgO layer before reaching the electrode. This yields a RC time constant of $\tau \approx 11\,\mathrm{ns}$, defining the system response time of the time-resolved electroluminescence measurements.

4.5 Atomic Force Microscopy

Atomic force microscopy (AFM) (or *scanning force microscopy*, SFM) is a special form of scanning probe microscopy (SPM) allowing to detect the surface morphology of plane samples down to the sub-nanometer range. It was developed by *Binnig et. al.* in 1985.[135] In contrast to scanning tunneling microscopy, where the tunnel current between a conductive sample and a measurement tip is measured, in AFM only mechanical forces between sample and tip are regarded. Therefore it is especially well suited for electrically insulating samples, but not restricted to these. The forces to be taken into account are quantum mechanical repulsion due to the Pauli principle and the van der Waals interaction between atomic nuclei and electrons, forming a Lennard-Jones potential.[136] The strength of other forces of origins like covalent molecular bondings and surface tension can also be analyzed in specialized measurement conditions.

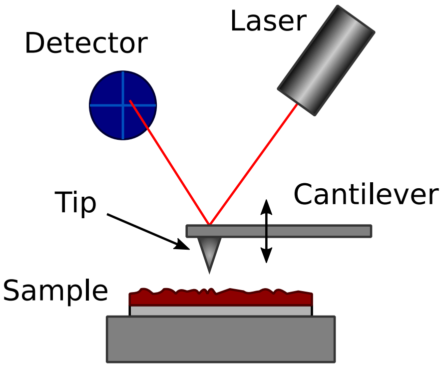

Figure 4.7: Schematic depiction of an atomic force microscope: Light from a laser source is reflected by the backside of the cantilever onto a quadrant detector array. Small movements of the measurement tip can be sensed at resolutions in the sub-nanometer range.

In order to measure the small forces exerted onto the measurement tip, it is mounted onto a silicon cantilever (or etched from the same material). Small displacements of the cantilever are measured by focusing a laser beam onto the top flat of the cantilever. The reflected laser light is sensed by a quadrant detector array. From its exact positioning, the surface morphology can be calculated. There are two different methods of force measurement: contact mode and tapping mode. In contact mode, the tip is being bent upward by direct interaction with the sample. Due to the short distance between tip and sample this method is very precise, however, the sample surface can be damaged from mechanical contact with the tip. For soft samples like organic molecules and polymers the tapping mode is the method of choice, in which the measurement tip is oscillating at or slightly off its eigenfrequency while not touching the sample surface. Any forces exercised on the measurement tip change the resonance frequency of the cantilever, so that the strength of interaction can be calculated.[137] In the commonly used *amplitude modulation* mode the amplitude of the cantilever oscillation is kept constant by adjusting the distance between sample and tip with a z scanner. An image of the sample surface can be created by scanning the measurement tip over the sample in x and y direction either by moving the sample beneath the tip or moving the cantilever itself and performing force measurements for each point. This is usually done by piezoelectric actuators. Joining x-y position of the cantilever with the measured interaction strength from the sample, a 3D landscape of the sample surface can be created. All AFM measurements shown in this work were performed with a Bruker MultiMode 8 equipment in tapping mode under air. The silicon measurement tips have a spring constant of ca. $42\,\mathrm{N/m}$ and a resonance frequency of ca. $300\,\mathrm{kHz}$. The thickness of evaporated or spin-coated organic layers on a mechanically stable surface like zinc oxide can be controlled by scanning over a scratch in the organic layer. Such a scratch can be produced either externally with a needle or with the measurement tip itself by performing a scan in contact mode with strong force applied onto the cantilever.

A common parameter for the roughness of a surface is the root mean squared roughness or RMS. It is defined as the standard deviation of the sample surface height compared to its mean value.

$$RMS = \sqrt{\frac{1}{MN}\sum_{m=1}^{M}\sum_{n=1}^{N}\left(z(x_m, y_n) - \bar{z}\right)^2} \tag{4.2}$$

where M and N are the number of rows and lines of the scanned image, and $\bar{z}$ the mean height given by

$$\bar{z} = \frac{1}{MN}\sum_{m=1}^{M}\sum_{n=1}^{N} z(x_m, y_n). \tag{4.3}$$

Chapter 5

Zinc Oxide Based Hybrid Photovoltaics

Earlier research on organic photovoltaic heterojunctions has shown the important role of carrier delocalization in the charge separation process.[138, 139] On the one hand, pairs of electrons and holes situated in extended band structures have a reduced Coulomb attraction due to an increased distance from each other, which facilitates full carrier separation. On the other hand, recombination processes are effectively reduced by decreasing the wavefunction overlap between both particles.

While semi-crystalline polymers like regio-regular P3HT offer very high mobilities in their crystalline domains involving stacked π-systems,[110] the presence of organic acceptor molecules (e.g. fullerene derivatives) along with a reduced carrier mobility imposes a serious limitation on the charge separation process in organic photovoltaic devices.[140] A feasible way to overcome this drawback is to combine an organic donor with of a crystalline inorganic material as acceptor. Due to its high electron affinity of over $4\,\mathrm{eV}$, Zinc oxide is a promising candidate for efficient hybrid photovoltaics. Its wide band gap of ca. $3.3\,\mathrm{eV}$ makes it transparent in the whole visible spectrum, so that incident light can pass through it to a donor material.

A thorough study of the charge separation process in a photovoltaic heterojunction requires a model system which provides a controllable environment for quantitative measurements. A special focus has to be put on the structure of the active area in which photovoltaic power conversion occurs. Only a planar heterojunction of donor and acceptor allows an analytical study of exciton dissociation and carrier recombination processes on a molecular scale as well as their influence on the behavior of a photovoltaic model device.

In this chapter a model system consisting of atomically flat zinc oxide grown by molecular beam epitaxy and the polymer P3HT will be presented. Measurements of diode characteristics in the dark and under illumination allow to asses the photovoltaic functionality of the material system. Electroluminescence spectroscopy provides valuable knowledge on energy levels in proximity of the boundary between donor and acceptor and thus allows to evaluate photovoltage losses in the power conversion process.

The first research on zinc oxide as an acceptor material in solar cells has already been conducted in 1980 by *Aranovich et. al.* who reached a power conversion efficiency of 8.8 % with a ZnO/CdTe heterojunction grown by spray pyrolysis.[141] In the 2000s organic photovoltaics emerged exploiting the benefits of small molecules and polymers, especially their strong light-matter coupling for good light absorption. However, their weaknesses in charge carrier mobility and their low stability brought oxide materials like ZnO back into the focus of research. The combination of an organic donor with an inorganic acceptor was expected to increase the efficiency of charge separation and prevent interfacial losses due to its better transport properties. In some studies, ZnO was also used as an electron extracting interlayer added to an entirely organic donor-acceptor system.[142]

For gaining optimal profit from ZnO/organic heterojunctions, several layer morphologies were examined in order to maximize the interface area and thus to enhance charge separation. ZnO nanoparticles[10], nanofibers[15] and nanorods[124] were employed, but despite the promising perspective of hybrid photovoltaics, power conversion efficiency barely exceeded 0.5 % for the best devices, significantly lagging behind other material combinations. Different mechanisms for increasing photovoltaic charge separation were investigated, like the introduction of an organic monolayer providing an interface dipole to assist the dissociation of excitons, for instance. In such a model system, the charge separation of a ZnO/P3HT solar cell could be increased by a factor of 3.[143]

Chemical doping of ZnO opens a variety of ways to manipulate the interface energetics between inorganic and organic component. The introduction of nitrogen atoms into ZnO leads to a de-trapping of electrons from interfacial defect states and thereby reduces interfacial recombination with photogenerated holes in P3HT.[144] A similar reduction of surface defect states can be reached by Cs doping of ZnO, leading to a significantly improved charge separation efficiency.[145] As a common drawback of eliminating trap states a reduced conductivity in ZnO can be observed, again limiting the photovoltaic functionality.

Manipulating the interface energetics by alloying ZnO with MgO only allows a small increase in photovoltaic efficiency.[146] A systematic widening of the inorganic band gap, however, can serve as a basis for a detailed study of the processes involved in photovoltaic charge generation at a hybrid inorganic-organic heterojunction. This will be reported in detail in chapter 6 of this work.

5.1 Epitaxially Grown ZnO and ZnMgO Acceptor Layers

Using molecular beam epitaxy (MBE) for fabrication of ZnO or ZnMgO acceptor layers, as described in section 3.2.1, results in atomically flat layers of a well-defined orientation, which are suited for detailed study and quantitative investigation on the processes of charge separation and recombination. It also offers the possibility for angle-resolved measurements, because the orientation of an entirely flat interface is constant over a large sample area. Figure 5.1(a) shows an AFM scan of an oxygen-terminated $(0\,0\,0\,\bar{1})$ ZnO surface grown by MBE on a sapphire substrate, revealing terraces of single-atomic steps.

In the layout of a solar cell, a transparent backside electrode is necessary. The commonly used indium tin oxide (ITO) is not suitable here as it disallows epitaxial overgrowth with ZnO

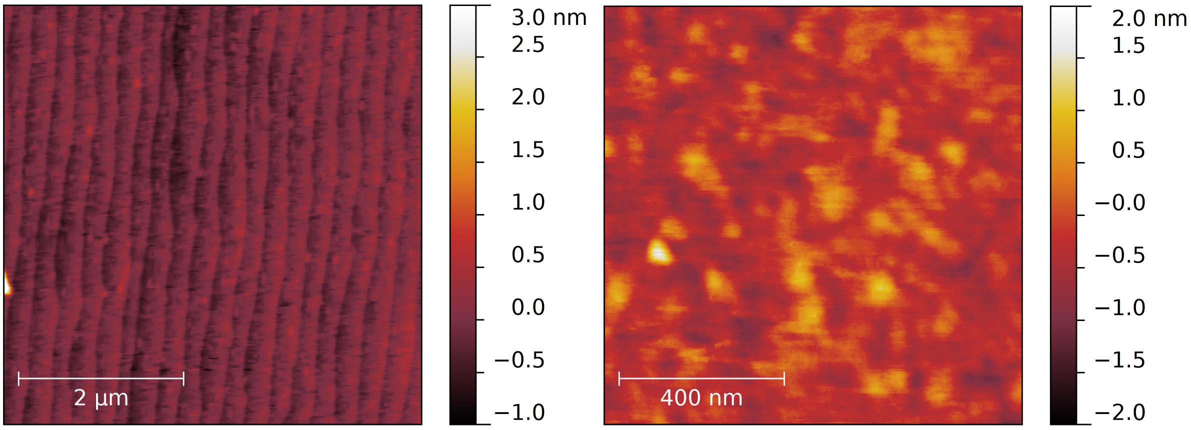

(a) ZnO $(0\,0\,0\,\overline{1})$ (b) ZnMgO $(0\,0\,0\,\overline{1})$

Figure 5.1: (a) AFM scan of an oxygen-polar $(0\,0\,0\,\overline{1})$ $100\,\mathrm{nm}$ ZnO layer grown by molecular beam epitaxy on a sapphire substrate (b) AFM scan of an oxygen-polar $(0\,0\,0\,\overline{1})$ $100\,\mathrm{nm}$ ZnMgO layer grown on top of a $150\,\mathrm{nm}$ ZnMgO:Ga layer on a sapphire substrate.

and its alloys. ZnO and ZnMgO, however, offer the possibility of gallium doping, thereby increasing its conductivity from $2.6\,\Omega^{-1}\mathrm{cm}^{-1}$ to $900\,\Omega^{-1}\mathrm{cm}^{-1}$ without losing the well-ordered crystal structure[108] as described in section 3.1.4. Band-gap widening in a strongly doped semiconductor due to the Burstein-Moss shift guarantees a transparent electrode in the whole transparency range of the undoped layer. The band gap of gallium doped ZnMgO shifts upward with increasing Mg content in the same way as in the undoped case, ensuring that ZnMgO:Ga always offers a transparent backside electrode independent of its Mg content. Figure 5.1(b) shows an AFM scan of the full acceptor system consisting of a $150\,\mathrm{nm}$ ZnMgO:Ga layer with a $100\,\mathrm{nm}$ ZnMgO layer grown on a sapphire substrate. The Mg content is $14\,\%$. The layer is still very flat and smooth, and the RMS roughness has only increased from $2.0\,\text{Å}$ to $3.2\,\text{Å}$, which is still below the size of a ZnMgO unit cell.[98]

5.2 ZnO and P3HT as Donor and Acceptor

ZnO and P3HT form a type II interface when brought into contact. This enables the possibility of charge separation at the interface by producing excitons in P3HT, which diffuse to the interface. Subsequently, the electron can transfer to the conduction band of ZnO. A common way to monitor this process is time-resolved photoluminescence spectroscopy. Excitons in P3HT can either recombine, producing a characteristic photoluminescence spectrum, or dissociate at the interface without light emission.

The addition of a second decay channel shortens the fluorescence lifetime. A mean charge transfer time τ_{CT} can be defined as

$$\tau_{\mathrm{CT}}^{-1} = \tau_{\mathrm{Hy}}^{-1} - \tau_0^{-1} \tag{5.1}$$

with τ_{Hy} being the fluorescence lifetime of the new hybrid system and τ_0 the lifetime of the unmodified system alone. The efficiency of electron transfer η_{CT} is then given as

$$\eta_{\mathrm{CT}} = \frac{\tau_{\mathrm{Hy}}}{\tau_{\mathrm{CT}}}. \tag{5.2}$$

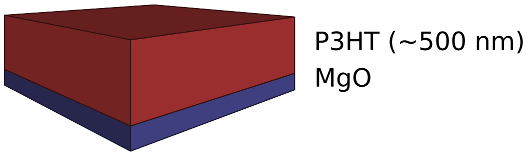

(a) P3HT on MgO

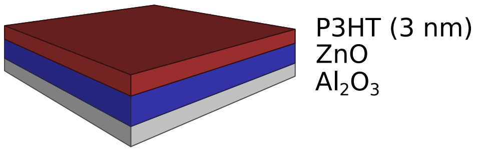

(b) P3HT on ZnO

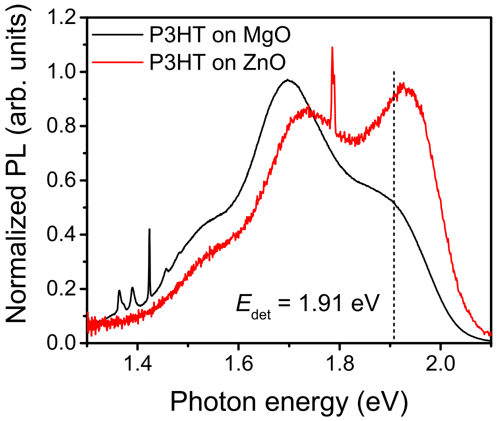

(c) PL spectra

Figure 5.2: (a) and (b) Schematic depictions of the samples used in photoluminescence transient measurements: (a) ca. $500\,\mathrm{nm}$ thick layer of P3HT on a single-crystalline MgO substrate. (b) $3\,\mathrm{nm}$ P3HT on a ZnO $(0\,0\,0\,\overline{1})$ layer grown on a sapphire substrate. (c) Normalized photoluminescence spectra of P3HT on ZnO $(0\,0\,0\,\overline{1})$ and MgO substrates including typical Raman lines for ZnO and MgO. The contribution of the $S_{1,\nu=0} \rightarrow S_{0,\nu=0}$ transition at ca. $1.9\,\mathrm{eV}$ decreases in a thicker P3HT layer due to re-absorption and increased crystallinity.[147] $E_{\mathrm{det}} = 1.91\,\mathrm{eV}$ marks the detection energy for photoluminescence transients. The excitation energy is $2.33\,\mathrm{eV}$ with a density of ca. $600\,\mathrm{mW/cm^2}$.

Two samples are fabricated to prove charge separation at the ZnO/P3HT interface. One sample consists of an epitactically grown ZnO $(0\,0\,0\,\overline{1})$ layer on top of a sapphire substrate with a very thin spin-coated P3HT layer of only $3\,\mathrm{nm}$ thickness on top. The thin organic layer ensures that all produced excitons are likely to reach the interface in spite of their limited diffusion length of only a few nanometers. The second sample is fabricated to measure the intrinsic fluorescence lifetime of P3HT without contact to any interface. Therefore an inert single-crystalline MgO substrate is used which disallows transfer of both electrons and holes from P3HT due to its very wide band gap. As spin coating of P3HT fails due to a significant lack of adhesion forces, a ca. $500\,\mathrm{nm}$ layer of P3HT is fabricated by drop-casting.

Figure 5.2(c) shows the normalized photoluminescence spectra of P3HT on ZnO and MgO measured with an excitation energy of $2.33\,\mathrm{eV}$. Photoluminescence transients are measured at a detection energy of $E_{\mathrm{det}} = 1.91\,\mathrm{eV}$ in the maximum of the $S_{1,\nu=0} \rightarrow S_{0,\nu=0}$ transition peak.

The transients recorded in time-resolved photoluminescence measurements show the effective quenching of excitons in P3HT by opening charge transfer as an additional decay channel. Their mean lifetime decreases from $\tau_0 = 600\,\mathrm{ps}$ in a thick bulky layer on an inert substrate to $\tau_{\mathrm{CT}} = 148\,\mathrm{ps}$ in contact with a ZnO acceptor surface. This yields a mean charge transfer time

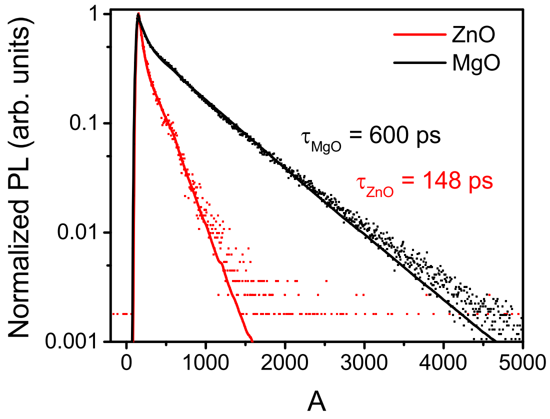

Figure 5.3: Photoluminescence transients of P3HT photoluminescence on ZnO $(0\,0\,0\,\bar{1})$ and MgO substrates show a clear shortening of fluorescence lifetime due to exciton quenching at the ZnO/P3HT interface.

of $\tau_{\mathrm{CT}} = 196\,\mathrm{ps}$ and corresponds to an exciton dissociation rate of $\eta \approx 0.76$. Dissociation of excitons at the type II interface is a process of good efficiency which promotes the combination of ZnO and P3HT as an interesting candidate for inorganic-organic hybrid photovoltaics.

5.3 ZnO/P3HT Planar Heterojunction Photodiodes

Photodiodes fabricated from a ZnO/ZnO:Ga acceptor and a $240\,\mathrm{nm}$ thick P3HT layer as donor show a very good rectification behavior. Figure 5.4 shows the current-voltage characteristic of a ZnO/P3HT photodiode with a rectification ratio $\beta = \frac{J(+1\,\mathrm{V})}{J(-1\,\mathrm{V})}$ of more than 10^5. The current in forward direction begins to grow exponentially, but then undergoes a current roll-off at an applied bias above $0.3\,\mathrm{V}$. The characteristics are well reproducable between several diode contacts on the same sample.

Under illumination, a ZnO/P3HT diode produces a photocurrent. In the spectrum of external quantum efficiency (EQE) in figure 5.5(a) it is visible that light absorption in both P3HT and ZnO contribute to the current output. The absorption spectrum of P3HT is clearly visible in the EQE spectrum, but also excitons produced in ZnO can migrate to the interface and dissociate there. This results in the contribution at ca. $3.3\,\mathrm{eV}$. At higher photon energies a filter effect due to the thick ZnO and ZnO:Ga layers sets in, which prevents further photocurrent. As the sample is illuminated from the backside, excitons are only produced within the absorption length of ca. $50\,\mathrm{nm}$[148] after entering the inorganic layer. The distance that these excitons would have to diffuse to the interface is too far to give a significant contribution to power conversion.

The room temperature EQE at the maximum of P3HT absorption of ca. $1\,\%$ appears to be low compared to other photovoltaic devices. The main reason for this is the short exciton diffusion length in P3HT of $L_{\mathrm{D}} \approx 5 - 8.5\,\mathrm{nm}$[22, 79] limiting the range from where excitons can reach the interface for charge separation to a slice, which is thin compared to the optical absorption

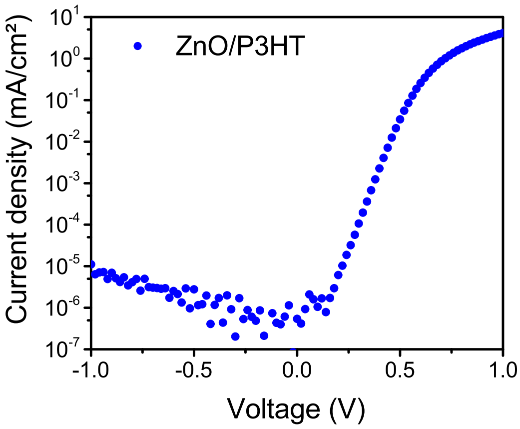

Figure 5.4: A ZnO/P3HT photodiode shows very good rectification over more than 5 orders of magnitude.

depth of P3HT (ca. $60\,\mathrm{nm}$). $L_\mathrm{D} \cdot \alpha \approx 0.1$, meaning that only $10\,\%$ of all photons are absorbed in the relevant range for charge generation, while 90 % of all excitons emerge far away from the interface and recombine without getting the opportunity for charge separation. For this reason, in actual photovoltaic devices nano-structured oxide layers are employed in order to minimize the pathway for excitons in the donor to reach the interface.

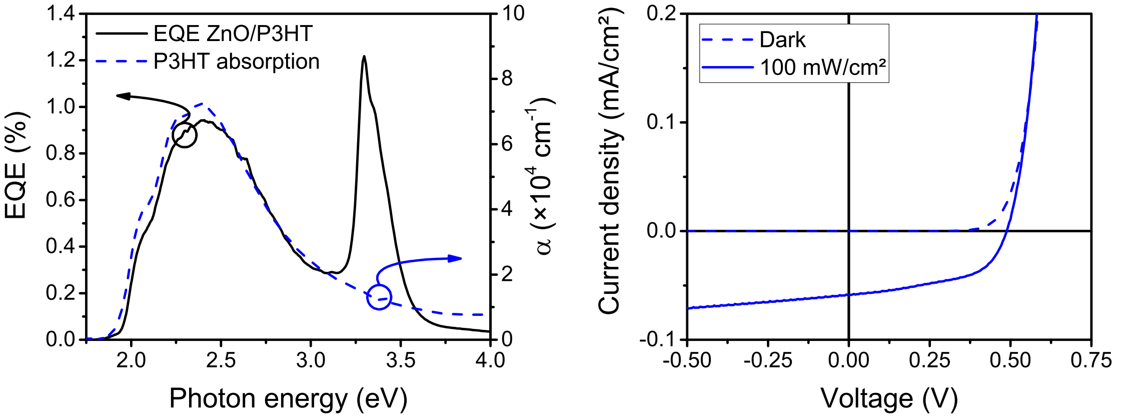

(a) EQE spectrum (b) J-V characteristic under 1 sun illumination

Figure 5.5: (a) In the external quantum efficiency (EQE) spectrum of a ZnO/P3HT photodiode photocurrent produced by absorption in both components can be observed. α gives the absorption coefficient measured from a P3HT layer on a sapphire substrate. (b) Current-voltage characteristics of a ZnO/P3HT solar cell in the dark and under $100\,\mathrm{mW/cm^2}$ AM 1.5G simulated solar spectrum (with UV cut off).

Under the modified $100\,\mathrm{mW/cm^2}$ AM 1.5G simulated sunlight spectrum with UV irradiation cut off by a $395\,\mathrm{nm}$ edge filter, a short circuit current of $0.058 \pm 0.004\,\mathrm{mA/cm^2}$ is produced. The open circuit voltage is $0.46 \pm 0.03\,\mathrm{V}$ with a fill factor of $52\,\% \pm 2\,\%$, resulting in a power conversion efficiency of $0.014\,\% \pm 0.002\,\%$.

In table 5.1 the obtained performance data from this solar cell is compared to the results from other planar ZnO/P3HT devices from literature with ZnO fabricated by other methods. The higher values of V_{OC} and fill factor indicate a high sample quality with a very small contribution from a shunt resistance. However the produced photocurrent significantly lags behind most of the literature values. This can be attributed to the increased surface area of ZnO fabricated by other methods providing less crystalline quality like wet-chemical sol-gel processing and spray pyrolysis.

Table 5.1: Comparison between the ZnO/P3HT solar cells employing MBE grown zinc oxide and other planar ZnO/P3HT devices from literature, including atomic layer deposition (ALD), spray pyrolysis and wet chemical sol gel deposition. The last row shows a planar P3HT/PCBM device.

ZnO	V_{OC} (V)	J_{SC} (mA/cm^2)	Fill factor	PCE
This work	0.46 ± 0.03	0.058 ± 0.004	$52\,\% \pm 2\,\%$	$0.014\,\% \pm 0.002\,\%$
ALD[144]	0.22	0.17	37 %	0.014 %
Spray pyrolysis[143]	0.21	0.47	42 %	0.04 %
Sol gel[149]	0.31	0.40	44 %	0.055 %
Sol gel[145]	0.24	0.97	49 %	0.12 %
P3HT/PCBM[150]	0.50	1.51	53 %	0.40 %

The growth of single-crystalline ZnO acceptor films by MBE is the only fabrication method to obtain a well-defined layer morphology and uniform surface termination, which cannot be guaranteed by other fabrication methods. This opens the possibility for a quantitative study of photovoltaic function and recombination processes.

To compare the presented hybrid inorganic/organic solar cells to entirely organic cells, the data of a planar P3HT/PCBM device from literature is displayed here. The heterojunction of P3HT/PCBM is expected to have a similar energetic configuration to ZnO/P3HT which enables an evaluation of the individual efficiencies and losses. The planar P3HT/PCBM device, however, outclasses all presented ZnO/P3HT devices in every single category. None of the hybrid devices can reach the values of organic diodes, neither in photocurrent nor in open circuit voltage or in fill factor. The power conversion efficiency of P3HT/PCBM amounts to seven times the efficiency of the best ZnO/P3HT device.

While fill factor and open circuit voltage of the MBE grown ZnO/P3HT diodes are very similar to those of P3HT/PCBM, the short circuit current is decreased by more than one order of magnitude. Consequently, there must be an intrinsic mechanism leading to severe recombination losses in the ZnO/P3HT solar cells. Careful investigation of the photovoltaic power conversion process will provide insight into the factors determining the efficiency of hybrid solar cells.

5.4 Temperature-dependent ZnO/P3HT Photovoltaics

5.4.1 V_{OC} and J_{SC} at Different Light Intensities

Commonly, the short circuit current in photovoltaic devices is directly proportional to the illumination density as long as charge extraction is not limited by a high series resistance. In figure 5.6 it is shown that this relation fits well to the measured data of a ZnO/P3HT solar cell up to an illumination density 3 times higher than standardized solar irradiation. A power law fit $J_{\mathrm{SC}} \propto P_{\mathrm{light}}^{\alpha}$ yields a value of $\alpha = 0.94$ indicating only a slight deviation from linear behavior at high irradiation densities. At lower temperatures, charge extraction from the interface is hampered by a reduced carrier mobility in the P3HT layer. This behavior becomes visible as an s-shape in the diode characteristics under illumination, and leads to a deviation from the proportionality between illumination density and short circuit current. A detailed description of the photovoltaic efficiency at lower temperatures will be elaborated in section 6.4.1.

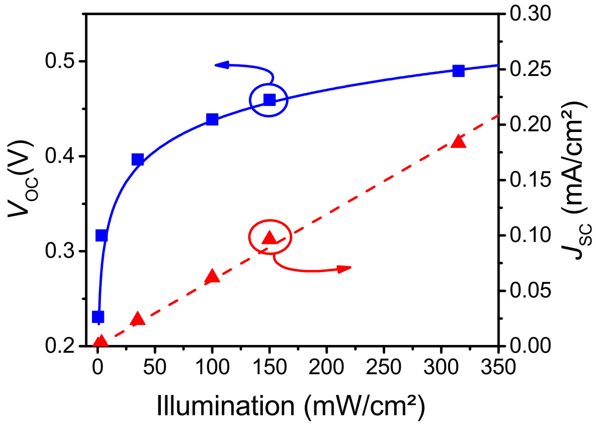

Figure 5.6: J_{SC} (red triangles) and V_{OC} (blue squares) of a ZnO/P3HT diode with $d_{\mathrm{P3HT}} = 240\,\mathrm{nm}$ at illumination intensities between $0.35\,\mathrm{mW/cm^2}$ and $315\,\mathrm{mW/cm^2}$ together with a linear fit for J_{SC} (red dashed line) and a fit according to equation 5.3 (blue solid line).

The open circuit voltage of a diode can be obtained from the Shockley equation 2.6 by imposing the condition $J = 0$ and assuming that the photocurrent J_{ph} is equal to the short circuit current J_{SC} at any applied voltage, yielding the relation

$$V_{\mathrm{OC}} = \frac{n k_{\mathrm{B}} T}{q} \ln\left(\frac{J_{\mathrm{SC}}}{J_0}\right). \tag{5.3}$$

A combination of both relations allows to determine the ideality factor n and recombination current J_0 of a device by evaluating measurements at different illumination intensities. For the ZnO/P3HT device analyzed in figure 5.6 $n \approx 1.6$ and $J_0 \approx 1.0 \times 10^{-6}\,\mathrm{mA/cm^2}$ are obtained, which justifies the assumption $\frac{J_{\mathrm{SC}}}{J_0} \gg 1$. This is necessary for replacing $\ln\left(\frac{J_{\mathrm{SC}}}{J_0} - 1\right)$ by $\ln\left(\frac{J_{\mathrm{SC}}}{J_0}\right)$ when simplifying equation 2.15 to equation 5.3.

Constant monitoring of the incident light intensity, however, is neither practical nor accurate in actual laboratory measurements. Therefore, it is recommendable to directly evaluate the quantities V_{OC} and J_{SC} as they can be measured easily and precisely.

5.4.2 Eliminating Transport Losses from the Diode Characteristics

Current-voltage characteristics of real devices are always influenced by series and shunt resistances as described in equation 2.7. If photovoltaic data is available over several temperatures and a series of illumination densities, the influence of transport phenomena can be isolated following the J_{SC}-V_{OC} method which is explained in more detail in section 2.3.6.1.

In the J-V curve of a ZnO/P3HT diode, no significant shunting behavior can be detected. The exponential regime reaches down to current densities below the detection limit of the measurement hardware. Consequently, only a series resistance is active here, limiting the diode current in forward direction.

Pairing the measured J_{SC} and V_{OC} for different illumination intensities yields points of a hypothetical loss-less characteristic of the bare heterojunction. In figure 5.7 a measured diode curve is compared to an ideal diode modeled from the V_{OC} and J_{SC} measured from the same device. At a temperature slightly below room temperature, $275\,\mathrm{K}$, the voltage drop at the heterojunction hardly differs from the external bias applied to the diode, while at $T = 190\,\mathrm{K}$ the voltage losses rapidly increase with higher current density.

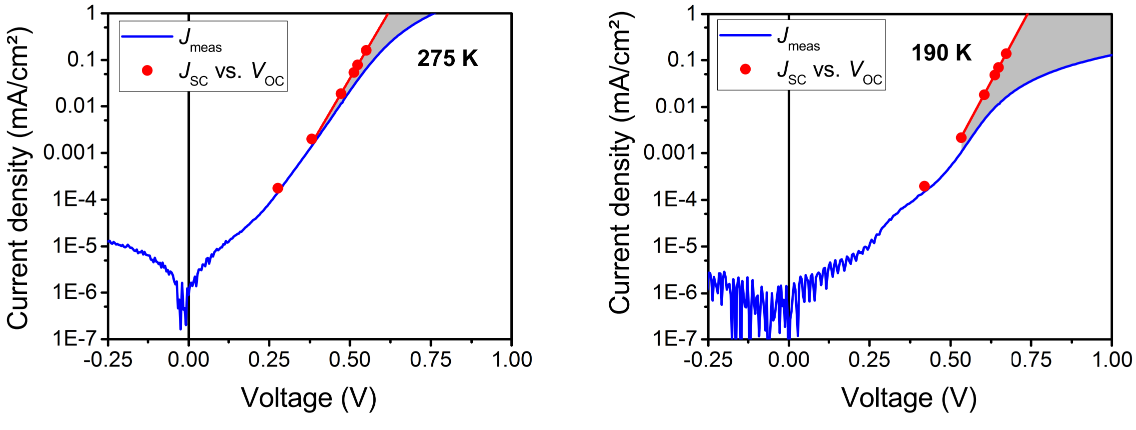

(a) $T = 275\,\mathrm{K}$

(b) $T = 190\,\mathrm{K}$

Figure 5.7: Measured J-V characteristic (blue line) compared to an ideal diode modeled from J_{SC} and V_{OC} values for illumination intensities between $0.35\,\mathrm{mW/cm^2}$ and $315\,\mathrm{mW/cm^2}$ (red circles). Temperatures: (a) $275\,\mathrm{K}$ and (b) $190\,\mathrm{K}$. The grey area shows the transport losses occurring at a forward bias greater than $0.3\,\mathrm{V}$.

In a ZnO/P3HT diode, transport losses emerge at a forward bias greater than $0.3\,\mathrm{V}$. This can be related to the built-in voltage of the device. At higher bias a space charge region forms in the P3HT hampering current transport. A detailed model describing the transport losses for

ZnMgO/P3HT diodes is discussed in section 6.2.1.1.

5.4.3 Ideality Factor n and Carrier Recombination in a ZnO/P3HT Diode

The simple form of the Shockley equation (equation 2.6) can be used to determine the ideality factor n and recombination current J_0 from V_{OC} and J_{SC} values. More insight into the physical processes at the heterojunction is provided by the differential method to determine the ideality factor n depending on the photocurrent density as described in section 2.3.6.1.

$$n = \frac{q}{k_{\mathrm{B}}T} \cdot \frac{\partial V_{\mathrm{OC}}}{\partial \left(\ln J_{\mathrm{SC}}\right)} \tag{5.4}$$

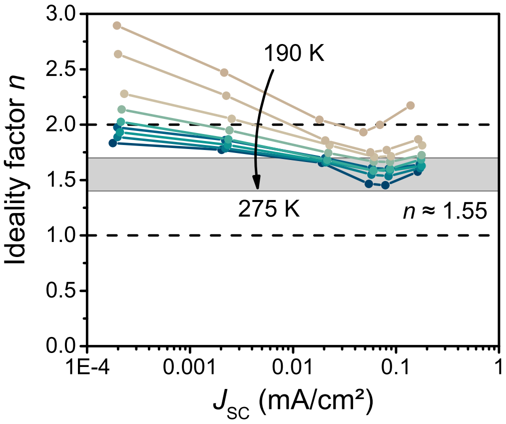

Figure 5.8: Ideality factor n of a ZnO/P3HT heterojunction calculated via the differential method for illumination densities from 0.35 to $315\,\mathrm{mW/cm^2}$ at temperatures between $190\,\mathrm{K}$ and $275\,\mathrm{K}$.

Under very low illumination density, in figure 5.8 the residual influence of a parallel shunt resistance is visible in the increased values of n. In this regime, n is highly dependent on temperature and reaches values significantly larger than 2 at lower temperatures. This behavior can also be observed in organic heterojunctions.[65, 66] Under stronger illumination, the calculated ideality factors lie between 1 and 2, as expected from the simplistic model of radiative bimolecular and trap-assisted recombination as the only recombination channels.

At temperatures around room temperature, an ideality factor of $n = 1.55 \pm 0.20$ can be derived from the differential analysis. Between $293\,\mathrm{K}$ and $240\,\mathrm{K}$, n only shows a slight variation with increasing temperature.

Recent modeling of organic heterojunctions has shown that an exponential tail of trap-states contributing to non-radiative losses of a solar cell are likely to lead to a strongly temperature-dependent ideality factor n proportional to $\frac{1}{T}$.[65] The negligible variation of n indicates that the losses at a ZnO/P3HT heterojunction are dominated by another form of recombination. Bimolecular band-to-band recombination of free carriers and radiative or non-radiative recombination in a localized density of discrete trap states are likely to happen instead.

5.4.4 Thermal Activation of Recombination Current

The n and J_0 values obtained from fitting the V_{OC} and J_{SC} data to the ideal diode equation at different temperatures can serve to calculate an estimate for the activation barrier for the recombination current in the diode. In order to minimize the influence of a shunt resistance detected in the previous section, only values with illumination densities greater than $3.5\,\mathrm{mW/cm^2}$ are considered in this calculation. Figure 5.9(a) shows the extraction of n and J_0 values from photovoltaic data measured at temperatures between $115\,\mathrm{K}$ and $293\,\mathrm{K}$. Below $190\,\mathrm{K}$ the relation between V_{OC} and J_{SC} deviates from a simple exponential behavior and shows a significantly reduced short circuit current at higher illumination densities. Therefore, the following evaluation is only performed for the temperature range between $190\,\mathrm{K}$ and room temperature.

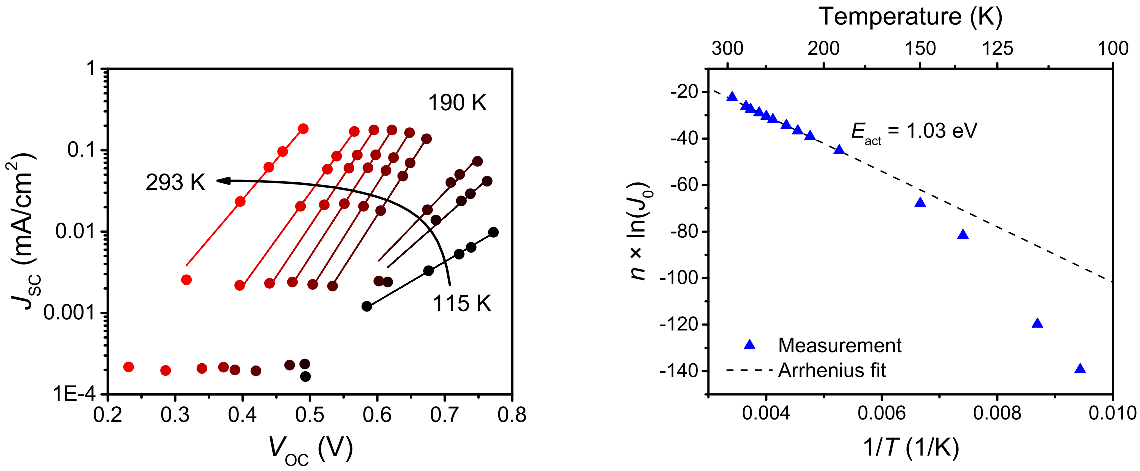

(a) J_{SC} vs. V_{OC}

(b) Activation energy

Figure 5.9: (a) J_{SC} as a function of V_{OC} at temperatures between $115\,\mathrm{K}$ and room temperature ($293\,\mathrm{K}$). The solid lines represent the data fits for extraction of n and J_0 values. Only illumination densities between $3.5\,\mathrm{mW/cm^2}$ and $315\,\mathrm{mW/cm^2}$ were taken into account for the calculation. (b) A modified Arrhenius plot displaying $n \times \ln(J_0)$ against $\frac{1}{T}$ yields an activation energy of $1.03 \pm 0.03\,\mathrm{eV}$ for the recombination current in a ZnO/P3HT diode.

Departing from equation 2.22, a modified Arrhenius plot can be set up to determine the activation energy for the recombination current in the diode E_{act}:

$$n \times \ln(J_0) = n \times \ln(J_{00}) - \frac{E_{\mathrm{act}}}{k_{\mathrm{B}}} \left(\frac{1}{T}\right) \tag{5.5}$$

Knowing the values of n, J_0 and the thermal energy $k_{\mathrm{B}}T$, only the coupling parameter J_{00} and the activation energy E_{act} serve as parameters in a linear fit, depicted in figure 5.9(b), yielding values of $E_{\mathrm{act}} = 1.03 \pm 0.03\,\mathrm{eV}$ and $J_{00} = 8.1 \times 10^5\,\mathrm{mA/cm^2}$. An equivalent analysis can be performed using the parameters n and J_0 obtained from a data fit to a diode model which involves transport losses in the organic acceptor layer, as described in section 2.3.8. Such an analysis will be performed for ZnMgO/P3HT devices in section 6.2.1.1.

5.4.5 Temperature-dependence of V_{OC}

Combined analysis of V_{OC} measurements with variable light intensity and temperature yields additional information about the energetic properties of a donor-acceptor interface in a device. In figure 5.10 temperature dependent V_{OC} measurements of a ZnO/P3HT device at several illumination intensities between $0.35\,\mathrm{mW/cm^2}$ and $315\,\mathrm{mW/cm^2}$ are shown. Towards lower temperatures, the open circuit voltage increases in all cases until it experiences a drop at temperatures below $120\,\mathrm{K}$. This reduction can be connected to the presence of a large but finite shunt resistance in the device, whose influence only becomes visible at low photocurrent densities.[151] The series resistance imposed by passage through the doped ZnMgO:Ga and undoped ZnO layer in the measurement circuit does not play a role here, as no net current flows outside the device per definition.

Using a linear extrapolation departing from the high temperature region of the V_{OC} vs. T curve, the maximally possible open circuit voltage $V_{\mathrm{OC,max}}$ can be estimated. Following the simplistic model in equation 2.17, this value corresponds to the HCTS transition energy at the interface. Figure 5.9(a) shows that J_{SC} is approximately constant for temperatures between $200\,\mathrm{K}$ and room temperature, so this temperature range will be considered for the analysis. The linear extrapolations approach each other towards lower temperatures, but do not exactly intersect at $0\,\mathrm{K}$ as expected from the theoretical model.

The deviations between different illumination intensities again result from the shunt resistance. *M. Runge* showed that by considering the photovoltage losses induced by leaking photocurrent through a shunt resistance, this effect can almost entirely be eliminated.[151] Values for the highest light intensities remain almost unchanged by these corrections, so the influence of a shunt resistance is minimized under these conditions. Consequently, a value of $V_{\mathrm{OC,max}} = 0.98 \pm 0.05\,\mathrm{V}$ can be calculated from experimental data.

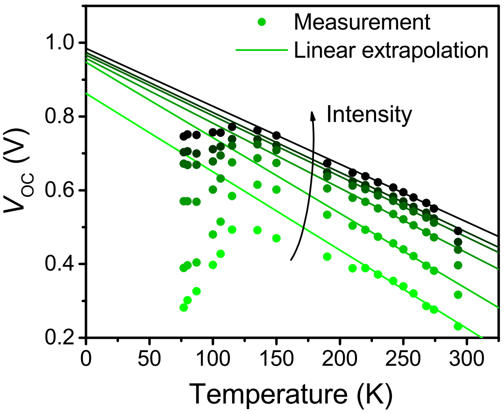

Figure 5.10: Combined light intensity and temperature dependent analysis of the V_{OC} of a ZnO/P3HT diode. The solid lines mark linear extrapolations from the temperature region between $200\,\mathrm{K}$ and room temperature. Light intensities between $0.35\,\mathrm{mW/cm^2}$ and $315\,\mathrm{mW/cm^2}$ have been chosen. The straight lines do not converge perfectly at $0\,\mathrm{K}$, but approach each other for illumination densities above $35\,\mathrm{mW/cm^2}$. A $V_{\mathrm{OC,max}}$ value of $0.98 \pm 0.05\,\mathrm{V}$ is extrapolated.

This, however, does not exactly correspond to the HCTS transition energy E_{HCTS} as in the simplified model used here only radiative carrier recombination in the device is considered. A thorough analysis of the influence of non-radiative processes on the photovoltaic performance of hybrid devices is performed in section 6.4.2.

5.5 HCTS Electroluminescence from a ZnO/P3HT Interface

Electroluminescence (EL) measurements are a powerful tool for studying the properties of a hybrid interface. From the signatures of radiative emissions knowledge about the recombination processes of carriers between the two components can be gained and the situation of energy levels can be deduced.

Applying forward bias to a planar ZnO/P3HT photodiode produces an electroluminescence (EL) spectrum consisting of two components: A signal from P3HT bulk luminescence in the visible red spectral range similar to its PL spectrum and an additional broad feature in the near infrared. The latter is approximately Gaussian-shaped and can be assigned to direct HCTS recombination at the interface. Figure 5.11 schematically depicts the processes connected to the two features. Distribution between the two components can depend on applied voltage, device temperature and the injection barrier ΔE_{c} determined by interfacial level alignment.

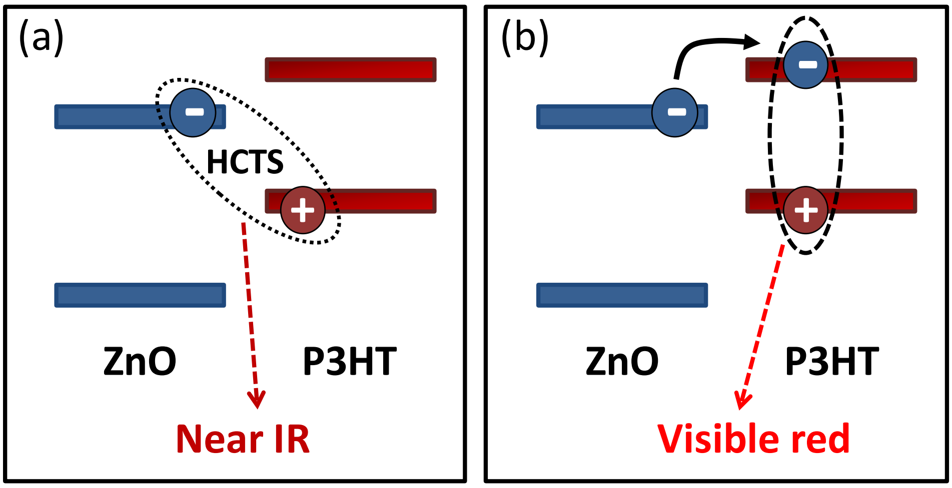

Figure 5.11: Under forward bias two processes can produce an electroluminescence signal: (a) Direct HCTS recombination at the interface, yielding a signal in the near infrared spectral range. (b) Electron injection into P3HT with subsequent formation and recombination of Frenkel excitons in P3HT. The bulk luminescence spectrum of P3HT is situated predominantly in the visible red.

In figure 5.12(a) two EL spectra of a ZnO/P3HT diode with $d_{\mathrm{P3HT}} = 90\,\mathrm{nm}$ measured at applied voltages of $2.25\,\mathrm{V}$ and $4.0\,\mathrm{V}$ are shown. With higher applied bias the spectrum does not only grow in intensity but also alters its shape. The maximum of the HCTS peak shifts towards higher energies by about $80\,\mathrm{meV}$ without detectable broadening. The linewidth given by the variance σ remains constant at $117 \pm 15\,\mathrm{meV}$. Furthermore, the composition of the spectrum undergoes a clear change: While at low bias the P3HT bulk luminescence is hardly visible, it clearly dominates the spectrum at $4.0\,\mathrm{V}$. The comparison to a photoluminescence spectrum of the same device shows that there is no detectable HCTS peak upon optical excitation.

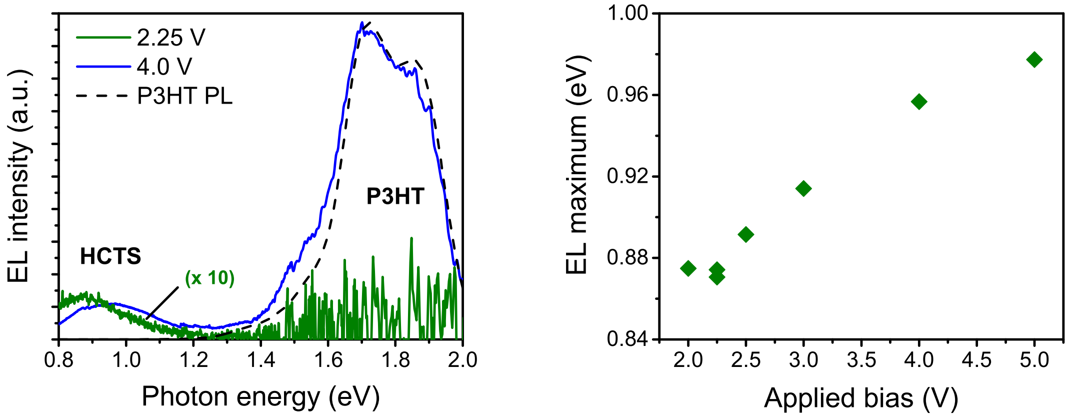

(a) ZnO/P3HT EL spectra

(b) HCTS Peak positions

Figure 5.12: (a) Room temperature electroluminescence spectra of a ZnO/P3HT diode with $d_{\mathrm{P3HT}} = 90\,\mathrm{nm}$ measured at applied voltages $2.25\,\mathrm{V}$ (green line) and $4.0\,\mathrm{V}$ (blue line). Photoluminescence spectrum of P3HT on the same device upon optical excitation with $\lambda = 532\,\mathrm{nm}$ does not show an HCTS peak (black dashed line). (b) Voltage-dependent peak positions for HCTS luminescence from the same diode.

Figure 5.12(b) gives the progression of HCTS EL peak positions over a range between $2\,\mathrm{V}$ and $5\,\mathrm{V}$, showing a continuous blue-shift towards higher bias with a slightly sub-linear growth mode. A similar behavior has been observed for luminescence from charge-transfer states at organic[33] and hybrid[41] heterojunctions before, with its origin still being heavily discussed. A conclusive explanation along with more experimental data will be given in section 6.3.1.

The position of the EL maximum $E_{\mathrm{EL,max}}$ together with the spectral linewidth σ can be used to estimate the transition energy E_{HCTS} according to the relation given in section 2.3.3:

$$E_{\mathrm{HCTS}} = E_{\mathrm{EL,max}} + \frac{\sigma^2}{2k_{\mathrm{B}}T} \tag{5.6}$$

In order to minimize the influence of the voltage-dependent EL blue-shift, the measurement with lowest applied bias is considered here. With this value, the calculation yields an HCTS transition energy of $1.14\,\mathrm{eV}$.

5.6 Discussion of Results

As expected from its type II interface alignment, the heterojunction formed by ZnO and P3HT is able to dissociate excitons into free charge carriers. The high quenching ratio of 76 % at room temperature obtained in time-resolved photoluminescence quenching measurements promises efficient photovoltaic power conversion for photovoltaic devices made from this material system. Prototypical photodiode devices of ZnO and P3HT prove a photovoltaic effect at the hybrid interface. Light absorption in both materials can contribute to a photocurrent. Due to permanent ionization of trap states in the inorganic component under UV irradiation, only photocurrent produced by dissociation of Frenkel excitons in P3HT allows a quantitative treatment.

The main objective in this study is to reveal the connection between interface energetics, generation and recombination processes and photovoltaic losses. The HCTS transition energy E_{HCTS} plays a central role in the device physics. In this section, three approaches to determine this energy are presented.

From thermal activation of the recombination current in a ZnO/P3HT diode an energetic barrier of $1.03 \pm 0.03\,\mathrm{eV}$ can be determined. The n and J_0 values used in this calculation are determined by employing the J_{SC}-V_{OC} method, which eliminates the influence of parallel and shunt resistances in the device. From temperature-dependent measurements of the open circuit voltage a maximal value $V_{\mathrm{OC,max}} = 0.98 \pm 0.05\,\mathrm{eV}$ for $T \to 0$ can be extrapolated. The two methods produce a fairly good agreement, but both of them are based on a simplistic model, assuming a single carrier recombination mechanism and particularly neglecting any non-radiative processes. Electroluminescence measurements have shown, however, that interfacial carrier recombination involves at least two radiative processes. Therefore, a more sophisticated model has to be derived to gain a wider understanding of device physics.

From peak position and linewidth in electroluminescence measurements, a higher value for E_{HCTS} can be deduced, $1.14\,\mathrm{eV}$. As the spectral position of the HCTS EL signal depends on bias applied to the heterojunction, it requires a deeper understanding of the underlying processes in order to correctly interpret the measured data. As the electroluminescence peak experiences a bias-dependent blue-shift, it is likely, that E_{HCTS} is smaller than the value determined here. Consequently, all three measurements yield HCTS transition energies in the region around $1.0\,\mathrm{eV}$.

The open circuit voltage measured at room temperature $V_{\mathrm{OC}} = 0.46\,\mathrm{V}$ remains rather small. The photovoltage losses at the heterojunction of ca. $540\,\mathrm{meV}$ are comparable to the sum of losses in purely organic systems like P3HT/PCBM[25] and fit well into the commonly cited empirical relation for organic solar cells $qV_{\mathrm{OC}} = \Delta E_{\mathrm{IO}} - 0.6\,\mathrm{eV}$.[24] This is in contrast to the expectations to an inorganic-organic hybrid systems, as high carrier mobility in ZnO is expected to contribute to a more efficient charge separation and to prevent recombination processes.

In the next chapter a model system with tunable interfacial energy gap will be set up in order to study the photovoltaic charge separation processes in hybrid oxide/organic solar cells in greater detail. This allows to understand the processes of charge carrier recombination and to quantify and explain the inflicted photovoltage losses.

Chapter 6

ZnMgO as a Model System for Oxide/Organic Photovoltaics

A planar heterojunction of ZnMgO and P3HT is chosen as a model system to investigate the charge separation process and the role of hybrid charge transfer states in photocurrent production and losses therein. Partial alloying of ZnO with MgO as described in section 3.1.2 allows to continuously increase its band gap energy without altering its crystalline structure and background doping density.[98] A set of photodiodes with different Mg contents is fabricated for a detailed investigation of the connection between device behavior and interface energetics.

The photovoltaic function of ZnMgO/P3HT heterojunctions will be studied in order to understand the charge generation process and to derive a conclusive model for HCTS dissociation. Time-integrated and time-resolved electroluminescence measurements provide valuable knowledge on the physical properties of HCTS and photovoltaic losses inflicted by their interfacial recombination. Combined analysis of UV photoelectron spectroscopy, temperature-dependent photovoltaics and EL spectroscopy will yield information on interface energetics and help to estimate the photovoltage losses in a metal-oxide/organic heterojunction. The goal of research is to establish a generalized device model suitable for metal-oxide/organic heterojunctions independently from the exact choice of inorganic and organic materials.

6.1 Interface Energetics at ZnMgO/P3HT Heterojunctions

The magnesium content x in the set of $\mathrm{Zn}_{1-x}\mathrm{Mg}_x\mathrm{O}$/P3HT photodiodes presented in this chapter spans over a range from $1\,\%$ to $14\,\%$. According to optical transmission experiments, a Mg content of $1\,\%$ results in an increase in the ZnMgO band gap of about $50\,\mathrm{meV}$ compared to pure ZnO, while a Mg content of $14\,\%$ widens the band gap by about $300\,\mathrm{meV}$ (see figure 3.2(a)). In previous studies the photovoltaic functionality of ZnMgO/P3HT devices for Mg contents up to $35\,\%$ has been shown.[146] In this section the influence of this band gap widening on the interface energetics will be clarified before the effect on photodiode behavior is discussed.

UV photoelectron spectroscopy measurements are performed in order to obtain information on the interface energetics of a ZnMgO/P3HT interface. Particularly the influence of inorganic band gap widening on the hybrid interface gap energy ΔE_{IO} between ZnMgO conduction band and P3HT HOMO can be studied by interpreting the experimental data. In figure 6.1 the UPS spectra for a $\mathrm{Zn_{0.99}Mg_{0.01}O}$/P3HT interface is depicted, figure 6.2 shows the spectra for a Mg content of $x = 0.14$.

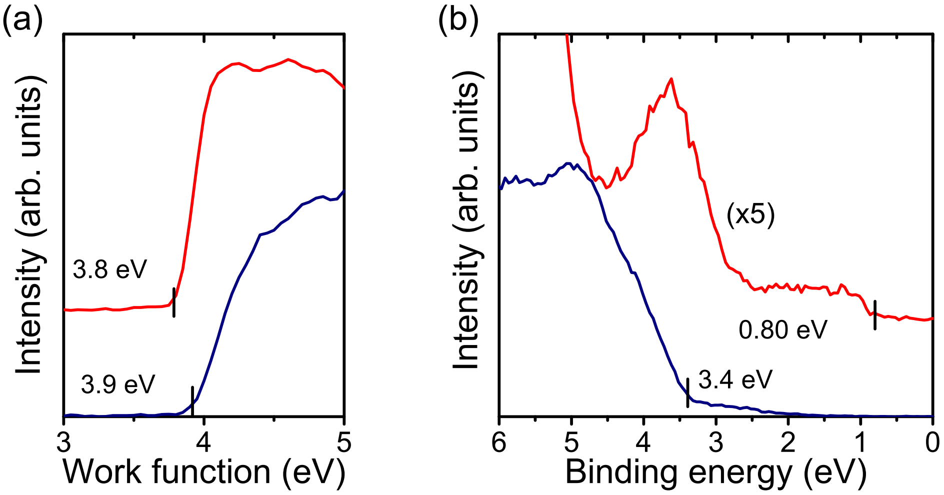

Figure 6.1: UPS measurement of a $\mathrm{Zn_{0.99}Mg_{0.01}O}$/P3HT interface: (a) SECO and (b) valence band spectra of the pristine $\mathrm{Zn_{0.99}Mg_{0.01}O}$ surface (blue) and the corresponding hybrid interface (red). The onset energies are rounded to $50\,\mathrm{meV}$ to account for measurement uncertainty. The P3HT thickness is $15\,\mathrm{nm}$.

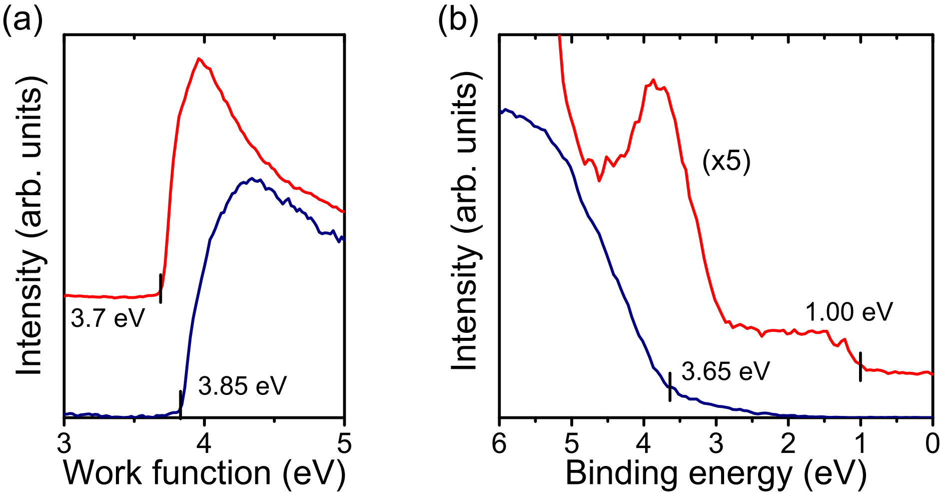

Figure 6.2: UPS measurement of a $\mathrm{Zn_{0.86}Mg_{0.14}O}$/P3HT interface: (a) SECO and (b) valence band spectra of the pristine $\mathrm{Zn_{0.86}Mg_{0.14}O}$ surface (blue) and the corresponding hybrid interface (red).

The valence band onsets of pristine $\mathrm{Zn_{1-x}Mg_xO}$ are found at $3.39\,\mathrm{eV}$ for $x = 0.01$ and $3.63\,\mathrm{eV}$ for $x = 0.14$ below the Fermi energy E_F. Both samples show a sharp onset from the background to the slope of the valence band similar to the valence band onset of ZnO reported in literature.[152] This indicates a low density of intermediate trap states between valence and conduction band for both Mg contents as well as for intrinsic ZnO.

The secondary electron cut off (SECO) yields work functions $\Phi = 3.92\,\mathrm{eV}$ ($x = 0.01$) and $\Phi = 3.85\,\mathrm{eV}$ ($x = 0.14$). After deposition of a $15\,\mathrm{nm}$ P3HT layer by spin-coating the features of the polymer's HOMO orbital become visible showing a pronounced onset at $0.81\,\mathrm{eV}$ for $x = 0.01$ and $1.01\,\mathrm{eV}$ for $x = 0.14$. Upon deposition of P3HT the work function is slightly reduced by $100\,\mathrm{meV}$ ($x = 0.01$) respectively $150\,\mathrm{meV}$ ($x = 0.14$). A similar effect has been observed at heterojunctions between ZnO and small molecules before[153] and is attributed to an electron push-back effect, in which the electron cloud of an organic adsorbate pushes back the charge carriers in the inorganic substrate leading to a reduction in work function for the hybrid compound.[154] The positions of the inorganic conduction bands are taken from optical transmission measurements on $\mathrm{Zn}_{1-x}\mathrm{Mg}_x\mathrm{O}$ taking into account the exciton binding energy of ca. $60\,\mathrm{meV}$[89] which is added to the measured optical gap values to obtain the exact conduction band position. The energetic position of the P3HT LUMO is calculated using the P3HT HOMO energies and adding the band gap energy $2.5\,\mathrm{eV}$ taken from direct and inverse photoemission spectroscopy data in literature.[112]

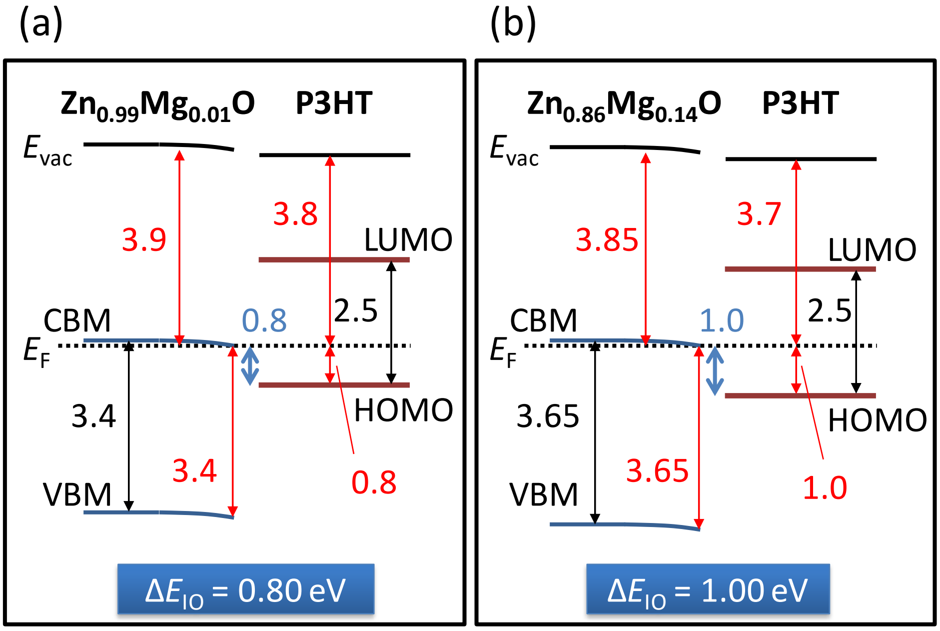

Figure 6.3: Energy level alignment at $\mathrm{Zn}_{1-x}\mathrm{Mg}_x\mathrm{O}$/P3HT interfaces with (a) $x = 0.01$ and (b) $x = 0.14$. All values are given in eV and rounded to $50\,\mathrm{meV}$ to account for the uncertainty of the UPS measurements. The red arrows mark the values derived from UPS onsets, the black arrows indicate optical band gap energies determined by optical transmission. The energy gap ΔE_{IO} is marked by blue arrows.

The energy level alignment obtained from UPS measurements and optical transmission spectroscopy is depicted in figure 6.3. A background doping density of ca. $10^{17} cm^{-3}$ in ZnMgO places the Fermi level about $100\,\mathrm{meV}$ below the conduction band minimum. In the surface region the bands are slightly bent downwards so that the conduction band touches the Fermi level. The measured ionization potential of P3HT of $4.6 \pm\ 0.1\,\mathrm{eV}$ corresponds very well to literature values.[112] The energy offset between the P3HT LUMO and the ZnMgO conduction band provides the driving force for interfacial charge separation. It is large ($1.7\,\mathrm{eV}$ for

$x = 0.01$ and $1.5\,\mathrm{eV}$ for $x = 0.14$) and exceeds the exciton binding energy of P3HT which is ca. $700\,\mathrm{meV}$.[113] This means that ca. $1\,\mathrm{eV}$ of exciton energy will be lost in the power conversion process. Recent research on organic heterojunctions has shown that very small LUMO offset energies in the range of $10\,\mathrm{meV}$ can suffice to effectively drive a charge separation process.[155]

The most relevant parameter for photovoltaic operation is the hybrid energy gap ΔE_{IO} between the $Zn_{1-x}Mg_xO$ conduction band minimum and the P3HT LUMO. It is found to scale from $0.80 \pm 0.05\,\mathrm{eV}$ for $x = 0.01$ to $1.00 \pm 0.05\,\mathrm{eV}$ for $x = 0.14$. Consequently, the variation of the Mg content in ZnMgO allows tuning the interface energetics between organic and inorganic semiconductors, which is the base of the quantitative research on photovoltaic device parameters presented in this chapter. The widening by $200\,\mathrm{meV}$ upon increasing the Mg content in $Zn_{1-x}Mg_xO$ from 1 % to 14 % means that ca. 75 % of the inorganic gap widening contribute to an upward shift of the conduction band while ca. 25 % lower the valence band. This is a higher contribution from the conduction band than the values previously published in literature, which, however, still lie within the margin of error.[101]

6.2 Planar ZnMgO/P3HT Photodiodes

After confirming the assumption that ZnMgO and P3HT form a type II interface, in this section the basic photovoltaic functionality of ZnMgO/P3HT photodiodes is probed. J-V characteristics in the dark and under AM 1.5G illumination are studied at various temperatures between $148\,\mathrm{K}$ and room temperature.

6.2.1 Diode Characteristics in the Dark

Following the sample layout described in section 3.4, planar $Zn_{1-x}Mg_xO$/P3HT diodes with Mg contents of $x = 0.01$, $x = 0.05$ and $x = 0.14$ both in the Ga-doped and undoped part are fabricated with a P3HT thickness of $240\,\mathrm{nm}$. All diodes show a very good rectification over at least five orders of magnitude as depicted in figure 6.4.

6.2.1.1 Modeling Diode Characteristics

The diode characteristics measured at different temperatures can be analyzed by fitting them to the model for space-charge limited current in a hybrid inorganic/organic diode device developed by Renshaw, Panda, Forrest et. al.[42, 55] as described in section 2.3.8.

$$J(V_{\mathrm{a}}) = J_0 \cdot \left(\frac{V_a - \Delta E_{\mathrm{f,p}}}{n k_{\mathrm{B}} T} \right) \tag{6.1}$$

Here $\Delta E_{\mathrm{f,p}}$ denotes the change of Fermi level over the organic layer due to a space charge layer which causes a current roll-off at higher bias in forward direction. V_{a} denotes the voltage

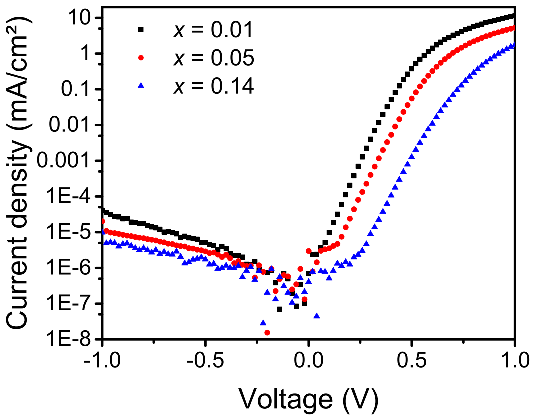

Figure 6.4: Representative current-voltage characteristics for $Zn_{1-x}Mg_xO$/P3HT devices in logarithmic scale show the very pronounced rectification ratio of more than 10^5 independent of the Mg content in the acceptor layer.

applied to the device, $k_{\mathrm{B}}T$ gives the thermal energy. The dark saturation current J_0 and the ideality factor n are used as fit parameters together with the carrier mobility in the organic μ_{O} which enters into the formula for $\Delta E_{\mathrm{f,p}}$.

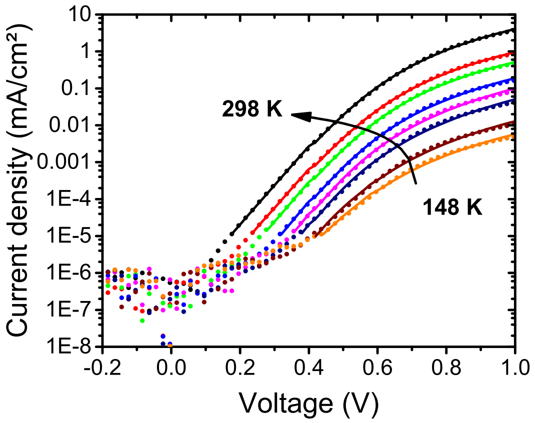

Figure 6.5: Current-voltage characteristics of a $Zn_{0.95}Mg_{0.05}O$/P3HT diode with a P3HT thickness of $240\,\mathrm{nm}$ measured in the dark at temperatures between $148\,\mathrm{K}$ and room temperature (solid dots). Fits according to the model presented in section 2.3.8 are performed in regions of $J(V) > 10^{-5}\mathrm{mA/cm^2}$ and marked as solid lines.

Figure 6.5 shows J-V characteristics from a $Zn_{0.95}Mg_{0.05}O$/P3HT diode measured at temperatures between 148 and $298\,\mathrm{K}$ in the dark. The forward current hereby decreases over several orders of magnitude towards lower temperatures. The curves are fitted with the model mentioned above in the region where the current $J(V) > 10^{-5}\mathrm{mA/cm^2}$ which accounts for the specified sensitivity of the Keithley 2601 SourceMeter used for the measurements, i.e. $(100\,\mathrm{pA}$ corresponding to a current density of $10^{-5}\mathrm{mA/cm^2})$.

The fit parameters J_0 and n obtained by fitting the model to the J-V characteristics from figure

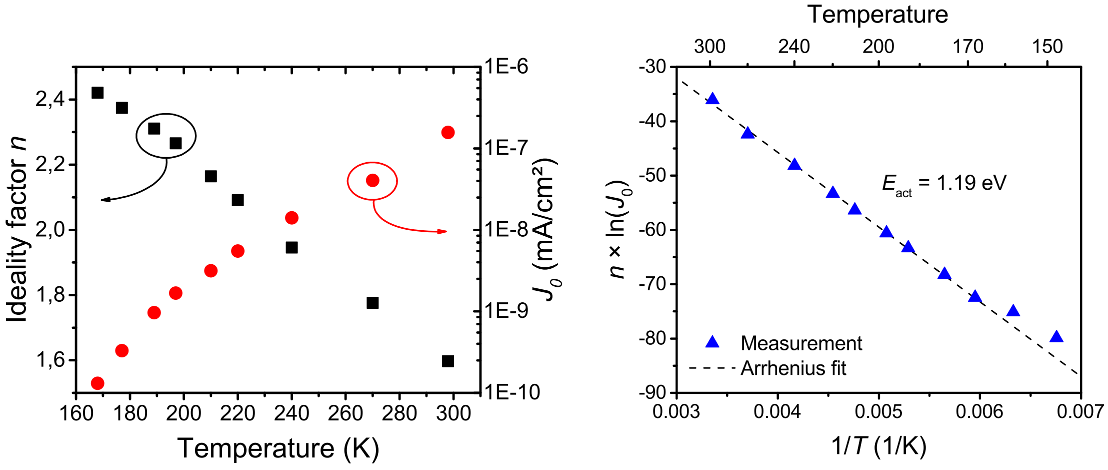

(a) Fit parameters n and J_0 (b) Barrier height calculation

Figure 6.6: (a) Fit parameters J_0 and n obtained from the fits to the J-V characteristics from figure 6.5. (b) Modified Arrhenius plot: The slope of $n \times \ln(J_0)$ vs. $\frac{1}{T}$ gives the activation energy E_{act} for recombination current in the diode.

6.5 are depicted in figure 6.6(a). The saturation current decreases by more than three orders of magnitude between 298 and 168 K while the ideality factor increases from ca. 1.6 to 2.4. Equation 2.22 can be employed to calculate the activation energy for dark current in the diode. As the ideality factor n depends on temperature a modified form of an Arrhenius plot has to be used here, following equation 6.2.

$$n \times \ln(J_0) = n \times \ln(J_{00}) - \frac{E_{\mathrm{act}}}{k_B}\left(\frac{1}{T}\right) \tag{6.2}$$

The activation energy values calculated from $\mathrm{Zn_{0.95}Mg_{0.05}O}$/P3HT and $\mathrm{Zn_{0.86}Mg_{0.14}O}$/P3HT diodes are listed in table 6.1. Assuming that all diode current is realized by recombination of interfacial charge transfer states, this activation energy corresponds to the transition energy of an HCTS. Consequently, by widening the interface energy gap ΔE_{IO}, the HCTS transition energy E_{HCTS} increases analogously, which shows the direct connection between both quantities.

This analysis is equivalent to the determination of E_{act} from the parameters obtained by using the J_{SC}-V_{OC} method, as in both cases transport losses inflicted by limited carrier mobility in the organic acceptor layer are separated from the charge generation and recombination processes at the interface. Similar evaluations to analyze the interface energetics have been successfully performed before in organic[33] and hybrid[55] heterojunction systems.

Table 6.1: Calculated dark current activation energies

Mg concentration	$x = 0.05$	$x = 0.14$
E_{act}	$1.18 \pm 0.08\, eV$	$1.32 \pm 0.10\, eV$

From the parameters μ_{O} obtained in the curve fit the activation energy for μ_{O} can be calculated

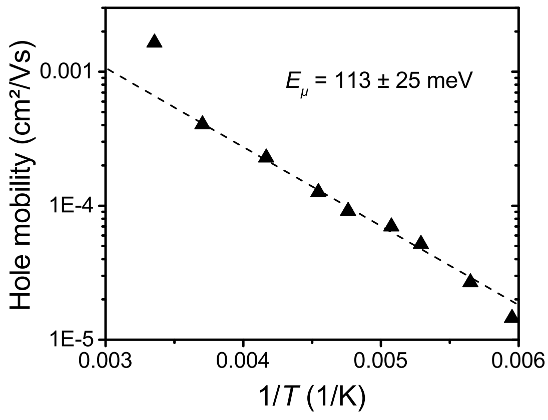

Figure 6.7: Thermal activation of charge carrier mobility in P3HT calculated from fit data of a $Zn_{0.95}Mg_{0.05}O$/P3HT diode.

by setting up an Arrhenius plot as depicted in figure 6.7. The hole mobility μ_O is plotted over 1/T in logarithmic scale with the slope of the curve yielding the activation energy E_μ. Analysis of all evaluated diodes with Mg contents of $x = 0.05$ and $x = 0.14$ yields an average activation energy of $E_\mu = 113 \pm 25\,\mathrm{meV}$, which is a typical value for a hopping transport mechanism in a weakly ordered polymer.[87, 156]

6.2.2 ZnMgO/P3HT Photovoltaics

Figure 6.8(a) shows External quantum efficiency (EQE) spectra of three $Zn_{1-x}Mg_xO$/P3HT diodes with $x = 0.01$, $x = 0.05$ and $x = 0.14$ and a common P3HT thickness of $240\,\mathrm{nm}$. The different onsets on the high-energy side show that not only light absorption in both P3HT produces a photocurrent, but also absorption in ZnMgO gives its contribution. Depending on the inorganic band gap, the high-energy absorption onset shifts, but for all Mg contents it only produces a small peak. The Ga-doped ZnMgO with its slightly higher band gap energy layer acts as an optical filter, blocking light with higher photon energies from reaching the interface region. Over the whole absorption spectrum, the charge separation efficiency decreases with increasing Mg content. The spectrally integrated EQE over the whole excitation spectrum drops from 1.13 % ± 0.10 % for $x = 0.01$ to 0.85 % ± 0.10 % for $x = 0.05$ down to 0.50 % ± 0.05 % for $x = 0.14$.

The external quantum efficiency of planar ZnMgO/P3HT heterojunctions is limited by the small exciton diffusion length in P3HT in the same way as measured before with samples involving ZnO. However, the quantum efficiency of ZnMgO/P3HT diodes with low Mg content is clearly superior to the samples made from ZnO and reaches over 2.5 % for $x = 0.01$ at the peak of P3HT absorption and thus more than twice the value of pure ZnO.

Figure 6.8(b) shows J-V characteristics for all samples taken in the dark and under AM 1.5G simulated solar illumination. UV irradiation is cut off from the spectrum to avoid excitation of ZnMgO and its defects due to persistent photocurrent effects (see appendix A). For all devices

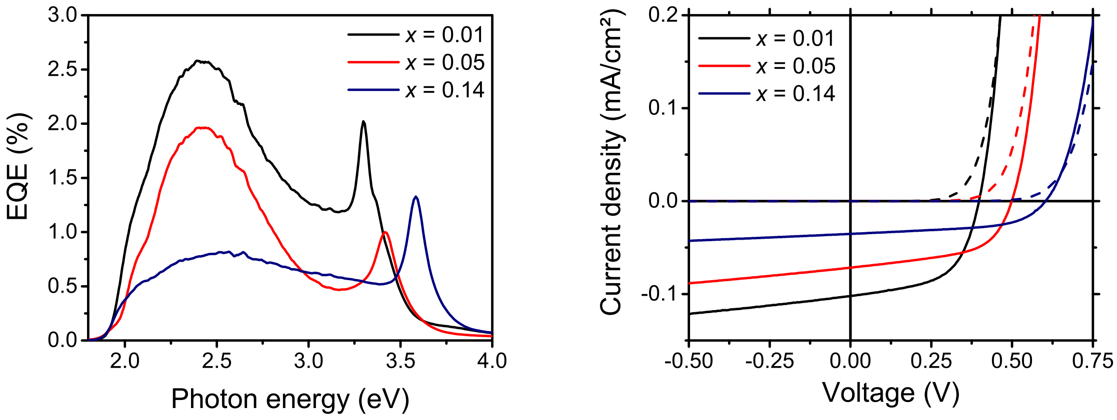

(a) EQE spectra

(b) J-V characteristics

Figure 6.8: (a) External quantum efficiency (EQE) spectra of Zn$_{1-x}$Mg$_x$O/P3HT diodes for $x = 0.01$, $x = 0.05$ and $x = 0.14$ show a decreasing charge separation efficiency with increasing Mg content, while the high-energy onset of photocurrent shifts towards higher energies. (b) Current-voltage characteristics for Zn$_{1-x}$Mg$_x$O/P3HT devices with a magnesium content x. Dashed lines mark dark current curves, solid lines are recorded under $100\,\mathrm{mW/cm^2}$ AM 1.5G illumination with an additional filter to cut off UV radiation.

the fill factor is between 52 % and 56 % and thus independent of Mg content. The short circuit current J_{SC} decreases with increasing Mg content in ZnMgO from $0.098 \pm 0.005\,\mathrm{mA/cm^2}$ for $x = 0.01$ to $0.034 \pm 0.001\,\mathrm{mA/cm^2}$ for $x = 0.14$. This happens in analogy to the decrease in EQE. Consequently, the overall power conversion efficiency drops by ca. 50 % between $x = 0.01$ and $x = 0.14$.

The open circuit voltage V_{OC} increases from $0.40 \pm 0.01\,\mathrm{V}$ to $0.60 \pm 0.01\,\mathrm{V}$ by ca. $200\,\mathrm{meV}$ between $x = 0.01$ and $x = 0.14$. This is in good agreement with the results previously reported by *Olson et. al.*[146] This increase corresponds to the widening of $\Delta E_{\mathrm{IO}}/q$ measured by UV photoelectron spectroscopy (see section 6.1) and proves the close connection between V_{OC} and the hybrid energy gap. The discrepancy between V_{OC} as measured at room temperature and the interfacial gap energy derived from UPS measurements, however, shows the significant presence of photovoltaic losses.

6.3 Radiative Recombination of HCTS

A profound model of inorganic-organic photovoltaic devices requires an accurate description of the physical processes related to their interface. Electroluminescence spectroscopy from ZnO/P3HT diodes (see section 5.5) has shown the presence of hybrid charge transfer states (HCTS) involving an electron in ZnO and a hole in P3HT. In the following, their physical properties will be investigated by analyzing the signal of their radiative recombination. Time-integrated EL spectroscopy will yield knowledge about the energetic structure of a hybrid interface. Additional time-resolved measurements will reveal valuable information on the internal structure of HCTS and the related mechanisms of radiative and non-radiative recombination.

6.3.1 HCTS Electroluminescence Spectroscopy

As mentioned before in section 5.5, recombination of HCTS at a metal-oxide/organic interface produces a luminescence signal which can be detected in EL spectroscopy. The HCTS signal observed from a ZnO/P3HT heterojunction is situated in the near IR, so the spectrum resulting from ZnMgO/P3HT heterojunctions is expected to be situated in the same range. Similar to the signal from ZnO/P3HT diodes described in section 5.5, the EL spectrum here also consists of two components, direct HCTS recomination at the interface and radiative recombination of Frenkel excitons in bulk P3HT resulting from electron injection into the organic LUMO.

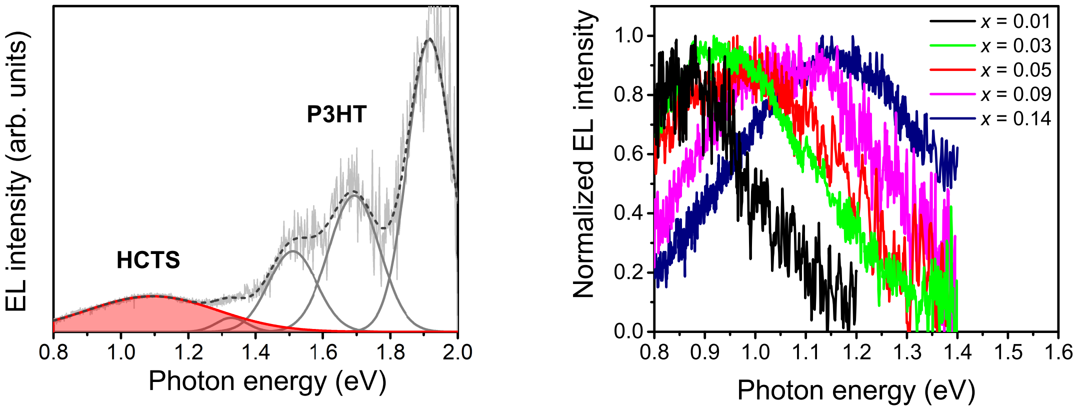

(a) Full EL spectrum for $x = 0.09$ (b) HCTS EL peaks for $x = 0.01..0.14$

Figure 6.9: (a) EL spectrum of a $Zn_{0.91}Mg_{0.09}O$/P3HT diode with a P3HT thickness of $150\,\mathrm{nm}$ driven at $2.87\,\mathrm{V}$ with a current density of $58\,\mathrm{mA/cm^2}$ (blue line). The EL spectrum comprises P3HT emission as well as an additional emission feature centered at ca. $1.1\,\mathrm{eV}$ and assigned to indirect HCTS radiative recombination. The emissions of $S_{1,\nu=0} \to S_{0,\nu=0..4}$ transitions in P3HT are modeled by 4 Gaussian peaks (grey lines) and subtracted from the spectrum to isolate the HCTS peak (red area). (The noise in the P3HT spectrum is due to the low efficiency of the InGaAs detector in this spectral range.) (b) Normalized HCTS peaks in EL spectra after subtraction of P3HT bulk luminescence for $Zn_{1-x}Mg_xO$/P3HT diodes with Mg contents between $x = 0.01$ and $x = 0.14$ at an applied bias of ca. $2.5\,\mathrm{V}$. HCTS emission undergoes a blue shift with increasing Mg content in ZnMgO.

The HCTS luminescence peak of ZnMgO/P3HT diodes is situated at higher energies than luminescence from devices involving ZnO. The exact energy shift depends on Mg content in ZnMgO and will be discussed later. As a consequence, however, the signals of interfacial recombination and P3HT bulk luminescence tend to overlap each other. For an exact determination of peak positions and linewidths, both contributions have to be disentangled first. This is done by interpreting the P3HT luminescence as a series of Gaussian fits with Poisson intensity distribution for the $S_{1,\nu=0} \to S_{0,\nu=0..4}$ transitions as depicted in figure 6.9(a).[147, 157] After subtraction of the P3HT bulk features, the single remaining peak can be assigned to indirect HCTS recombination over the interface (see figure 6.9(b)). Its spectral shape is approximately Gaussian, so that a fit to a normal distribution is used for determining the spectral position of its maximum and its linewidth given by the variance σ.

For several diodes with a Mg content in ZnMgO varying from $x = 0.01$ to $x = 0.14$, the spectral position of P3HT luminescence features remains unchanged and is very similar to its PL signal. The broad HCTS luminescence peak, however, shifts towards higher energies by ca. $250\,\mathrm{meV}$ as visible in figure 6.9. This indicates a direct connection between EL maximum and the hybrid energy gap ΔE_{IO} measured in UPS spectroscopy.

With increasing Mg content in ZnMgO, the injection barrier E_{C} between ZnMgO conduction band and P3HT LUMO becomes smaller. This leads to an increased contribution of P3HT bulk luminescence to the EL spectrum. At a Mg content above $x = 0.20$, the HCTS luminescence peak is entirely buried in the low-energy tail of the P3HT bulk signal and therefore cannot be isolated and analyzed.

6.3.1.1 Delocalization of Charge Carriers in HCTS

As observed before for ZnO/P3HT diodes, the spectral position of HCTS luminescence does not only depend on the band gap energies of the involved materials, but also varies with applied bias for the same device. For increasing voltage, a blue shift can be resolved. Similar effects have already been observed for organic heterojunctions.[33]

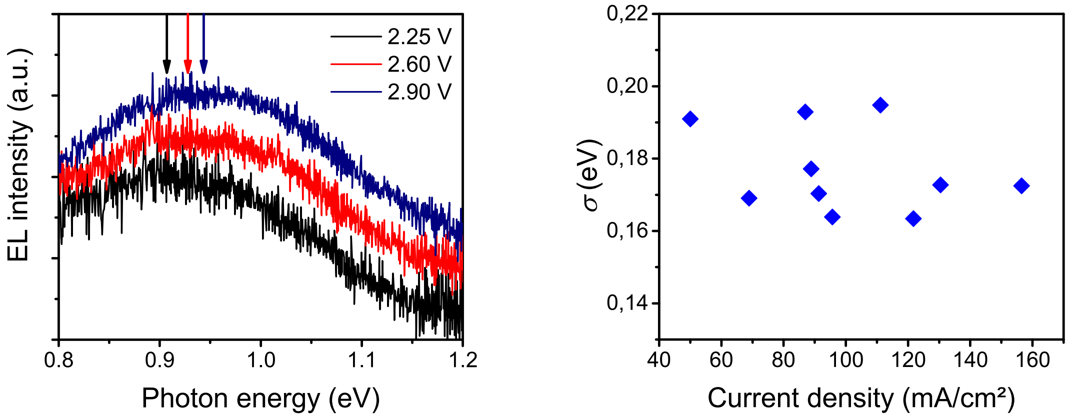

(a) Voltage-dependent shift of HCTS EL

(b) Current-dependent HCTS EL linewidth

Figure 6.10: (a) The HCTS EL peak of a $Zn_{0.95}Mg_{0.05}O$/P3HT diode with $d_{\mathrm{P3HT}} = 240\,\mathrm{nm}$ shifts towards higher energies with higher applied voltage. The arrows mark the three peak positions determined from Gaussian fits to the spectrum. No linewidth broadening can be observed. (b) The HCTS EL peak linewidth of a $Zn_{0.86}Mg_{0.14}O$/P3HT diode with $d_{\mathrm{P3HT}} = 240\,\mathrm{nm}$ does not undergo a systematical change under different current densities. All measurements were performed at room temperature.

Figure 6.10(a) shows the indirect HCTS electroluminescence of a ZnMgO/P3HT device shifting to higher energies with higher applied voltage. The linewidth of the measured peak does not depend on applied voltage and neither on current as depicted in figure 6.10(b).

The absence of a current-dependent peak broadening rules out a filling mechanism of localized interface states as the origin of the spectral shift in HCTS luminescence. The involvement of higher-lying states in recombination processes due to high population in an excited state maintains the low-energy onset of emission and only shifts the spectral maximum by broadening the whole emission peak towards higher energies. This effect can be observed in the dynamic Burstein-Moss effect in case of strong optical excitation to semiconductor structures.[158, 159] Furthermore, in UPS measurements it has been shown that ZnO has an exponentially decreasing defect density below the band gap energy and does not provide a Gaussian shaped distribution of states suitable for explanation of the observed EL spectrum.[152]

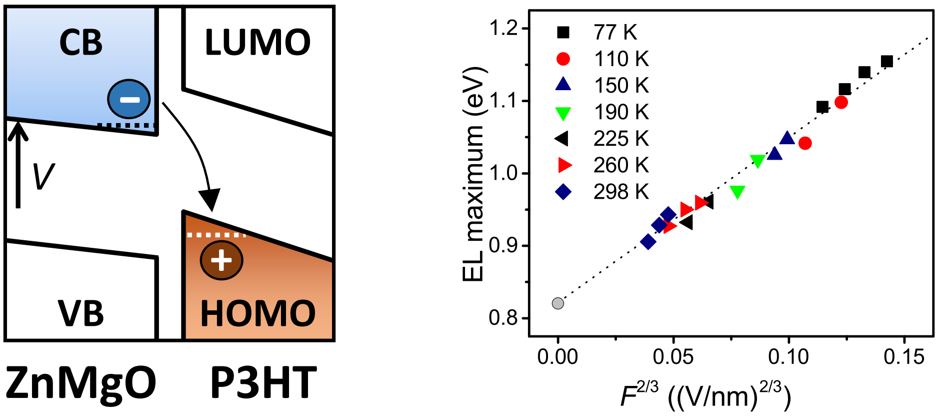

(a) Energetic scheme

(b) Field-dependent EL shift

Figure 6.11: (a) The Electric field forms a triangular quantum well in the ZnMgO conduction band and P3HT HOMO, thus increasing the separation between the ground state energies with increasing electric field. (b) The EL maximum of a Zn$_{0.95}$Mg$_{0.05}$O/P3HT diode with $d_{\mathrm{P3HT}} = 240\,\mathrm{nm}$ shifts towards higher energies proportionally to $F^{\frac{2}{3}}$. The spectral position of the hypothetical field-free electroluminescence is marked with a grey circle.

From electroluminescence measurements with several applied voltages, a spectral shift depending on the applied voltage to the power of $\frac{2}{3}$ has been found instead. Such a relation is produced by a model regarding the donor and acceptor bands as triangular quantum wells between the interface boundary and the inclined conduction band/HOMO levels under an electric field as depicted in figure 6.11(a). This leads to a field-dependent widening of the energy gap between the ground state energies for electrons and holes

$$E_1(F) = \left(\frac{\hbar^2}{2m^*}\right)^{\frac{1}{3}} \left(\frac{9\pi q F}{8}\right)^{\frac{2}{3}} \tag{6.3}$$

with the electric field F, the reduced Planck constant $\hbar$ and the relative carrier mass m^*. Because of the difference in background carrier concentrations between ZnMgO and P3HT, it can be assumed that the electric field in the inorganic is screened almost entirely and that all voltage drop consequently occurs in the P3HT layer, producing the electric field

$$F = \frac{V_{\mathrm{a}} - V_{\mathrm{bi}}}{d_{\mathrm{P3HT}}}. \tag{6.4}$$

The difference of work functions between cathode and anode contact leads to a built-in voltage V_{bi} in reverse direction which decreases the electric field in the P3HT layer. After calculating the voltage drop in P3HT, it is divided by the P3HT layer thickness d_{P3HT} to obtain the electric field in the organic.

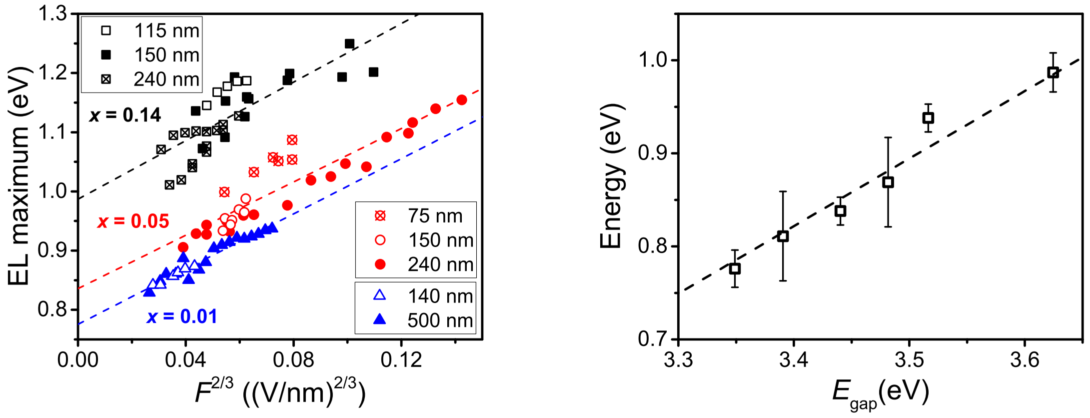

(a) Full EL data

(b) Extrapolated EL peaks for $F \to 0$

Figure 6.12: (a) Spectral positions of EL maxima from $\mathrm{Zn}_{1-x}\mathrm{Mg}_x\mathrm{O}$/P3HT diodes with Mg contents of $x = 0.01$, $x = 0.05$ and $x = 0.14$ and varying P3HT thicknesses show the dependence of the EL signal on the electric field F in the organic layer. This data is used for extrapolation of hypothetical electroluminescence peak positions with $F \to 0$. (b) Extrapolated HCTS electroluminescence values for $F \to 0$ from $\mathrm{Zn}_{1-x}\mathrm{Mg}_x\mathrm{O}$/P3HT diodes with Mg contents between $x = 0.01$ and $x = 0.14$. The x-axis gives the band gap energy of the ZnMgO layer in each device. The slope of the dashed line represents the widening of the hybrid energy gap ΔE_{IO} as determined by UV photoelectron spectroscopy (see section 6.1).

Figure 6.11(b) shows the relation between the electric field in the P3HT layer and the resulting EL maximum shift for a $\mathrm{Zn}_{0.95}\mathrm{Mg}_{0.05}\mathrm{O}$/P3HT diode with $d_{\mathrm{P3HT}} = 240\,\mathrm{nm}$. External bias between $2\,\mathrm{V}$ and $13\,\mathrm{V}$ is applied to the diode. The dependence of EL peak energy on temperature is negligible compared to the voltage-induced shift. A similar energetic shift in EL emission has also been observed for interfaces between ZnO and small molecules.[160]

This model can be verified by comparing electroluminescence spectra of diodes with different P3HT thicknesses. In figure 6.12(a) it is clearly visible how the HCTS EL maximum shifts with the electric field, varying either by increasing the applied voltage or by using different P3HT thicknesses. Moreover, it depends on the hybrid energy gap ΔE_{IO} which is apparent from comparison of $\mathrm{Zn}_{1-x}\mathrm{Mg}_x\mathrm{O}$/P3HT diodes with different Mg contents.

To compare the positions of HCTS EL maxima for diodes with different hybrid energy gaps, a hypothetical EL maximum value obtained by extrapolation to $F \to 0$ is used. This eliminates the influence of a field-induced spectral shift and yields the values depicted in figure 6.12(b). The EL maximum shifts by $200\,\mathrm{meV}$ upon increasing the Mg content from $1\,\%$ to $14\,\%$ which is in good accordance to the widening of the hybrid energy gap ΔE_{IO}.

The fact that the EL maximum energy reacts to the electric field which is present in the P3HT layer means that a hole bound to the interface in a hybrid charge transfer state is not confined to the very surface, but extends its wavefunction into the organic layer. The degree of delocalization is determined by the effective hole mass m^* in P3HT, which is used as a fit parameter in equation 6.3. All ZnMgO/P3HT diodes yield the same value of $m^* \approx 0.05 \cdot m_{\mathrm{e}}$. Such a small effective mass might appear as a surprise at first glance,[161] but in highly ordered polymers in contact to an acceptor layer, similar low values have been found.[162]

The solution of the Schrödinger equation for a particle in a triangular quantum well formed by an infinite boundary at $z = 0$ and an electric field F is given by an Airy function $Ai(z)$.[163] The wavefunction of its ground state can be written as:

$$\Psi(x) = A \cdot Ai\left(\left(\frac{2m^*}{\hbar^2 q^2 F^2}\right)^{\frac{1}{3}} (qFz - E_1)\right) \tag{6.5}$$

A is a proportionality constant which is to be determined by normalization, E_1 is the energy of the ground state as given in equation 6.3. Figure 6.13 shows the wavefunction of a hole in a triangular quantum well under similar conditions as the room temperature EL measurements performed earlier in this section. The wave function maximum z_{m} is situated more than $5\,\mathrm{nm}$ away from the interface, and only about $4\,\%$ of the particle's probability distribution is located within a distance of $2\,\mathrm{nm}$ from the interface.

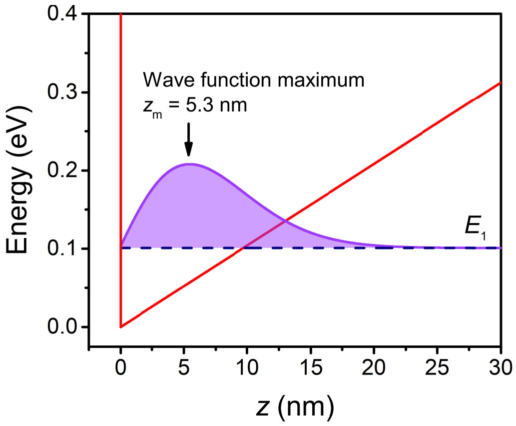

Figure 6.13: Energy diagram of a triangular quantum well formed in a P3HT layer of $240\,\mathrm{nm}$ thickness with a total voltage drop of $2.5\,\mathrm{V}$ over the whole layer. The black dashed line gives the position of the ground state energy E_1 for an effective hole mass of $m^* = 0.05 m_{\mathrm{e}}$ with the blue area being the wavefunction of the hole ground state in the triangular quantum well.

This indicates that electron and hole in an HCTS are bound to each other only loosely, while both carriers are delocalized perpendicularly to the interface. The simplistic picture of localized carriers bound to each other at the interface as previously described in section 2.1.4 is not valid for a ZnMgO/P3HT heterojunction.

6.3.1.2 HCTS EL Broadening Mechanisms

The spectral linewidth of an HCTS EL peak does not depend on voltage or current density as described above. However, there are other parameters influencing the width of the Gaussian distribution describing the luminescence peak. One contribution to the peak width is the chemical composition of the ZnMgO layer. Alloy broadening effects of ZnMgO (which can also be observed in transmission measurements, see figure 3.2(a)) cause an increase in HCTS peak width due to a less steep onset of the conduction band density of states.[98] When increasing the Mg content in ZnMgO from $1\,\%$ to $14\,\%$, the HCTS peak width σ increases from $124 \pm 5\,\mathrm{meV}$ to $177 \pm 18\,\mathrm{meV}$ by almost $50\,\%$, as shown in figure 6.14(b). As reported before in section 5.5, the linewidth measured at a ZnO/P3HT interface is slightly smaller due to the complete absence of any alloy broadening.

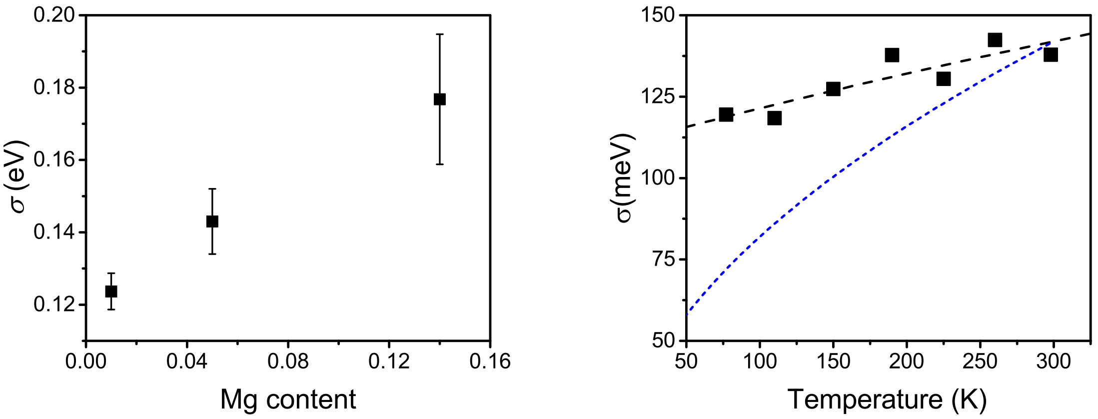

(a) EL linewidth vs. Mg content

(b) EL linewidth vs. temperature

Figure 6.14: (a) The variance σ of an HCTS emission peak increases towards higher Mg contents in ZnMgO. This broadening effect can be assigned to alloy broadening, which is also visible in optical absorption measurements of ZnMgO.[98] (b) Variance σ of temperature-dependent EL measurements on a $Zn_{0.95}Mg_{0.05}O$/P3HT diode (black squares). Purely homogeneous broadening would lead to a stronger decrease in linewidth (blue dashed line), while a combination of homogeneous and inhomogeneous broadening (black dashed line) yields an inhomogeneous contribution to broadening of ca. $110\,\mathrm{meV}$.

At temperatures below room temperature, the linewidth of an HCTS EL peak decreases (see figure 6.14). The shrinking is, however, less pronounced than expected from a model of homogeneous broadening according to Marcus theory (see section 2.3.3). This means that inhomogeneous broadening plays an important role in the emission spectrum. Separating the contributions of homogeneous and inhomogeneous broadening using the equation $\sigma = \sqrt{\sigma_\mathrm{h}^2 + \sigma_\mathrm{i}^2}$

yields an contribution of inhomogeneous broadening $\sigma_\mathrm{i} \approx 110\,\mathrm{meV}$ for a $\mathrm{Zn_{0.95}Mg_{0.05}O}$/P3HT interface.

Inhomogeneous broadening mainly originates from disorder at a ZnMgO/P3HT interface. Localized irregularities produce a bumpy landscape of transition energies over the interface plane. Aside from alloy broadening effects on the inorganic side, the main source of inhomogeneous broadening are the randomly ordered polymer chains of P3HT. The difference in ionization potential between different geometrical conformations of P3HT on an acceptor layer of more than $300\,\mathrm{meV}$[114] gives a convincing explanation for the strong inhomogeneous broadening in HCTS recombination.

6.3.1.3 Quantum Efficiency of HCTS Electroluminescence

Once a pair of charges forming an HCTS recombines, it cannot contribute to a photocurrent and therefore contributes to the losses in the photovoltaic process. This applies to both radiative and non-radiative recombination processes. Analyzing the quantum efficiency of electroluminescence $\mathrm{EQE_{EL}}$ provides insight into the nature of loss processes in a photovoltaic device. As a first step it can be stated after analysis of integrated EL spectra, that no correlation of $\mathrm{EQE_{EL}}$ with the applied voltage or current density is found. For a direct comparison between quantum efficiencies at different temperatures, the relative quantum efficiency $\mathrm{EQE_{EL,rel}}$ is introduced, which gives the $\mathrm{EQE_{EL}}$ values of different temperatures as a fraction of the highest measured value at $77\,\mathrm{K}$:

$$\mathrm{EQE_{EL,rel}}(T) = \frac{\mathrm{EQE_{EL}}(T)}{\mathrm{EQE_{EL}}(77\,\mathrm{K})}. \tag{6.6}$$

In figure 6.15 is shown how the relative EL quantum efficiency strongly increases while cooling the device from room temperature to $77\,\mathrm{K}$. This indicates the presence of a thermally-activated non-radiative recombination channel.

The formulation

$$\mathrm{EQE_{EL}}(T) = \frac{\mathrm{EQE_0}}{1 + \alpha \cdot \exp\left(\frac{-E_\mathrm{nr}}{k_\mathrm{B}T}\right)} \tag{6.7}$$

gives a model for the EL quantum efficiency including an alternative decay channel, weighted by the factor α, with the activation energy E_nr. $\mathrm{EQE_0}$ denotes the quantum efficiency at $0\,\mathrm{K}$. This formula is used to fit the measured efficiency in figure 6.15. Fitting this model to experimental data yields an activation energy of $70 \pm 10\,\mathrm{meV}$ for the non-radiative process.

As the EL quantum decreases by two orders of magnitude between $77\,\mathrm{K}$ and $295\,\mathrm{K}$, at room temperature less than 1 % of the charge carriers recombine radiatively. The actual quantum efficiency at room temperature $\mathrm{EQE_{EL}}(293\,\mathrm{K})$ is probably even smaller by orders of magnitude, but no exact value can be given here. Consequently, non-radiative recombination is by far the

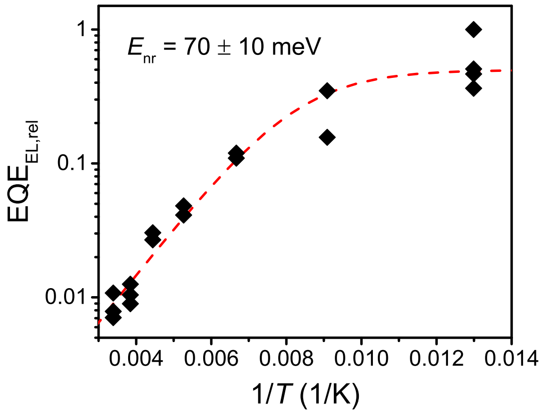

Figure 6.15: Temperature-dependence of the relative EL quantum yield $\mathrm{EQE}_{\mathrm{EL,rel}}(T)$ of a diode with Mg content $x = 0.05$. The different data points correspond to spectra for several applied bias values. No correlation of the relative EL quantum efficiency to the voltage drop over the diode is found. The dashed line shows the data fit according to the model described in equation 6.7. The decrease in EQE towards room temperature can be connected to a thermally activated non-radiative decay channel with an activation energy of $E_{\mathrm{nr}} = 70 \pm 10\,\mathrm{meV}$.

dominating mechanism. In accordance with the principles of thermodynamics, radiative recombination is an inevitable process in photovoltaic devices[7], while non-radiative processes impose additional losses, which are theoretically avoidable. In case of the ZnMgO/P3HT heterojunction, the dominance of non-radiative processes at room temperature means a drastic limitation to device efficiency.

The fact that E_{nr} is in the range of the activation energy for diffusion of single hole carriers in P3HT[87, 156] can give a hint that carrier migration processes can play a role in recombination behavior. CTS in organic heterojunctions have been shown to move geminately along the interface plane driven by energetic disorder and diffusion.[164] Due to a strong difference in dielectric constants and carrier mobilities between ZnMgO and P3HT, such a movement of an HCTS would be mainly determined by polaron hopping of the hole in P3HT, while the electron can move along the interface more freely or even bond to one hole after another. A non-radiative quenching mechanism of localized defect sizes as previously observed in pristine layers of regio-regular P3HT[165] might be the reason for thermally activated non-radiative recombination at the hybrid interface.

6.3.2 Recombination Dynamics of HCTS

Studying the recombination dynamics of hybrid charge transfer states at oxide/organic interfaces can help to gain a deeper understanding of the loss processes in photovoltaic charge generation. Therefore, sharply edged voltage pulses are applied to the diode structure using a function generator. A combination of a spectrograph and a InP/InGaAsP photomultiplier allows to measure transients of HCTS electroluminescence in the near-IR and calculate decay times for different ranges of photon energies.

A voltage pulse length of 10 µs is chosen so that the electric field at the heterojunction is able to reach a steady state (marked by a constant EL rate). When the applied bias is switched off, the luminescence transient is measured over a time of 10 µs. In each measurement cycle of 20 µs the incidence time of photons arriving at the detector is recorded after a trigger signal given by a function generator. Incident photons are sorted into bins of 2 ns width. A typical measurement time for a single transient curve is 400 million cycles, corresponding to slightly over 2 hours.

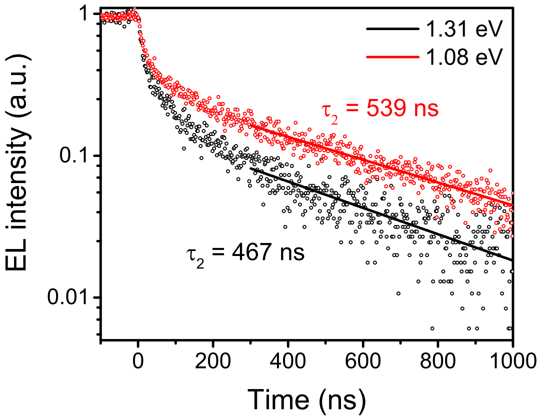

Figure 6.16: Electroluminescence transients from a $Zn_{0.86}Mg_{0.14}O$/P3HT diode with $d_{\mathrm{P3HT}} = 240\,\mathrm{nm}$ with voltage pulses of 10 µs and $V_a = 3.5\,\mathrm{V}$ yield a short decay with $\tau_1 \approx 20\,\mathrm{ns}$ and a long-lived process with $\tau_2 = 467 \pm 13\,\mathrm{ns}$ at a detection energy of 1.31 eV and $\tau_2 = 539 \pm 12\,\mathrm{ns}$ at a detection energy of 1.08 eV. The ratio of long-lived and short-lived process depends on the spectral position. The share of the long-lived charge transfer signal rises from 64 % detected at 1.31 eV to 82 % at 1.08 eV. HCTS lifetimes are determined from single exponential fits in the time range between 300 ns and 1000 ns.

The EL transient curves of a ZnMgO/P3HT diode consist of a short decay with a time constant in the region of the resistance-capacitance time of the measurement circuit ($\tau_{\mathrm{RC}} \approx 9\,\mathrm{ns}$, see section 4.4.1) and a long decay with a lifetime τ_2 between 400 and 550 ns. Depending on spectral position, the distribution between both decay channels changes. This indicates that the short-lived transient represents the tail of P3HT bulk emission with a lifetime shorter than the instrumental response function (ca. 600 ps as measured in section 5.2 and in reference [166]). EL transient measurements on a ZnO/P3HT diode with an HCTS peak situated further in the infrared, outside the detectable range only yield a single short-lived decay with $\tau \approx 5\,\mathrm{ns}$ originating from the P3HT low energy tail (data not shown here). Pulsed excitation does not alter the shape of the EL spectrum compared to continuous excitation with the same voltage.

From the transient curves comprising two individual exponential decay regimes like in figure 6.16, the branching ratio into two underlying processes can be calculated. It is defined as the share of both decays from the total initial population.

The initial population N_0 of an exponential decay $A(t) = A_0 \cdot \exp\left(-\frac{t}{\tau}\right)$ with a time constant τ and an initial avtivity A_0 for $t = 0$ can be calculated as follows:

$$N_0 = \int_0^\infty A(t)\mathrm{d}t = A_0 \cdot \tau. \tag{6.8}$$

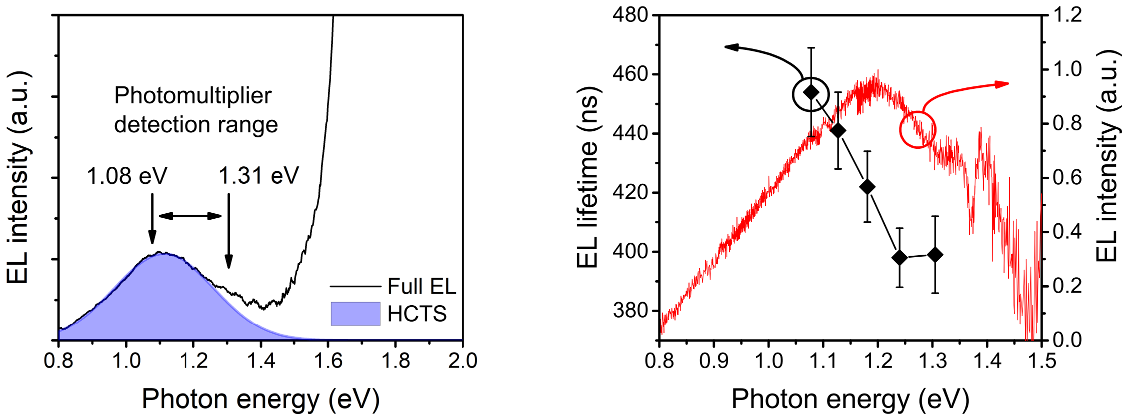

(a) EL spectrum under pulsed excitation

(b) Spectrally resolved HCTS lifetimes

Figure 6.17: (a) Time-integrated EL spectrum taken from a $Zn_{0.86}Mg_{0.14}O$/P3HT diode with $d_{\mathrm{P3HT}} = 240\,\mathrm{nm}$ using $10\,\mu\mathrm{s}$ long voltage pulses of $V_a = 3.5\,\mathrm{V}$. Its spectral shape exactly matches spectra taken with continuous excitation at the same voltage. This spectrum reflects the different branching ratios between P3HT bulk and HCTS luminescence at $1.08\,\mathrm{eV}$ and $1.31\,\mathrm{eV}$ as visible in figure 6.16. (b) HCTS spectrum of a $Zn_{0.86}Mg_{0.14}O$/P3HT diode with $d_{\mathrm{P3HT}} = 115\,\mathrm{nm}$ under pulsed excitation with $V_a = 3.5\,\mathrm{V}$ after subtracting P3HT bulk luminescence (red line). EL lifetimes τ_2 measured under the same excitation conditions for spectral energies between $1.08\,\mathrm{eV}$ and $1.31\,\mathrm{eV}$ show a clear decrease towards higher photon energies (black diamonds).

Comparing the integral of the whole transient curve to the calculated initial population of the long-lived decay, a share of $82\,\%$ for the HCTS emission is obtained for a measurement at $1.08\,\mathrm{eV}$. At $1.31\,\mathrm{eV}$ it is decreased to only $64\,\%$. As visible in figure 6.17(a), the low-energy tail of P3HT bulk emission contributes to the EL emission in the latter case, but does not extend further into the infrared.

By means of a spectrometer a Series of EL transients over a range of photon energies can be recorded. Figure 6.17(b) shows an overlay of calculated HCTS lifetimes together with a time-integrated HCTS spectrum of a $Zn_{0.86}Mg_{0.14}O$/P3HT diode with $d_{\mathrm{P3HT}} = 115\,\mathrm{nm}$ after subtraction of the P3HT bulk luminescence. The black marks show the long lifetime τ_2 calculated from HCTS transients measured at several emission energies. In the range between $1.08\,\mathrm{eV}$ and $1.31\,\mathrm{eV}$ it decreases from ca. $460\,\mathrm{ns}$ to $400\,\mathrm{ns}$. Note that despite the significantly thinner P3HT layer, the charge carrier lifetimes are comparable to the values reported before in figure 6.16 measured on a diode with a thicker P3HT layer. This rules out re-filling effects of holes flowing from the P3HT layer to the interface forming new HCTS during the decay process.

A common feature observed for both samples is the decreasing HCTS lifetime towards higher photon energies. Due to the conformational disorder of the P3HT polymer chains on a ZnMgO surface, the energetic landscape is not homogeneous. This has already been observed before in temperature-dependent electroluminescence measurements, showing a strong influence of inhomogeneous broadening (see section 6.3.1.2). Consequently, electrons and holes can be situated on different energetic levels depending on their exact site, which results in an uneven landscape of HCTS transition energies. It is likely that electron and hole forming an HCTS are able to migrate geminately along the interface plane during their long lifetime of more than 400 ns. A decreased radiative lifetime at higher HCTS transition energies indicates diffusion towards sites of lower local energies, which temporally act as a sink and thus show longer lifetimes.

The lifetimes given in this section, however, do not correspond to radiative decay rates of HCTS, as these are additionally quenched non-radiatively. The purely radiative lifetime can be estimated to be significantly longer than the measured 400 to 600 ns. Taking into account that at room temperature more than 99 % of all HCTS vanish through a competing non-radiative recombination channel as shown in section 6.3.1.3, a lower boundary of $100 \cdot \tau_2 \approx 50\,\mu\mathrm{s}$ can be calculated for the radiative lifetime of HCTS. As the actual $\mathrm{EQE}_{\mathrm{EL}}$ is likely to be even smaller by orders of magnitudes, even values in the range of milliseconds, as proposed by simulations in literature[41] are not unthinkable.

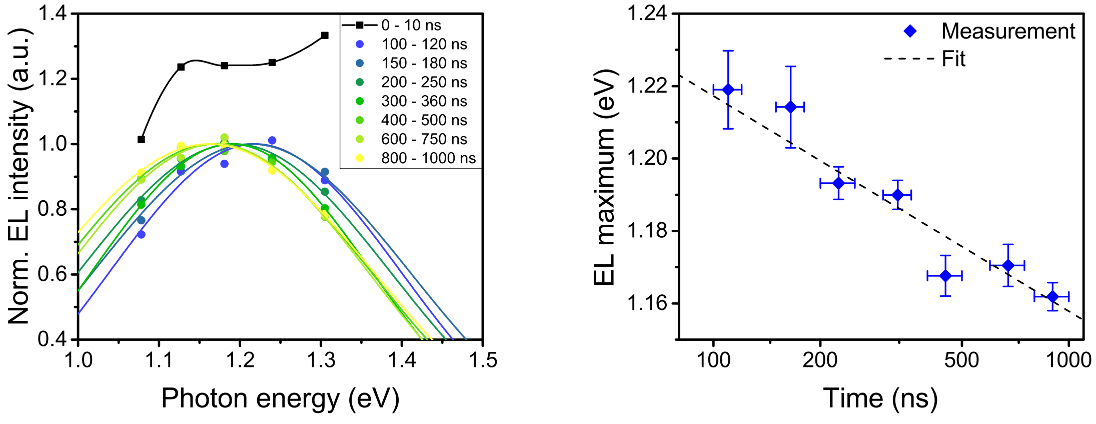

(a) (b)

Figure 6.18: (a) Normalized, time-resolved EL intensity spectra extracted from five transients by piecewise integration of incident photons and normalizing the resulting spectra. The solid lines represent Gaussian fits to model an HCTS spectrum from extracted data. Black squares and a spline fit show that the influence of P3HT bulk luminescence is restricted to the first 10 ns of the transient. Calculated EL spectra are not corrected for spectral sensitivity of the monochromator and photomultiplier. (b) The peak energy of the extracted EL spectra shifts towards lower energies with increasing time as expected from an energetic relaxation process.

Figure 6.18 shows normalized intensity distributions at different times of the transient together with reconstructed HCTS peaks by means of Gaussian fits. This gives a vivid overview of the temporal progression of EL emission. In the first 10 ns residual bulk emission from the low-energy tail of P3HT singlet emission contributes to the spectrum, all other spectra can be replicated well with a single Gaussian distribution representing the HCTS signal. The width of the extrapolated spectra from times 100 ns to 1000 ns slightly increases with time, and its peak notably shifts towards lower energies with time. The difference between the peak position at decay times of 100 and 1000 ns is ca. 60 meV.

The dashed fit line in figure 6.18(b) serves as guide to the eye and corresponds to a spectral shift which increases logarithmically with time. Such a relaxation behavior has been observed before for P3HT and other polymers featuring a hopping-like transport of charges in a disordered system.[167, 168]

A long lifetime of charge transfer states is advantageous for solar cells as it reduces the probability of interfacial carrier recombination and losses. For CTS in organic donor-acceptor systems consisting of small molecules, a broad range of lifetimes can be found in literature from a few hundred of picoseconds[169] to values that are several orders of magnitude higher. *Deotare et. al.* observed a similar behavior as the measurements above at an organic/organic heterojunction with CTS radiative lifetimes in the range of microseconds.[164] Electron-hole pairs at the interface can even migrate together over a distance of several nanometers and have been shown to be more mobile than Frenkel excitons in the organic bulk. Their movement was described as ”inchworm-like” transport of electron and hole moving independently from each other in their respective materials while remaining bound to each other by Coulomb interaction. The results of this section indicate that a similar model also holds true for oxide/organic heterojunctions.

6.4 Temperature-dependent Photovoltaic Measurements

In this section, the influence of temperature on photovoltaic charge generation will be discussed. Firstly, a detailed analysis will show which steps towards photovoltaic power conversion have to be taken by thermal activation and which intrinsic loss processes limit device efficiency. The question of the binding energy of electron and hole in an HCTS and the mechanism to overcome this attractive force plays a central role here.

In the second part of the section, photovoltage losses of a ZnMgO/P3HT heterojunction will be studied by means of a temperature-dependent analysis, showing the impact of the previously studied loss mechanisms on actual device performance.

6.4.1 Thermal Activation of Charge Separation

Temperature-dependent photovoltaic measurements are performed in order to gain insight into the mechanisms governing the conversion of incident photons into free electrons and holes. As charge generation is a complex multistep process, a combined analysis of both EQE spectra and J-V characteristics offers the possibility to separate influences of various partial processes from each other.

Figure 6.19 depicts the four main steps in the process of photovoltaic current generation. Each part of it depends on the properties of involved materials and has its own thermal activation behavior which will be discussed in short here.

1. Light Absorption:
Absorption of light in an organic layer is almost entirely independent of temperature. The transition from ground state to excited state upon absorbing a photon is governed by the transition matrix element in Fermi’s golden rule. The exact shape of P3HT absorption spectra varies only slightly between 10 K and 300 K.[170] This justifies the restriction on one single photon energy

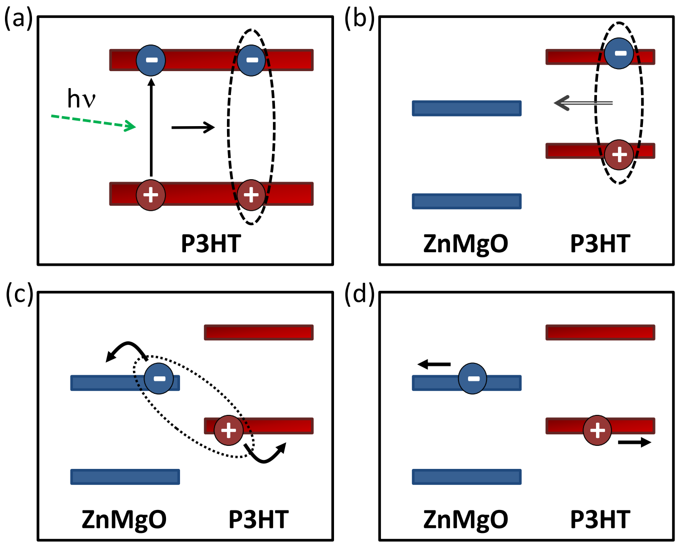

Figure 6.19: The four steps of photovoltaic charge generation: (a) Absorption of a photon in P3HT and formation of a Frenkel exciton (b) The exciton diffuses to the interface (c) Formation of a hybrid charge transfer state at the interface and subsequent dissociation (d) Transport of electron and hole to the respective electrodes.

for studying the thermal activation instead of integrating conversion efficiencies over the whole absorption spectrum.

2. Exciton Diffusion:
When a photon is absorbed in P3HT, a localized Frenkel exciton is produced. It can only contribute to a photocurrent, if it reaches the interface before vanishing by recombination. Exciton transport in a disordered polymer occurs either via energy transfer (Förster resonant energy transfer) or combined transport of electron and hole (Dexter electron transfer). While Förster transfer is independent of temperature, Dexter transfer strongly depends on carrier mobility and is therefore closely related to temperature. Luminescence quenching experiments with dispersed acceptor molecules have shown that both types of transfer can be found in disordered semiconductor polymers.[171] Theoretic modeling and measurements of the exciton diffusion length in conjugated polymers suggest that thermally activated processes are dominating the transport.[82]

The short radiative lifetime of excitons in P3HT of ca. $600\,\mathrm{ps}$[166] combined with the low carrier mobility in disordered organic semiconductors limits the diffusion length of excitons in P3HT to a couple of nanometers at room temperature.[22, 79] This diffusion length is decreasing towards lower temperatures, but might approach a residual value defined by a temperature-independent Förster transfer process.[77] Exciton diffusion length in ZnO exceeds $100\,\mathrm{nm}$ at all temperatures between $0\,\mathrm{K}$ and $300\,\mathrm{K}$.[172] However, due to the type II interface energy level alignment, excitons created in P3HT cannot cross the interface.

3. HCTS Formation and Dissociation:
Once an exciton in P3HT reaches the interface towards ZnMgO, its electron is driven to the

conduction band of the inorganic by the large band offset $\Delta E_\mathrm{c} > 1\,\mathrm{eV}$. However, both carriers remain bound at the interface by Coulomb interaction and form an HCTS until they either dissociate or recombine. Typical HCTS lifetimes of ca.$500\,\mathrm{ns}$ have been measured in the previous section. During this lifetime, the HCTS is possibly able to migrate along the interface in a process of energetic relaxation as indicated by a time-dependent redshift of transition energies.

If electron and hole are able to overcome their Coulomb attraction, an HCTS is dissociated into two free carriers on opposite sides of the interface. The strength of binding determines if this process occurs spontaneously or requires a thermal activation. The thermal activation behavior of HCTS dissociation yields information on the related processes. For a careful interpretation of temperature-dependent charge generation, however, the process of HCTS dissociation has to be isolated from other thermally activated processes involved in photovoltaic charge generation.

4. Charge Extraction:
After separating electron and hole at the interface, both carriers have to be transported to the respective electrodes. As electron mobility in ZnMgO exceeds hole mobility in P3HT by several orders of magnitude at all temperatures, only the thermal activation of the latter is relevant for the interpretation of measurements. Hole transport in P3HT occurs via a polaron-hopping process and therefore strongly decreases towards lower temperatures. At higher temperatures, phonon scattering processes and dynamical disorder in the quasi-crystalline domains of P3HT can possibly limit the carrier mobility.[81, 84] The activation barriers reported in literature range between 50 and $120\,\mathrm{meV}$.[83, 87, 156] As electrons and holes are charged particles, the electric field in the respective layer also influences the charge transport.

Not only holes, but also electrons have to be extracted from the heterojunction after HCTS dissociation. The carrier mobilities of ZnMgO and ZnMgO:Ga layers have been measured by using the Hall effect. In both cases, carrier mobility was almost constant over a wide temperature range between 150 and $300\,\mathrm{K}$ (see figure 9.3 in the appendix). As the overall conductivity is larger than in P3HT by orders of magnitude, it can be excluded that the inorganic layers act as a bottleneck in charge extraction at any temperature.

Based on this scheme, the physical processes can now be analyzed. Figure 6.20(a) shows EQE spectra of a diode with an intermediate Mg content of $x = 0.09$ and a P3HT layer of $150\,\mathrm{nm}$ thickness measured over a temperature range between $77\,\mathrm{K}$ and $295\,\mathrm{K}$. The excitation density is low and does not exceed $260\,\mathrm{\mu W/cm^2}$ at any wavelength. In order to avoid direct excitation of ZnMgO and its trap states, the measurement has been restricted to a range between 1.75 and $3.1\,\mathrm{eV}$.

The EQE measured at room temperature at the maximum of P3HT absorption of ca. $3.5\,\%$ is higher than the values measured before for ZnO/P3HT and ZnMgO/P3HT systems. This shows that optimization of the photovoltaic performance is possible by using thinner P3HT layers. If the electric field originating from the built-in voltage is spread over a smaller layer thickness, transport of dissociated carriers is facilitated. Again, the main limiting factor to device efficiency is the small exciton diffusion length of $L_\mathrm{D} \approx 5-8.5\,\mathrm{nm}$[22, 79], only allowing less than $10\,\%$ of all Frenkel excitons to reach the interface area.

The EQE increases from $77\,\mathrm{K}$ to $140\,\mathrm{K}$ by more than one order of magnitude. At higher temperatures it remains almost constant and slightly drops until room temperature. As the low-energy

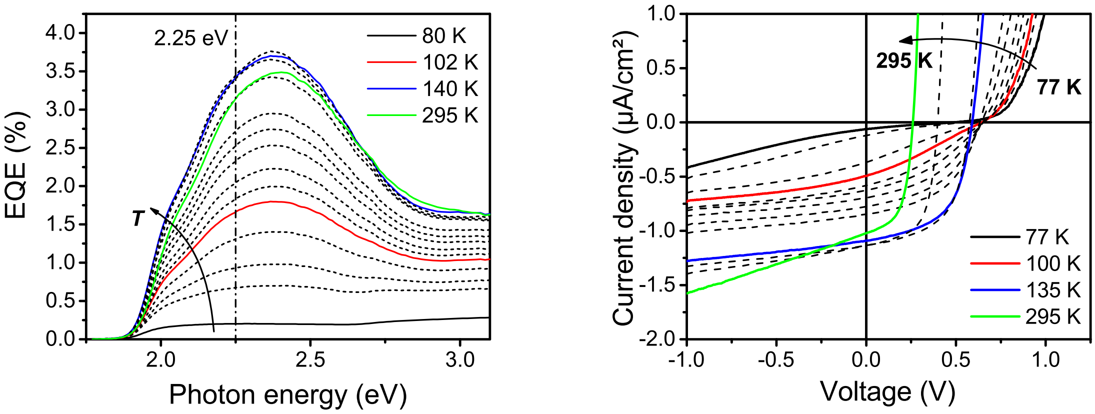

(a) EQE spectra (b) J-V characteristics

Figure 6.20: (a) EQE spectra of a $Zn_{0.91}Mg_{0.09}O$/P3HT diode measured at temperatures between $77\,K$ and $295\,K$. Intermediate temperatures are marked by black dashed lines. The EQE increases from $77\,K$ to $140\,K$ before it slightly drops until room temperature. The absorption spectrum of P3HT is visible in all measured curves and indicates, that the charge carriers are produced by absorption in the organic layer. The spectral position of $2.25\,eV$ marked in the spectra is used for a quantitative comparison of temperature-dependent charge separation efficiencies. (b) J-V characteristics from the same $Zn_{0.91}Mg_{0.09}O$/P3HT diode under monochromatic excitation at $2.25\,eV$ with a light intensity of $80\,\mu W/cm^2$. Black, red, green and blue lines represent the measurements at $77\,K$, $100\,K$, $135\,K$, and $295\,K$. Measurements at intermediate temperatures are marked by dashed black lines.

shoulder of the P3HT contribution to the photocurrent does not change its shape with temperature, the EQE values of a single spectral position at a photon energy of $2.25\,eV$ are used for comparison in the next steps of the analysis.

Figure 6.20(b) shows J-V characteristics of the same $Zn_{0.91}Mg_{0.09}O$/P3HT diode under monochromatic excitation with a photon energy of $2.25\,eV$ and a light intensity of $80\,\mu W/cm^2$ measured at temperatures between $77\,K$ and room temperature. Analyzing the shape of the J-V curves, three different regimes can be distinguished:

1. In the range below $100\,K$ the curve is s-shaped and thus has a fill factor of less than $25\,\%$. The short circuit current is growing with temperature by bulging the kink in the J-V curve and reducing the slope around $V \approx 0$.

2. Between $100\,K$ and $140\,K$ the curve has reached the common shape of a photodiode characteristics with a fill factor of more than $50\,\%$ and a very small slope in the vicinity $V \approx 0$. The short circuit current is growing with temperature by shifting downwards the whole curve.

3. Above $140\,K$ the produced photocurrent is almost independent of temperature, it only slightly decreases until room temperature. Due to a steeper onset of recombination current, the open circuit voltage decreases with temperature approaching room temperature.

The monochromatic light excitation for recording the J-V curves in figure 6.20(b) has been chosen to exactly match the conditions of an EQE measurement at a photon energy of $2.25\,\mathrm{eV}$ as marked in figure 6.20(a). Consequently, each measured short circuit current density can be converted into a corresponding quantum efficiency. Values obtained in this measurement series can then be joined into a common Arrhenius plot together with the temperature-dependent values extracted from the EQE spectra. This plot is shown in figure 6.21.

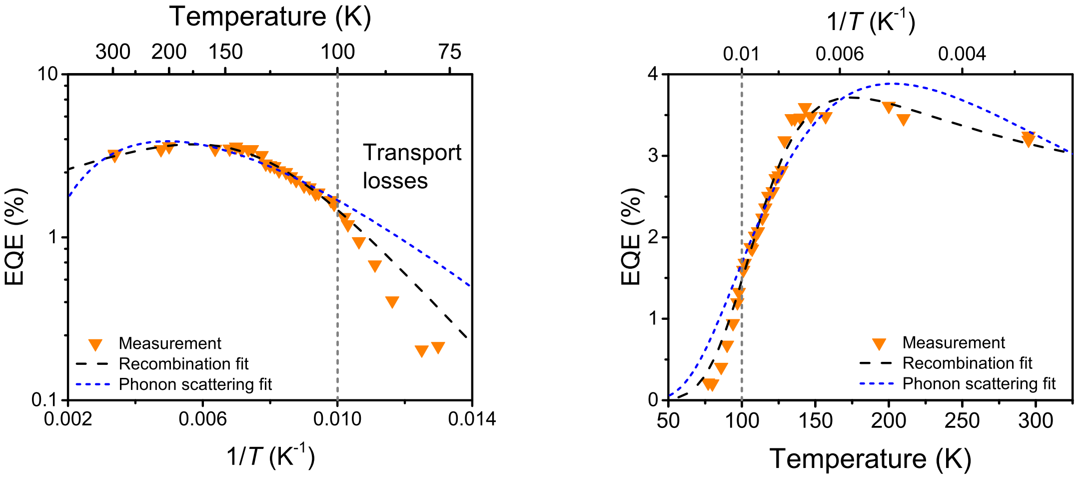

(a) Arrhenius plot

(b) Linear scale

Figure 6.21: Temperature-dependent EQE values of a $\mathrm{Zn_{0.91}Mg_{0.09}O}$/P3HT diode extracted from EQE spectra (figure 6.20(a)) and J-V characteristics (figure 6.20(b)). Dashed and dotted lines represent fit curves of the recombination model and phonon scattering model (details in text). At temperatures below $100\,\mathrm{K}$, limited carrier extraction decreases the charge generation efficiency. This region beyond the grey dashed line is excluded from data fits. (a) Arrhenius plot (b) Temperature and EQE in linear scale.

Starting at $77\,\mathrm{K}$, the power conversion efficiency is rapidly growing with increasing temperature. In this region the s-shape in the J-V characteristic disappears (see figure 6.20(b)), which increases both fill factor and short circuit current. The fill factor of a photodiode can be directly related to the ratio between the rates of charge extraction and recombination $\theta = \frac{k_{\mathrm{ex}}}{k_{\mathrm{rec}}}$.[173] A low fill factor is a consequence of limited carrier extraction which is caused by imbalanced carrier mobilities in donor and acceptor or energetic barriers between active layers and electrodes.[174, 175] Due to the strongly decreasing carrier mobility of P3HT towards lower temperatures, it is likely that a space charge region in the organic layer inhibits effective collection of charges.

Consequently, holes from previously dissociated HCTS remain in the proximity of the interface unable to reach the electrodes and eventually return to form an HCTS again or recombine non-radiatively at the interface. Only an applied bias in reverse direction creates an electric field in the organic layer, which helps to extract all the produced carriers. This dependence on applied bias causes the kink in the s-shaped J-V curve at low temperatures. Increasing the temperature to $100\,\mathrm{K}$ enhances the conductivity of the organic layer sufficiently to extract all the produced carriers at the low excitation density chosen for this experiment. Consequently, the s-shape in the characteristic has vanished at temperatures higher than $100\,\mathrm{K}$ as visible in figure 6.20(b).

The thermal activation energy of the EQE in the temperature range below $100\,\mathrm{K}$ of ca. $70\,\mathrm{meV}$ lies close to the activation of hole mobility in P3HT from literature.[83, 87, 156] However, as photocurrent production is a complex process, there is no direct correspondence between the two quantities.

Depending on illumination intensity (and the number of produced Frenkel excitons) the limitation of carrier extraction can prevail at higher temperatures. At $100\,\mathrm{mW/cm^2}$ AM 1.5 G illumination an s-shaped curve can be observed until ca. $200\,\mathrm{K}$. Therefore in the measurements presented in this section the illumination intensity is chosen as low as $80\,\mathrm{\mu W/cm^2}$.

At temperatures above $100\,\mathrm{K}$ the slope of the J-V curve is near zero, which means that all dissociated carriers can be extracted from the interface without an additional electric field. Then carrier mobility is not a limiting factor to photocurrent generation anymore. Up to ca. $140\,\mathrm{K}$ a further increase in quantum efficiency is observed before it saturates and eventually slightly decreases as the temperature approaches $295\,\mathrm{K}$. Possible explanations for this unusual physical behavior of interrupted thermal activation will be discussed in the following two paragraphs.

6.4.1.1 The Phonon Scattering Model

Once extraction of charges is not a limiting factor to photodiode performance anymore, the decisive figure, apart from dissociation efficiency, is the number of excitons reaching the interface. Exciton diffusion is a thermally activated process as previously stated in literature.[77, 78, 171] Investigating the temperature-dependent charge generation in an organic P3HT/PCBM heterojunction, *Presselt et. al.* concluded that phonon scattering limits charge generation efficiency.[52] The interplay of thermally activated exciton transport and phonon scattering is expressed in the following model for a temperature-dependent quantum efficiency:

$$\mathrm{EQE}(T) = A \cdot T^{-m} \exp\left(\frac{-E_{\mathrm{A}}}{k_{\mathrm{B}}T}\right) \tag{6.9}$$

with the activation energy for exciton diffusion E_{A}, a sample-dependent prefactor A and an exponent m expressing the influence of phonon scattering processes in the organic layer. It is claimed that this is the mechanism which causes the EQE to saturate and eventually decrease at higher temperatures.

According to theoretical models in literature, phonon scattering is a process limiting transport of single charged particles in compounds of organic semiconductor molecules or polymers by introducing a prefactor T^{-m} with a fixed exponent of $m = \frac{3}{2}$.[84] In this case, only extraction of electrons and holes after exciton dissociation is affected. As concluded before, in the presented device this would decrease the device's fill factor and cause an s-shaped J-V characteristics. But this is not the case at temperatures above $100\,\mathrm{K}$. However, *Presselt et. al.* claim that phonon scattering also affects the exciton transport towards the heterojunction, which alters the value of the exponent m to values of 1.1 to 2.1 for PCBM and 2.1 to 2.5 for P3HT. Extrapolations from current transport measurements show that conductivity of P3HT follows a behavior of thermal activation up to more than $100\,\mathrm{K}$ above room temperature. Decreasing conductivity is likely to happen only at temperatures near the point of chemical degradation.[82] Therefore, transport phenomena in P3HT cannot be the reason for a stagnating and decreasing EQE above $150\,\mathrm{K}$. Additionally, Hall measurements have shown that carrier mobilities in ZnMgO and ZnMgO:Ga do not decrease over a broad temperature range up to $300\,\mathrm{K}$ (see section B in the appendix).

In figure 6.21(a) and 6.21(b) a data fit following the phonon scattering model is shown as a blue dashed line. All data points between $100\,\mathrm{K}$ and room temperature are included into the fit. The values $m = 2.60 \pm 0.43$ and $E_\mathrm{A} = 45 \pm 6\,\mathrm{meV}$ are similar to the data described in reference [52] for P3HT. Data from other ZnMgO/P3HT and ZnO/P3HT devices yield values for m up to 3.98 and activation energies E_A between $47\,\mathrm{meV}$ and $62\,\mathrm{meV}$ (see appendix C). The activation energies obtained from the fits are higher than values found in literature[52, 83], and the physical meaning of m values significantly higher than $3/2$ remains unclear. The data fits can reproduce an increasing EQE which eventually reaches a maximum and decreases towards room temperature, but the position of the maximum around $200\,\mathrm{K}$ and the strong temperature-dependence at room temperature does not correspond well to experimental data.

6.4.1.2 The Model of Activated Recombination

As described in section 2.2.2, the external quantum efficiency of a solar cell is the product of the quantum efficiencies of six sequenced processes.

$$\eta = \eta_\text{absorption} \cdot \eta_\text{diffusion} \cdot \eta_\text{transfer} \cdot \eta_\text{dissociation} \cdot \eta_\text{transport} \cdot \eta_\text{extraction} \tag{6.10}$$

The absorption efficiency in P3HT $\eta_\text{absorption}$ is independent of temperature,[170] and the transfer efficiency for an electron from a Frenkel exciton in P3HT to the inorganic side of the interface η_transfer is assumed to be unity due to the strong driving force provided by the conduction band offset of $\Delta E_\mathrm{c} > 1\,\mathrm{eV}$. At sufficiently high temperatures the transport and extraction of dissociated carriers does not impose a limitation on photocurrent, and therefore $\eta_\text{transport}$ and $\eta_\text{extraction}$ can be assumed to be unity as well. Consequently, the efficiencies of only two processes will determine the external quantum efficiency of the device: The probability that an exciton absorbed in P3HT will diffuse to the interface $\eta_\text{diffusion}$ and the ratio $\eta_\text{dissociation}$ of HCTS that will be dissociated into free carriers at the interface.

As the optical absorption depth for P3HT of ca. $60\,\mathrm{nm}$ is significantly larger than the exciton diffusion length L_D, the ratio of produced Frenkel excitons per photon can be approximated as the number of photons absorbed in a P3HT slice with the thickness L_D. As exciton diffusion is a thermally activated process, this yields

$$\eta_\text{absorption}(E) \cdot \eta_\text{diffusion}(T) \approx L_\mathrm{D}(T) \cdot \alpha(E) = A_0 \cdot \exp\left(\frac{-E_\mathrm{A}}{k_\mathrm{B}T}\right) \tag{6.11}$$

with the absorption coefficient $\alpha(E)$ for the photon energy E and the activation energy for exciton diffusion E_A.

The dissociation efficiency of HCTS into free carriers is determined by the rates for dissociation and recombination k_{diss} and k_{rec}:

$$\eta_{\text{dissociation}}(T) = \frac{k_{\text{diss}}(T)}{k_{\text{diss}}(T) + k_{\text{rec}}(T)} = \frac{1}{1 + \frac{k_{\text{rec}}(T)}{k_{\text{diss}}(T)}} \tag{6.12}$$

Both processes of HCTS dissociation and recombination are assumed to be thermally activated with their activation energies E_{diss} and E_{rec}. This gives the expression for the HCTS dissociation efficiency

$$\eta_{\text{dissociation}}(T) = \frac{1}{1 + k_0 \cdot \exp\left(\frac{-(E_{\text{rec}} - E_{\text{diss}})}{k_{\text{B}}T}\right)} \tag{6.13}$$

with the prefactors for recombination and dissociation rates lumped together into k_0. The whole model for the temperature-dependent EQE then reads:

$$\text{EQE}(T) = \frac{A_0 \cdot \exp\left(\frac{-E_{\text{A}}}{k_{\text{B}}T}\right)}{1 + k_0 \cdot \exp\left(\frac{-(E_{\text{rec}} - E_{\text{diss}})}{k_{\text{B}}T}\right)} \tag{6.14}$$

It has to be noted that from this calculation the activation energies for HCTS dissociation and recombination cannot be determined separately. Only the difference of both quantities is accessible. Further discussion, however, will provide insight into the two processes.

A fit of this model to experimental data is displayed in figure 6.21 as a black dashed line. In the whole range between $100\,\text{K}$ and $295\,\text{K}$ the model nicely reproduces the experimental data. The activation energies $E_{\text{A}} = 44 \pm 7\,\text{meV}$ and $(E_{\text{rec}} - E_{\text{diss}}) = 58 \pm 3\,\text{meV}$ are obtained.

Table 6.2: Activation energies E_{A} and $(E_{\text{rec}} - E_{\text{diss}})$ obtained from data fits to temperature-dependent EQE measurements for photodiodes involving different acceptor materials.

Acceptor material	E_{A}	$(E_{\text{rec}} - E_{\text{diss}})$
$\text{Zn}_{1-x}\text{Mg}_x\text{O}$ ($x = 0.01$)	$54 \pm 6\,\text{meV}$	$68 \pm 4\,\text{meV}$
$\text{Zn}_{1-x}\text{Mg}_x\text{O}$ ($x = 0.09$)	$44 \pm 7\,\text{meV}$	$58 \pm 3\,\text{meV}$
$\text{Zn}_{1-x}\text{Mg}_x\text{O}$ ($x = 0.14$)	$31 \pm 7\,\text{meV}$	$53 \pm 10\,\text{meV}$
ZnO	$45 \pm 15\,\text{meV}$	$65 \pm 6\,\text{meV}$

Table 6.2 shows the activation energies obtained from data fits to EQE measurements for several ZnMgO/P3HT and ZnO/P3HT diodes (see diagrams in appendix C).

The activation energies E_{A} for exciton transport in a P3HT layer between $31\,\text{meV}$ and $54\,\text{meV}$ provide a better agreement to values obtained from literature than the higher energies obtained from the phonon scattering model.[52, 83] For the difference $(E_{\text{rec}} - E_{\text{diss}})$ values between $53\,\text{meV}$ and $68\,\text{meV}$ are obtained in the data fits.

The latter activation energy can be related to the results of electroluminescence measurements discussed in section 6.3.1.3. In quantitative analysis of EL spectra a thermally activated non-radiative recombination process is found which annihilates HCTS at the interface. The activation energy of this process is determined as $E_{\text{nr}} = 70\,\text{meV}$. Taking into account the very low quantum efficiency of radiative HCTS recombination which could be encountered in all EL measurements, in a first approximation all interfacial charge carrier recombination can be regarded as non-radiative. Consequently, interfacial recombination in general is a thermally activated process.

HCTS which recombine at the interface, be it radiatively or non-radiatively, cannot contribute to photovoltaic power conversion. Consequently, a thermally activated recombination process produces losses which increase exponentially towards higher temperatures. Despite the different situations at the interface in photovoltaic operation and electroluminescence measurements - particularly regarding the electric field in the device under external bias - the two loss processes can be compared to each other. If the activation energy for photovoltaic losses E_{rec} is assumed to be identical to the activation energy for non-radiative recombination in EL E_{nr}, then the experimental values for the difference $(E_{\text{rec}} - E_{\text{diss}})$ give a hint, that the activation barrier for HCTS dissociation E_{diss} can only be in the range of a couple of meV, or even zero. This fits nicely to the HCTS model obtained in previous measurements, showing a high degree of delocalization and a wide effective binding radius, which both drastically decrease the Coulomb interaction betweeen electron and hole in an HCTS. Consequently, the dissociation process separating HCTS into free carriers at the heterointerface only weakly depends on temperature, or is even temperature-independent.

It can be concluded that the model of thermally activated recombination provides a significantly better agreement with experimental data than the previously discussed phonon scattering model. Furthermore, the activation energies obtained as fit parameters are in the expected range and can be related to data obtained in other measurements and literature. An energetic barrier for dissociation of HCTS could not be determined so far. Instead it is likely that the HCTS separation process depends only weakly on temperature. A similar behavior has already been found for organic photovoltaic devices before[30]. Even if the binding forces between carriers are stronger, entropic effects can lead to a similar temperature-independent dissociation rate.[32]

6.4.2 Temperature Dependence of the Open-Circuit Voltage

With the knowledge gained in the previous sections, the photovoltaic losses of the prototypical heterojunction ZnMgO/P3HT can be estimated by analyzing the temperature-dependence of the open circuit voltage. The most important tool for this purpose is the relation between V_{OC} and the HCTS transition energy E_{HCTS} as explained in section 2.3.2.1.

$$qV_{\text{OC}} \approx E_{\text{HCTS}} - k_{\text{B}}T \ln\left(\frac{J_{00}}{J_{\text{SC}}}\right) \tag{6.15}$$

Hereby, V_{OC} is given as the difference between E_{HCTS}/q and the photovoltage losses inflicted by carrier recombination described by the second term. Previous measurements involving a

ZnO/P3HT heterojunction in section 5.4.5 confirm that the open circuit voltage increases towards lower temperatures. Following equation 6.15, this increase is linear under the assumption that the photocurrent J_{SC} is constant. In this case, an extrapolation of V_{OC} with $T \to 0$ produces the intersection $V_{\mathrm{OC,max}}$. It can be interpreted as the hypothetical maximal open circuit voltage, which would only be attainable in absence of any recombination current in the device. As such, $qV_{\mathrm{OC,max}}$ gives a good estimate for the HCTS transition energy E_{HCTS}.

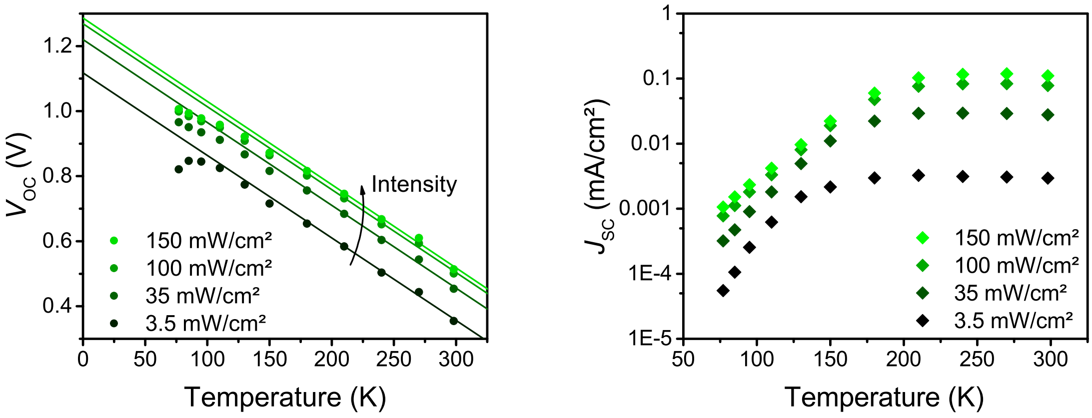

(a) V_{OC} vs. T (b) J_{SC} vs. T

Figure 6.22: (a) Temperature-dependent V_{OC} measurements of a $\mathrm{Zn_{0.95}Mg_{0.05}O}$/P3HT diode with $d_{\mathrm{P3HT}} = 240\,\mathrm{nm}$ measured at illumination densities between $3.5\,\mathrm{mW/cm^2}$ and $150\,\mathrm{mW/cm^2}$. (b) Corresponding J_{SC} values from the same device. Between 200 K and room temperature the photocurrent is approximately constant for all illumination intensities.

Although photocurrent generation is a complex multistep process, the short circuit current of a photodiode is approximately constant between 200 K and room temperature for all illumination intensities between 3.5 and $150\,\mathrm{mW/cm^2}$ (see figure 6.22(b)). This gives the range which is used for a calculation of $V_{\mathrm{OC,max}}$. Figure 6.22(a) shows V_{OC} of a ZnMgO/P3HT diode with a Mg content of $x = 0.05$ for different illumination intensities together with linear extrapolations from the range between $200\,\mathrm{K}$ and $300\,\mathrm{K}$. Note that the slopes do not intersect at a single point at $T = 0\,\mathrm{K}$ as expected in a simplistic model. This happened similarly for $x = 0.01$ and $x = 0.14$ to a smaller extent and can be explained by contributions from series and shunt resistances in the device.[36] As *M. Runge* pointed out, effects from shunt resistances become less influential at higher illumination densities.[151] Therefore, for extrapolation of $V_{\mathrm{OC,max}}$ only the values measured at an illumination intensity of $35\,\mathrm{mW/cm^2}$ and more were taken into account. Deviations from a common intersection between different illumination conditions were taken into account when calculating error ranges.

Figure 6.23 shows the V_{OC} under $100\,\mathrm{mW/cm^2}$ AM 1.5G illumination for three ZnMgO/P3HT diodes at temperatures between $77\,\mathrm{K}$ and room temperature. The range between $200\,\mathrm{K}$ and $300\,\mathrm{K}$ is used for linear extrapolations in order to obtain $V_{\mathrm{OC,max}}$. The values gained from intersections at $T = 0\,\mathrm{K}$ are shown in table 6.3.

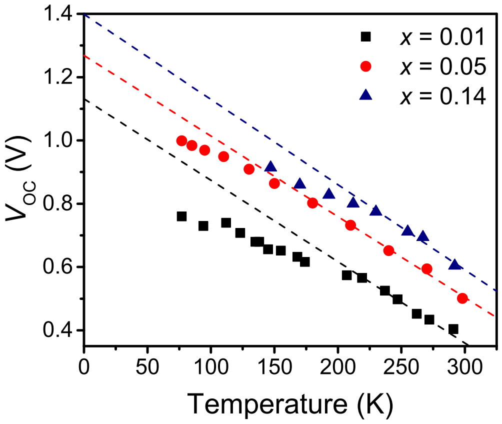

Figure 6.23: Temperature dependence of the V_{OC} of $\mathrm{Zn}_{1-x}\mathrm{Mg}_x\mathrm{O}$/P3HT diodes with different Mg content x measured at $100\,\mathrm{mW/cm}^2$ AM 1.5G illumination. The dashed lines mark linear fits involving only data points from 200 K to room temperature.

Table 6.3: $V_{\mathrm{OC,max}}$ values extracted from temperature-dependent measurements of V_{OC}

x	$V_{\mathrm{OC,max}}$
0.01	$1.13 \pm 0.06\,\mathrm{V}$
0.05	$1.27 \pm 0.06\,\mathrm{V}$
0.14	$1.40 \pm 0.09\,\mathrm{V}$

The exact identity $E_{\mathrm{HCTS}} = qV_{\mathrm{OC,max}}$ is only valid under the assumption that all losses are produced by a single recombination channel with a transition energy E_{HCTS}. The previous sections, however, have shown the strong presence of non-radiative processes in a ZnMgO/P3HT heterojunction. Consequently, these have to be included into the model for an in-depth analysis of the interface energetics in order to obtain a reliable value of E_{HCTS}.

6.4.2.1 The Influence of Non-radiative Recombination

In the previous sections it was pointed out that the main loss mechanism in a ZnMgO/P3HT photovoltaic device is non-radiative recombination. Electroluminescence measurements have shown that at room temperature, less than $1\,\%$ of HCTS recombination contributes to an EL signal, while more than $99\,\%$ occur without emission of a photon in the near IR. In order to account for these circumstances, the model for interface energetics will have to be altered and extended.

Detailed balance as described in section 2.3.2 imposes a relation between recombination current and charge generation in a solar cell. Restricted to direct absorption of the hybrid charge transfer state and only considering radiative recombination, the detailed balance relation (equation 2.12) reads:

$$J_0^{\text{rad}} = q \int_0^\infty \text{EQE}_{\text{PV}}(E) \cdot \Phi_{\text{bb}}^T(E)\,\mathrm{d}E \tag{6.16}$$

Mirror symmetry according to Marcus theory (see section 2.3.3) between the spectra of absorption and emission of an HCTS suggests a Gaussian lineshape of direct interfacial HCTS absorption $\text{EQE}_{\text{PV}}(E)$. Its peak energy is denominated E_0 here. Measurements of sub-bandgap photovoltaic efficiency at an interface of ZnO and small molecules confirm such an assumption.[39]

$$\text{EQE}_{PV}(E) = \frac{f}{E\sqrt{2\pi}\sigma} \exp\left(-\frac{(E_0 - E)^2}{2\sigma^2}\right) \tag{6.17}$$

$\Phi_{\text{bb}}^T(E)$ in equation 6.16 is the emission spectrum of a radiating blackbody held at the temperature T

$$\Phi_{\text{BB}}^T = \frac{2\pi}{h^3c^2} E^2 \exp\left(-\frac{E}{k_BT}\right), \tag{6.18}$$

where h is the Planck constant, c the speed of light and $k_\text{B}T$ the thermal energy. Partial integration in equation 6.16 yields the relation

$$J_0^{\text{rad}} \approx J_{00}^{\text{rad}} \exp\left(-\frac{E_0 - \frac{\sigma^2}{2k_BT}}{k_BT}\right). \tag{6.19}$$

The detailed evaluation of the integral is described in appendix D. The saturation current of radiative recombination is thermally activated with the activation energy $E_0 - \frac{\sigma^2}{2k_\text{B}T}$, which can be assigned to the HCTS transition energy E_{HCTS}. HCTS absorption and emission spectra are expected to lie symmetrically around this energy value, which nicely reproduces the emission maximum at an energy of $E_{\text{HCTS}} - \frac{\sigma^2}{2k_\text{B}T}$ as pointed out earlier in EL measurements. The proportionality constant $J_{00}^{\text{rad}} = qf^*E_{\text{HCTS}}$ gives the coupling strength between the electron and hole states at the heterointerface.

As only radiative recombination is thermally activated with the HCTS transition energy E_{HCTS}, it has to be separated from all non-radiative processes. The thermal activation behavior of all non-radiative processes is not known and has to be excluded from calculation here. So equation 2.17 only considering the radiative recombination current J_0^{rad} then reads:

$$qV_{\text{OC}} \approx k_\text{B}T\ \ln\left(\frac{J_{\text{SC}}}{J_0^{\text{rad}}}\right). \tag{6.20}$$

However, non-radiative processes can re-enter the calculation by considering the emission quantum efficiency EQE_{EL} and scaling up the radiative recombination current by this prefactor: $J_0 = J_0^{\text{rad}} \cdot \text{EQE}_{\text{EL}}^{-1}$. Repeating the calculation performed in equation 2.25 then yields the following relation for the temperature-dependence of V_{OC}:[176]

$$qV_{\mathrm{OC}} \approx E_{\mathrm{HCTS}} - k_{\mathrm{B}}T \ln\left(\frac{J_{00}^{\mathrm{rad}}}{\mathrm{EQE}_{\mathrm{EL}} \cdot J_{\mathrm{SC}}}\right) \tag{6.21}$$

Consequently, by inclusion of the radiative quantum efficiency in electroluminescence, which was investigated in section 6.3.1.3, a suitable model for the photovoltage of a ZnMgO/P3HT heterojunction is obtained.

This relation predicts an increase of V_{OC} with the energy E_{HCTS} which is indeed observed by measuring samples with different Mg content (see figure 6.8(b) and 6.23).

However, the convenient procedure of extending the initial slope of the V_{OC} vs. T curve to $0\,\mathrm{K}$ in order to obtain the maximal possible open circuit voltage $V_{\mathrm{OC,max}}$ corresponding to the HCTS transition energy E_{HCTS}, does not produce correct results following this model. $\mathrm{EQE}_{\mathrm{PV}}$ respectively the produced photocurrent J_{SC} are constant at temperatures between $200\,\mathrm{K}$ and room temperature (see figure 6.22(b)), but the EL quantum efficiency $\mathrm{EQE}_{\mathrm{EL}}$ rapidly decreases between $200\,\mathrm{K}$ and room temperature due to thermal activation of a non-radiative decay channel. This alters the value of the logarithm in equation 6.21 and leads to an incorrect result of the extrapolation process.

Inserting the temperature-dependent model for $\mathrm{EQE}_{\mathrm{EL}}$ as obtained in temperature-dependent EL measurements in section 6.3.1.3 into the fundamental relation of equation 6.21, yields

$$qV_{\mathrm{OC}} \approx E_{\mathrm{HCTS}} + E_{\mathrm{nr}} - k_{\mathrm{B}}T \ln\left(\frac{J_{00}^{\mathrm{rad}}}{J_{\mathrm{SC}}} \cdot \frac{\alpha}{\mathrm{EQE}_0}\right). \tag{6.22}$$

The values α and EQE_0 obtained in the analysis of the temperature-dependence of $\mathrm{EQE}_{\mathrm{EL}}$ now contribute to the slope of the V_{OC} vs. T curve, but do not alter the intersection point for $T \to 0$. The linearly extrapolated value of V_{OC} is then given as $V_{\mathrm{OC,max}} = E_{\mathrm{HCTS}} + E_{\mathrm{nr}}$. Consequently, linear extrapolation overestimates E_{HCTS} by approximately the activation energy of the non-radiative recombination process $E_{\mathrm{nr}} \approx 70\,\mathrm{meV}$. Correcting the extrapolated values according to this consideration, yields the estimates of the E_{HCTS} reported in table 6.4.

Table 6.4: HCTS transition energies determined from temperature-dependent measurements of the V_{OC}

x	E_{HCTS}
0.01	$1.06 \pm 0.07\,\mathrm{eV}$
0.05	$1.20 \pm 0.07\,\mathrm{eV}$
0.14	$1.33 \pm 0.10\,\mathrm{eV}$

Gathering all results of the previously described measurements and analysis, the photovoltaic losses for prototypical model system ZnMgO/P3HT can now be assessed. Knowledge gained on the physical properties of hybrid charge transfer states can be used to understand the origin of recombination losses.

6.5 Discussion of Results

Combined analysis of the results gained by UPS, EL spectroscopy and photovoltaic measurements allows to give a detailed description of the properties of HCTS and the underlying physical processes. Based on this knowledge, the potential of inorganic/organic hybrid interfaces in photovoltaic applications can be estimated. By comparison to interface energetics, inherent losses can be calculated.

6.5.1 Photovoltaic Losses of a ZnMgO/P3HT Heterojunction

The energy diagram in figure 6.24 summarizes all relevant energy levels, which are obtained by different measurement procedures in the previous sections analyzing three different types of $\mathrm{Zn}_{1-x}\mathrm{Mg}_x\mathrm{O}$/P3HT diodes with Mg contents of $x = 0.01$, $x = 0.05$ and $x = 0.14$. Three independent measurements yield values for HCTS transition energy E_{HCTS}. One value is derived as $qV_{\mathrm{OC,max}} - E_{\mathrm{nr}}$ from analysis of the temperature-dependent V_{OC} measurements, another one comes as activation energy E_{act} for the recombination current and was gained from temperature-dependent dark current fits. Finally, the hybrid gap energy ΔE_{IO} is taken from UPS measurements. All these values are compared to qV_{OC} measured under $100\,\mathrm{mW/cm^2}$ AM 1.5G illumination at room temperature in order to estimate losses in photovoltaic operation.

All quantities follow the same linear progression with a slope that directly corresponts to the widening of the optical gap energy ΔE_{IO} as measured by UPS. This proves that all photovoltaic parameters are directly linked to each other and have a close relation to the HCTS transition energy E_{HCTS}.

The ΔE_{IO} derived from UPS measurements are about $300\,\mathrm{meV}$ smaller than the E_{HCTS} deduced from both photovoltaic measurements and dark current fits. This can be explained as follows: The UV radiation used for photoelectron spectroscopy has only a very limited penetration depth significantly smaller than the $15\,\mathrm{nm}$ layer thickness and thus measures the ionization potential of P3HT at the surface and not at the interface to ZnMgO. It is likely that P3HT chains in proximity of an oxide surface prefer a face-on orientation, while the polymers in the bulk are randomly oriented. This morphological difference can account for the difference in measured gap energies,[114] promoting the E_{HCTS} derived from photovoltaic measurements as the correct interface gap energies.

From the difference between E_{HCTS} deduced from temperature-dependent V_{OC} measurements and the open circuit voltage measured at room temperature the photovoltaic losses of the system can be estimated. These are the sum of radiative and non-radiative losses. They amount to about (680 ± 80) meV and are independent of the hybrid energy gap defined by magnesium content in ZnMgO. The quantity of losses is thus an intrinsic feature of the ZnMgO/P3HT heterojunction. Thereby, the device efficiency is significantly reduced as these limitations exceed the photovoltage loss of a planar P3HT/PCBM heterojunction (ca. $530\,\mathrm{meV}$[25]).

Despite the negligible influence of an HCTS binding energy onto the charge separation process, interfacial recombination effectively competes with photocurrent generation. Temperature-

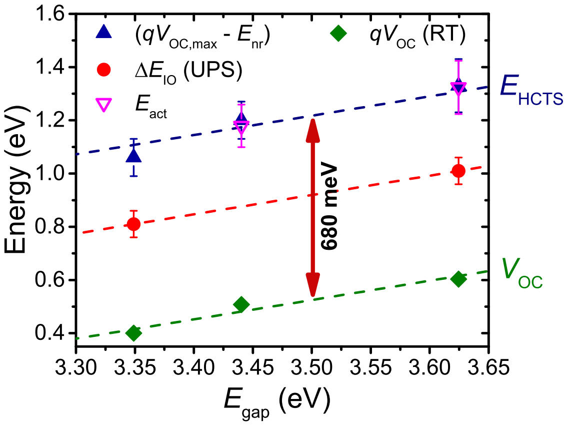

Figure 6.24: Summary of HCTS transition energies determined by several procedures: $E_{\mathrm{HCTS}} = V_{\mathrm{OC,max}} - E_{\mathrm{nr}}$ derived from the analysis of temperature-dependent V_{OC} measurements (blue solid triangles), activation energies for the recombination current E_{act} from dark current diode fits (pink open triangles), ΔE_{IO} values measured by UV photoelectron spectroscopy (red circles) and room temperature qV_{OC} under $100\,\mathrm{mW/cm^2}$ AM 1.5G illumination (green diamonds). The slope of the dashed lines corresponds to the hybrid band gap widening measured by UPS. The red arrow marks the losses in photovoltage between the photovoltaic energy gap and the actually measured open circuit voltage at room temperature.

dependent measurements of electroluminescence quantum efficiency show that at room temperature the biggest part of carrier recombination occurs non-radiatively. As only radiative recombination is inevitable in the charge separation process[7], non-radiative processes impose additional losses which can theoretically be avoided by suitable interface tailoring.

6.5.2 Structure and Properties of Hybrid Charge Transfer States

In figure 6.25 the electroluminescence maxima from a ZnMgO/P3HT heterojunction extrapolated for $F \to 0$ are shown together with the HCTS energy E_{HCTS} determined by photovoltaic measurements and dark current fits. Analysis of the HCTS electroluminescence performed in section 6.3.1 shows that the EL maximum is directly linked to the hybrid gap energy ΔE_{IO} and thus depends on the Mg content x in $\mathrm{Zn}_{1-x}\mathrm{Mg}_x\mathrm{O}$.

Independent from the hybrid gap energy, the extrapolated EL maxima lie ca. $350\,\mathrm{meV}$ below the HCTS transition energy. This Stokes shift corresponds to the expected value of $\frac{\sigma^2}{2k_{\mathrm{B}}T}$, indicating that the recombination indeed occurs between a free electron in the ZnMgO conduction band and a hole in the P3HT HOMO. This rules out a contribution from interfacial trap states in ZnMgO as reported by *Panda et. al.*[41] Such a constitution would lead to a further red shift in emission.

In addition to this, the voltage-dependent shift of the HCTS EL peak indicates that not only the electron in an HCTS is mobile in the conduction band of ZnMgO, but also the hole is delocalized in the P3HT layer perpendicularly to the heterointerface. This leads to a larger

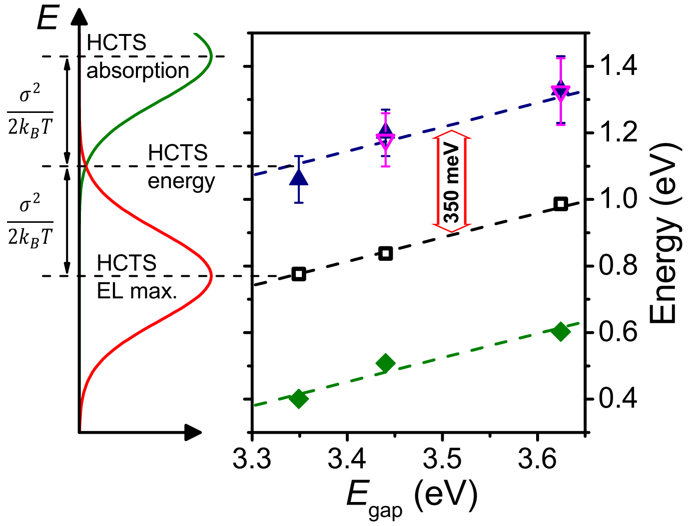

Figure 6.25: HCTS transition energy E_{HCTS} of three different ZnMgO/P3HT devices compared to HCTS EL maxima and qV_{OK} values measured at room temperature. E_{HCTS} derived from the analysis of the temperature-dependent V_{OC} measurements (blue solid triangles), activation energies for diode recombination current E_{act} from dark current diode fits (pink open triangles), electroluminescence maxima extrapolated for $F \to 0$ (black open squares), and room temperature qV_{OC} under $100\,\text{mW/cm}^2$ AM 1.5G illumination. The slope of the dashed lines corresponds to the hybrid band gap widening measured by UPS. The red arrow marks the energy difference between E_{HCTS} and EL energy. On the left side, the HCTS energy E_{HCTS} with respect to the HCTS absorption and emission spectra is schematically depicted. For a homogeneously broadened transition, $\frac{\sigma^2}{2k_{\text{B}}T}$ corresponds to the reorganization energy. It is apparent that the EL emission maxima correspond to values expected from Marcus theory.

effective distance between electron and hole and reduces the binding energy of an HCTS to a small value in the range of a few meV. These findings are supported by the long life time of HCTS which were measured to be ca. $500\,\text{ns}$. Within this time, electron and hole in an HCTS are likely to geminately migrate along the hybrid interface in lateral direction.

Despite the relatively loose binding force between electron and hole in an HCTS, interfacial recombination effectively competes with the charge separation and causes severe losses in the photovoltaic device efficiency. Long HCTS lifetimes in the range of $500\,\text{ns}$ do not guarantee an effective charge separation. Electroluminescence measurements have shown that a thermally activated non-radiative process is responsible for the loss of a high quantity of excitons during the HCTS dissociation process. Localized defects at the interface are likely to promote non-radiative recombination of HCTS. Due to the high mobilty and delocalization of HCTS around the interface, these sites are reachable for many carriers due to their thermally activated movement.

As the binding forces inside of an HCTS do not impose a limitation on photocurrent generation, a significant improvement in device performance can only be attained by improving the charge separation process. This can happen via a faster extraction of carriers from the interfacial region. Once the carriers are funneled away from the interface, non-radiative recombination processes during the HCTS dissociation process can effectively be suppressed.

Chapter 7

Tin Dioxide Based Hybrid Photovoltaics

7.1 SnO_2 as a New Acceptor Material

The results gained in the previous chapters have shown the general functionality of ZnO and ZnMgO as acceptor materials for hybrid photovoltaics. Nevertheless, a detailed analysis of device performance and losses reveals that ZnO/P3HT and ZnMgO/P3HT are not ideal heterojunctions for power conversion. Interfacial recombination processes lead to severe losses in photocurrent and open circuit voltage. Particularly the high rate of non-radiative recombination of hybrid charge transfer states at the interface is detrimental to photovoltaic device efficiency. Despite their long lifetime of several hundreds of nanoseconds, there is no efficient dissociation into free carriers in the P3HT HOMO and Zn(Mg)O conduction band.

Pump-probe measurements monitoring the electron injection upon optical excitation from organic adsorbates into crystalline inorganic semiconductor materials have shown that electrons injected into SnO_2 reach the conduction band almost one order of magnitude faster than electrons injected into ZnO.[16] Rapid thermalization of excited interface states into the conduction band enables an efficient transport away from the heterojunction in the direction of the electrode. This can possibly provide a more efficient HCTS dissociation mechanism than observed in ZnO/organic and ZnMgO/organic interfaces, and may significantly increase the quantum yield of photovoltaic power conversion.

Measurements of photovoltaic function and spectroscopy of HCTS in electroluminescence measurements will analyze the potential of the SnO_2/organic heterojunction in photovoltaic applications in this chapter. The large band gap of SnO_2 of ca. $3.9\,\mathrm{eV}$ ensures that the inorganic acceptor material is transparent throughout the visible spectrum, again providing the possibility to employ a sample layout in which the photovoltaic heterojunction is illuminated through the inorganic substrate and acceptor layer. The high work function and ionization potential of SnO_2 creates a type II level alignment if brought into contact with most organic semiconductor materials. Consequently, poly(3-hexylthiophene) (P3HT) will again be used as an organic donor material.

The high series resistance of crystalline SnO_2 requires the implementation of a conductive layer behind the undoped acceptor material in a similar way as ZnMgO:Ga was used to enhance the conductivity of ZnMgO. As described in section 3.1.4, antimony can be included into SnO_2 as an n-type dopant without affecting the crystal structure in epitaxial growth. Again, the band gap of a degeneratively doped semiconductor is larger than in the undoped case due to the Burstein-Moss effect. This guarantees that a SnO_2/SnO_2:Sb layer system is transparent for photons up to the band gap energy of undoped SnO_2. The doping density of antimony atoms in the transparent electrode is $2.4 \times 10^{21}\,\mathrm{cm}^{-3}$, the layer then reaches a conductivity of $62\,\Omega^{-1}\mathrm{cm}^{-1}$ which is high enough for fabrication of prototypical devices.

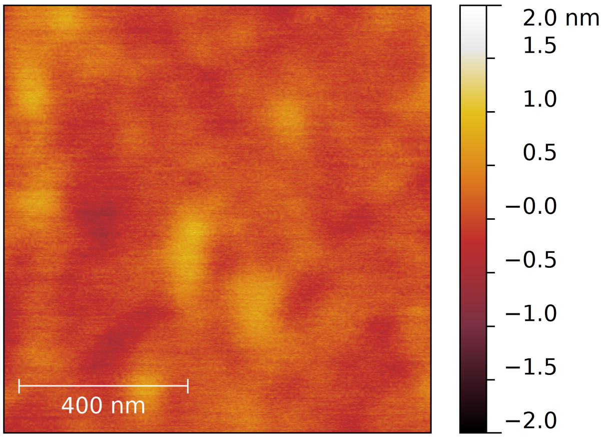

Figure 7.1: AFM picture of a $100\,\mathrm{nm}$ thick $(1\,0\,1)$ polar SnO_2 layer on top of a $200\,\mathrm{nm}$ thick Sb-doped SnO_2 layer of the same crystalline orientation. Both were grown by molecular beam epitaxy on a sapphire substrate.

Figure 7.1 shows an AFM scan of a SnO_2 layer on top of a doped SnO_2:Sb layer, establishing a combination of an intrinsic acceptor layer for photovoltaic function with a transparent conductive electrode ensuring low series resistance for photovoltaic devices. Its low RMS roughness of $0.51\,\mathrm{nm}$ and its high crystallinity with a well-defined $(1\,0\,1)$ surface termination guarantee optimal conditions for quantitative photovoltaic measurements.

7.2 The SnO_2 Surface in UV Photoelectron Spectroscopy

The process of photovoltaic current generation at ZnO/P3HT and ZnMgO/P3HT heterojunctions is clearly dominated by band-to-band transitions of free charge carriers. In none of the samples studied in the previous sections a significant influence of interfacial defect states and trapped carriers can be detected. UV photoemission spectroscopy carried out in section 6.1 shows a steep single onset of the valence band for ZnMgO which is also found on a ZnO interface.[152]

In contrast to this, in photoelectron spectroscopy measurements tin dioxide shows a pronounced additional feature below the band gap (see figure 7.2). While the valence band onset is situated at ca. $3.4\,\mathrm{eV}$, a second onset is formed at ca. $1.75\,\mathrm{eV}$. These states within the band gap can be assigned to Sn_2^+ defects originating from oxygen deficiency in the proximity of the surface.[177]

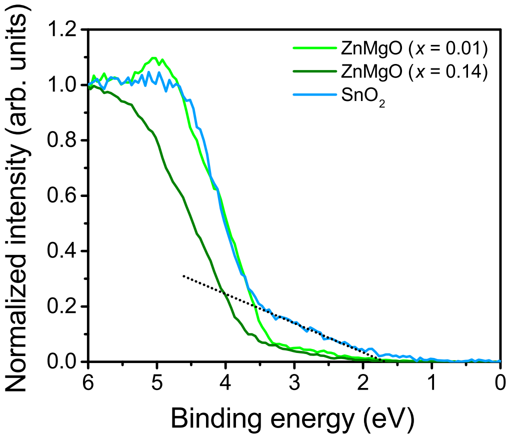

Figure 7.2: Valence band onset of SnO$_2$ compared to Zn$_{1-x}$Mg$_x$O alloys with $x = 0.01$ and $x = 0.14$. The black dashed line shows a pronounced defect emission onset at a binding energy of ca. $1.75\,\mathrm{eV}$ lying below the valence band onset at ca. $3.4\,\mathrm{eV}$.

Calculations based on density-functional theory have shown that several types of oxygen vacancies are stable on a SnO$_2$ $(1\,1\,0)$ surface in thermal equilibrium, leading to a distribution of electronic states between valence band and conduction band.[178] The surface stoichiometry of SnO$_2$ samples can also be manipulated intentionally by sputtering, either with a gas containing O$_2$ to restore the oxidized state or with Ar$^+$ ions to reduce cross-linking between tin atoms, yielding an imbalanced SnO$_{2-x}$ stochiometry and Sn clusters on the surface. Consequently, with an appropriate sputtering gas, the quantity of interfacial defects on a SnO$_2$ surface can be varied.[177, 179]

For the photovoltaic functionality of tin dioxide based solar cells the unoccupied states in proximity of the conduction band are of particular importance. They can be investigated using inverse photoemission spectroscopy (IPES). Measurements performed by *Hollamby et al.* have shown a broad and featureless shoulder of unoccupied states below the conduction band of polycrystalline SnO$_2$.[180]

Consequently, in the investigation of the photovoltaic functionality of a SnO$_2$/P3HT heterojunction, the influence of interfacial defect states will have to be analyzed carefully. A comparison between the behavior of ZnO based heterojunctions and SnO$_2$ based devices is likely to provide knowledge about the role of interfacial defect states onto the photovoltaic device physics of metal-oxide/organic heterojunctions.

7.3 SnO$_2$/P3HT Photovoltaic Devices

Planar photodiodes using the heterojunction of SnO$_2$ and P3HT are fabricated using the same layout as ZnO/P3HT and ZnMgO/P3HT devices in previous chapters. Antimony doping of SnO$_2$ allows the creation of a transparent conductive electrode on which SnO$_2$ can grow epitaxially. Consequently, both photovoltaic measurements and electroluminescence spectroscopy can equally be performed through the sapphire substrate, and produce results which are directly comparable to the ones gained in earlier chapters.

7.3.1 Room Temperature Photovoltaics

Figure 7.3 shows the room temperature J-V characteristic of a photodiode made of SnO_2 and a $240\,\mathrm{nm}$ thick P3HT layer following the recipe described in section 3.4. The rectification ratio between forward and reverse direction of the diode $\beta = \frac{J(+1\,\mathrm{V})}{J(-1\,\mathrm{V})}$ is greater than 10^4. However, after a region of exponentially growing current in forward direction up to ca. $0.25\,\mathrm{V}$, a current roll-off emerges already at low current densities. The combined influence of a space charge region in P3HT and a series resistance in the SnO_2/SnO_2:Sb substrate leads to a significant deviation from exponential growth towards greater forward bias.

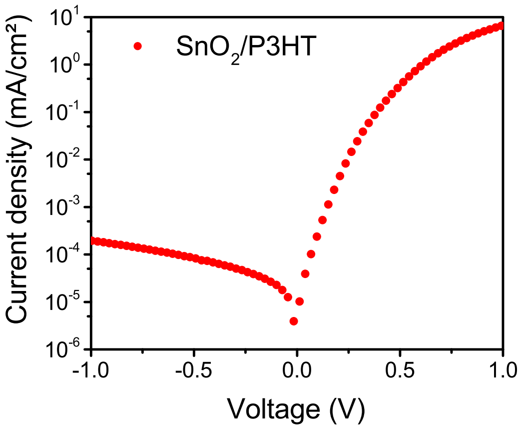

Figure 7.3: J-V characteristic of SnO_2/P3HT diode with $d_{\mathrm{P3HT}} = 240\,\mathrm{nm}$ shows a rectification ratio of more than 10^4. At forward bias greater than $0.25\,\mathrm{V}$ a pronounced current roll-off sets in.

Measurement of the external quantum efficiency at room temperature shows that absorption in both P3HT and SnO_2 produces a photocurrent. Additionally to the inorganic band gap at ca. $3.9\,\mathrm{eV}$, absorption in defect states below the band-gap energy contributes to charge generation and forms a broad feature at ca. $3.45\,\mathrm{eV}$. This can be connected to Sn_2^+ defects originating in the altered stoichiometry in the vicinity of the inorganic surface as visible from UV photoelectron spectroscopy measurements. The spectral feature of photocurrent produced by band-gap absorption in SnO_2 is broader than the corresponding peak in ZnO/P3HT and ZnMgO/P3HT devices. The reason for this is the broadened absorption edge of SnO_2, which is also visible in optical absorption measurements (see figure 3.4).

In time series measurements, no permanent changes in the device function upon UV irradiation are detected. Unlike devices involving ZnO or ZnMgO, the photovoltaic function of a SnO_2/P3HT heterojunction is not decreased by permanent trap state ionization in the inorganic component (see appendix A). Consequently, for all photovoltaic measurements involving simulated sunlight, the AM 1.5G spectrum can be employed without the necessity of additional filters.

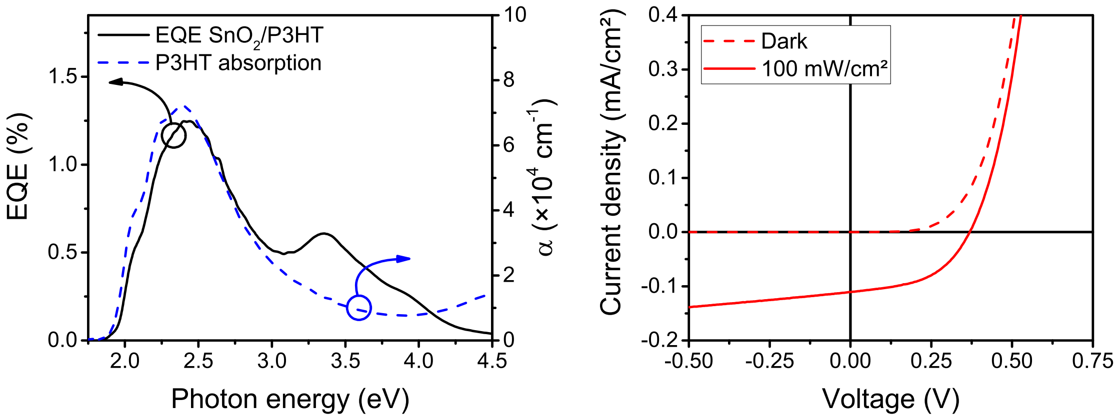

(a) EQE spectrum

(b) J-V characteristics

Figure 7.4: (a) EQE spectrum of a SnO$_2$/P3HT photodiode (black solid line) and optical absorption of a P3HT film (blue dashed line). Absorption both in P3HT as well as bang gap absorption in SnO$_2$ can produce a photocurrent. The broad feature at $3.45\,\mathrm{eV}$ shows that excitons produced by absorption in defects in the SnO$_2$ bulk can be dissociated and contribute to the power conversion. (b) J-V characteristics of a SnO$_2$/P3HT device with $d_{\mathrm{P3HT}} = 240\,\mathrm{nm}$ measured in the dark and under $100\,\mathrm{mW/cm^2}$ AM 1.5G simulated sunlight at room temperature.

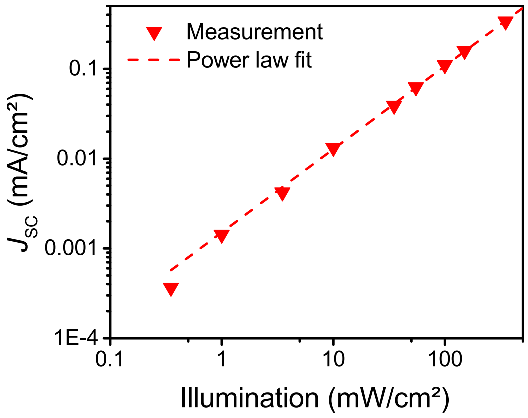

Figure 7.5: Short circuit current of a SnO$_2$/P3HT device with $d_{\mathrm{P3HT}} = 240\,\mathrm{nm}$ at room temperature under AM 1.5G simulated sunlight for light intensities between 0.35 and $350\,\mathrm{mW/cm^2}$ (red triangles) with a linear fit (red dashed line).

Under $100\,\mathrm{mW/cm^2}$ AM 1.5G illumination, a planar SnO$_2$/P3HT photodiode with a P3HT thickness of $240\,\mathrm{nm}$ produces a short circuit current $J_{\mathrm{SC}} = 0.098 \pm 0.014\,\mathrm{mA/cm^2}$ and an open circuit voltage $V_{\mathrm{OC}} = 0.37 \pm 0.10\,\mathrm{V}$ as depicted in figure 7.4(b). The measured fill factor of 49 % ± 1 % shows that charge carrier extraction occurs with a similar efficiency as measured for the devices presented in previous chapters of this work. The total power conversion efficiency under 1 sun illumination amounts to 0.018 % ± 0.003 %. This is superior to the efficiency of a comparable ZnO/P3HT heterojunction, but does not exceed the values obtained from ZnMgO/P3HT devices.

The short circuit current scales almost linearly with illumination density as depicted in figure 7.5. Fitting the relation with a power law yields an exponent of 0.93 for this heterojunction. At higher illumination densities, J_{SC} seems to deviate notably from a strictly linear growth. However, the measurement of illumination densities is not precise and therefore not suitable under practical conditions. All following analysis will base on J_{SC} and V_{OC} which can be measured with higher accuracy.

7.3.2 Temperature-dependent Photovoltaics

As a first step, the transport losses in a SnO_2/P3HT device will be analyzed according to the $J_{SC} - V_{OC}$ method introduced in section 2.3.6.1. In figure 7.6 the measured J_{SC} and V_{OC} values for illumination densities between 0.35 and $350\,\mathrm{mW/cm^2}$ are paired and compared to a J-V characteristic recorded in the dark.

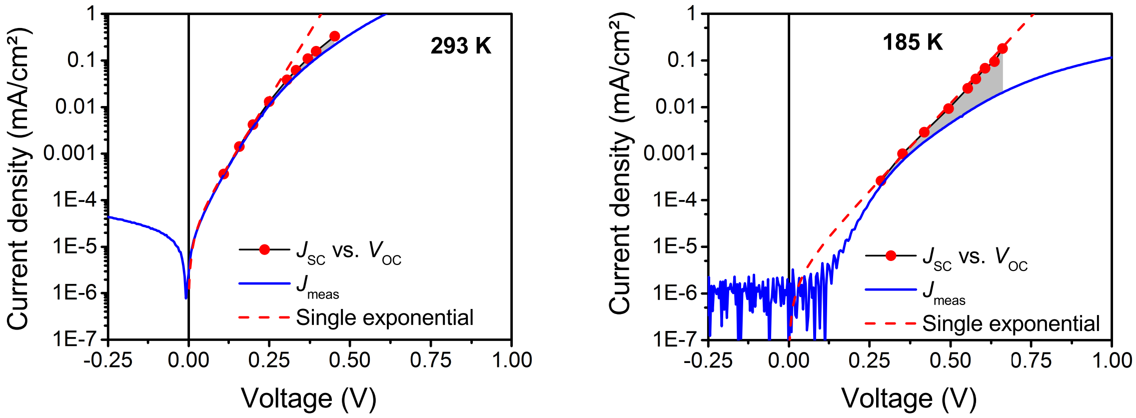

(a) $T = 293\,\mathrm{K}$ (b) $T = 185\,\mathrm{K}$

Figure 7.6: Measured J-V characteristic (blue line) compared to an ideal diode modeled from J_{SC} and V_{OC} values for illumination intensities between $0.35\,\mathrm{mW/cm^2}$ and $350\,\mathrm{mW/cm^2}$ (red circles). Temperatures: (a) $293\,\mathrm{K}$ and (b) $185\,\mathrm{K}$. The dashed red lines show a single exponential fit according to the standard Shockley equation, the grey area shows the transport losses occurring at a forward bias greater than $0.25\,\mathrm{V}$.

At room temperature, the $\ln(J_{SC})$ vs. V_{OC} curve deviates from a linear growth above illumination densities of $10\,\mathrm{mW/cm^2}$ and flattens out towards higher intensities. Consequently, a simple diode fit according to the Shockley equation is not applicable here. The influence of a shunt resistance is not visible here, but a pronounced current roll-off from a series resistance limits the current in forward direction starting from a bias of $0.30\,\mathrm{V}$. Per definition, a series resistance cannot be the reason for the deviation from a single exponential curve as the $J_{SC} - V_{OC}$ method explicitly eliminates such influence. However, dissociation of excitons into free carriers can depend on the density of charges at the heterojunction. Another possibility is a variable distribution between several recombination mechanisms saturating at different current densities.

The J_{SC} vs. V_{OC} curve measured at $185\,\mathrm{K}$ shows the strong influence of a series resistance here, as the J-V curve already deviates from the standard Shockley model at the lowest illumination density of $0.35\,\mathrm{mW/cm^2}$. The whole series of values can be fitted easily with a single exponential curve; however, its slope in logarithmic scale does not correspond to the exponential regime of the J-V curve.

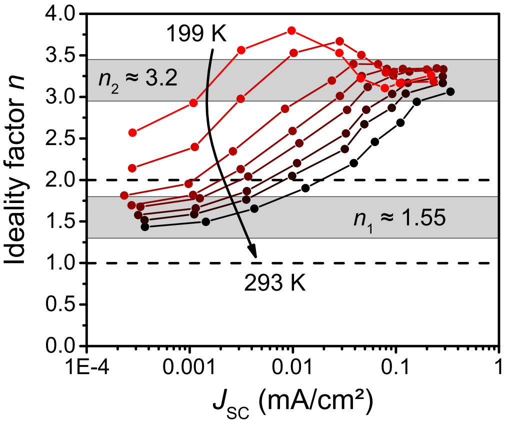

Figure 7.7: Ideality factor n of a SnO_2/P3HT device calculated using the differential method. For low illumination densities, n values group around 1.55, while at higher excitation densities n values of ca. 3.2 emerge.

The knee in the J_{SC} vs. V_{OC} curve leads to the formation of two plateau regions of the ideality factor n plotted over the current density. At lower current, n lies around 1.55 which corresponds to the value for a ZnO/P3HT device as described before. At higher illumination densities, the ideality factor finds a second plateau at ca. 3.2, which is significantly larger than two and does not fit to the common assumption that the ideality factor is simply determined by the predominant recombination mechanism in the device. However, previous studies on organic photovoltaics show a connection between ideality factors up to $n = 3$ and the presence of deep localized states in the interfacial gap.[181, 182]

Figure 7.8(a) shows temperature-dependent J_{SC} vs. V_{OC} data of a SnO_2/P3HT device along with separate exponential fits for the two regimes of low and high illumination densities. The dashed lines in the range between 0.35 and $3.5\,\mathrm{mW/cm^2}$ have a higher slope than the solid lines in the range between 10 and $350\,\mathrm{mW/cm^2}$. Using equation 2.22, the activation energy for the recombination current can be calculated in the same way as performed previously for devices based on ZnO. Due to the significant deviation between the two regimes of low and high excitation densities, this estimate has to be performed separately for these two cases as depicted in figure 7.8(b). It yields a value of $E_{\mathrm{act}}^{\mathrm{low}} = 0.91 \pm 0.04\,\mathrm{eV}$ for low excitation densities and $E_{\mathrm{act}}^{\mathrm{high}} = 1.11 \pm 0.03\,\mathrm{eV}$ under stronger illumination.

The energetic conformation at a hybrid heterojunction is not a fixed parameter. It highly depends on applied bias, device temperature and on the carrier density induced by illumination. The results gained in this section show the variable behavior of a SnO_2/P3HT heterojunction under different illumination densities and give a hint towards the involvement of several recombination processes. For practical purposes in photovoltaics, the relevant regime of device physics is

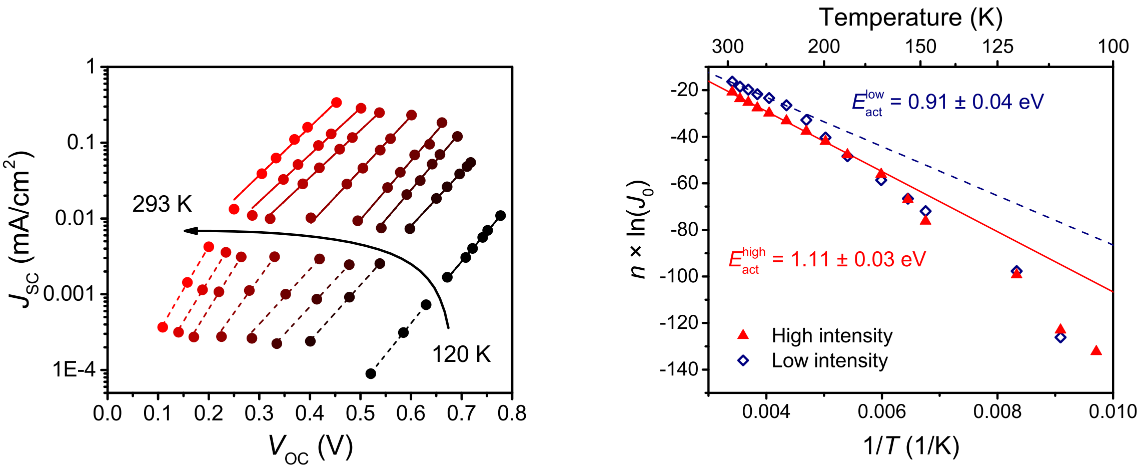

(a) J_{SC} vs. V_{OC}

(b) Estimation of the hybrid energy gap

Figure 7.8: (a) $J_{SC} - V_{OC}$ curves for temperatures between $120\,\mathrm{K}$ and $293\,\mathrm{K}$ measured at illumination densities between 0.35 and $350\,\mathrm{mW/cm^2}$. The dashed lines give data fits in the regime of low illumination density between 0.35 and $3.5\,\mathrm{mW/cm^2}$, the fits for the regime of higher intensities between 10 and $350\,\mathrm{mW/cm^2}$ are shown as solid lines. (b) A modified Arrhenius plot to determine the activation energy E_{act} for recombination current. The analysis in the regime of high illumination intensities yields an activation energy of $E_{act}^{high} = 1.11 \pm 0.03\,\mathrm{eV}$, while the calculated value under low excitation E_{act}^{low} is smaller by ca. $200\,\mathrm{meV}$.

situated around an illumination density of 1 sun. Consequently, this analysis will focus on data gained under AM 1.5G illumination with excitation densities of $10\,\mathrm{mW/cm^2}$ and more. Data for the low-excitation regime between 0.35 and $3.5\,\mathrm{mW/cm^2}$ is only given for the sake of completeness without deeper interpretation.

Figure 7.9 shows temperature-dependent V_{OC} values measured under AM 1.5G simulated sunlight for intensities between 0.35 and $350\,\mathrm{mW/cm^2}$ together with linear extrapolations from the region between $200\,\mathrm{K}$ and room temperature to $T \rightarrow 0$. Similar to the results for a ZnO/P3HT diode shown in figure 5.10, the extrapolated $V_{OC,max}$ value depends on illumination density. This effect has been attributed to the influence of a shunt resistance in the device.[151]

At temperatures below $120\,\mathrm{K}$, the V_{OC} vs. T curve bends upward and produces larger $V_{OC,max}$ values than expected from the initial extrapolation slope. A similar behavior has been observed in planar organic 6T/C_{60} devices.[183] An analytical expression describing the recombination current in the presence of an exponential density of trap states below the conduction band of the donor material as proposed by *Hawks et. al.*[182] is able to reproduce the shape of the V_{OC} vs. T curve under the assumption of a constant photocurrent.[183] This gives another hint towards the influence of interfacial carrier traps onto the device physics of tin-oxide based photovoltaic devices.

The average of extrapolated $V_{OC,max}$ values for illumination densities above $35\,\mathrm{mW/cm^2}$ is $1.00\,\mathrm{V}$. Taking into account the contribution of non-radiative recombination processses as described in section 6.4.2, an HCTS transition energy of $E_{HCTS} = qV_{OC,max} - E_{nr} = 0.92\,\mathrm{eV}$ is

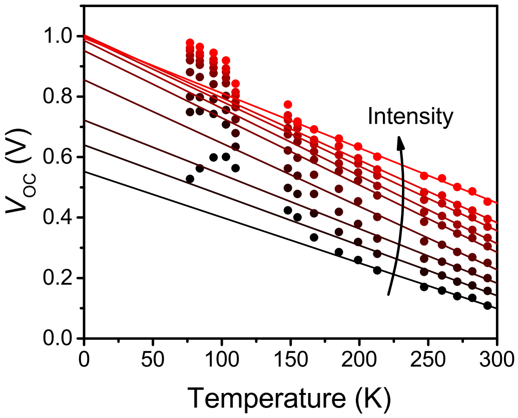

Figure 7.9: Open circuit voltage of a SnO$_2$/P3HT device measured at temperatures between $77\,\mathrm{K}$ and $293\,\mathrm{K}$ and AM 1.5G simulated sunlight illumination with intensities between 0.35 and $350\,\mathrm{mW/cm^2}$. Data fits are linear extrapolations of data measured between $200\,\mathrm{K}$ and room temperature. A $V_{\mathrm{OC,max}}$ value of $1.00\,\mathrm{V}$ is obtained from converging slopes at illumination densities above $35\,\mathrm{mW/cm^2}$.

obtained. $E_{\mathrm{nr}} = 77\,\mathrm{meV}$ represents the activation energy of non-radiative recombination as obtained from temperature-dependent EL measurements in section 7.4. As the upward bending of the V_{OC} vs. T curve is not included into the analysis, the E_{HCTS} value calculated here only stands as a rough estimate. In particular, the HCTS transition energy might be higher by $100\,\mathrm{meV}$ or even more, depending on the way in which the shape of the curve is included into a more detailed extrapolation model.

7.3.3 Temperature-dependent Charge Separation

The external quantum efficiency of a SnO$_2$/P3HT heterojunction measured at room temperature is larger than the one for ZnO/P3HT and comparable to the one for ZnMgO/P3HT devices with low magnesium contents. In the following, the temperature dependence of EQE will be investigated in order to gain insight into the charge separation process at a SnO$_2$/P3HT interface.

The following analysis will be performed using the four step model derived for the charge generation process in ZnMgO/P3HT in section 6.4.1. At very low temperature below $100\,\mathrm{K}$ the charge extraction process is limited due to insufficient carrier mobility in P3HT, which causes an s-shaped J-V characteristic under illumination[174] (data not shown here). Above $100\,\mathrm{K}$, quantum efficiency increases with temperature until it reaches a maximum at ca. $150\,\mathrm{K}$. Up to room temperature, it slightly drops by ca. $20\,\%$.

The data can be fitted nicely to the model derived in section 6.4.1 and yields the values $E_{\mathrm{A}} = 50 \pm 6\,\mathrm{meV}$ and $E_{\mathrm{rec}} - E_{\mathrm{diss}} = 78 \pm 8\,\mathrm{meV}$. This shows that the mechanism of charge separation and non-radiative losses follows the same model as previously derived for the ZnO/P3HT and ZnMgO/P3HT heterojunctions. The possible presence of interfacial trap states found on SnO$_2$ does not affect the thermal excitation behavior of the charge separation process, which is independent of the choice of inorganic acceptor materials. Comparing the value for $E_{\mathrm{rec}} - E_{\mathrm{diss}}$

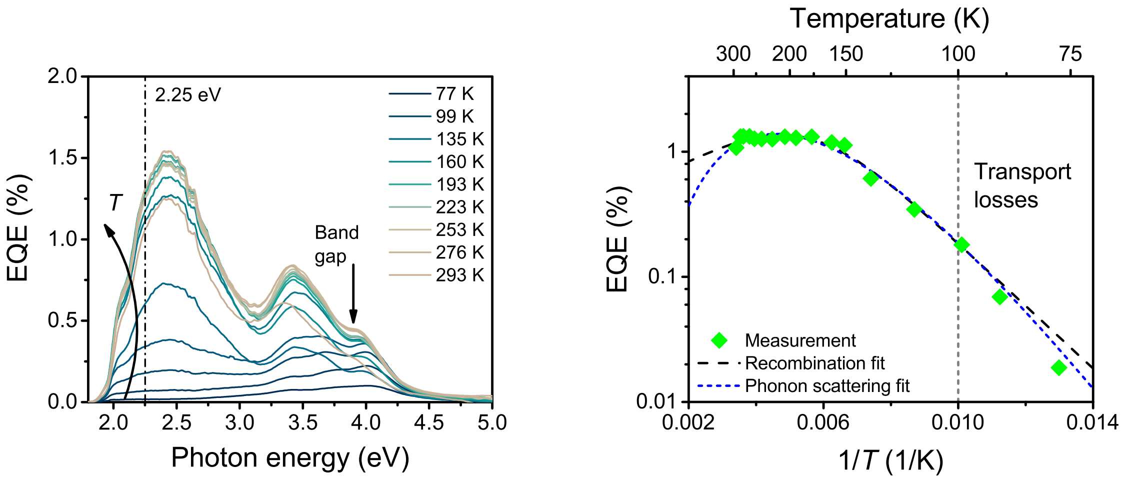

(a) Temperature-dependent EQE spectra

(b) Arrhenius plot for EQE$(2.25\,\mathrm{eV})$

Figure 7.10: a) External quantum efficiency for the charge generation in a SnO_2/P3HT device with $d_{\mathrm{P3HT}} = 240\,\mathrm{nm}$ measured at temperatures between $77\,\mathrm{K}$ and room temperature. b) Arrhenius plot for the external quantum efficiency at a photon energy of $2.25\,\mathrm{eV}$ along with the two fit models as described in the text.

to the thermal activation energy for non-radiative recombination in EL measurements, it can be concluded that the temperature-dependence of HCTS dissociation is very small. Consequently, similarly to the previous results no significant thermal activation energy of HCTS dissociation can be detected.

7.4 Electroluminescence of SnO_2/P3HT Heterojunctions

Applying an external bias to a SnO_2/P3HT hybrid diode produces an electroluminescence signal. Similar to the previously measured spectra it consists of a combination of singlet exciton recombination in P3HT mostly in the visible red and a broad feature in the near infrared. The latter can again be assigned to recombination of interfacial charge transfer states (see figure 7.11). The ratio between P3HT and HCTS signal varies with temperature and applied bias.

Taking a closer look at the EL spectrum in the near-infrared reveals that the HCTS emission is separated into two distinguishable features. At room temperature, one broad peak is situated at ca. $0.9\,\mathrm{eV}$. At its edge towards lower energy, a second emission feature is adjoined, reaching further into the IR, beyond the detection range of the spectrometer used in this experiment. Upon variable applied bias, these two components of the HCTS emission behave differently, as depicted in figure 7.12(a). The emission at lower photon energy remains almost unchanged when increasing the applied bias from $4.8\,\mathrm{V}$ to $6.6\,\mathrm{V}$. At the same time a Gaussian shaped peak emerges from its shoulder, growing in intensity and shifting towards higher energies. The P3HT bulk emission simultaneously increases with higher voltage (not shown here).

The spectral shift of the Gaussian-shaped broad peak follows a proportionality towards $F^{\frac{2}{3}}$ with

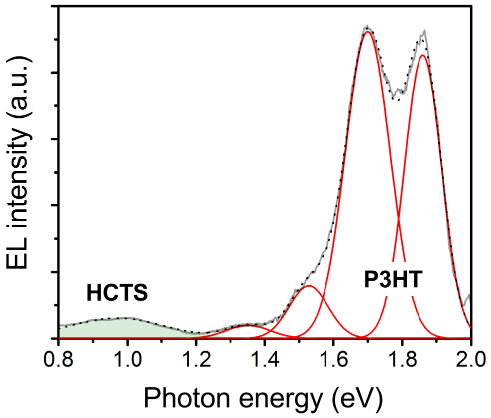

Figure 7.11: Full electroluminescence spectrum of a SnO_2/P3HT photodiode with $d_{\mathrm{P3HT}} = 280\,\mathrm{nm}$ for an applied bias of $13\,\mathrm{V}$, measured at $190\,\mathrm{K}$. Features of P3HT bulk luminescence and HCTS recombination are clearly separated from each other.

F being the electric field in the P3HT layer (see figure 7.12(b)). Consequently, it behaves in the same way as the band-to-band recombination of free carriers forming an HCTS as observed in diodes involving ZnO and ZnMgO in section 6.3.1 and can thus be connected to an identical process in the present material system. The slope in figure 7.12(b) is almost identical to the progression reported for ZnMgO (see figure 6.12(a)) and yields the same effective hole mass in P3HT $m^* = 0.05 \cdot m_{\mathrm{e}}$. This confirms that the model of a field dependent electroluminescence shift holds true, independent from the choice of inorganic acceptor material. Furthermore, delocalization of electron and hole in an HCTS are intrinsic features of all comparable hybrid inorganic-organic interfaces.

The low energy shoulder of the near-IR peak shows a different saturation behavior. It appears to be saturated already at the lowest applied bias of $4.8\,\mathrm{V}$, and its share of the spectrum continuously drops towards higher applied bias. Due to its spectral position at lower energies than the HCTS it is likely that this feature is produced by trap-assisted recombination of holes in P3HT and localized electrons in SnO_2 caught in interfacial defect states. The presence of these states was already indicated in several other measurements presented in this chapter. Figure 7.13 schematically depicts both possible recombination processes. Bimolecular recombination of free carriers forming an HCTS is marked as a blue arrow, while trap-assisted processes are represented by a black arrow. Localized trap states are only filled with carriers below the Fermi level, which is situated in direct proximity of the SiO_2 conduction band. Consequently, emission of trap-assisted recombination is expected to be situated in the near infrared at lower photon energies than the bimolecular HCTS recombination.

From the recorded spectra it is not possible to determine if the low energy shoulder of the peak follows the same field-dependent energetic shift as the bimolecular HCTS recombination. As it cannot be clearly isolated from the band-to-band contribution to the EL signal, even the spectral shape of this electroluminescence component is not accessible from the present data. At higher applied bias, the intensity of the Gaussian-shaped EL feature significantly grows and finally dominates the spectrum, giving it a similar appearance as all the previously measured HCTS

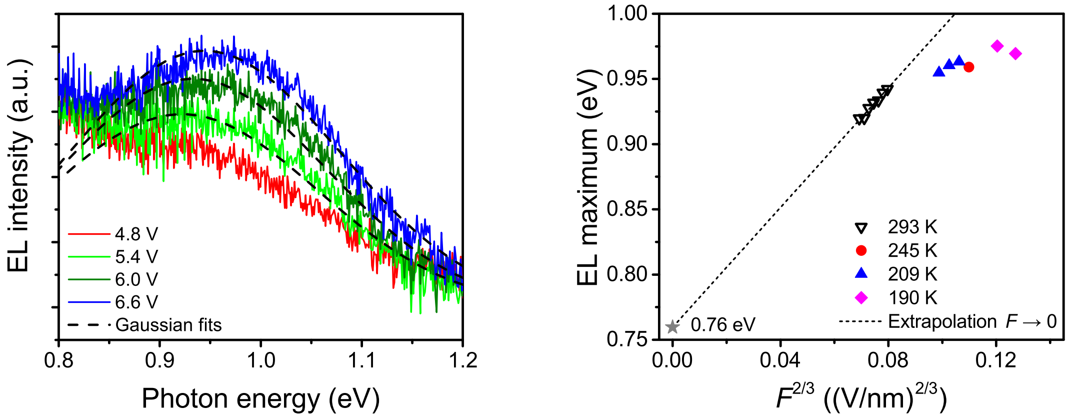

(a) HCTS EL peak and trap-related luminescence

(b) HCTS EL peak positions

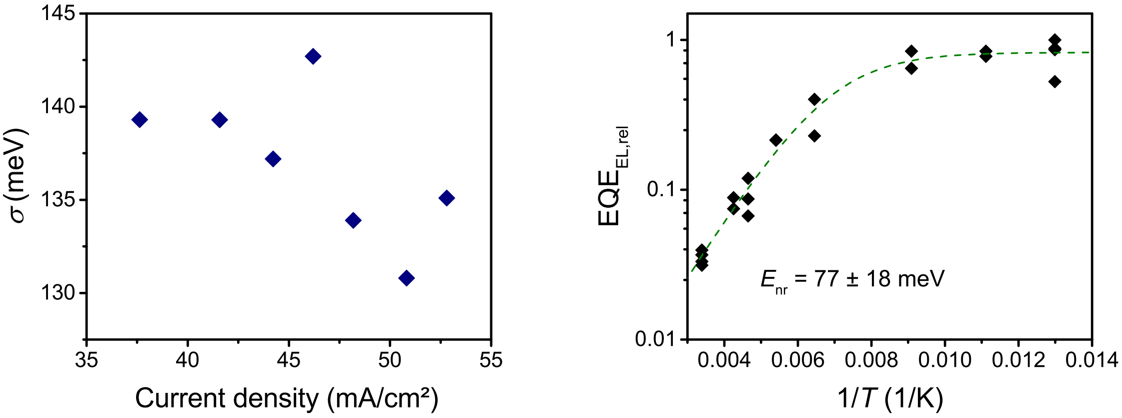

(c) Variance σ of HCTS EL

(d) $\mathrm{EQE}_{\mathrm{EL,rel}}(T)$

Figure 7.12: Electroluminescence of a $\mathrm{SnO_2}$/P3HT photodiode with $d_{\mathrm{P3HT}} = 280\,\mathrm{nm}$ (a) Room temperature EL in the near-IR spectral range for applied bias between $4.8\,\mathrm{V}$ and $6.6\,\mathrm{V}$ shows a constant feature at lower energies and an emerging Gaussian-shaped peak. Dashed lines are fits to the Gaussian-shaped peak. (b) Spectral positions of the band-to-band EL maxima measured at different temperatures. From the room temperature data, a value of $0.76 \pm 0.02\,\mathrm{eV}$ can be extrapolated for $F \rightarrow 0$. (c) The spectral variance of isolated HCTS band-to-band recombination peak does not increase with current density. (d) Similarly to ZnMgO/P3HT heterojunctions, the quantum yield of HCTS recombination at a $\mathrm{SnO_2}$/P3HT decreases by almost two orders of magnitude between $77\,\mathrm{K}$ and room temperature. A fit involving a thermally activated non-radiative loss process yields an activation energy of $E_{\mathrm{nr}} = 77 \pm 18\,\mathrm{meV}$.

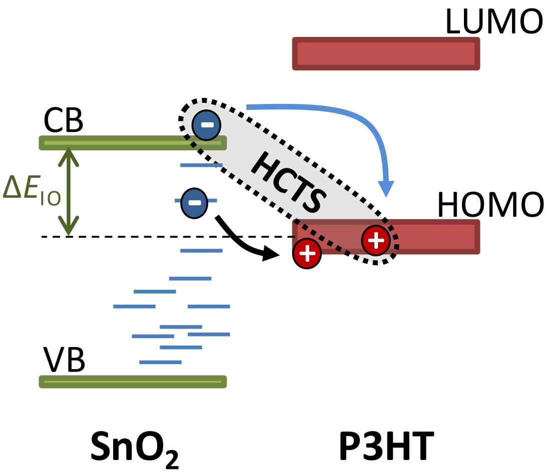

Figure 7.13: If carrier recombination involving trapped electrons (black arrow) is a relevant process in a hybrid device, it would introduce an additional mechanism in addition to the bimolecular HCTS recombination (blue arrow) of free carriers in the P3HT HOMO and SnO$_2$ conduction band. Its transition energy would be smaller than the one of direct band-to-band recombination.

luminescence spectra for other diodes without a significant contribution from interfacial traps.

The variance σ of the Gaussian EL peak assigned to band-to-band recombination of free carriers in an HCTS does not depend on current density as depicted in figure 7.12(c). Consequently, its spectral shift towards higher energies is not a result of a state-filling process involving localized trap states. The average peak width at room temperature is $\sigma = 137 \pm 60\,\mathrm{meV}$. Extrapolating the EL peak position for $F \to 0$ yields a peak energy for a hypothetical field-free HCTS recombination of $0.76 \pm 0.02\,\mathrm{eV}$. EL maxima at lower temperatures do not appear on the same slope as the room temperature measurements. They are shifted towards lower transition energies instead. A possible reason for this is an increased series resistance in the device due to lower conductivity of SnO$_2$ and SnO$_2$:Sb. If the voltage drop over the inorganic bulk SnO$_2$ cannot be neglected anymore, the electric field at the heterojunction is being reduced.

Figure 7.12(d) shows the relative EL quantum yield

$$\mathrm{EQE}_{\mathrm{EL,rel}}(T) = \frac{\mathrm{EQE}_{\mathrm{EL}}(T)}{\mathrm{EQE}_{\mathrm{EL}}(77\,\mathrm{K})}. \tag{7.1}$$

as the quotient of EL quantum efficiencies at $77\,\mathrm{K}$ and room temperature. Approaching room temperature, it drops by almost two orders of magnitude. Analogous to the analysis performed on ZnMgO/P3HT heterojunctions, measured data can be fitted to a model involving a thermally activated non-radiative recombination process given in equation 6.7. A similar activation energy of $E_{\mathrm{nr}} = 77 \pm 18\,\mathrm{meV}$ is determined from the fit curve, indicating that non-radiative loss processes of metal-oxide/P3HT photodiodes follow a common mechanism which is not related to a specific inorganic material. This value can also be used for correction of the temperature determination of the HCTS transition energy from temperature-dependent measurements of V_{OC}

in section 7.3.2.

7.5 Discussion of Results

7.5.1 HCTS at a SnO_2/P3HT Heterojunction

Combined analysis of photovoltaic measurements and electroluminescence spectroscopy from planar SnO_2/P3HT photodiodes reveals a mechanism of charge generation, which is very similar to the processes in the previously studied systems involving ZnO and ZnMgO. Light absorption in both donor and acceptor can contribute to a photocurrent. Prior to full charge separation, electron and hole remain tied to each other at the interface in an HCTS.

Temperature-dependent measurements of photovoltaic charge generation show that the 4-step process including a thermally activated loss channel, which was derived before in section 6.4.1, holds true for SnO_2/P3HT heterojunctions as well. It is able to reproduce EQE data over a range between $100\,\mathrm{K}$ and room temperature. From the activation energies, which serve as fit parameters, can be deduced that the binding energy of electron and hole in an HCTS is as small as a couple of meV. Its dissociation does not show a detectable thermal activation. Such a model of strongly delocalized electron and hole in an HCTS leading to a small binding energy is consistent to the field-dependency of the electroluminescence signal produced by band-to-band recombination in a SnO_2/P3HT diode.

Extraction of the hypothetical field-free EL maximum yields a value of $0.76\,\mathrm{eV}$. The peak width of $\sigma = 137\,\mathrm{meV}$ is very similar to values measured in previous chapters. The interpolated HCTS luminescence maximum for $F \to 0$ is situated $\frac{\sigma^2}{2k_\mathrm{B}T} \approx 350\,\mathrm{meV}$ below the HCTS transition energy $E_\mathrm{act}^\mathrm{high} = 1.11\,\mathrm{eV}$ calculated from V_OC and J_SC data recorded at AM 1.5G illumination with light intensities around 1 sun. According to the framework established in section 2.3.3, this confirms that the measured Gaussian peak originates from bimolecular recombination of free carriers forming an HCTS. Any emission spectrally located further in the infrared is then likely to originate from carriers situated in localized defects.

Figure 7.13 shows the interface formed by SnO_2 and P3HT including the position of potential interfacial defect states. Although the analyzed measurements do not provide indisputable evidence in favor of their existence, a couple of indications can be found both in literature and experimental data. One of these hints is an additional feature in electroluminescence spectra, which is situated on the low-energy shoulder of the HCTS peak and reaches further into the infrared. Voltage-dependent measurements show that it tends to saturate at low carrier density and loses its significance under higher forward bias. Such a behavior can be expected for recombination in localized sub-bandgap defects due to state-filling effects.

Other hints towards the existence of interfacial defect states are given by the strong presence of occupied electronic states between valence and conduction band as visible in UV photoelectron spectroscopy as well as by the appearance of an additional feature in photovoltaic EQE measurements at a photon energy of ca. $3.4\,\mathrm{eV}$. The overall influence of trapped carriers to power generation can, however, be considered small. In spite of this, their role in loss processes and their influence on interface energetics has to be studied in more detail. For a definite answer to the question if carriers at a SnO_2/P3HT heterojunction can recombine in localized trap states or not, additional experiments are necessary. Inverse photoelectron spectroscopy of the SnO_2 $(1\,0\,1)$ surface might show the presence of unoccupied electron states below the inorganic band gap of the interface. Careful EQE measurements in the infrared can show photocurrent generation from direct absorption in HCTS and reveal a contribution of defect states at even lower photon energies. Electroluminescence spectroscopy reaching further into the infrared can reveal the spectral structure of the second feature in the EL spectra and possibly give hints towards its origin. Another promising route is a detailed analysis of the band-tail recombination processes in the diode by studying the behavior of the ideality factor following the model proposed by *Hawks et. al.* for organic systems.[182]

7.5.2 Photovoltaic Losses

A detailed analysis of photovoltaic losses in a SnO_2/P3HT heterojunction requires an appropriate analysis of interface energetics. Photovoltaic measurements and electroluminescence spectroscopy provide extensive experimental data, thus a combined analysis of the results gained in both procedures will yield a suitable model for estimating the photovoltaic performance and losses of SnO_2/P3HT devices. As the carrier recombination process at the interface and particularly the role of localized carrier traps is not fully understood so far, this analysis is restricted to a rough estimate and a quantitative comparison to the other material systems investigated in the previous sections.

For an estimate of the photovoltaic potential of a SnO_2/P3HT heterojunction, the HCTS transition energy is compared to the actual photovoltage output of a device. In section 7.3.2, E_{HCTS} is determined in two different ways. Firstly, it is calculated as the activation energy for the recombination current according to temperature-dependent measurements of V_{OC} and J_{SC}. As a second approach, it is extrapolated as an intersection point from V_{OC} vs. T curves.

The calculation of the activation energy E_{act} yields different values, depending on illumination density. Two regimes of low and high excitation can be separated from each other, resulting in the two activation energies $E_{\mathrm{act}}^{\mathrm{low}} = 0.91 \pm 0.04\,\mathrm{eV}$ and $E_{\mathrm{act}}^{\mathrm{high}} = 1.11 \pm 0.03\,\mathrm{eV}$. Future research is likely to establish a broader understanding of the underlying physical processes and might find an analytical model, which gives a complete description of the heterojunction under all external conditions. As the diode behavior under 1 sun illumination is most relevant for practical photovoltaic applications, only the latter value is chosen here for a quantitative analysis of photovoltaic performance and losses.

The HCTS transition energy obtained from the maximal open circuit voltage $qV_{\mathrm{OC,max}} - E_{\mathrm{nr}} = 0.93\,\mathrm{eV}$ is determined from temperature-dependent V_{OC} measurements. It is almost $200\,\mathrm{meV}$ smaller than E_{act}. This big deviation might be a consequence of the simple extrapolation model, which does not account for the steep increase of the V_{OC} below $120\,\mathrm{K}$ (see figure 7.9). Indeed, the position of the HCTS electroluminescence maximum extrapolated to zero field at $0.76 \pm 0.02\,\mathrm{eV}$ makes it appear plausible, that the real HCTS transition energy is greater than $0.93\,\mathrm{eV}$.

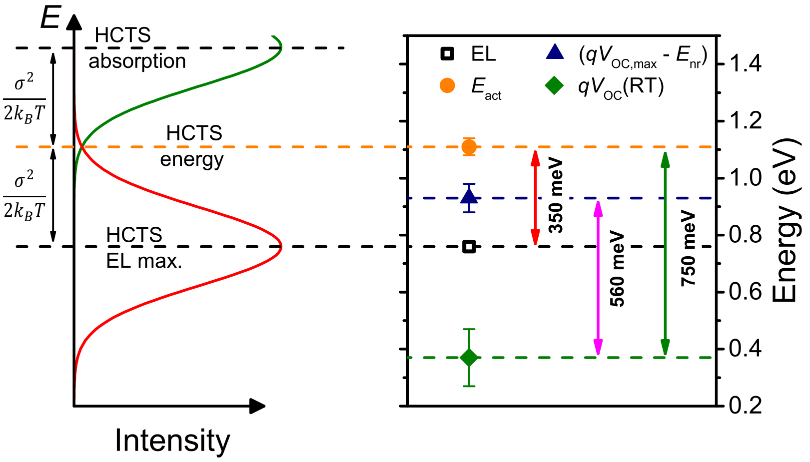

Figure 7.14: Left: Distribution of transition energies in HCTS emission and direct HCTS absorption (not measured) are mirror-symmetrical to the HCTS transition energy E_{HCTS} according to Marcus theory. Right: HCTS transition energy E_{HCTS} calculated from V_{OC}-J_{SC} measurements (orange circle), Energetic position of HCTS electroluminescence extrapolated to $F \rightarrow 0$ (black square), $(qV_{\mathrm{OC,\,max}} - E_{\mathrm{nr}})$ (blue triangle) and qV_{OC} at room temperature (green diamond). The red arrow shows the energetic difference between HCTS transition energy and its emission maximum of $350\,\mathrm{meV}$ which equals $\frac{\sigma^2}{2k_{\mathrm{B}}T}$ as predicted for bimolecular band-to-band transition of free carriers. The blue and green arrows mark the photovoltaic losses at room temperature compared to the different E_{HCTS} values.

In figure 7.14 the energetic situation at a SnO_2/P3HT heterojunction is depicted schematically. On the left side the relation between HCTS absorption and emission defining its transition energy is shown, as postulated by Marcus theory (see section 2.3.3). This model gives a good description of the behavior of ZnMgO/P3HT devices as observed in previous chapters. In the diagram on the right side of the figure all quantities necessary for calculating interfacial photovoltage losses are shown: E_{act} is represented by an orange circle, $qV_{\mathrm{OC,max}} - E_{\mathrm{nr}}$ is marked as a blue triangle, the extrapolated HCTS electroluminescence maximum at $F \rightarrow 0$ is shown as a black square and the V_{OC} at room temperature is marked as a green diamond.

Both E_{HCTS} values derived here can be used for a rough estimate of the photovoltage losses in planar SnO_2/P3HT photovoltaic devices. As the open circuit voltage at room temperature is only $0.37 \pm 0.10\,\mathrm{V}$, the photovoltage losses inflicted by interfacial carrier recombination amount to a value between $560\,\mathrm{mV}$ and $750\,\mathrm{mV}$. Consequently, the quantity of losses is similar to those of a ZnMgO/P3HT device as analyzed in section 6.5.1. Common organic systems like P3HT:PCBM have smaller photovoltage losses between $400\,\mathrm{mV}$ and $550\,\mathrm{mV}$.[25, 28, 184]

Consequently, the rapid relaxation of carriers from excited states in organic adsorbates to the SnO_2 conduction band[16] does not bring a benefit in solar cells with the material combination SnO_2/P3HT. On the contrary, this heterojunction produces high photovoltage losses, which lead to an open circuit voltage at room temperature of only $370\,\mathrm{mV}$, which is the smallest value measured in this work and not suitable for application in photovoltaic devices on a larger scale.

Chapter 8

Results and Discussion

In the experimental studies contributing to this work, three different material systems have been studied extensively in order to gain knowledge about metal-oxide/organic heterojunctions and their potential for photovoltaic devices. Hereby, the focus of research is set on understanding the fundamental physical processes involved in the charge separation process at the interface. From experimental results taken from planar photodiode devices involving the three heterojunctions ZnO/P3HT, ZnMgO/P3HT and SnO_2/P3HT a remarkable number of parallelisms can be deduced which provide a framework for a fundamental understanding of metal-oxide/organic heterojunctions in general. Careful analysis also reveals a couple of differences which have to be taken into account in the evaluation of experimental results.

8.1 Hybrid Inorganic-Organic Photovoltaics

8.1.1 Device Performance of Metal-Oxide/Organic Heterojunctions

All diode structures involving one of the three metal-oxide acceptor materials were able to produce a photocurrent upon light absorption. A model system for comparison of device performances is given by a series of planar photodiodes combining a $240\,\mathrm{nm}$ thick P3HT layer with one of the following inorganic acceptor materials: ZnO, $Zn_{0.99}Mg_{0.01}O$, $Zn_{0.95}Mg_{0.05}O$, $Zn_{0.86}Mg_{0.14}O$ and SnO_2. Figure 8.1 shows J-V characteristics of all model devices both in the dark and under 1 sun AM 1.5G illumination. All photovoltaic parameters are shown in table 8.1.

Regarding material systems involving ZnMgO, it can be concluded that increasing the Mg percentage in the acceptor does not improve the performance of a photovoltaic device as previously reported by *Olson et. al.*[146] It only seems to shift weights between V_{OC} and J_{SC}. At higher Mg contents a significant drop of conversion efficiency can be observed.

SnO_2 as acceptor material produces a power conversion efficiency which is similar to the values measured for ZnMgO at low Mg contents. Its photocurrent is among the highest ones measured

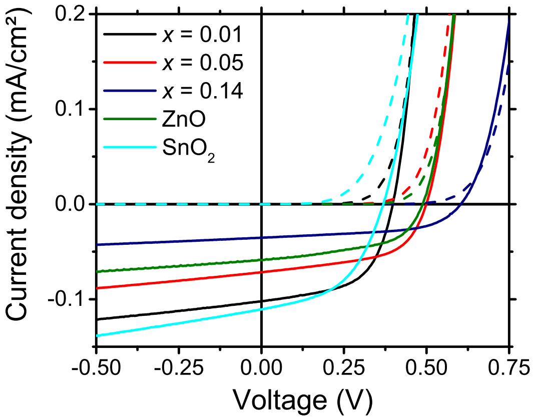

Figure 8.1: Characteristics in the dark (dashed lines) and under $100\,\mathrm{mW/cm^2}$ AM1.5 simulated sunlight (solid lines) taken from planar photodiodes with a $240\,\mathrm{nm}$ thick P3HT donor layer and the following acceptor materials: ZnO (green), $\mathrm{Zn_{0.99}Mg_{0.01}O}$ (black), $\mathrm{Zn_{0.95}Mg_{0.05}O}$ (red), $\mathrm{Zn_{0.86}Mg_{0.14}O}$ (dark blue) and SnO_2 (light blue).

in this work, but its low V_{OC} nevertheless indicates severe recombination losses.

Surprisingly, the open circuit voltage of ZnO/P3HT devices is higher than values of $\mathrm{Zn_{0.99}Mg_{0.01}O}$/P3HT diodes. This, however, occurs at the cost of a significantly smaller photocurrent, with its power conversion efficiency being about 40 % smaller than the one of ZnMgO/P3HT diodes with Mg contents of 1 % and 5 %. This irregularity will be discussed in more detail in the next section.

Table 8.1: Performance parameters for all photovoltaic model devices presented in this work.

Heterojunction	V_{OC} (V)	J_{SC} (mA/cm^2)	Fill factor	PCE
ZnO/P3HT	0.46 ± 0.03	0.058 ± 0.004	52 % ± 2 %	0.014 % ± 0.002 %
$\mathrm{Zn_{0.99}Mg_{0.01}O}$/P3HT	0.40 ± 0.01	0.098 ± 0.005	56 % ± 1 %	0.022 % ± 0.002 %
$\mathrm{Zn_{0.95}Mg_{0.05}O}$/P3HT	0.51 ± 0.01	0.075 ± 0.009	52 % ± 4 %	0.020 % ± 0.001 %
$\mathrm{Zn_{0.86}Mg_{0.14}O}$/P3HT	0.60 ± 0.01	0.034 ± 0.001	54 % ± 2 %	0.011 % ± 0.001 %
SnO_2/P3HT	0.37 ± 0.10	0.098 ± 0.014	49 % ± 1 %	0.018 % ± 0.003 %

8.1.2 $\mathrm{Zn_1Mg_0O}$ = ZnO?

Alloying ZnO with MgO to ZnMgO allows gradual tuning of its electrical and optical properties, which can nicely be monitored by the behavior of ZnMgO/P3HT photodiodes. Between Mg contents of 1 % and 14 % the HCTS transition energy is connected linearly to the optical band gap of the acceptor material. As a consequence, photovoltaic parameters and EL emission maxima equally follow the same progression. Values for V_{OC} and HCTS EL peaks are well predictable on the basis of experimental data, once the Mg content in a planar ZnMgO/P3HT device is known.

On this background, it comes rather as a surprise that the behavior of a ZnO/P3HT diode does not fit into this scheme. According to analysis of ZnMgO/P3HT diodes in chapter 6, its V_{OC} under $100\,\mathrm{mW/cm^2}$ AM 1.5G illumination at room temperature could be expected to be around $0.38\,\mathrm{V}$ (see e.g. figure 6.25). Its actual value of $0.46\,\mathrm{V}$ is significantly larger than this. At the same time, its J_{SC} is smaller than expected by at least $40\,\%$, which leads to a severely reduced power conversion efficiency (see table 8.1). Although the Mg content in the most similar ZnMgO diode is only $x = 0.01$, a clear qualitative difference between both devices can be detected.

Taking into account the whole set of temperature-dependent photovoltaic data reveals the strong similarity between all ZnMgO/P3HT diodes regardless of their Mg content (see figure 8.2(a)). The slope of the linear fit in the range between $200\,\mathrm{K}$ and room temperature is almost identical, meaning that following equation 6.15, the quotient between photocurrent and recombination losses is the same for all ZnMgO/P3HT devices that were studied in this work. This, however, does not apply for a heterojunction of pristine ZnO and P3HT. Whereas its V_{OC} at room temperature is bigger than the value measured from a $\mathrm{Zn_{0.99}Mg_{0.01}O}$/P3HT diode, its extrapolation towards $0\,\mathrm{K}$ is significantly less steep and yields a $V_{\mathrm{OC,max}}$ value of $0.98\,\mathrm{V}$, which is even slightly below the expected range.

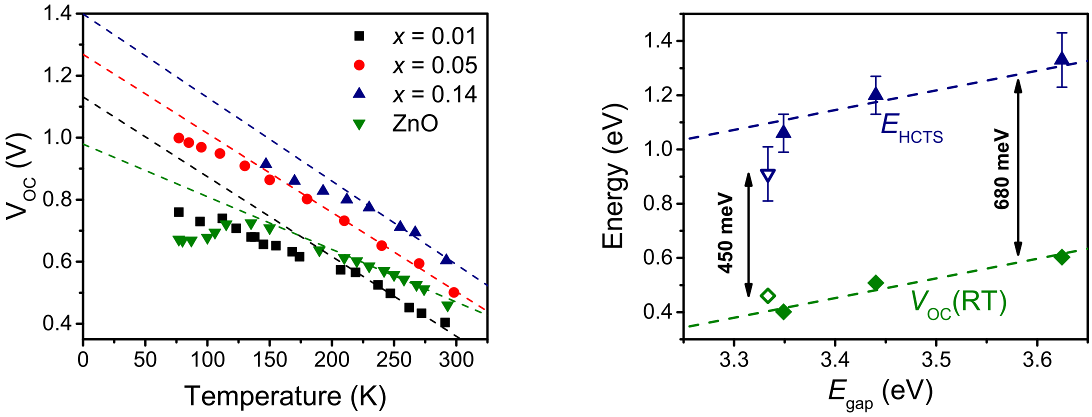

(a) V_{OC} vs. T

(b) Photovoltage losses

Figure 8.2: (a) Temperature-dependent V_{OC} measurements under $100\,\mathrm{mW/cm^2}$ AM 1.5G illumination from $\mathrm{Zn_{1-x}Mg_xO}$/P3HT diodes with Mg contents of $x = 0.01$, $x = 0.05$ and $x = 0.14$ and a ZnO/P3HT diode. P3HT thickness is $240\,\mathrm{nm}$ for all devices. Dashed lines show extrapolations from the region between $200\,\mathrm{K}$ and room temperature towards $T \rightarrow 0$ for determination of $V_{\mathrm{OC,max}}$. (b) HCTS transition energies obtained from temperature-dependent V_{OC} measurements from $\mathrm{Zn_{1-x}Mg_xO}$/P3HT diodes with Mg contents of $x = 0.01$, $x = 0.05$ and $x = 0.14$ (filled triangles) and a ZnO/P3HT diode (open triangle) plotted with respect to the optical gap of the inorganic acceptor layer. Filled and open diamonds show the respective V_{OC} measured at room temperature under $100\,\mathrm{mW/cm^2}$ AM 1.5G illumination. Dashed lines represent the slope of increasing ΔE_{IO} as measured in UV photoelectron spectroscopy.

The smaller slope towards lower temperatures indicates a less dominant influence of interfacial recombination losses. Minor changes in interface energetics are not suitable as explanation for the drastic differences in photocurrent between heterojunctions containing $\mathrm{Zn_{0.99}Mg_{0.01}O}$ and

ZnO. What it more likely is the influence of interfacial disorder upon alloying ZnO and MgO, which becomes active even at such low alloy grades of only $1\,\%$. Consequently, the behavior of ZnO is not equal to a hypothetical ZnMgO alloy with a magnesium content of zero. The interfacial carrier trap density might be altered as well as the conformation of polymer chains on the crystalline surface. Both effects can equally have a strong impact on device behavior.[111, 114, 145]

This irregularity is also reflected in a smaller photovoltage loss depicted in figure 8.2(b). While the room temperature V_{OC} of ZnMgO/P3HT photodiodes lies ca. $680\,\mathrm{meV}$ below the HCTS transition energy independent of Mg content, this difference only amounts to ca. $450\,\mathrm{meV}$ for a ZnO/P3HT diode. However as seen before, this does not mean that ZnO/P3HT photodiodes have the best device performance of all devices studied in this work. In fact, its power conversion efficiency is about $40\,\%$ smaller than the one of ZnMgO/P3HT diodes with Mg contents of $1\,\%$ and $5\,\%$. In spite of its reduced photovoltage losses, its photocurrent yield is surprisingly low. Apparently, even an energetic difference of ca. $1.5\,\mathrm{eV}$ between organic LUMO and inorganic conduction band driving the charge separation process does not guarantee for efficient exciton dissociation. A conclusive description for the qualitative differences in photovoltaic behavior between heterojunctions with ZnMgO and ZnO as acceptor material cannot be given here.

8.1.3 A Common Mechanism for Charge Separation

All three material combinations show a photovoltaic effect, which means that excitons produced on either side of the interface can be dissociated and contribute to a photocurrent. By means of a temperature-dependent analysis of the charge separation process, a multistep process can be outlined (see section 6.4.1).

At low temperatures, the efficiency of charge separation in a planar heterojunction is governed by two thermally activated transport processes: Exciton diffusion from the place of photon absorption towards the interface on the one hand, and extraction of dissociated carriers towards the electrodes on the other hand. Consequently, power conversion becomes more efficient with increasing temperature. However, this effect only continues up to ca. $150\,\mathrm{K}$, when the photocurrent begins to stagnate and finally diminishes when approaching room temperature. As a reason for this, a thermally activated recombination process could be identified. After overcoming an activation barrier of ca. $60\,\mathrm{meV}$, it becomes active to annihilate charge carriers right in the middle of the charge separation process. As neither exciton transport towards the interface nor carrier extraction after charge separation shows this declining behavior towards higher temperatures, the loss process must involve direct recombination of hybrid charge transfer states (HCTS) at the interface between organic donor and inorganic acceptor.

In table 8.2, two activation energies obtained from fits to experimental data from all material combinations of ZnO/P3HT, ZnMgO/P3HT and SnO_2/P3HT are referenced. E_{A} describes the increasing exciton mobility in P3HT which leads to a rising photocurrent in the temperature range of up to $150\,\mathrm{K}$. The values obtained from experimental data between 30 and $45\,\mathrm{meV}$ are in good agreement with previous publications on thermal activation of exciton diffusion in P3HT

Table 8.2: Activation energies of exciton diffusion E_A and differences between activation energy for HCTS recombination process E_rec and HCTS dissociation energy E_diss. All quantities are described in greater detail in section 6.4.1.

Heterojunction	E_A	$E_\mathrm{rec} - E_\mathrm{diss}$
ZnO/P3HT	$45 \pm 15\,\mathrm{meV}$	$65 \pm 6\,\mathrm{meV}$
ZnMgO/P3HT	$43 \pm 12\,\mathrm{meV}$	$60 \pm 8\,\mathrm{meV}$
SnO_2/P3HT	$31 \pm 7\,\mathrm{meV}$	$53 \pm 10\,\mathrm{meV}$

in literature.[83] The term $E_\mathrm{rec} - E_\mathrm{diss}$ describes the difference in activation energies between the process leading to interfacial HCTS recombination (E_rec) and the HCTS dissociation process (E_diss). Although the binding energy of HCTS cannot be extracted directly from photovoltaic measurements, it is most likely small compared to other thermal activation energies and thus in the range of only a few meV.

The fact that diodes with three different acceptor materials produce very similar values for E_A and $E_\mathrm{rec} - E_\mathrm{diss}$ underlines the universal validity of these findings for any hybrid heterojunction. Even in organic photovoltaics the weak temperature dependence of J_SC around room temperature[31] might be interpreted more conclusively than in previously published models involving phonon scattering processes.[52]

Temperature-dependent measurements of photovoltaic efficiency have revealed the signature of a thermally activated recombination process at the hybrid interface between P3HT and an inorganic acceptor. More knowledge on the mechanism of photovoltaic losses in hybrid heterojunctions can be gained from electroluminescence spectroscopy.

8.2 Electroluminescence from Hybrid Charge Transfer States

The presence of HCTS at the heterojunctions ZnO/P3HT, ZnMgO/P3HT and SnO_2/P3HT, can directly be proven by electroluminescence spectroscopy. In all three hybrid material systems a broad Gaussian-shaped signal in the near IR can be detected. The spectral position of its emission maximum scales with the hybrid energy gap ΔE_IO between the inorganic conduction band and the organic HOMO as shown for ZnMgO/P3HT heterojunctions in section 6.3.1. Comparing EL spectra of diodes with different ZnMgO alloys yields the information that about $75\,\%$ of inorganic band gap widening contributes to an upward shift of its conduction band. Consequently, the increase of ΔE_IO amounts to $75\,\%$ of the widening of the inorganic band gap. Figure 8.3 shows that this progression can be extended to pure ZnO.

Combined analysis of EL spectra and photovoltaic data reveals that the HCTS emission with a peak variance of $\sigma \approx 135\,\mathrm{meV}$ is situated ca. $350\,\mathrm{meV}$ below the HCTS transition energy. This matches nicely the prediction of Marcus theory postulating an energetic shift of $\lambda = \frac{\sigma^2}{2k_\mathrm{B}T}$, which can be interpreted either as reorganization energy in a homogeneously broadened system or as transport energy in case of inhomogeneous broadening.[62, 63] In conclusion this means, that HCTS are formed by free carriers in HOMO and conduction band. As interfacial trap states are not involved in the processes of charge separation and recombination, the proposed

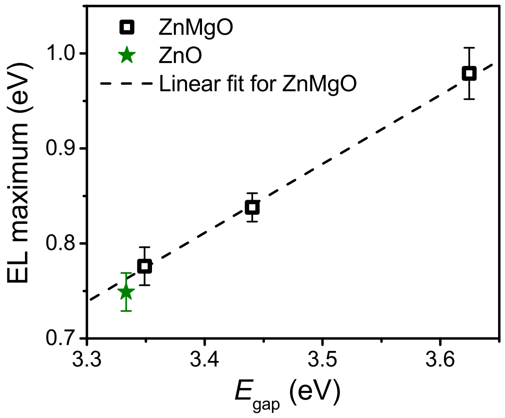

Figure 8.3: Extrapolated HCTS EL maxima for $F \to 0$ of three $Zn_{1-x}Mg_xO$/P3HT diodes with Mg contents of $x = 0.01$, $x = 0.05$ and $x = 0.14$ (black squares) and a ZnO/P3HT diode (green star). The dashed line gives the slope of increasing ΔE_{IO} with increasing Mg content as measured by UPS.

model is an intrinsic property of all inorganic/organic hybrid heterojunctions, regardless of their crystalline structure and orientation, their chemical composition and the presence of localized defects.

By systematically studying the influence of temperature and electric fields onto the HCTS recombination process, more knowledge about physical properties of hybrid charge transfer states can be gained. At last, electroluminescence transients provide insight into recombination dynamics of HCTS and reveal connections towards other findings in this work.

8.2.1 Voltage-Dependent Shift of HCTS Electroluminescence

In all three material systems the HCTS electroluminescence peak shifts towards higher energies with increasing voltage applied. In contrast to previous work in which this effect is attributed to a current-dependent filling of localized defect states,[41] a proportionality between EL maximum shift and the electric field F in the P3HT layer to the power of $\frac{2}{3}$ can be found. As described in section 6.3.1.1, this behavior can be reproduced by the upward shift of the ground state in a triangular potential well which is formed by the P3HT HOMO in proximity of the interface.

The blue-shift in all three material combinations follows the same field-dependent behavior and yields a similar slope with respect to $F^{\frac{2}{3}}$. Consequently, the density of states on the surface of ZnO, ZnMgO and SnO_2 does not play a role here; the effect is solely produced by carrier delocalization in P3HT. By extrapolating the EL maximum for $F \to 0$, the field-dependent shift can be eliminated and a hypothetical spectral position of a field-free EL signal can be determined. This value is used for the determination of the difference between HCTS transition energy and EL emission maximum.

The EL spectrum of HCTS at ZnO/P3HT and ZnMgO/P3HT interfaces consists of a single

Gaussian peak, which can be assigned to direct recombination of electrons in the inorganic conduction band and holes in the organic HOMO. It is only in the EL spectrum of a SnO_2/P3HT diode that a second feature appears. It is situated further in the infrared and might be a consequence of recombination from interfacial trap states on the SnO_2 surface. There are several hints towards their presence, e.g. the pronounced sub-bandgap absorption below the valence band onset in UPS (see section 7.2), and an additional feature in EQE spectra. However, further research is necessary to confirm this assignment.

8.2.2 Quantum Efficiency of HCTS Electroluminescence

EL spectroscopy measurements show a strongly increased external quantum efficiency in emission $\mathrm{EQE_{EL}}$ if performed at low temperatures. At $77\,\mathrm{K}$ the ratio of charge carriers contributing to an HCTS EL signal is two orders of magnitude higher than at room temperature. This behavior could be observed identically for ZnMGO/P3HT and SnO_2/P3HT heterojunctions. In both cases a model involving a thermally activated non-radiative decay channel could be fitted to experimental data, yielding activation energies of around $70\,\mathrm{meV}$. Such a behavior can be explained by increased mobility of HCTS along the interfacial plane in presence of localized defect sites which promote non-radiative recombination.

The comparison between $\mathrm{EQE_{EL}}$ at low and high temperatures shows that at room temperature at least 99 % of all charge carriers recombine non-radiatively. Consequently, non-radiative processes are the main loss channel in hybrid photovoltaic devices. This fact has to be included into analysis of photovoltaic data and interface energetics, as it is performed in section 6.4.2.1.

8.2.3 Time-Resolved HCTS Migration and Recombination

Time-resolved EL measurements show a slow decay of HCTS emission in the order of $500\,\mathrm{ns}$. Consequently, HCTS persist about 1000 times longer than bulk excitons in P3HT. Taking into acount the strong presence of non-radiative decay channels at room temperature of at least 99 %, the characteristic time constant for radiative recombination of HCTS can be estimated to be at least $50\,\mu\mathrm{s}$ (see 6.3.2). Such a long lifetime is a consequence of the strong delocalization of electron and hole in an HCTS, as it can be determined from field-dependent EL measurements (see 6.3.1.1). It is also in good agreement to the small binding energy of an HCTS, seen in the thermal activation of photovoltaic charge separation in section 6.4.1.

Comparison of HCTS EL transients at different spectral positions reveals a shortening of lifetimes towards higher photon energies. Such a behavior is produced if charge carriers in an HCTS are able to migrate along the interfacial plane. As the local ionization potential of P3HT can shift by more than $300\,\mathrm{meV}$ depending on different orientations on an acceptor surface,[114] HCTS are situated in a ”bumpy” energetic landscape. The difference in carrier lifetimes between emission energies reflects their ability to migrate from sites with high transition energy to energetically lower places. This mobility along the interfacial plane sets up an additional decay channel for localized states at the high-energy edge of the HCTS emission peak, which is not present in the lower part of the spectrum. A similar behavior of mobile charge transfer states at an interface plane has been observed in a purely organic system.[164]

It is likely that HCTS migration along the interface is the underlying process for the rise of non-radiative recombination in EL measurements with increasing temperature. It might also be connected to thermally activated annihilation of charge carriers as observed in temperature-dependen photovoltaics, as both processes show a similar activation energy of ca. $70\,\mathrm{meV}$. Consequently, the signatures of exciton migration and non-radiative HCTS decay could be observed in all three material systems studied in this work. Altogether a detailed understanding of photovoltaic power conversion and loss processes provides a solid framework for new device concepts and further improvement in the whole class of inorganic/organic hybrid heterojunctions.

Chapter 9

Conclusions and Outlook

9.1 Role and Properties of Hybrid Charge Transfer States

For several years, the scientific community has been discussing the reasons for poor performances of hybrid inorganic-organic solar cells. Despite the prospected advantages of a hybrid system combining an organic donor with a high absorption coefficient and a crystalline inorganic acceptor with high carrier mobility, actual devices could not fulfill the hopes for efficient power conversion and improved device stability. They even fail to reach the performance of purely organic systems.

This work provides experimental evidence for bound states between electrons and holes on opposite sides of the donor-acceptor interface hindering efficient charge separation. The charges in such a hybrid charge transfer state (HCTS) are bound to each other by Coulomb interaction; only after dissociation of an HCTS can a contribution to photocurrent be made. This mechanism was observed in three material combinations: ZnO/P3HT, ZnMgO/P3HT and SnO_2/P3HT. As only frontier orbitals in the organic and valence and conduction band in the inorganic are involved, the findings can be extended to a whole class of organic/metal-oxide heterojunctions.

Electroluminescence spectroscopy proved to be a powerful tool for giving immediate evidence for the existence of HCTS and in the analysis of their physical properties. The wavefunction overlap of electron and hole in an HCTS is large enough to produce a detectable luminescence signal in the near infrared if a forward bias is applied to a planar photodiode. The spectral position of the HCTS luminescence peak directly depends on the interfacial band gap ΔE_{IO} between inorganic conduction band and organic HOMO. It can be varied by choice of different materials and even tuned continuously by choosing $Zn_{1-x}Mg_xO$ with a variable Mg content x as acceptor. This enables a quantitative study of interface energetics and photovoltaic losses.

From a field-dependent energetic shift in emission can be concluded that both carriers forming an HCTS are delocalized perpendicularly to the interface. This observation matches well with the long decay times in the range of $500\,\mathrm{ns}$ as measured in time-resolved EL spectroscopy. A high degree of delocalization produces a long effective distance between electron and hole, and thus a weak Coulomb interaction in the range of a few meV. Consequently, carriers in HCTS are bound to each other only loosely. During their long lifetime, HCTS undergo an energetic relaxation process towards sites of lower local transition energy. This means that they are able to migrate geminately along the interface plane, a similar behavior was reported recently for an organic heterojunction as well.[164]

From these observations the question arises, how such a weak binding mechanism can severely hinder charge separation and finally lead to severe losses in photovoltaic power conversion. The answer can probably be found in a ratio of more than $99\,\%$ of all HCTS, which recombine non-radiatively at room temperature. By means of temperature-dependent electroluminescence measurements, the thermal activation of this recombination process can be studied. A connection between non-radiative recombination and HCTS mobility is likely.

9.2 Thermal Activation of Photovoltaic Charge Generation

Photovoltaic power conversion is a complex multistep process which besides HCTS dissociation involves transport of excitons towards the donor-acceptor interface and extraction of electrons and holes after charge separation. A conclusive model for its thermal activation behavior could be derived and successfully applied to experimental data from all material combinations investigated in this study:

While extraction of single carriers is a limiting factor to power conversion only at low temperatures and under high illumination densities, thermally activated exciton transport from the donor layer towards the interface is directly responsible for the increase in photovoltaic quantum efficiency up to its maximum at temperatures around $150\,\mathrm{K}$. At higher temperatures however, a thermally activated loss process becomes significant, which produces a stagnating and even slightly decreasing EQE when approaching room temperature. As expected from previous findings on the structure of HCTS, the actual charge separation process at the interface only plays a minor role in the temperature-dependent description of photovoltaic power conversion, and does not leave a significant footprint in its thermal activation behavior. In previous work by *M. Gerhard* a binding energy for a charge transfer state in a purely organic heterojunction of $46\,\mathrm{meV}$ is given,[29] consequently an even smaller value for a hybrid system appears to be reasonable.

9.3 Interface Energetics and Photovoltage Losses

Two fundamental ways to obtain a reliable value for the HCTS transition energy E_{HCTS} were pursued in this work: Extrapolation of temperature-dependent open circuit voltage measurements on the one hand, and determination of the thermal activation energy of the recombination current from fits to diode characteristics on the other hand. Its value can be utilized to construct a detailed image of the interface energetics and thus estimate the photovoltage losses of the different material combinations.

Comparing E_{HCTS} to the spectral position of the EL signal measured from the same diode yields an energetic shift of ca. $350\,\mathrm{meV}$ for ZnMgO/P3HT and SnO_2/P3HT heterojunctions. Taking into account an emission linewidth of $\sigma = 135\,\mathrm{meV}$, this corresponds well to the expected energetic shift $\frac{\sigma^2}{k_\mathrm{B}T}$ for an inhomogeneously broadened emission. This proves that HCTS recombination occurs as a bimolecular band-to-band recombination process between free carriers in the inorganic conduction band and organic HOMO orbital, as any involvement of localized trap states at the interface would lead to a further redshift. The EL spectrum from a SnO_2/P3HT interface indeed shows an additional feature located further in the infrared. It seems likely that it originates in a recombination process involving trapped carriers, but no decisive proof can be given in this work.

Independently from the Mg content x in the acceptor material, the difference between the calculated E_HCTS and the V_OC of a $Zn_{1-x}Mg_xO$/P3HT photodiode measured under $100\,\mathrm{mW/cm^2}$ AM 1.5G illumination at room temperature amounts to ca. $680\,\mathrm{mV}$. This figure clearly exceeds literature values for losses in purely organic solar cells and stands as an example of poor device performances of inorganic-organic photovoltaic systems. The losses in devices involving unalloyed ZnO are ca. $180\,\mathrm{mV}$ lower, but at the expense of a significantly lower photocurrent, which leads to an even lower power conversion efficiency. The two material systems ZnMgO/P3HT and ZnO/P3HT show a qualitative difference in photovoltaic parameters, which most likely can be attributed to the influence of surface reconstruction and disorder phenomena.

The photovoltage losses at a SnO_2/P3HT heterojunction are approximately as high as those measured at ZnMgO/P3HT devices. In separate experimental procedures, a corridor between $560\,\mathrm{meV}$ and $750\,\mathrm{meV}$ could be determined. In terms of power conversion efficiency, this material system is on the same level as a ZnMgO/P3HT heterojunction with a low Mg content. The faster electron transfer from an organic adsorbate to the SnO_2 conduction band as reported in literature[16] could not make a positive impact on the photovoltaic efficiency.

After analysis of three metal-oxide/organic material systems, it can be concluded that photovoltaic losses caused by interfacial recombination remain a serious issue in hybrid inorganic-organic solar cells. Despite the favorable effects of carrier delocalization in both donor and acceptor material, bound states at the interface inhibit an effective charge separation. The long radiative lifetime of HCTS, which was determined in time-resolved electroluminescence spectroscopy, fails to prevent interfacial carrier recombination. Even though dissociation of HCTS into free electrons and holes does not impose a detectable energetic barrier to the photocurrent generation process, the competition between charge separation and interfacial recombination commonly does not end with a success. As a consequence, hybrid inorganic-organic heterojunctions cannot catch up with the efficiency of purely organic solar cells.

Non-radiative recombination of HCTS appears to be the most incisive loss process. This indicates that these losses are theoretically avoidable according to Shockley's law.[7] Further research on improved concepts for rapid carrier separation is necessary in order to fully exploit the potential of hybrid inorganic-organic photovoltaics.

9.4 Future Applications for Hybrid Inorganic/Organic Heterojunctions

One hint towards more efficient charge separation can be obtained from the photosynthesis reaction occurring in all green plant cells. Hereby, chlorophyll acts as donor, which passes an electron over to an acceptor molecule upon light absorption. By means of a cascade of subsequent transfer processes, rapid detachment of electrons and holes is achieved.[185] This mechanism efficiently limits re-capture and recombination of carriers at the interface.

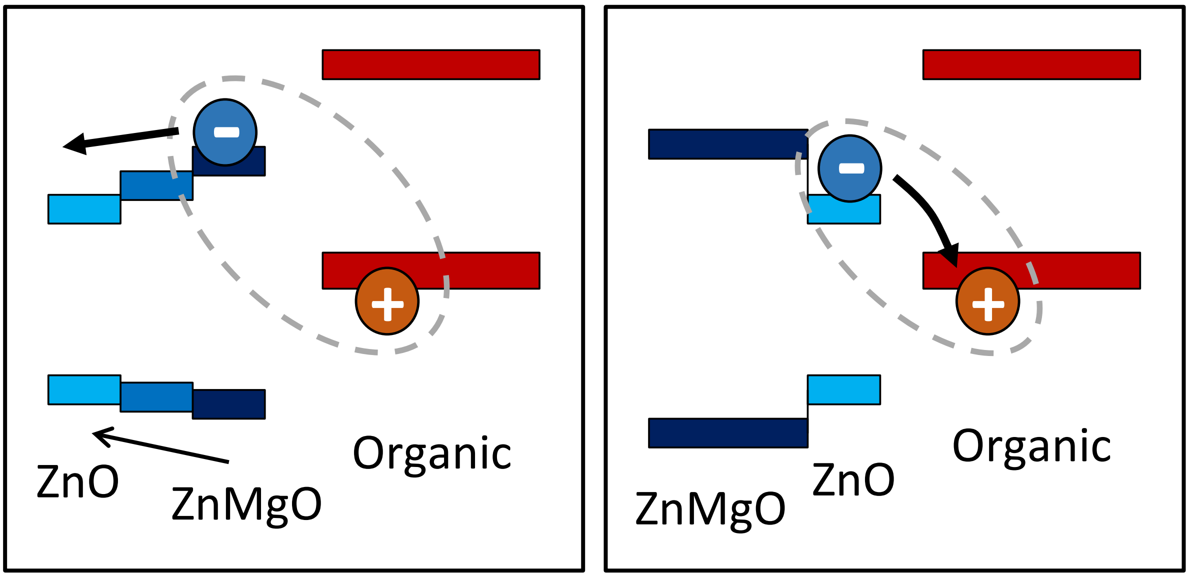

(a) Solar cell with cascade (b) Infra-red LED with HCTS confinement

Figure 9.1: (a) Energy levels of a ZnMgO/P3HT solar cell with a band gap cascade to rapidly funnel the electron away from the interface (b) Proposed infra-red LED with HCTS confinement for an increased radiative recombination rate

A similar energetic cascade can be realized by a stack of ZnMgO layers with increasing Mg content towards the interface as depicted in figure 9.1(a). By that means, electrons can efficiently be dragged away from the interface, which can prevent interfacial losses. By layering several types of small molecules, a similar effect can be reached for holes on the organic side of the heterojunction. Future research on hybrid photovoltaics will evaluate the potential of novel device architecture in order to push the limit towards higher efficiencies.

For fabrication of narrow-band hybrid light emitting diodes in the near infrared, the same principle can be reversed. By inserting a thin ZnO layer into a ZnMgO/P3HT heterojunction, a step in the potential for a close confinement of HCTS to the interface is created (see figure 9.1(b)). The reduced delocalization and mobility of HCTS is likely to enhance radiative recombination, which can be exploited in the construction of novel type light sources.

Appendix

A Influence of UV Irradiation onto ZnO/P3HT and SnO_2/ P3HT Photodiodes

Carrier concentration and physical properties of crystalline semiconductor materials can temporally be altered by excitation of charge carriers situated in sub-bandgap traps. In case of ZnO, such an effect can last over several hours.[186] In order to obtain accurate and reproducible measurements, the sensibility of photovoltaic devices to light irradiation at different photon energies has to be examined. For this reason time-dependent photocurrent measurements were performed for two photodiodes with ZnO/P3HT and SnO_2/P3HT as active layers. For each diode the response to UV irradiation at a wavelength slightly below the inorganic band-gap was probed. Figure 9.2 shows that the EQE of a ZnO/P3HT device rapidly decreases upon illumination with a photon energy of $3.30\,\mathrm{eV}$, while the quantum efficiency of a SnO_2/P3HT device remains constant under illumination with a photon energy of $3.54\,\mathrm{eV}$. For both devices the power conversion efficiency is not altered upon excitation of the P3HT donor material with a photon energy of $2.25\,\mathrm{eV}$.

For this reason in all photovoltaic measurements involving ZnO or ZnMgO as acceptor material a modified AM 1.5G spectrum was used with a $395\,\mathrm{nm}$ long pass filter removing all UV irradiation as shown in figure 4.4. All experiments with SnO_2/P3HT diodes could be performed without this additional filter.

B Carrier Mobilities in ZnMgO and ZnMgO:Ga

Figure 9.3 shows carrier mobilities measured in $400\,\mathrm{nm}$ thick $\mathrm{Zn_{0.91}Mg_{0.09}O}$ and $\mathrm{Zn_{0.91}Mg_{0.09}O}$:Ga layers measured using the Hall effect. Both layers were fabricated by molecular beam epitaxy on top of a sapphire substrate as described in section 3.1.2. In the pure ZnMgO layer the electron mobility slightly increases in the range between $75\,\mathrm{K}$ and room temperature, while it remains at a constant value for ZnMgO:Ga. The measured carrier concentrations are ca. $4.3 \times 10^{20}\,\mathrm{cm^{-3}}$ in the gallium doped layer and $2.0 \times 10^{18}\,\mathrm{cm^{-3}}$ in the undoped layer, independent of temperature.

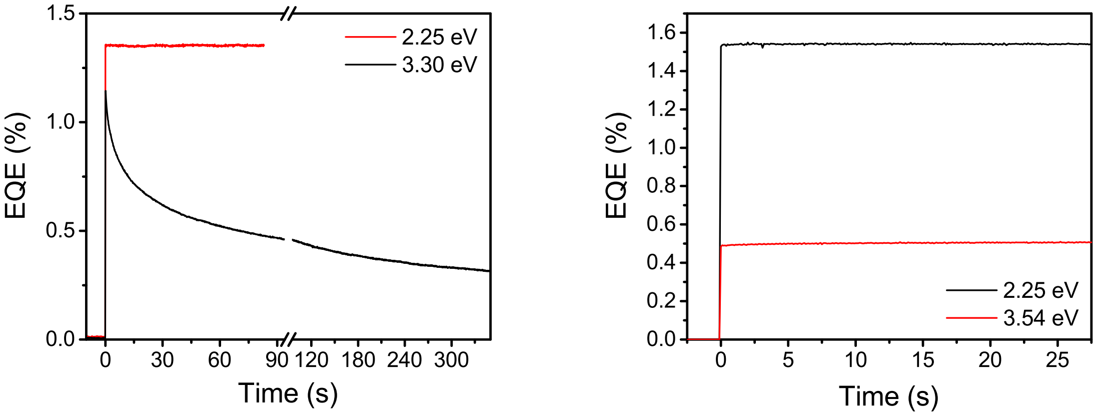

(a) ZnO/P3HT (b) SnO_2/P3HT

Figure 9.2: (a) Timelines of photovoltaic efficiency of a ZnO/P3HT photodiode upon illumination with photon energies of $3.3\,\mathrm{eV}$ and $2.25\,\mathrm{eV}$. At the time $t = 0$ illumination is switched on. (b) EQE timelines of a SnO_2/P3HT device for illumination with photon energies of $3.54\,\mathrm{eV}$ and $2.25\,\mathrm{eV}$.

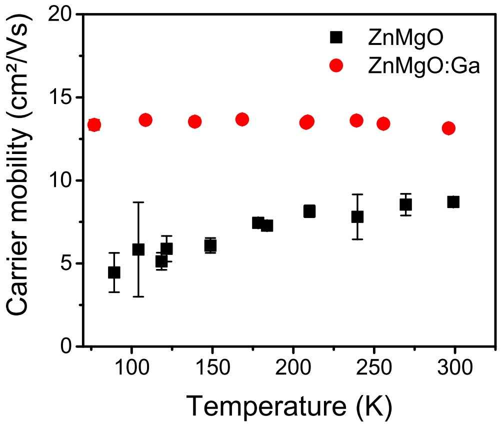

Figure 9.3: Electron mobilities in $Zn_{0.91}Mg_{0.09}O$ and $Zn_{0.91}Mg_{0.09}O$:Ga layers measured using the Hall effect at temperatures between $75\,\mathrm{K}$ and room temperature.

C Thermal Activation of Photocurrent Generation

ZnO/P3HT Heterojunction

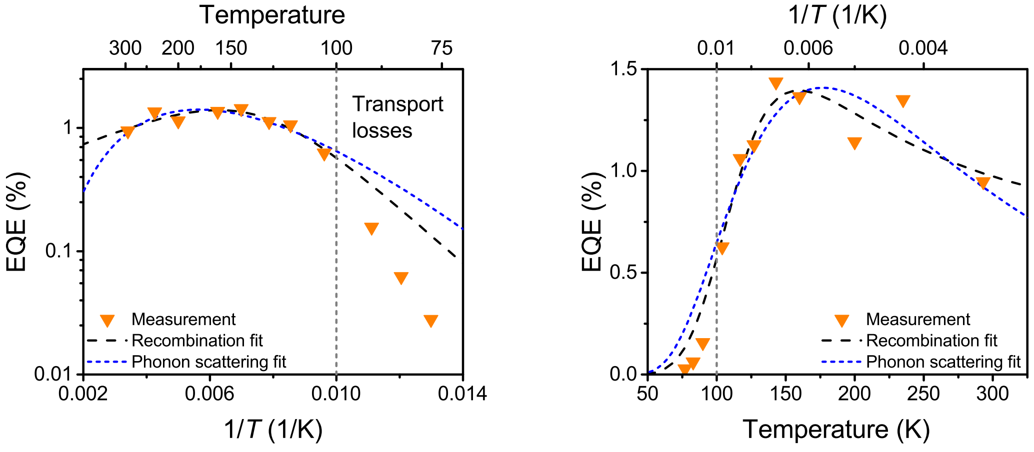

(a) Arrhenius plot (b) Linear scale

Figure 9.4: Temperature-dependent EQE values of a ZnO/P3HT diode with $d_{\mathrm{P3HT}} = 240\,\mathrm{nm}$ under monochromatic excitation with a photon energy of $2.25\,\mathrm{eV}$. Fit range between $100\,\mathrm{K}$ and $295\,\mathrm{K}$. Recombination model fit parameters: $E_\mathrm{A} = 45 \pm 15\,\mathrm{meV}$ and $(E_\mathrm{rec} - E_\mathrm{diss}) = 65 \pm 6\,\mathrm{meV}$. Phonon scattering model fit parameters: $E_\mathrm{A} = 60 \pm 16\,\mathrm{meV}$ and $m = 3.92 \pm 1.19$.

$\mathrm{Zn}_{0.99}\mathrm{Mg}_{0.01}\mathrm{O}$/P3HT Heterojunction

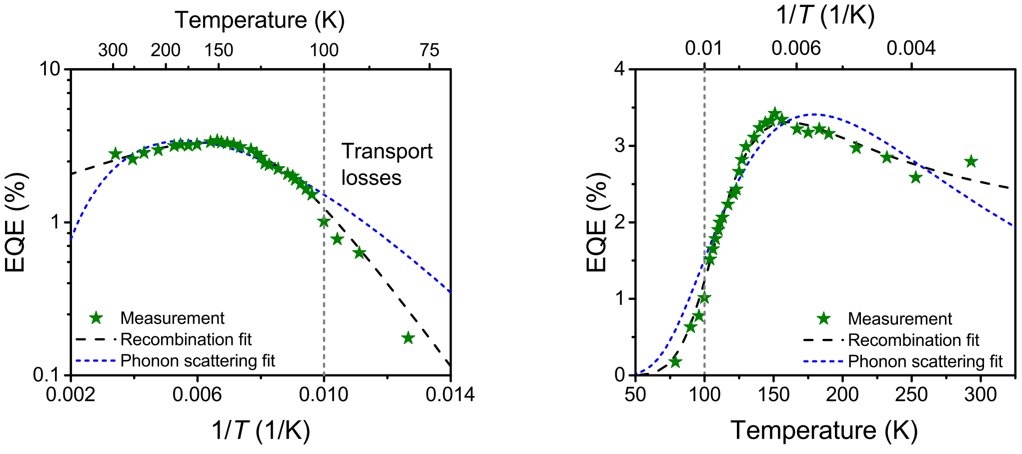

(a) Arrhenius plot (b) Linear scale

Figure 9.5: Temperature-dependent EQE values of a $\mathrm{Zn}_{0.99}\mathrm{Mg}_{0.01}\mathrm{O}$/P3HT diode with $d_{\mathrm{P3HT}} = 240\,\mathrm{nm}$ under monochromatic excitation with a photon energy of $2.25\,\mathrm{eV}$. Fit range between $100\,\mathrm{K}$ and $295\,\mathrm{K}$. Recombination model fit parameters: $E_\mathrm{A} = 54 \pm 6\,\mathrm{meV}$ and $(E_\mathrm{rec} - E_\mathrm{diss}) = 68 \pm 4\,\mathrm{meV}$. Phonon scattering model fit parameters: $E_\mathrm{A} = 62 \pm 6\,\mathrm{meV}$ and $m = 3.98 \pm 0.38$.

$Zn_{0.86}Mg_{0.14}O$/P3HT Heterojunction

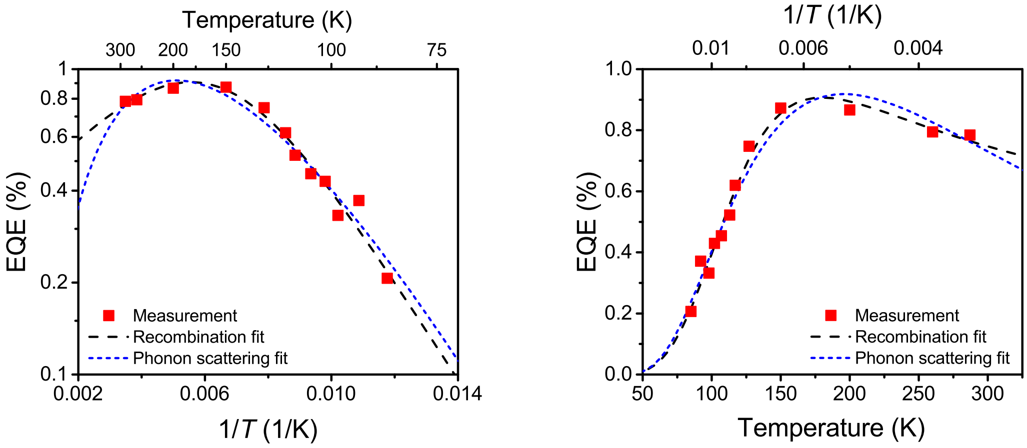

(a) Arrhenius plot

(b) Linear scale

Figure 9.6: Temperature-dependent EQE values of a $Zn_{0.86}Mg_{0.14}O$/P3HT diode with $d_{\text{P3HT}} = 115\,\text{nm}$ under monochromatic excitation with a photon energy of $2.25\,\text{eV}$. Due to the thin P3HT layer and the low photocurrent no s-shaped J-V characteristics is observed at low temperatures. Therefore the fit is performed for all measurements between $80\,\text{K}$ and $295\,\text{K}$. Recombination model fit parameters: $E_{\text{A}} = 31 \pm 7\,\text{meV}$ and $(E_{\text{rec}} - E_{\text{diss}}) = 53 \pm 10\,\text{meV}$. Phonon scattering model fit parameters: $E_{\text{A}} = 54 \pm 6\,\text{meV}$ and $m = 3.29 \pm 0.47$.

D Derivation of the Radiative Recombination Current

In this section the evaluation of the integral for the radiative recombination current J_0^{rad} as used in the discussion in section 6.4.2 is described.

The radiative recombination current J_0^{rad} is the fraction of the total recombination current J_0 and the radiative quantum efficiency EQE_{EL} of a heterojunction.

$$J_0^{\text{rad}} = J_0 \cdot \text{EQE}_{\text{EL}}. \tag{9.1}$$

The detailed balance model establishes a relation between the radiative recombination current and the charge generation of the device by thermal excitation in the dark. [61]

$$J_0^{\text{rad}} = q \int_0^{\infty} \text{EQE}_{PV} \Phi_{\text{BB}} E \, \mathrm{d}E. \tag{9.2}$$

The contribution of HCTS to the EQE of a solar cell is given as the absorption spectrum of hybrid charge transfer states $\sigma_A(E)$ at a planar interface, multiplied by the charge extraction efficiency η. In organic and hybrid systems, the absorption spectrum of interfacial charge transfer states is described by a Gaussian peak around the energy E_0.[25, 39]

$$\mathrm{EQE}_{PV}(E) = \eta\sigma_A(E) = \frac{\eta}{E\sqrt{2\pi}\sigma}\exp\left(-\frac{(E-E_0)^2}{2\sigma^2}\right) \tag{9.3}$$

Φ_{BB}^{T} is the blackbody radiation spectrum of the device with its temperature T.

$$\Phi_{\mathrm{BB}}^{T}(E) = \frac{2\pi}{h^3c^2}E^2\exp\left(-\frac{E}{k_BT}\right) \tag{9.4}$$

Equations 9.3 and 9.4 inserted into equation 9.2. The product $\frac{2\pi}{h^3c^2}\eta$ will be lumped into the constant f^*.

$$J_0^{\mathrm{rad}} = qf^*\int_0^\infty \frac{E}{\sqrt{2\pi}\sigma}\exp\left(-\frac{(E-E_0)^2}{2\sigma^2}\right)\times\exp\left(-\frac{E}{k_BT}\right)\mathrm{d}E. \tag{9.5}$$

Pulling together the two exponential functions:

$$J_0^{\mathrm{rad}} = qf^*\int_0^\infty \frac{E}{\sqrt{2\pi}\sigma}\exp\left(-\frac{(E^2-2EE_0)+E_0^2+\frac{2\sigma^2}{k_BT}E}{2\sigma^2}\right)\mathrm{d}E. \tag{9.6}$$

Rearranging and completing the square:

$$J_0^{\mathrm{rad}} = qf^*\exp\left(\frac{E_0^2-\left(E_0-\frac{\sigma^2}{k_BT}\right)^2}{2\sigma^2}\right)\int_0^\infty \frac{E}{\sqrt{2\pi}\sigma}\exp\left(-\frac{\left(E-\left(E_0-\frac{\sigma^2}{k_BT}\right)\right)^2}{2\sigma^2}\right)\mathrm{d}E. \tag{9.7}$$

In the integral appears the normalized formula of a Gaussian with its peak $E_0 - \frac{\sigma^2}{k_BT}$ multiplied by the photon energy E. Integration thus yields a value close to peak of the normal distribution.

$$J_0^{\mathrm{rad}} = qf^*\left(E_0-\frac{\sigma^2}{k_BT}\right)\exp\left(-\frac{E_0-\frac{\sigma^2}{2k_BT}}{k_BT}\right) \tag{9.8}$$

Consequently, $E_{\mathrm{HCTS}} = E_0 - \frac{\sigma^2}{2k_BT}$ is the activation energy for the radiative recombination current

$$J_0^{\mathrm{rad}} = qf^*E_{\mathrm{HCTS}}\exp\left(-\frac{E_0-\frac{\sigma^2}{2k_BT}}{k_BT}\right). \tag{9.9}$$

Abbreviations

Abbreviation	**Description**
AFM	Atomic Force Microscopy
ALD	Atomic Layer Deposition
AM 1.5G	Air Mass 1.5 Global Spectrum
CB	Conduction Band
CT	Charge Transfer
CTS	Charge Transfer State
EL	Electroluminescence
EQE	External Quantum Efficiency
FF	Fill Factor
FWHM	Full Width at Half Maximum
HCTS	Hybrid Charge Transfer State
HOMO	Highest Occupied Molecular Orbital
ITO	Indium Tin Oxide
IR	Infrared
J_{SC}	Short Circuit Current
J-V characteristic	Current-Voltage Characteristic
LUMO	Lowest Unoccupied Molecular Orbital
MBE	Molecular Beam Epitaxy
MPP	Maximum Power Point
NIR	Near Infrared
P3HT	Poly(3-hexylthiophene)
PCBM	Phenyl-C_{61}-butyric Acid Methyl Ester
PCE	Power Conversion Efficiency
PL	Photoluminescence
PV	Photovoltaics
RHEED	Reflection High Energy Electron Diffraction
RMS	Root Mean Square
SECO	Secondary Electron Cut-Off
UPS	UV Photoelectron Spectroscopy
UV	Ultraviolet
VB	Valence Band
V_{OC}	Open Circuit Voltage

Bibliography

[1] Intergovernmental Panel on Climate Change, „Climate Change 2014: Synthesis Report“, 39–74 (2015).

[2] A. J. Weaver, K. Zickfeld, A. Montenegro, and M. Eby, „Long term climate implications of 2050 emission reduction targets“, Geophysical Research Letters **34**, 4–7 (2007).

[3] J. Rockström, O. Gaffney, J. Rogelj, M. Meinshausen, N. Nakicenovic, and H. J. Schellnhuber, „A roadmap for rapid decarbonization“, Science **355**, 1269–1271 (2017).

[4] Bundesministerium für Wirtschaft und Energie, „Erneuerbare Energien in Zahlen“, 6–32 (2016).

[5] Verband Deutscher Maschinen- und Anlagenbau, „International Technology Roadmap for Photovoltaic (ITRPV), 2016 Results“, 1–37 (2016).

[6] C. Sener and V. Fthenakis, „Energy policy and financing options to achieve solar energy grid penetration targets: Accounting for external costs“, Renewable and Sustainable Energy Reviews **32**, 854–868 (2014).

[7] W. Shockley and H. J. Queisser, „Detailed balance limit of efficiency of p-n junction solar cells“, Journal of Applied Physics **32**, 510–519 (1961).

[8] D. Weißbach, G. Ruprecht, A. Huke, K. Czerski, S. Gottlieb, and A. Hussein, „Energy intensities, EROIs (energy returned on invested), and energy payback times of electricity generating power plants“, Energy **52**, 210–221 (2013).

[9] M. T. Dang, L. Hirsch, and G. Wantz, „P3HT:PCBM, best seller in polymer photovoltaic research“, Advanced Materials **23**, 3597–3602 (2011).

[10] W. J. E. Beek, M. M. Wienk, and R. A. J. Janssen, „Hybrid solar cells from regioregular polythiophene and ZnO nanoparticles“, Advanced Functional Materials **16**, 1112–1116 (2006).

[11] M. Schierhorn, S. W. Boettcher, J. H. Peet, E. Matioli, G. C. Bazan, G. D. Stucky, and M. Moskovits, „CdSe Nanorods Dominate Photocurrent of Hybrid CdSe-P3HT Photovoltaic Cell“, **4**, 6132–6136 (2010).

[12] K. J. Jiang, K. Manseki, Y. H. Yu, N. Masaki, K. Suzuki, Y. L. Song, and S. Yanagida, „Photovoltaics based on hybridization of effective dye-sensitized titanium oxide and hole-conductive polymer P3HT“, Advanced Functional Materials **19**, 2481–2485 (2009).

[13] S. D. Oosterhout, M. M. Wienk, S. S. van Bavel, R. Thiedmann, L. J. A. Koster, J. Gilot, J. Loos, V. Schmidt, and R. A. J. Janssen, „The effect of three-dimensional morphology on the efficiency of hybrid polymer solar cells“, Nature materials **8**, 818–824 (2009).

[14] S. Wu, Q. Tai, and F. Yan, „Hybrid photovoltaic devices based on poly (3-hexylthiophene) and ordered electrospun ZnO nanofibers“, Journal of Physical Chemistry C **114**, 6197–6200 (2010).

[15] D. C. Olson, J. Piris, R. T. Collins, S. E. Shaheen, and D. S. Ginley, „Hybrid photovoltaic devices of polymer and ZnO nanofiber composites“, Thin Solid Films **496**, 26–29 (2006).

[16] J. B. Asbury, E. Hao, Y. Wang, H. N. Ghosh, and T. Lian, „Ultrafast Electron Transfer Dynamics from Molecular Adsorbates to Semiconductor Nanocrystalline Thin Films“, The Journal of Physical Chemistry B **105**, 4545–4557 (2001).

[17] C. Kittel, *Introduction to solid state physics* (John Wiley & Sons, Hoboken, New Jersey, 2004).

[18] S. M. Sze and K. K. Ng, *Semiconductor Devices: Physics and Technology* (John Wiley & Sons, Hoboken, New Jersey, 2006).

[19] G. H. Wannier, „The structure of electronic excitation levels in insulating crystals“, Physical Review **52**, 191–197 (1937).

[20] M. Höfner, S. Sadofev, B. Kobin, S. Hecht, and F. Henneberger, „Hybrid polaritons in a resonant inorganic/organic semiconductor microcavity“, Applied Physics Letters **107**, 181109 (2015).

[21] Y. Frenkel, „On the transformation of light into heat in solids. I“, Physical Review **37**, 17–44 (1931).

[22] O. V. Mikhnenko, H. Azimi, M. Scharber, M. Morana, P. W. M. Blom, and M. A. Loi, „Exciton diffusion length in narrow bandgap polymers“, Energy & Environmental Science **5**, 6960–6965 (2012).

[23] S. D. Stranks, G. E. Eperon, G. Grancini, C. Menelaou, M. J. P. Alcocer, T. Leijtens, L. M. Herz, A. Petrozza, and H. J. Snaith, „Electron-Hole Diffusion Lengths Exceeding 1 Micrometer in an Organometal Trihalide Perovskite Absorber“, Science **342**, 341–344 (2013).

[24] K. Vandewal, „Interfacial Charge Transfer States in Condensed Phase Systems“, Annual Review of Physical Chemistry **67**, 113–133 (2016).

[25] K. Vandewal, K. Tvingstedt, A. Gadisa, O. Inganäs, and J. V. Manca, „Relating the open-circuit voltage to interface molecular properties of donor:acceptor bulk heterojunction solar cells“, Physical Review B - Condensed Matter and Materials Physics **81**, 125204 (2010).

[26] K. Tvingstedt, K. Vandewal, A. Gadisa, F. Zhang, J. Manca, and O. Inganäs, „Electroluminescence from charge transfer states in polymer solar cells“, Journal of the American Chemical Society **131**, 11819–11824 (2009).

[27] C. Kästner, K. Vandewal, D. A. M. Egbe, and H. Hoppe, „Revelation of Interfacial Energetics in Organic Multiheterojunctions“, Advanced Science, 1600331 (2017).

[28] K. Vandewal, A. Gadisa, W. D. Oosterbaan, S. Bertho, F. Banishoeib, I. Van Severen, L. Lutsen, T. J. Cleij, D. Vanderzande, and J. V. Manca, „The Relation Between Open-Circuit Voltage and the Onset of Photocurrent Generation by Charge-Transfer Absorption in Polymer: Fullerene Bulk Heterojunction Solar Cells“, Advanced Functional Materials **18**, 2064–2070 (2008).

[29] M. Gerhard, „Photoexcitation dynamics and disorder effects in organic donor/acceptor systems“, PhD dissertation (Philipps-Universität Marburg, 2016).

[30] W. J. Grzegorczyk, T. J. Savenije, T. E. Dykstra, J. Piris, J. M. Schins, and L. D. A. Siebbeles, „Temperature-independent charge carrier photogeneration in P3HT-PCBM blends with different morphology“, Journal of Physical Chemistry C **114**, 5182–5186 (2010).

[31] A. Petersen, A. Ojala, T. Kirchartz, T. A. Wagner, F. Würthner, and U. Rau, „Field-dependent exciton dissociation in organic heterojunction solar cells“, Physical Review B - Condensed Matter and Materials Physics **85**, 245208 (2012).

[32] T. M. Clarke and J. R. Durrant, „Charge photogeneration in organic solar cells“, Chemical Reviews **110**, 6736–6767 (2010).

[33] U. Hörmann, J. Kraus, M. Gruber, C. Schuhmair, T. Linderl, S. Grob, S. Kapfinger, K. Klein, M. Stutzman, H. J. Krenner, and W. Brütting, „Quantification of energy losses in organic solar cells from temperature-dependent device characteristics“, Physical Review B - Condensed Matter and Materials Physics **88**, 235307 (2013).

[34] I. Lange, J. Kniepert, P. Pingel, I. Dumsch, S. Allard, S. Janietz, U. Scherf, and D. Neher, „Correlation between the Open Circuit Voltage and the Energetics of Organic Bulk Heterojunction Solar Cells“, The Journal of Physical Chemistry Letters **4**, 3865–3871 (2013).

[35] Y. Zou and R. J. Holmes, „Correlation between the Open-Circuit Voltage and Charge Transfer State Energy in Organic Photovoltaic Cells“, ACS Applied Materials & Interfaces **7**, 18306–18311 (2015).

[36] T. Linderl, U. Hörmann, S. Beratz, M. Gruber, S. Grob, A. Hofmann, and W. Brütting, „Temperature dependent competition between different recombination channels in organic heterojunction solar cells“, Journal of Optics **18**, 024007 (2016).

[37] G. Wu, Z. Li, X. Zhang, and G. Lu, „Charge separation and exciton dynamics at polymer/ZnO interface from first-principles simulations“, Journal of Physical Chemistry Letters **5**, 2649–2656 (2014).

[38] Y. Vaynzof, A. A. Bakulin, S. Gélinas, and R. H. Friend, „Direct observation of photoinduced bound charge-pair states at an organic-inorganic semiconductor interface“, Physical Review Letters **108**, 246605 (2012).

[39] F. Piersimoni, R. Schlesinger, J. Benduhn, D. Spoltore, S. Reiter, I. Lange, N. Koch, K. Vandewal, and D. Neher, „Charge transfer absorption and emission at ZnO/organic interfaces“, Journal of Physical Chemistry Letters **6**, 500–504 (2015).

[40] I. Lange, S. Reiter, M. Pätzel, A. Zykov, A. Nefedov, J. Hildebrandt, S. Hecht, S. Kowarik, C. Wöll, G. Heimel, and D. Neher, „Tuning the Work Function of Polar Zinc Oxide Surfaces using Modified Phosphonic Acid Self-Assembled Monolayers“, Advanced Functional Materials **24**, 7014–7024 (2014).

[41] A. Panda, K. Ding, X. Liu, and S. R. Forrest, „Free and trapped hybrid charge transfer excitons at a ZnO/small-molecule heterojunction“, Physical Review B - Condensed Matter and Materials Physics **94**, 125429 (2016).

[42] C. K. Renshaw and S. R. Forrest, „Excited state and charge dynamics of hybrid organic/inorganic heterojunctions. I. Theory“, Physical Review B - Condensed Matter and Materials Physics **90**, 045302 (2014).

[43] P. Würfel and U. Würfel, *Physics of solar cells: from basic principles to advance concepts* (John Wiley & Sons, Weinheim, Germany, 2009).

[44] M. A. Green, *Solar cells: operating principles, technology, and system applications* (Prentice-Hall Inc., Englewood Cliffs, NJ, 1982).

[45] Z. He, B. Xiao, F. Liu, H. Wu, Y. Yang, S. Xiao, C. Wang, T. P. Russell, and Y. Cao, „Single-junction polymer solar cells with high efficiency and photovoltage“, Nature Photonics **9**, 174–179 (2015).

[46] Y. Liu, C.-C. Chen, Z. Hong, J. Gao, Y. M. Yang, H. Zhou, L. Dou, G. Li, and Y. Yang, „Solution-processed small-molecule solar cells: breaking the 10% power conversion efficiency“, Scientific Reports **3**, 3356 (2013).

[47] S. Li, L. Ye, W. Zhao, S. Zhang, S. Mukherjee, H. Ade, and J. Hou, „Energy-Level Modulation of Small-Molecule Electron Acceptors to Achieve over 12% Efficiency in Polymer Solar Cells“, Advanced Materials **28**, 9423–9429 (2016).

[48] M. Grätzel, „Dye-sensitized solar cells“, Journal of Photochemistry and Photobiology C: Photochemistry Reviews **4**, 145–153 (2003).

[49] M. A. Green, A. Ho-Baillie, and H. J. Snaith, „The emergence of perovskite solar cells“, Nature Photonics **8**, 506–514 (2014).

[50] M. Saliba, T. Matsui, J.-Y. Seo, K. Domanski, J.-P. Correa-Baena, M. K. Nazeeruddin, S. M. Zakeeruddin, W. Tress, A. Abate, A. Hagfeldt, and M. Grätzel, „Cesium-containing triple cation perovskite solar cells: improved stability, reproducibility and high efficiency“, Energy & Environmental Science **9**, 1989–1997 (2016).

[51] „Directive 2011/65/EU of the European Parliament and of the Council of 8 June 2011 on the restriction of the use of certain hazardous substances in electrical and electronic equipment“, Official Journal of the European Union **174**, 88–110 (2011).

[52] M. Presselt, F. Herrmann, H. Hoppe, S. Shokhovets, E. Runge, and G. Gobsch, „Influence of phonon scattering on exciton and charge diffusion in polymer-fullerene solar cells“, Advanced Energy Materials **2**, 999–1003 (2012).

[53] C. L. Braun, „Electric field assisted dissociation of charge transfer states as a mechanism of photocarrier production“, The Journal of Chemical Physics **80**, 4157–4161 (1984).

[54] T. C. Banwell and A. Jayakumar, „Exact analytical solution for current flow through diode with series resistance“, Electronics Letters **36**, 291 (2000).

[55] A. Panda, C. K. Renshaw, A. Oskooi, K. Lee, and S. R. Forrest, „Excited state and charge dynamics of hybrid organic/inorganic heterojunctions. II. Experiment“, Physical Review B - Condensed Matter and Materials Physics **90**, 045303 (2014).

[56] J. C. Blakesley and D. Neher, „Relationship between energetic disorder and open-circuit voltage in bulk heterojunction organic solar cells“, Physical Review B - Condensed Matter and Materials Physics **84**, 075210 (2011).

[57] American Society for Testing and Materials, „ASTM G173-03(2012), Standard Tables for Reference Solar Spectral Irradiances: Direct Normal and Hemispherical on 37 Degrees Tilted Surface“, 1–21 (2012).

[58] T. Kirchartz, J. Mattheis, and U. Rau, „Detailed balance theory of excitonic and bulk heterojunction solar cells“, Physical Review B - Condensed Matter and Materials Physics **78**, 235320 (2008).

[59] N. C. Giebink, G. P. Wiederrecht, M. R. Wasielewski, and S. R. Forrest, „Thermodynamic efficiency limit of excitonic solar cells“, Physical Review B - Condensed Matter and Materials Physics **83**, 195326 (2011).

[60] G. R. Kirchhoff, „Ueber das Verhältniss zwischen dem Emissionsvermögen und dem Absorptionsvermögen der Körper für Wärme und Licht“, Annalen der Physik **185**, 275–301 (1860).

[61] U. Rau, „Reciprocity relation between photovoltaic quantum efficiency and electroluminescent emission of solar cells“, Physical Review B - Condensed Matter and Materials Physics **76**, 85303 (2007).

[62] R. A. Marcus, „Relation between Charge Transfer Absorption and Fluorescence Spectra and the Inverted Region“, The Journal of Physical Chemistry **93**, 3078–3086 (1989).

[63] H. Bässler and B. Schweitzer, „Site-Selective Fluorescence Spectroscopy of Conjugated Polymers and Oligomers“, Accounts of Chemical Research **32**, 173–182 (1999).

[64] K. Vandewal, J. Benduhn, S. Schellhammer, T. Vangerven, J. E. Rückert, F. Piersimoni, R. Scholz, O. Zeika, S. Barlow, D. Neher, S. R. Marder, J. V. Manca, D. Spoltore, G. Cuniberti, and F. Ortmann, „Charge-Transfer Absorption Tails of Photovoltaic Donor:C_{60} Blends Provide Insight into Thermally Activated Vibrations and Polaron Relaxation“, Journal of the American Chemical Society **139**, 1699–1704 (2017).

[65] K. Tvingstedt and C. Deibel, „Temperature Dependence of Ideality Factors in Organic Solar Cells and the Relation to Radiative Efficiency“, Advanced Energy Materials **6**, 1502230 (2016).

[66] T. Kirchartz, F. Deledalle, P. S. Tuladhar, J. R. Durrant, and J. Nelson, „On the differences between dark and light ideality factor in polymer:Fullerene solar cells“, Journal of Physical Chemistry Letters **4**, 2371–2376 (2013).

[67] A. Cuevas, „The recombination parameter J_0“, Energy Procedia **55**, 53–62 (2014).

[68] W. J. Potscavage Jr., S. Yoo, and B. Kippelen, „Origin of the open-circuit voltage in multilayer heterojunction organic solar cells“, Applied Physics Letters **93**, 193308 (2008).

[69] M. Wolf and H. Rauschenbach, „Series resistance effects measurements“, Advanced Energy Conversion **3**, 455–479 (1963).

[70] R. A. Sinton and A. Cuevas, „A quasi-steady-state open-circuit voltage method for solar cell characterization“, Proceedings of the 16th European Photovoltaic Solar Energy Conference, 1152–1155 (2000).

[71] V. D. Mihailetchi, L. J. A. Koster, J. C. Hummelen, and P. W. M. Blom, „Photocurrent generation in polymer-fullerene bulk heterojunctions“, Physical Review Letters **93**, 19–22 (2004).

[72] S. Albrecht, W. Schindler, J. Kurpiers, J. Kniepert, J. C. Blakesley, I. Dumsch, S. Allard, K. Fostiropoulos, U. Scherf, and D. Neher, „On the Field Dependence of Free Charge Carrier Generation and Recombination of PCPDTBT/PC$_{70}$BM: Influence of Solvent Additives“, The Journal of Physical Chemistry Letters **3**, 640–645 (2012).

[73] N. C. Giebink, G. P. Wiederrecht, M. R. Wasielewski, and S. R. Forrest, „Ideal diode equation for organic heterojunctions. I. Derivation and application“, Physical Review B - Condensed Matter and Materials Physics **82**, 155305 (2010).

[74] T. Förster, „Zwischenmolekulare Energiewanderung und Fluoreszenz“, Annalen der Physik **437**, 55–75 (1948).

[75] D. L. Dexter, „A Theory of Sensitized Luminescence in Solids“, The Journal of Chemical Physics **21**, 836–850 (1953).

[76] E. J. W. List, C. H. Kim, J. Shinar, A. Pogantsch, G. Leising, and W. Graupner, „Charged defects in highly emissive organic wide-band-gap semiconductors“, Applied Physics Letters **76**, 2083–2085 (2000).

[77] O. V. Mikhnenko, F. Cordella, A. B. Sieval, J. C. Hummelen, P. W. M. Blom, and M. A. Loi, „Temperature Dependence of Exciton Diffusion in Conjugated Polymers“, The Journal of Physical Chemistry B **112**, 11601–11604 (2008).

[78] S. Athanasopoulos, E. V. Emelianova, A. B. Walker, and D. Beljonne, „Exciton diffusion in energetically disordered organic materials“, Physical Review B - Condensed Matter and Materials Physics **80**, 195209 (2009).

[79] P. E. Shaw, A. Ruseckas, and I. D. W. Samuel, „Exciton diffusion measurements in poly(3-hexylthiophene)“, Advanced Materials **20**, 3516–3520 (2008).

[80] L. D. Landau and S. I. Pekar, „Effective Mass of a Polaron“, Journal of Experimental and Theoretical Physics **18**, 419–423 (1948).

[81] T. Holstein, „Studies of Polaron Motion: Part 1. The Molecular-Crystal Model“, Annals of Physics **8**, 325–342 (1959).

[82] I. I. Fishchuk, A. K. Kadashchuk, J. Genoe, M. Ullah, H. Sitter, T. B. Singh, N. S. Sariciftci, and H. Bässler, „Temperature dependence of the charge carrier mobility in disordered organic semiconductors at large carrier concentrations“, Physical Review B - Condensed Matter and Materials Physics **81**, 045202 (2010).

[83] G. Dicker, M. P. D. Haas, J. M. Warman, D. M. D. Leeuw, and L. D. A. Siebbeles, „The Disperse Charge-Carrier Kinetics in Regioregular Poly (3-hexylthiophene)“, Journal of Physical Chemistry B **108**, 17818–17824 (2004).

[84] E. Johansson and S. Larsson, „Electronic structure and mechanism for conductivity in thiophene oligomers and regioregular polymer“, Synthetic Metals **144**, 183–191 (2004).

[85] W. Meyer and H. Neldel, „Ueber die Beziehungen zwischen der Energiekonstanten und der Mengenkonstanten a in der Leitwerts Temperaturformel bei oxydischen Halbleitern“, Zeitschrift für technische Physik **18**, 588 (1937).

[86] R. J. Kline, M. D. McGehee, E. N. Kadnikova, J. Liu, J. M. J. Fréchet, and M. F. Toney, „Dependence of regioregular poly(3-hexylthiophene) film morphology and field-effect mobility on molecular weight“, Macromolecules **38**, 3312–3319 (2005).

[87] R. Noriega, J. Rivnay, K. Vandewal, F. P. V. Koch, N. Stingelin, P. Smith, M. F. Toney, and A. Salleo, „A general relationship between disorder, aggregation and charge transport in conjugated polymers“, Nature Materials **12**, 1038–1044 (2013).

[88] N. F. Mott and R. W. Gurney, *Electronic processes in ionic crystals* (Clarendon Press, 1940).

[89] Ü. Özgür, Y. I. Alivov, C. Liu, A. Teke, M. A. Reshchikov, S. Doğan, V. Avrutin, S. J. Cho, and H. Morkoç, „A comprehensive review of ZnO materials and devices“, Journal of Applied Physics **98**, 041301 (2005).

[90] P. Ravirajan, A. M. Peiró, M. K. Nazeeruddin, M. Grätzel, D. D. C. Bradley, J. R. Durrant, and J. Nelson, „Hybrid polymer/zinc oxide photovoltaic devices with vertically oriented ZnO nanorods and an amphiphilic molecular interface layer“, Journal of Physical Chemistry B **110**, 7635–7639 (2006).

[91] Public Domain, *Wurtzite Crystal Structure*, `http://commons.wikimedia.org/wiki/File:Wurtzite_polyhedra.png` (visited on 04/10/2018).

[92] H. Morkoç and Ü. Özgür, *Zinc Oxide: Fundamentals, Materials and Device Technology* (Wiley-VCH Verlag GmbH & Co. KGaA, Weinheim, Germany, 2009).

[93] R. Heinhold, G. T. Williams, S. P. Cooil, D. a. Evans, and M. W. Allen, „Influence of polarity and hydroxyl termination on the band bending at ZnO surfaces“, Physical Review B - Condensed Matter and Materials Physics **88**, 235315 (2013).

[94] S. Akhter, K. Lui, and H. H. Kung, „Comparison of the chemical properties of the zinc-polar, the oxygen-polar, and the nonpolar surfaces of zinc oxide“, The Journal of Physical Chemistry **89**, 1958–1964 (1985).

[95] S. Blumstengel, S. Sadofev, and F. Henneberger, „Electronic coupling of optical excitations in organic/inorganic semiconductor hybrid structures“, New Journal of Physics **10**, 065010 (2008).

[96] R. Schlesinger, Y. Xu, O. T. Hofmann, S. Winkler, J. Frisch, J. Niederhausen, A. Vollmer, S. Blumstengel, F. Henneberger, P. Rinke, M. Scheffler, and N. Koch, „Controlling the work function of ZnO and the energy-level alignment at the interface to organic semiconductors with a molecular electron acceptor“, Physical Review B - Condensed Matter and Materials Physics **87**, 155311 (2013).

[97] S. Sadofev, S. Blumstengel, J. Cui, J. Puls, S. Rogaschewski, P. Schäfer, and F. Henneberger, „Visible band-gap ZnCdO heterostructures grown by molecular beam epitaxy“, Applied Physics Letters **89**, 201907 (2006).

[98] S. Sadofev, S. Blumstengel, J. Cui, J. Puls, S. Rogaschewski, P. Schäfer, Y. G. Sadofyev, and F. Henneberger, „Growth of high-quality ZnMgO epilayers and ZnO/ZnMgO quantum well structures by radical-source molecular-beam epitaxy on sapphire“, Applied Physics Letters **87**, 091903 (2005).

[99] H. Yin, J. Chen, Y. Wang, J. Wang, and H. Guo, „Composition dependent band offsets of ZnO and its ternary alloys“, Scientific Reports **7**, 41567 (2017).

[100] G. Coli and K. K. Bajaj, „Excitonic transitions in ZnO/MgZnO quantum well heterostructures“, Applied Physics Letters **78**, 2861–2863 (2001).

[101] H. H. Zhang, X. H. Pan, B. Lu, J. Y. Huang, P. Ding, W. Chen, H. P. He, J. G. Lu, S. S. Chen, and Z. Z. Ye, „Mg composition dependent band offsets of $Zn_{1-x}Mg_xO$/ZnO heterojunctions“, Physical Chemistry Chemical Physics **15**, 11231–11235 (2013).

[102] E. Shanthi, V. Dutta, A. Banerjee, and K. L. Chopra, „Electrical and optical properties of undoped and antimony-doped tin oxide films“, Journal of Applied Physics **51**, 6243–6251 (1980).

[103] K. Rachut, C. Körber, J. Brötz, and A. Klein, „Growth and surface properties of epitaxial SnO_2“, Physica Status Solidi (a) **211**, 1997–2004 (2014).

[104] Public Domain, *Rutile Crystal Structure*, `http://commons.wikimedia.org/wiki/File:Rutile-unit-cell-3D-balls.png` (visited on 04/10/2018).

[105] V. T. Agekyan, „Spectroscopic Properties of Semiconductor Crystals with Direct Forbidden Energy Gap“, physica status solidi (a) **43**, 11–42 (1977).

[106] M. Batzill, A. M. Chaka, and U. Diebold, „Surface oxygen chemistry of a gas-sensing material: SnO_2 (101)“, Europhysics Letters (EPL) **65**, 61–67 (2004).

[107] S. S. Pan, Y. H. Tian, Y. Y. Luo, Y. X. Zhang, S. Wang, and G. H. Li, „Surface localized exciton emission from undoped SnO_2 nanocrystal films“, Applied Physics Letters **97**, 2–5 (2010).

[108] S. Sadofev, S. Kalusniak, P. Schäfer, and F. Henneberger, „Molecular beam epitaxy of n-Zn(Mg)O as a low-damping plasmonic material at telecommunication wavelengths“, Applied Physics Letters **102**, 181905 (2013).

[109] M. E. White, O. Bierwagen, M. Y. Tsai, and J. S. Speck, „Electron transport properties of antimony doped SnO_2 single crystalline thin films grown by plasma-assisted molecular beam epitaxy“, Journal of Applied Physics **106**, 093704 (2009).

[110] V. Skrypnychuk, G. J. A. Wetzelaer, P. I. Gordiichuk, S. C. Mannsfeld, A. Herrmann, M. F. Toney, and D. R. Barbero, „Ultrahigh Mobility in an Organic Semiconductor by Vertical Chain Alignment“, Advanced Materials **28**, 2359–2366 (2016).

[111] A. Hamidi-Sakr, L. Biniek, S. Fall, and M. Brinkmann, „Precise Control of Lamellar Thickness in Highly Oriented Regioregular Poly(3-Hexylthiophene) Thin Films Prepared by High-Temperature Rubbing: Correlations with Optical Properties and Charge Transport“, Advanced Functional Materials **26**, 408–420 (2016).

[112] Z. L. Guan, J. Bok Kim, Y. L. Loo, and A. Kahn, „Electronic structure of the poly(3-hexylthiophene):indene-C_{60} bisadduct bulk heterojunction“, Journal of Applied Physics **110**, 043719 (2011).

[113] C. Deibel, D. Mack, J. Gorenflot, A. Schöll, S. Krause, F. Reinert, D. Rauh, and V. Dyakonov, „Energetics of excited states in the conjugated polymer poly(3-hexylthiophene)“, Physical Review B - Condensed Matter and Materials Physics **81**, 085202 (2010).

[114] C. Poelking, M. Tietze, C. Elschner, S. Olthof, D. Hertel, B. Baumeier, F. Würthner, K. Meerholz, K. Leo, and D. Andrienko, „Impact of mesoscale order on open-circuit voltage in organic solar cells“, Nature Materials **14**, 434–439 (2015).

[115] A. W. Dweydari and C. H. B. Mee, „Work function measurements on (100) and (110) surfaces of silver“, Physica Status Solidi (a) **27**, 223–230 (1975).

[116] E. L. Ratcliff, B. Zacher, and N. R. Armstrong, „Selective Interlayers and Contacts in Organic Photovoltaic Cells“, Journal of Physical Chemistry Letters **2**, 1337–1350 (2011).

[117] L. J. Brillson and Y. Lu, „ZnO Schottky barriers and Ohmic contacts“, Journal of Applied Physics **109**, 121301 (2011).

[118] N. K. Reddy, Q. Ahsanulhaq, J. H. Kim, M. Devika, and Y. B. Hahn, „Selection of non-alloyed ohmic contacts for ZnO nanostructure based devices“, Nanotechnology **18**, 445710 (2007).

[119] M. Kröger, S. Hamwi, J. Meyer, T. Riedl, W. Kowalsky, and A. Kahn, „Role of the deep-lying electronic states of MoO_3 in the enhancement of hole-injection in organic thin films“, Applied Physics Letters **95**, 123301 (2009).

[120] J. Meyer, R. Khalandovsky, P. Görrn, and A. Kahn, „MoO_3 Films Spin-Coated from a Nanoparticle Suspension for Efficient Hole-Injection in Organic Electronics“, Advanced Materials **23**, 70–73 (2011).

[121] D. Y. Kim, J. Subbiah, G. Sarasqueta, F. So, H. Ding, and Y. Gao, „The effect of molybdenum oxide interlayer on organic photovoltaic cells“, Applied Physics Letters **95**, 093304 (2009).

[122] R. C. Shallcross, T. Stubhan, E. L. Ratcliff, A. Kahn, C. J. Brabec, and N. R. Armstrong, „Quantifying the extent of contact doping at the interface between high work function electrical contacts and poly(3-hexylthiophene) (P3HT)“, Journal of Physical Chemistry Letters **6**, 1303–1309 (2015).

[123] T. A. Papadopoulos, J. Meyer, H. Li, Z. Guan, A. Kahn, and J. L. Brédas, „Nature of the interfaces between stoichiometric and under-stoichiometric MoO_3 and 4,4’-N,N’-dicarbazole-biphenyl: A combined theoretical and experimental study“, Advanced Functional Materials **23**, 6091–6099 (2013).

[124] M. Wang, Y. Li, H. Huang, E. D. Peterson, W. Nie, W. Zhou, W. Zeng, W. Huang, G. Fang, N. Sun, X. Zhao, and D. L. Carroll, „Thickness dependence of the MoO_3 blocking layers on ZnO nanorod-inverted organic photovoltaic devices“, Applied Physics Letters **98**, 103305 (2011).

[125] D. W. Zhao, S. T. Tan, L. Ke, P. Liu, A. K. K. Kyaw, X. W. Sun, G. Q. Lo, and D. L. Kwong, „Optimization of an inverted organic solar cell“, Solar Energy Materials and Solar Cells **94**, 985–991 (2010).

[126] P. A. Maksym and J. L. Beeby, „A theory of RHEED“, Surface Science **110**, 423–438 (1981).

[127] A. Einstein, „Ueber einen die Erzeugung und Verwandlung des Lichtes betreffenden heuristischen Gesichtspunkt“, Annalen der Physik **322**, 132–148 (1905).

[128] F. Reinert and S. Hüfner, „Photoemission-Spectroscopy - from Early Days to Recent Applications“, New Journal of Physics **7**, 97 (2005).

[129] R. Schlaf, *Calibration of Photoemission Spectra and Work Function Determination*, `http://rsl.eng.usf.edu/Documents/Tutorials/PEScalibration.pdf` (visited on 04/10/2018).

[130] S. Krause, M. B. Casu, A. Schöll, and E. Umbach, „Determination of transport levels of organic semiconductors by UPS and IPS“, New Journal of Physics **10**, 085001 (2008).

[131] F. Verbakel, S. C. J. Meskers, and R. A. J. Janssen, „Electronic memory effects in diodes of zinc oxide nanoparticles in a matrix of polystyrene or poly(3-hexylthiophene)“, Journal of Applied Physics **102**, 083701 (2007).

[132] Y. Busby, S. Nau, S. Sax, E. J. W. List-Kratochvil, J. Novak, R. Banerjee, F. Schreiber, and J. J. Pireaux, „Direct observation of conductive filament formation in Alq3 based organic resistive memories“, Journal of Applied Physics **118**, 075501 (2015).

[133] S. Nau, C. Wolf, S. Sax, and E. J. W. List-Kratochvil, „Organic non-volatile resistive photo-switches for flexible image detector arrays“, Advanced Materials **27**, 1048–1052 (2015).

[134] S. Nau, C. Wolf, K. Popovic, A. Blümel, F. Santoni, A. Gagliardi, A. di Carlo, S. Sax, and E. J. W. List-Kratochvil, „Inkjet-printed resistive switching memory based on organic dielectric materials: From single elements to array technology“, Advanced Electronic Materials **1**, 1400003 (2015).

[135] G. Binnig and C. F. Quate, „Atomic Force Microscope“, Physical Review Letters **56**, 930–933 (1986).

[136] B. Cappella and G. Dietler, „Force-distance curves by atomic force microscopy“, Surface Science Reports **34**, 1–104 (1999).

[137] G. Meyer and N. M. Amer, „Novel optical approach to atomic force microscopy“, Applied Physics Letters **53**, 1045–1047 (1988).

[138] H. Tamura and I. Burghardt, „Ultrafast Charge Separation in Organic Photovoltaics Enhanced by Charge Delocalization and Vibronically Hot Exciton Dissociation“, Journal of the American Chemical Society **135**, 16364–16367 (2013).

[139] A. A. Bakulin, A. Rao, V. G. Pavelyev, P. H. M. van Loosdrecht, M. S. Pshenichnikov, D. Niedzialek, J. Cornil, D. Beljonne, and R. H. Friend, „The Role of Driving Energy and Delocalized States for Charge Separation in Organic Semiconductors“, Science **335**, 1340–1344 (2012).

[140] M. Stolterfoht, A. Armin, B. Philippa, and D. Neher, „The Role of Space Charge Effects on the Competition between Recombination and Extraction in Solar Cells with Low-Mobility Photoactive Layers“, Journal of Physical Chemistry Letters **7**, 4716–4721 (2016).

[141] J. A. Aranovich, D. Golmayo, A. L. Fahrenbruch, and R. H. Bube, „Photovoltaic properties of ZnO/CdTe heterojunctions prepared by spray pyrolysis“, Journal of Applied Physics **51**, 4260–4268 (1980).

[142] M. S. White, D. C. Olson, S. E. Shaheen, N. Kopidakis, and D. S. Ginley, „Inverted bulk-heterojunction organic photovoltaic device using a solution-derived ZnO underlayer“, Applied Physics Letters **89** (2006) `10.1063/1.2359579`.

[143] Y. Vaynzof, D. Kabra, L. Zhao, P. K. H. Ho, A. T.-S. Wee, and R. H. Friend, „Improved photoinduced charge carriers separation in organic-inorganic hybrid photovoltaic devices“, Applied Physics Letters **97**, 033309 (2010).

[144] K. P. Musselman, S. Albert-Seifried, R. L. Z. Hoye, A. Sadhanala, D. Muñoz-Rojas, J. L. MacManus-Driscoll, and R. H. Friend, „Improved Exciton Dissociation at Semiconducting Polymer:ZnO Donor:Acceptor Interfaces via Nitrogen Doping of ZnO“, Advanced Functional Materials **24**, 3562–3570 (2014).

[145] Y. Sevinchan, P. E. Hopkinson, A. A. Bakulin, J. Herz, M. Motzkus, and Y. Vaynzof, „Improving charge separation across a hybrid oxide/polymer interface by Cs doping of the metal oxide“, Advanced Materials Interfaces **3**, 1500616 (2016).

[146] D. C. Olson, S. E. Shaheen, M. S. White, W. J. Mitchell, M. F. A. M. Van Hest, R. T. Collins, and D. S. Ginley, „Band-offset engineering for enhanced open-circuit voltage in polymer-oxide hybrid solar cells“, Advanced Functional Materials **17**, 264–269 (2007).

[147] F. C. Spano, J. Clark, C. Silva, and R. H. Friend, „Determining exciton coherence from the photoluminescence spectral line shape in poly(3-hexylthiophene) thin films“, Journal of Chemical Physics **130**, 074904 (2009).

[148] J. F. Muth, R. M. Kolbas, a. K. Sharma, S. Oktyabrsky, and J. Narayan, „Excitonic structure and absorption coefficient measurements of ZnO single crystal epitaxial films deposited by pulsed laser deposition“, Journal of Applied Physics **85**, 7884–7887 (1999).

[149] E. D. Spoerke, M. T. Lloyd, E. M. McCready, D. C. Olson, Y. J. Lee, and J. W. P. Hsu, „Improved performance of poly(3-hexylthiophene)/zinc oxide hybrid photovoltaics modified with interfacial nanocrystalline cadmium sulfide“, Applied Physics Letters **95**, 95–98 (2009).

[150] A. Tada, Y. Geng, Q. Wei, K. Hashimoto, and K. Tajima, „Tailoring organic heterojunction interfaces in bilayer polymer photovoltaic devices“, Nature Materials **10**, 450–455 (2011).

[151] M. Runge, „Verlustmechanismen bei der Ladungsträgererzeugung in hybriden ZnO/ P3HT-Photovoltaikzellen“, Bachelor thesis (Humboldt-Universität zu Berlin, 2017).

[152] T. Schultz, R. Schlesinger, J. Niederhausen, F. Henneberger, S. Sadofev, S. Blumstengel, A. Vollmer, F. Bussolotti, J.-P. Yang, S. Kera, K. Parvez, N. Ueno, K. Müllen, and N. Koch, „Tuning the work function of GaN with organic molecular acceptors“, Physical Review B - Condensed Matter and Materials Physics **93**, 125309 (2016).

[153] S. Blumstengel, S. Sadofev, C. Xu, J. Puls, R. Johnson, H. Glowatzki, N. Koch, and F. Henneberger, „Electronic coupling in organic-inorganic semiconductor hybrid structures with type-II energy level alignment“, Physical Review B - Condensed Matter and Materials Physics **77**, 085323 (2008).

[154] B. H. Ishii, K. Sugiyama, E. Ito, and K. Seki, „Energy Level Alignment and Interfacial Electronic Structures at Organic/Metal and Organic/Organic Interfaces“, Advanced Materials **11**, 605–625 (1999).

[155] V. C. Nikolis, J. Benduhn, F. Holzmueller, F. Piersimoni, M. Lau, O. Zeika, D. Neher, C. Koerner, D. Spoltore, and K. Vandewal, „Reducing Voltage Losses in Cascade Organic Solar Cells while Maintaining High External Quantum Efficiencies“, Advanced Energy Materials **7**, 1700855 (2017).

[156] H. Sirringhaus, P. J. Brown, R. H. Friend, M. M. Nielsen, K. Bechgaard, B. M. W. Langeveld-Voss, a. J. H. Spiering, R. a. J. Janssen, E. W. Meijer, P. Herwig, and D. M. de Leeuw, „Two-dimensional charge transport in self-organized, high-mobility conjugated polymers“, Nature **401**, 685–688 (1999).

[157] J. Ruher, N. Colaneri, D. Bradley, R. Friend, and G. Wegner, „Photoexcited states in poly(3-alkyl thienylenes)“, Journal of Physics: Condensed Matter **2**, 5465–5477 (1999).

[158] P. V. Kamat, N. M. Dimitrijevic, and A. J. Nozik, „Dynamic Burstein-Moss shift in semiconductor colloids“, The Journal of Physical Chemistry **93**, 2873–2875 (1989).

[159] N. Shimosako, Y. Inose, H. Satoh, K. Kinjo, T. Nakaoka, T. Oto, K. Kishino, and K. Ema, „Carrier-density dependence of photoluminescence from localized states in InGaN/GaN quantum wells in nanocolumns and a thin film“, Journal of Applied Physics **118**, 1–6 (2015).

[160] F. Piersimoni, S. Zeiske, J. Benduhn, R. Schlesinger, N. Koch, K. Vandewal, and D. Neher, „Investigation of the hybrid charge transfer state at ZnO/organic interfaces“, Verhandlungen DPG Frühjahrstagung (2016).

[161] J. E. Northrup, „Atomic and electronic structure of polymer organic semiconductors: P3HT, PQT, and PBTTT“, Physical Review B - Condensed Matter and Materials Physics **76**, 245202 (2007).

[162] C. Schwarz, S. Tscheuschner, J. Frisch, S. Winkler, N. Koch, H. Bässler, and A. Köhler, „Role of the effective mass and interfacial dipoles on exciton dissociation in organic donor-acceptor solar cells“, Physical Review B - Condensed Matter and Materials Physics **87**, 155205 (2013).

[163] B. van Zeghbroeck, *Principles of Semiconductor Devices*, (2007) `http://ecee.colorado.edu/~bart/book/book/index.html` (visited on 04/10/2018).

[164] P. B. Deotare, W. Chang, E. Hontz, D. N. Congreve, L. Shi, P. D. Reusswig, B. Modtland, M. E. Bahlke, C. K. Lee, A. P. Willard, V. Bulović, T. Van Voorhis, and M. A. Baldo, „Nanoscale transport of charge-transfer states in organic donor-acceptor blends“, Nature materials **14**, 1130–1134 (2015).

[165] B. Xu, J. Lowe, and S. Holdcroft, „Non-radiative decay channels in poly(3-hexylthiophene) and poly(3-dodecylthiophene) and how to control them by molecular engineering“, Thin Solid Films **243**, 638–642 (1994).

[166] S. Cook, A. Furube, and R. Katoh, „Analysis of the excited states of regioregular polythiophene P3HT“, Energy & Environmental Science **1**, 294–299 (2008).

[167] G. R. Hayes, I. D. W. Samuel, and R. T. Phillips, „Exciton dynamics in electroluminescent polymers studied by femtosecond time-resolved photoluminescence spectroscopy“, Physical Review B - Condensed Matter and Materials Physics **52**, 569–572 (1995).

[168] B. Ferreira, P. F. Da Silva, J. S. Seixas De Melo, J. Pina, and A. MaçAnita, „Excited-state dynamics and self-organization of poly(3-hexylthiophene) (P3HT) in solution and thin films“, Journal of Physical Chemistry B **116**, 2347–2355 (2012).

[169] B. Bernardo, D. Cheyns, B. Verreet, R. D. Schaller, B. P. Rand, and N. C. Giebink, „Delocalization and dielectric screening of charge transfer states in organic photovoltaic cells“, Nature communications **5**, 3245 (2014).

[170] M. Sundberg, O. Inganäs, S. Stafström, G. Gustafsson, and B. Sjögren, „Optical absorption of poly(3-alkylthiophenes) at low temperatures“, Solid State Communications **71**, 435–439 (1989).

[171] E. List, C. Creely, G. Leising, N. Schulte, A. Schlüter, U. Scherf, K. Müllen, and W. Graupner, „Excitation energy migration in highly emissive semiconducting polymers“, Chemical Physics Letters **325**, 132–138 (2000).

[172] M. Noltemeyer, F. Bertram, T. Hempel, B. Bastek, A. Polyakov, J. Christen, M. Brandt, M. Lorenz, and M. Grundmann, „Excitonic transport in ZnO“, Journal of Materials Research **27**, 2225–2231 (2012).

[173] D. Bartesaghi, I. D. C. Pérez, J. Kniepert, S. Roland, M. Turbiez, D. Neher, and L. J. A. Koster, „Competition between recombination and extraction of free charges determines the fill factor of organic solar cells“, Nature Communications **6**, 7083 (2015).

[174] W. Tress, A. Petrich, M. Hummert, M. Hein, K. Leo, and M. Riede, „Imbalanced mobilities causing S-shaped IV curves in planar heterojunction organic solar cells“, Applied Physics Letters **98**, 063301 (2011).

[175] J. Wagner, M. Gruber, A. Wilke, Y. Tanaka, K. Topczak, A. Steindamm, U. Hörmann, A. Opitz, Y. Nakayama, H. Ishii, J. Pflaum, N. Koch, and W. Brütting, „Identification of different origins for s-shaped current voltage characteristics in planar heterojunction organic solar cells“, Journal of Applied Physics **111**, 054509 (2012).

[176] K. Vandewal, Z. Ma, J. Bergqvist, Z. Tang, E. Wang, P. Henriksson, K. Tvingstedt, M. R. Andersson, F. Zhang, and O. Inganäs, „Quantification of Quantum Efficiency and Energy Losses in Low Bandgap Polymer:Fullerene Solar Cells with High Open-Circuit Voltage“, Advanced Functional Materials **22**, 3480–3490 (2012).

[177] C. Körber, P. Ágoston, and A. Klein, „Surface and bulk properties of sputter deposited undoped and Sb-doped SnO_2 thin films“, Sensors and Actuators, B: Chemical **139**, 665–672 (2009).

[178] J. Oviedo and M. J. Gillan, „The energetics and structure of oxygen vacancies on the SnO_2 (110) surface“, Surface Science **467**, 35–48 (2000).

[179] S. Kumar, C. Mukherjee, and D. M. Phase, „Valence Band Onset and Valence Plasmons of SnO_2 and $In_{2-x}Sn_xO_3$ Thin Films“, ArXiv e-prints, arXiv:1406.3211 [cond-mat.mtrl-sci] (2014).

[180] P. C. Hollamby, P. S. Aldridge, G. Moretti, and R. G. Egdell, „The influence of oxygen deficiency and Sb doping on inverse photoemission spectra of SnO_2“, Surface Science **280**, 393–397 (1993).

[181] R. A. Street, A. Krakaris, and S. R. Cowan, „Recombination through different types of localized states in organic solar cells“, Advanced Functional Materials **22**, 4608–4619 (2012).

[182] S. A. Hawks, G. Li, Y. Yang, and R. A. Street, „Band tail recombination in polymer: Fullerene organic solar cells“, Journal of Applied Physics **116**, 074503 (2014).

[183] U. Hörmann, „V_{OC} from a morphology point of view: On the open circuit voltage of polycrystalline organic heterojunction solar cells“, PhD dissertation (Universität Augsburg, 2014).

[184] A. Opitz, J. Frisch, R. Schlesinger, A. Wilke, and N. Koch, „Energy level alignment at interfaces in organic photovoltaic devices“, Journal of Electron Spectroscopy and Related Phenomena **190**, 12–24 (2013).

[185] M. Calvin, „Photosynthesis As a Resource for Energy and Materials“, Photochemistry and Photobiology **23**, 425–444 (1976).

[186] T. E. Murphy, K. Moazzami, and J. D. Phillips, „Trap-related photoconductivity in ZnO epilayers“, Journal of Electronic Materials **35**, 543–549 (2006).

Publications

Scientific Publications

[1] M. Eyer, J. Frisch, S. Sadofev, E. List-Kratochvil, N. Koch, and S. Blumstengel, „Role of Hybrid Charge Transfer States in the Charge Generation at ZnMgO/P3HT Heterojunctions“, The Journal of Physical Chemistry C **121**, 21955–21961 (2017).

[2] B. Kobin, J. Schwarz, B. Braun-Cula, M. Eyer, A. Zykov, S. Kowarik, S. Blumstengel, and S. Hecht, „Spiro-Bridged Ladder-Type Oligo(para-phenylene)s: Fine Tuning Solid State Structure and Optical Properties“, Advanced Functional Materials **27**, 1704077 (2017).

[3] M. Eyer, S. Sadofev, J. Puls, and S. Blumstengel, „Charge transfer excitons at ZnMgO/P3HT heterojunctions: Relation to photovoltaic performance“, Applied Physics Letters **107**, 221602 (2015).

[4] S.-Y. Lee, M. Widmann, T. Rendler, M. W. Doherty, T. M. Babinec, S. Yang, M. Eyer, P. Siyushev, B. J. M. Hausmann, M. Loncar, Z. Bodrog, A. Gali, N. B. Manson, H. Fedder, and J. Wrachtrup, „Readout and control of a single nuclear spin with a metastable electron spin ancilla“, Nature Nanotechnology **8**, 487–492 (2013).

Submissions to Scientific Conferences

[1] M. Eyer, S. Kickhöfel, J. Frisch, S. Sadofev, J. Puls, E. List-Kratochvil, N. Koch, and S. Blumstengel, „Revealing the Loss Mechanisms in ZnO/Organic Hybrid Solar Cells“, Oral presentation, DPG Frühjahrstagung (Deutsche Physikalische Gesellschaft, Dresden, 2017).

[2] M. Eyer, J. Frisch, S. Sadofev, J. Puls, E. List-Kratochvil, N. Koch, and S. Blumstengel, „Hybrid Charge Transfer Excitons and Interface Energetics at ZnMgO/P3HT Heterojunctions“, Poster, International Conference on Internal Interfaces ICII-2016 (Philipps-Universität Marburg, 2016).

[3] M. Eyer, S. Sadofev, J. Puls, and S. Blumstengel, „Hybrid Charge Transfer Excitons at ZnMgO/P3HT Interfaces“, Oral presentation, DPG Frühjahrstagung (Deutsche Physikalische Gesellschaft, Regensburg, 2016).

[4] M. Eyer, S. Sadofev, J. Puls, and S. Blumstengel, „Hybrid Charge Transfer Excitons at ZnMgO/P3HT Interfaces“, Poster, Hybrid-Photovoltaics 2015 Symposium (Helmholtz Energie Allianz, Berlin, 2015).

Acknowledgments

This thesis could not have been written without the help of many people.

First of all, I would like to thank Prof. Oliver Benson for taking over the supervision of my scientific work and for providing his guidance to the whole AG Photonik group.

I would like to thank Prof. Emil List-Kratochvil for very interesting discussions and many helpful suggestions. I enjoyed feeling like a welcome guest in the meetings of his hybrid devices group during the last three years.

I would also like to thank Prof. Wolfgang Brütting from the Universität Augsburg for his agreement to be a member of my examination committee and for writing an external evaluation about this thesis.

Special thanks go to Priv.-Doz. Dr. Sylke Blumstengel for providing her help in many ways and consistently believing in the success of our scientific work.

Particularly I would like to thank Dr. Ulrich Hörmann, Dr. Fortunato Piersimoni and Prof. Dieter Neher from the Universität Potsdam for many interesting discussions and for a good and fruitful cooperation in the Collaborative Research Center 951.

Dr. Sergey Sadofev produced the inorganic acceptor layer structures for the planar photodiode devices. Many thanks to him, as well as to Dr. Joachim Puls for his efforts in the establishment of various characterization procedures, particularly the time-resolved electroluminescence spectroscopy.

Thanks a lot to Sebastian Kickhöfel and Matthias Runge for the good collaboration both in the laboratory and in the analysis and interpretation of our results.

I would like to thank Dr. Simon Halm for his scientific help and personal encouragement and for being a great team player in the early days of my work in the AG Photonik group.

My thanks go to Dr. Manuel Gensler and Valentin Reiter-Scherer for readily providing their technical knowledge and tireless help in the AFM characterization laboratory. Dr. Johannes Frisch is thanked for his support in UV photoelectron spectroscopy, and *muchas gracias* to Dr. Vanesa Hortelano Santos for her help in the Hall effect measurements.

Christian Kremer, Dagmar Fahnauer and Elfriede Renger made everything possible by finding solutions to all technical problems and always had an open ear for technical and non-technical issues. I would also like to thank Dr. Peter Schäfer, who provided valuable help on the long way to functioning diode devices by means of scanning electron microscopy.

Sebastian Kickhöfel, Tino Meisel, Evgenij Travkin, Niklas Mutz, Laura Orphal and Dr. Ulrich Hörmann did a great job in proofreading my thesis and gave me lots of comments and suggestions. Thanks a lot to all of you!

Special thanks go to my father Hans Eyer who checked the whole manuscript for errors in English grammar and orthography.

I would like to thank Francesco Bianchi and Dr. Jungtaek Kim for being my friends in the office 3.511 during the early days of my work. I also thank all the other people in and around the AG Photonik group, including Mino Sparenberg, Dr. Michael Höfner, Priv.-Doz. Dr. Ede Wünsche, Dr. Björn Kobin, Dr. Sascha Kalusniak, Dr. Sylvia Schikora, Hala Memmi and Beatrix Matthes for the nice atmosphere. Special thanks go to Dr. Maurizio Roczen for his help in all administrative issues and for a lot of encouragement in difficult times.

Very special thanks to my parents, my brother and my sister for tons of support and encouragement during the years of my work. It would not have been possible to finish this without you.

Particularly I would like to thank my girlfriend Jenny for the motivation she gave to me, for her endless patience and her open ears in case of all kinds of trouble I encountered on my way to the finalization of this thesis. I did it - and so will you! I love you!

Erklärung

Ich erkläre, dass ich die Dissertation selbständig und nur unter Verwendung der von mir gemäß §7 Abs. 3 der Promotionsordnung der Mathematisch-Naturwissenschaftlichen Fakultät angegebenen Hilfen und Hilfsmittel angefertigt habe. Ich habe mich nicht anderwärts um einem Doktorgrad im Promotionsfach Physik beworben und besitze keinen Doktorgrad im Promotionsfach Physik. Die Promotionsordnung der Mathematisch-Naturwissenschaftlichen Fakultät, veröffentlicht im Amtlichen Mitteilungsblatt der Humboldt-Universität zu Berlin Nr. 126/2014 am 18.11.2014, habe ich zur Kenntnis genommen.

Berlin, den 11.04.2018

Moritz Eyer